

Cover Page



Universiteit Leiden



The handle <http://hdl.handle.net/1887/67101> holds various files of this Leiden University dissertation.

Author: Unen, V. van

Title: Mucosal immunology revisited through mass cytometry : from biology to bioinformatics and back

Issue Date: 2018-11-27

Mucosal Immunology revisited through Mass Cytometry

From Biology to Bioinformatics and Back

Vincent van Unen

© 2018 Vincent van Unen, Leiden, the Netherlands

Mucosal Immunology revisited through Mass Cytometry: From Biology to Bioinformatics and Back.

All rights reserved. No part of this thesis may be reproduced or transmitted in any form, by any means, electronic or mechanical without prior written permission of the author, or where appropriate, of the publisher of the articles.

The work presented in this thesis was performed at the Department of Immunohematology and Blood Transfusion of the Leiden University Medical Center in the Netherlands.

ISBN: 978-94-9301-499-2

Printed by: Gildeprint Drukkerijen

Financial support for the publication of this thesis was kindly provided by Fluidigm Corporation.

Mucosal Immunology revisited through Mass Cytometry

From Biology to Bioinformatics and Back

Proefschrift

ter verkrijging van
de graad van Doctor aan de Universiteit Leiden,
op gezag van Rector Magnificus prof. mr. C.J.J.M. Stolker,
volgens besluit van het College voor Promoties
te verdedigen op dinsdag
27 november 2018 klokke 16:15 uur

door

Vincent van Unen

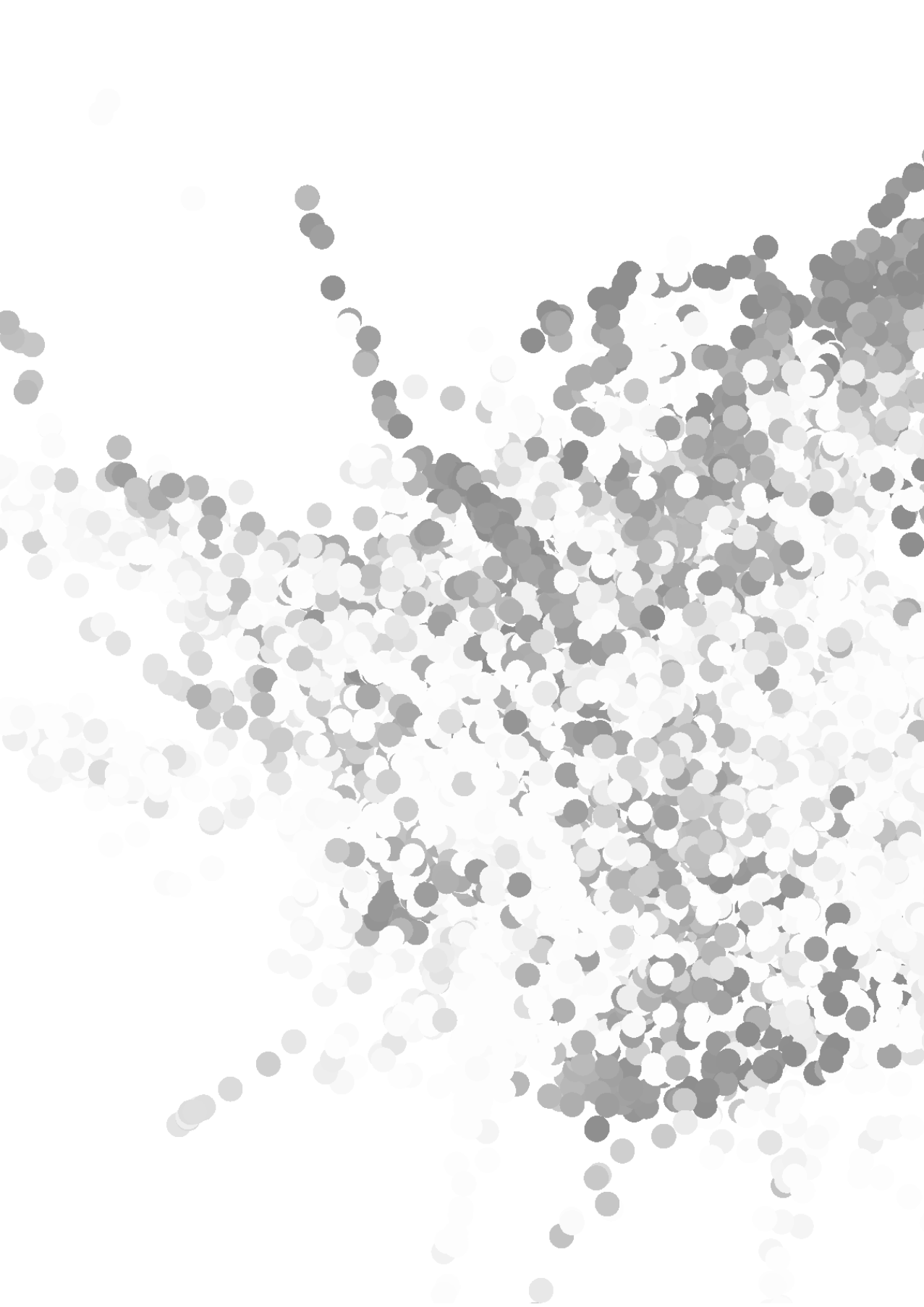
geboren te Vlaardingen
in 1989

Promotor : Prof. Dr. F. Koning

Leden Promotiecommissie : Prof. Dr. F. J. T. Staal
: Prof. Dr. R. E. Mebius
: Prof. Dr. J. Borst

TABLE OF CONTENT

Chapter 1	6
General introduction	
Chapter 2	16
Mass cytometry of the human mucosal immune system reveals tissue- and disease-associated immune subsets	
<i>Immunity</i> 44:5, 1227-1239 (2016)	
Chapter 3	48
Cytosplore: interactive immune cell phenotyping for large single-cell datasets	
<i>Computer Graphics Forum</i> 35:3, 171-180 (2016)	
Chapter 4	72
Visual analysis of mass cytometry data by hierarchical stochastic neighbour embedding reveals rare cell types	
<i>Nature Communications</i> 8:1, 1740 (2017)	
Chapter 5	106
Stratification of immune cell infiltrates in inflammatory bowel disease by high-dimensional mass cytometry	
<i>In preparation</i>	
Chapter 6	138
Mass cytometry reveals innate lymphoid cell differentiation pathways in the human fetal intestine	
<i>Journal of Experimental Medicine</i> 215:5, 1383-1396 (2018)	
Chapter 7	168
Summarising discussion	
Appendices	
Nederlandse samenvatting, list of publications, CV and acknowledgements	





CHAPTER I

General Introduction



CHAPTER I

General Introduction

The immune system

The immune system protects the body against bacterial, viral, and parasitic infections. It is one of the most dynamic and plastic systems in the human body, present in nearly every tissue type. Although the immune system is generally highly efficient, disruptions of homeostasis can occur leading to a variety of immune-mediated diseases, such as diabetes mellitus type I or Crohn's disease. The immune system can be divided into an innate and an adaptive compartment, and their cellular components consist of a variety of different cell populations. The innate immune system represents the first line of defense which comprises of the myeloid cell lineage, including antigen presenting cells, such as macrophages and dendritic cells, and innate lymphocytes, such as natural killer (NK) cells and innate lymphoid cells (ILCs). The adaptive immune system is more specialized and typified by the expression of antigen-specific receptors on B and T lymphocytes, the latter including CD4⁺ T cells and CD8⁺ T cells, and the capacity to develop immunological memory providing superior protection towards pathogens. In addition, we can distinguish innate-like unconventional T cell subsets that reside more prominently at barrier sites, including TCR $\gamma\delta$ cells, NKT cells and mucosal-associated invariant T (MAIT) cells¹. Immune processes are mediated by the crosstalk between these types of cells, tissue-resident as well as circulating immune cells, all interacting in specific micro-environmental contexts. Each of these immune cell types can be phenotypically defined through the expression of specific proteins on the cell surface, referred to as markers hereafter.

Flow cytometry

In the past decades, flow cytometry has been the benchmark technique to analyze markers expressed by individual immune cells, revealing their identity. By selecting a set of fluorochrome-conjugated antibodies that specifically recognize certain markers expressed on the cell surface, subpopulations of interest can be analyzed by measuring the fluorescent emission at the single-cell level. This has allowed us to gain a wide understanding of the composition of the immune system in health and disease². However, the primary drawback of traditional flow cytometry is that the number of markers that can simultaneously be measured is limited by spectral overlap (generally 8-12) (**Figure 1A**). In addition, the design of complex flow

cytometry antibody panels is laborious and challenging due to the spectral overlap. To capture all cell populations across all major innate and adaptive lineages of the immune system simultaneously, a higher level of multiparametric analysis of single cells is required that cannot currently be met with fluorescence-based technologies.

Mass cytometry

Mass cytometry (CyTOF, cytometry by time-of-flight) is a new generation of single-cell analysis technology offering a high-throughput platform for robust characterization of immune cells by overcoming this flow cytometry-intrinsic marker limitation³. The CyTOF is a mass-spectrometer-flow cytometer hybrid which analyzes antibodies conjugated with heavy metal isotopes instead of fluorescent reporters^{4,5}. It is thereby unhampered by interference from spectral overlap. The CyTOF allows the detection of currently up to 42 markers simultaneously, approximately 3-fold more than with traditional flow cytometry, and with much sharper peaks and less crosstalk between channels (**Figure 1B**). Theoretically, the number of markers detectable with mass cytometry could increase to about a 100, once the isotopic purification of metals and the chemical conjugation of metals to antibodies are improved, expected in the near future. In addition, flow cytometry measurements can be hindered by autofluorescence, the natural fluorescence that occurs in cells. However, since heavy metals do not occur in biological systems, mass cytometry has a strongly reduced biological background compared to flow cytometry, and is unhampered by autofluorescence. Moreover, mass cytometry has

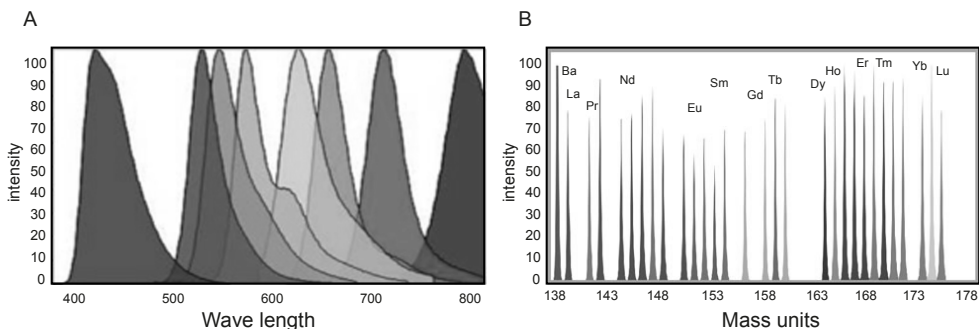


Fig. 1. Detection of antibody reporters by flow cytometry and mass cytometry (A) Example of emission spectra of several fluorescent reporters with flow cytometry. **(B)** Mass spectrum of 30 purified heavy metal isotopes with mass cytometry. Adapted from Maecker et al. (2015) and Tanner et al. (2013).

a minimal variation in the intensity of the individual metal reporters, unlike flow cytometry. A schematic overview of the mass cytometry workflow⁶ is depicted in **Figure 2**. Mass cytometry has therefore the ability to measure dozens of markers

on millions of cells collected within a reasonable timeframe (1 million cells per hour). Disadvantages of mass cytometry compared to flow cytometry are that the metal sensitivity is lower than the brightest fluorochromes (detection limit of 350 antibodies per cell), it has a lower throughput (300 cells per second), the sample recovery is incomplete (60%), there is no ability to recover viable analyzed cells (i.e., cell sorting) and light-based measures such as forward and side scatter cannot be measured. Nevertheless, mass cytometry is now widely adopted as it offers an unprecedented resolution in the analysis of cellular diversity of the immune system.

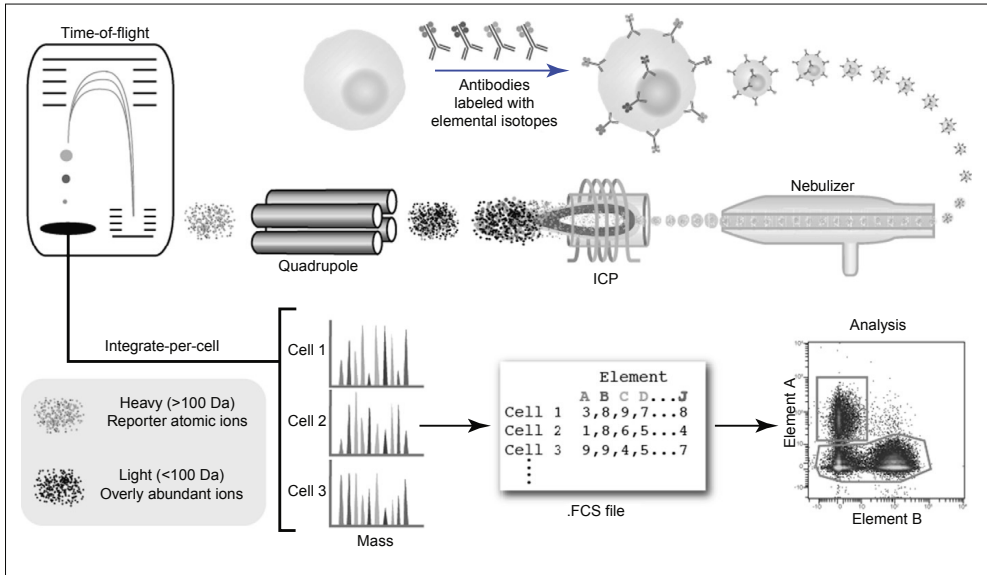


Fig. 2. Mass cytometry allows single-cell quantification of heavy metal isotope reporters A single-cell suspension is labeled with heavy metal isotope-conjugated antibodies, followed by introduction into the nebulizer where it is aerosolized. The aerosol droplets are directed into the inductively coupled plasma (ICP) torch where the cells are vaporized, atomized and ionized. Low mass ions are removed in the Quadrupole, resulting in a cloud of ions enriched for the heavy metal isotopes. The ion cloud then enters the Time-of-Flight (TOF) chamber where the ions are separated on the basis of their mass to charge ratio as they accelerate towards the detector. The time-resolved detector thus measures a mass spectrum that represents the identity and quantity of each metal ion on a single-cell basis. This is thus proportional to the number of antibodies originally bound per cell. Data is generated in .fcs format and analyzed in third-party software programs. Adapted from Bendall et al. (2012).

Data analysis

Conventional approaches for flow cytometry data analysis typically rely on the manual interpretation of a large number of 2-dimensional plots by selecting subsets of interest from parent populations, a strategy called ‘gating’. The high number of measurable single-cell markers with mass cytometry, however, brought a daunting

increase in the complexity of the data. With every additional marker simultaneously analyzed the amount of information obtained increase exponentially. Hypothetically, if a cell type would be characterized by the presence or absence of a given marker, even ignoring its quantitative nature of expression, a 40-antibody panel would yield 240 (1 trillion!) potential combinations of marker expression profiles. Even if one would go through all the 2-dimensional plots that could be generated, this does not reveal multidimensional relationships and single-cell correlations. In addition, it has been shown by various multicenter studies, such as the Human Immune Genome Project, that manual gating is one of the largest variables in the outcome of flow cytometry-based experiments^{7,8}. Therefore, such approaches are not scalable in the context of high-parametric marker expression data across millions of cells, suffer from individual user bias and require prior knowledge of the cell type of interest. Consequently, bioinformatics tools are required to extract relevant information from the generated high-dimensional datasets. Many algorithmic methods have recently been described to facilitate the analysis of mass cytometry data in an unbiased manner⁷, and these can roughly be divided into either being clustering-based or dimensionality reduction-based method.

An example of a clustering-based method specifically developed for mass cytometry data analysis is SPADE, unsupervised hierarchical clustering with minimum spanning tree projection⁹ (**Figure 3A**). With SPADE, cells are grouped into a pre-defined number of nodes based on phenotypic similarity for all markers simultaneously, and depicted in a dendrogram displaying the corresponding higher-order relatedness between those nodes. While SPADE provides an overview of the heterogeneity and the relatedness of cell populations of the immune system, it does not allow analysis at the single-cell level. Consequently, rare cells are difficult to visualize with the SPADE analysis.

The t-Distributed Stochastic Neighbor Embedding (t-SNE) analysis^{10,11} is a nonlinear dimensionality reduction method and has recently been implemented for the analysis of mass cytometry data¹². This method generates a 2-dimensional map where cells with similar multidimensional phenotypes are placed close to each other, while maintaining single-cell resolution (**Figure 3B**). It does so by taking all marker expressions into account simultaneously. Unlike principal component analysis (PCA), t-SNE effectively captures nonlinear relationships in the high-dimensional data, thereby preserving subpopulations of cell types with subtle differences in marker expression profiles. The presence or absence of multiple markers reveal

each cell's subset identity and result in a robust characterization of cell phenotypes that is captured and visualized in a single 2-dimensional t-SNE map. Notably, t-SNE dimensionality reduction alone does not assign cells to groups. Therefore, this approach was extended by introducing ACCENSE¹³, a tool that rather than by conventional manual gating, identifies phenotypically distinct subsets based on the t-SNE map using a density-peak algorithm (**Figure 3C**).

However, while non-linear methods like t-SNE do retain local data structure with single-cell resolution, they are limited by the number of cells that can be analyzed. In cytometry studies, this poses a problem, as datasets usually contain information on millions of cells. Therefore, substantial numbers of cells needs to be removed by random downsampling to make dimensionality reduction computationally feasible and reliable.

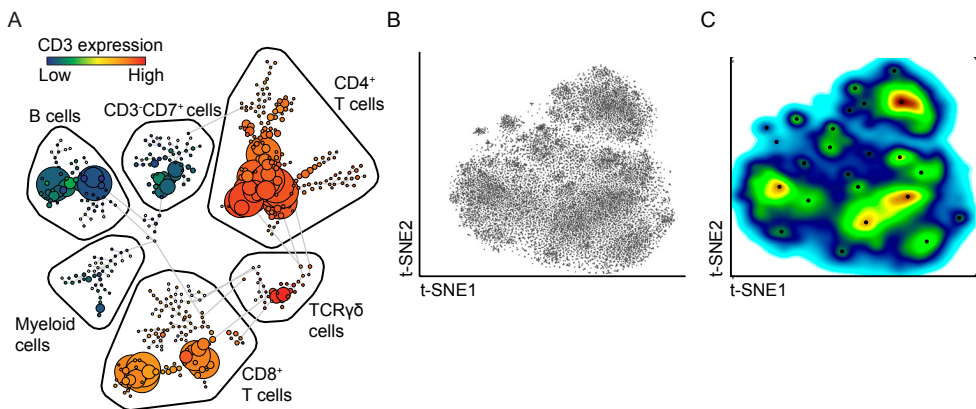


Figure 3. Computational tools implemented for mass cytometry data analysis (A) A SPADE tree analysis of a peripheral blood sample. Size of the nodes is proportional to the respective number of clustered cells. Color bar represents CD3 marker expression. (B) A t-SNE map showing murine CD8⁺ T cells. Each black dot represents a single cell. (C) A composite map depicting the local probability density of cells as embedded in panel B. Black dots represent centers of phenotypic subpopulations and were identified using a standard peak-detection algorithm. Color represents cell density. Adapted from van Unen et al. (2016) and Shekhar et al. (2013).

Intestinal immune system and pathology

The intestine contains a single epithelial cell layer separating the external environment or lumen from the underlying tissue, and represents the largest compartment of the immune system¹⁴. It has the task to provide protection against pathogens yet remaining tolerant to unharmed microbiota. To accomplish this, a complex intestinal immune system has evolved existing in homeostasis with the

microbiota. In the intestine, there is a substantial amount of organized lymphoid tissue and it contains large populations of innate and adaptive immune cells. It is continuously exposed to foreign antigens and other environmental antigens from the diet and the microbiota. The intestinal immune system therefore has the task to discriminate between harmful and beneficial antigens. This role is particularly impressive when one considers the vast mucosal surface and changing landscape along the gastrointestinal tract that the intestinal immune system must monitor. For example, the small intestine, whose primary function is in nutrient digestion and absorption, is anatomically highly distinct from the colon, whose function is in water absorption and final stages of the digestive process. This results in a gradual change in distribution of environmental factors along the length of the intestine¹⁴. Therefore, recent evidence demonstrated a proficient regional specialization within the intestinal immune system along the gastrointestinal tract^{14,15}.

Although strong protective immunity is essential to prevent invasion by pathogens, equivalent immune responses against dietary proteins or commensal bacteria can lead to chronic diseases. A complex interplay of regulatory mechanisms and continual crosstalk between various immune cell types normally prevents such unwanted responses. A disturbance of intestinal tolerance can therefore rewire immune cell composition and functionality, resulting in chronic inflammation and increased risk for infection.

Although the role of several immune subsets in driving intestinal pathology has been established, a system-wide approach that simultaneously interrogates all major lineages on a single-cell basis was lacking. High-dimensional mass cytometry is a powerful tool for dissecting the entire immune landscape, given that the accompanied challenges for efficient data analysis have been overcome. Bettering our understanding of the cellular composition of the immune system in immune-mediated diseases is key to obtain mechanistic insight and develop improved diagnostics and targeted therapeutic approaches.

Outline

At the start of my PhD project in 2013, mass cytometry was not yet implemented in the Netherlands. I was given the unique opportunity to implement high-dimensional mass cytometry as the first adopter in the Netherlands. We were the first to apply mass cytometry to the analysis of the composition of the immune system in biopsy material from patients with a variety of inflammatory intestinal diseases (**Chapter**

2). This revealed previously unrecognized immune cell heterogeneity, and identified immune subsets associated with the pathogenesis of complex intestinal disorders.

The large datasets generated with mass cytometry, however, posed a problem for proper data handling and analysis. Here, I have worked closely together with computational scientists at the LUMC and at the Technical University Delft for the development of appropriate tools for analysis and visualization of the large datasets generated. This has resulted in the development of Cytosplore (**Chapter 3**) and Hierarchical Stochastic Neighbour Embedding (HSNE) (**Chapter 4**), the latter a computational approach that overcomes the scalability limits of t-SNE-type approaches, thus enabling the analysis of tens of millions of cells without the need for subsampling of the data.

With these improved computational tools, we applied mass cytometry to biopsy material along the gastrointestinal tract from undiagnosed and untreated patients with inflammatory bowel disease (**Chapter 5**). This resulted in the stratification of immune cell infiltrate types in inflammatory bowel disease.

Finally, by visualizing the dynamics of the t-SNE computation over time, our research revealed extensive heterogeneity as well as multi-lineage differentiation trajectories of ILCs, important regulators of tissue integrity, in the human fetal intestine (**Chapter 6**). This study was one of the first where exploratory mass cytometry-based approaches to determine heterogeneity in the immune system were translated into functional analyses of newly identified immune subsets.

In **Chapter 7** the major findings of this thesis are discussed in the light of the current literature and the availability of imaging mass cytometry, allowing the simultaneous analysis of 36 markers on tissue sections at subcellular resolution. The implications of this for future research are discussed.

References

- 1 Fan, X. & Rudensky, A. Y. Hallmarks of Tissue-Resident Lymphocytes. *Cell* 164, 1198-1211, doi:10.1016/j.cell.2016.02.048 (2016).
- 2 Simoni, Y., Chng, M. H. Y., Li, S., Fehlings, M. & Newell, E. W. Mass cytometry: a powerful tool for dissecting the immune landscape. *Curr Opin Immunol* 51, 187-196, doi:10.1016/j.coi.2018.03.023 (2018).
- 3 Bandura, D. R. et al. Mass cytometry: technique for real time single cell multitarget immunoassay based on inductively coupled plasma time-of-flight mass spectrometry. *Anal Chem* 81, 6813-6822, doi:10.1021/ac901049w (2009).
- 4 Tanner, S. D., Baranov, V. I., Ornatsky, O. I., Bandura, D. R. & George, T. C. An introduction to mass cytometry: fundamentals and applications. *Cancer Immunol Immunother* 62, 955-965, doi:10.1007/s00262-013-1416-8 (2013).
- 5 Maecker, H. T. & Harari, A. Immune monitoring technology primer: flow and mass cytometry. *J Immunother Cancer* 3, 44, doi:10.1186/s40425-015-0085-x (2015).
- 6 Bendall, S. C., Nolan, G. P., Roederer, M. & Chattopadhyay, P. K. A deep profiler's guide to cytometry. *Trends Immunol* 33, 323-332, doi:10.1016/j.it.2012.02.010 (2012).
- 7 Mair, F. et al. The end of gating? An introduction to automated analysis of high dimensional cytometry data. *Eur J Immunol* 46, 34-43, doi:10.1002/eji.201545774 (2016).
- 8 Maecker, H. T., McCoy, J. P. & Nussenblatt, R. Standardizing immunophenotyping for the Human Immunology Project. *Nat Rev Immunol* 12, 191-200, doi:10.1038/nri3158 (2012).
- 9 Qiu, P. et al. Extracting a cellular hierarchy from high-dimensional cytometry data with SPADE. *Nat Biotechnol* 29, 886-891, doi:10.1038/nbt.1991 (2011).
- 10 van der Maaten, L. Accelerating t-SNE using Tree-Based Algorithms. *J Mach Learn Res* 15, 3221-3245 (2014).
- 11 van der Maaten, L. & Hinton, G. Visualizing Data using t-SNE. *J Mach Learn Res* 9, 2579-2605 (2008).
- 12 Amir el, A. D. et al. viSNE enables visualization of high dimensional single-cell data and reveals phenotypic heterogeneity of leukemia. *Nat Biotechnol* 31, 545-552, doi:10.1038/nbt.2594 (2013).
- 13 Shekhar, K., Brodin, P., Davis, M. M. & Chakraborty, A. K. Automatic Classification of Cellular Expression by Nonlinear Stochastic Embedding (ACCENSE). *Proc Natl Acad Sci U S A* 111, 202-207, doi:10.1073/pnas.1321405111 (2014).
- 14 Mowat, A. M. & Agace, W. W. Regional specialization within the intestinal immune system. *Nat Rev Immunol* 14, 667-685, doi:DOI 10.1038/nri3738 (2014).
- 15 Agace, W. W. & McCoy, K. D. Regionalized Development and Maintenance of the Intestinal Adaptive Immune Landscape. *Immunity* 46, 532-548, doi:10.1016/j.immuni.2017.04.004 (2017).





CHAPTER 2

Mass Cytometry of the Human Mucosal Immune System Reveals Tissue- and Disease-Associated Immune Subsets



CHAPTER 2

Mass Cytometry of the Human Mucosal Immune System Reveals Tissue- and Disease-Associated Immune Subsets

Vincent van Unen,¹ Na Li,¹ Ilse Molendijk,² Mine Temurhan,³ Thomas Höllt⁷, Andrea E. van der Meulen-de Jong,² Hein W. Verspaget,² M. Luisa Mearin,⁴ Chris J. Mulder,⁶ Jeroen van Bergen,¹ Boudewijn P. F. Lelieveldt,^{5,7} Frits Koning.¹

¹Department of Immunohematology and Blood Transfusion, ²Department of Gastroenterology, ³Department of Center for Proteomics, ⁴Department of Pediatrics, ⁵Department of LKEB Radiology, Leiden University Medical Center, The Netherlands. ⁶Department of Gastroenterology, VU Medical Center, Amsterdam, The Netherlands. ⁷Department of Pattern Recognition and Bioinformatics Group, Delft University of Technology, The Netherlands.

Immunity 44:5, 1227-1239 (2016)

ABSTRACT

Inflammatory intestinal diseases are characterized by abnormal immune responses and affect distinct locations of the gastrointestinal tract. Although the role of several immune subsets in driving intestinal pathology has been studied, a system-wide approach that simultaneously interrogates all major lineages on a single-cell basis is lacking. We used high-dimensional mass cytometry to generate a system-wide view of the human mucosal immune system in health and disease. We distinguished 142 immune subsets and through computational applications found distinct immune subsets in PBMCs and intestinal biopsies that distinguished patients from controls. In addition, mucosal lymphoid malignancies were readily detected as well as precursors from which these likely derived. These findings indicate that an integrated high-dimensional analysis of the entire immune system identifies immune subsets that are associated with the pathogenesis of complex intestinal disorders. This may have important implications for diagnostic procedures, immune-monitoring and treatment of intestinal diseases and mucosal malignancies.

INTRODUCTION

The intestinal immune system protects us from bacterial, viral and parasitic infections. Disruption of intestinal homeostasis, however, can lead to a variety of autoinflammatory intestinal diseases, including celiac disease (CeD) and Crohn's disease (D), which together have a prevalence of 1,500 per 100,000 adults in the Western world^{1,2}. Both diseases are multifactorial and encompass a broad spectrum of clinical phenotypes and ages of onset. CeD is a disease of the small intestine caused by pro-inflammatory CD4⁺ T cell responses specific for dietary gluten and concomitant destruction of the epithelium due to activation of intraepithelial CD8⁺ T cells. The introduction of a strict gluten-free diet constitutes a highly effective treatment for CeD but nevertheless 2-5% of patients develop refractory CeD type II (RCDII) with persistent inflammation. RCDII is characterized by a monoclonal outgrowth of aberrant intra-epithelial lymphocytes (IELs) from which an aggressive enteropathy-associated T cell lymphoma (EATL) evolves in 40% of patients³. In contrast, CD affects the terminal ileum and/or colon and results from aberrant immune responses against the microbiota⁴. CD is usually treated with the use of lifelong pharmacotherapy⁵, including biologicals (e.g. anti-TNF) to reduce chronic inflammation and to accomplish sustained remission. Despite achieving states of remission, perianal fistulas occur in 25% of CD patients and this is accompanied by multiple relapses and a poor prognosis due to insufficient healing^{6,7}.

Although the role of several immune subsets in driving intestinal pathology has been studied in CeD⁸, RCDII⁹ and CD¹⁰, a system-wide approach that simultaneously interrogates immune subsets across all major lineages on a single-cell basis is currently lacking. High-dimensional mass cytometry (cytometry by time-of-flight; CyTOF) now offers the possibility to analyze many cellular markers simultaneously, providing an opportunity to analyze the mucosal immune system with unprecedented resolution¹¹. Novel computational tools have been developed to handle the high-dimensional single-cell datasets that originate from mass cytometry¹²⁻¹⁴. In the current study we applied mass cytometry to analyze the composition of the immune compartment present in intestinal biopsies and paired peripheral blood mononuclear cell (PBMC) samples of patients with inflammatory intestinal diseases and controls. We identified 142 distinct immune cell subsets and through computational applications we found immune subsets in PBMCs and intestinal biopsies that distinguished patients with inflammatory diseases from controls. In addition,

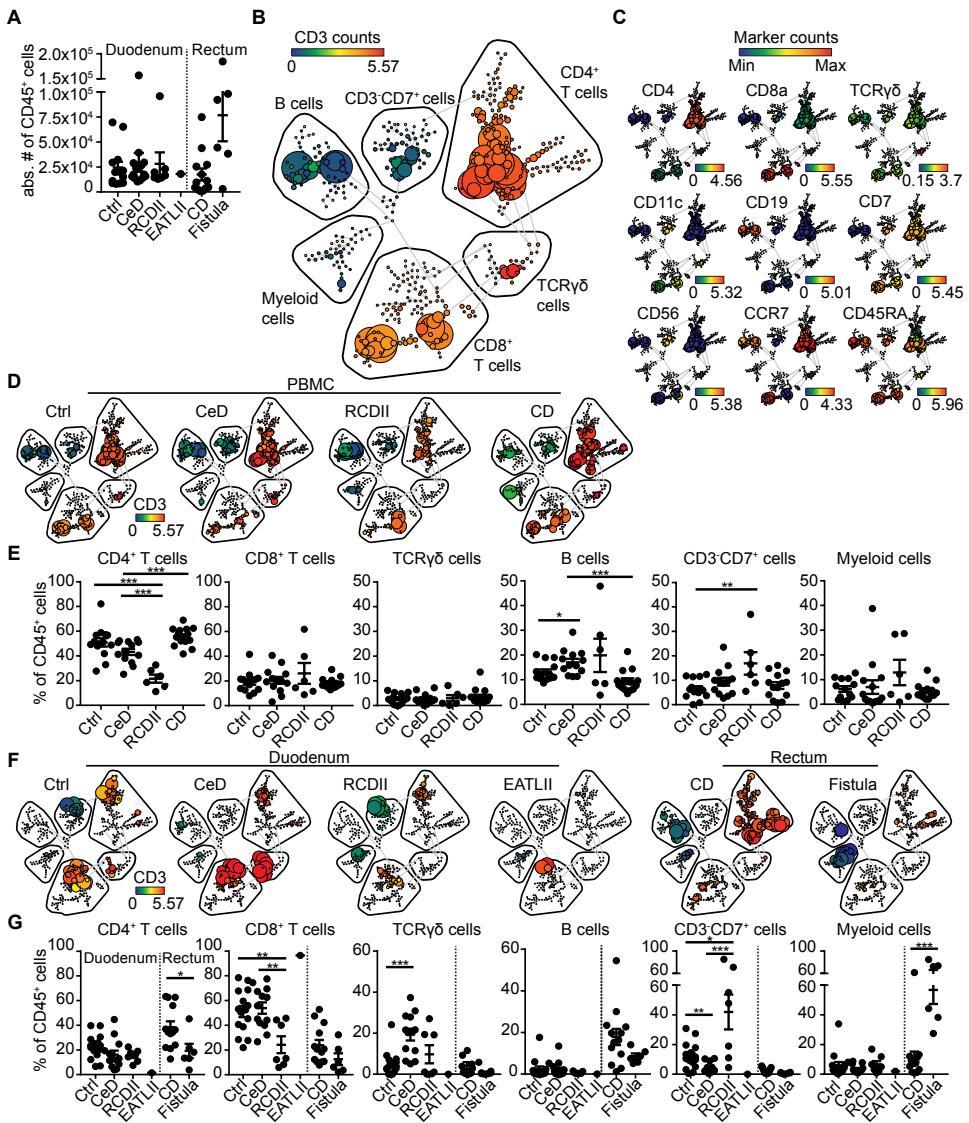


Figure 1. Collective SPADE analysis distinguishes major immune lineages in peripheral blood and intestine

(A) Live single CD45⁺ absolute cell number acquired for 55 intestinal biopsies. (B) A SPADE tree of a PBMC sample after analysis of the combined 102 sample dataset containing 5.2×10^6 cells. Size of the nodes is proportional to the respective number of clustered cells. Color bars represent ArcSinh5-transformed values for CD3 marker expression. The identities of major immune lineages are annotated on the basis of lineage marker expression. (C) Color of the PBMC sample represents expression values for each marker as shown. (D) Representative SPADE trees showing an individual PBMC sample from a control and 3 patients with intestinal diseases. Color represents CD3 marker expression as described in panel B. (E) Comparisons of cellular frequencies for major immune lineages from 47 PBMC samples. (F) Representative SPADE trees showing an individual intestinal biopsy from a control and 5 patients with intestinal diseases. (G) Comparisons of cellular frequencies for major immune lineages.

from 55 intestinal biopsies. Data are plotted as single values (each data point represents an individual sample). * $P < 0.05$; ** $P < 0.01$; *** $P < 0.001$, using Mann-Whitney U test. Error bars show means \pm s.e.m

mucosal lymphoid malignancies were readily detected as well as the precursors from which these likely derived. Thus, mass cytometry unveiled previously unappreciated heterogeneity in the immune system and our observations may help to develop improved diagnostic and therapeutic approaches for inflammatory bowel diseases.

2

RESULTS

SPADE analysis identifies major immune lineages in peripheral blood and intestine

We designed a CyTOF panel of 32 metal isotope-tagged monoclonal antibodies, which was designed to obtain a global overview of the heterogeneity of the innate and adaptive immune system (**Table S1**). For this purpose, the panel contained lineage markers that distinguish the major adaptive and innate immune cell populations. In addition, markers were included to distinguish naïve from memory cells, resting from activated cells, and to identify homing properties and potential responsiveness to humoral factors. With this panel, we analyzed single-cell suspensions from biological samples including duodenum biopsies (N=36), rectum biopsies (N=13), perianal fistulas (N=6) and peripheral blood mononuclear cells (PBMC) from control individuals (N=15) and from patients with inflammatory intestinal diseases (CeD, N=13; RCDII, N=5; EATLII, N=1 and CD, N=10) (**Table S2**). The large majority (N=28) of antibodies allowed clear discrimination of antibody-positive and -negative cells (**Figure S1**). To monitor the robustness of the measurements we included a standardized PBMC sample at regular intervals in the acquisition sessions during the entire 9-month study period. These consecutive control samples yielded highly similar results (**Figure S2A-C**), demonstrating the reproducibility of the data acquisition. We discriminated live, single CD45⁺ cells with DNA stains and event length. (**Figure S2D**). From the intestinal biopsies we acquired 27,500 duodenal, 17,500 rectal, and 76,500 perianal fistulous CD45⁺ cells on average (**Figure 1A**), and 76,500 CD45⁺ cells from the PBMC samples (data not shown). We visualized the global cellular heterogeneity by pooling all the acquired data on 5.2×10^6 cells and applying unsupervised hierarchical clustering with minimum spanning tree projection (SPADE), grouping the cells into a pre-defined number of nodes based on phenotypic similarity¹⁵. A dendrogram displayed the corresponding higher-order relatedness between those nodes (**Figure 1B**). The major branches in this dendrogram corresponded to CD4⁺ T cells, CD8⁺ T cells, TCR $\gamma\delta$ cells, B cells, innate lymphocytes

(referred to as CD3⁺CD7⁺ cells hereafter) and myeloid cells (**Figure 1C**). The cell frequencies of these major cell lineages obtained through SPADE were confirmed by traditional gating procedures using two-parameter dot plots (**Figure S3**).

In general, the subset distribution between PBMC samples from controls and patients was quite similar although a decrease in numbers of CD4⁺ T cells in patients with RCDII and some variability in the numbers of B cells and CD3⁺CD7⁺ cells was detected (**Figures 1D** and **1E**). In contrast, substantial differences were evident between the PBMC and intestinal samples. For example, duodenal CD4⁺ T cell, CD8⁺ T cell, CD3⁺CD7⁺ cell and rectal myeloid cell subsets were distinct from those in peripheral blood (**Figures 1D-1G**). In addition, the SPADE dendrograms revealed disease-associated signatures (**Figures 1D-1G**) exemplified by the disappearance of CD3⁺CD7⁺ cells and an increase in TCR $\gamma\delta$ cells in CeD relative to the control duodenal biopsies. Also, compared to controls and patients with CeD, an increase in CD3⁺CD7⁺ cells in the duodenum of patients with RCDII was observed. Of note is the dominant presence of a CD8⁺ T cell cluster in the duodenum of a patient with enteropathy-associated T cell lymphoma type II (EATLII). Finally, a highly diverse CD4⁺ T cell compartment was found in rectal biopsies of patients with CD and a dominant presence of myeloid cells in perianal fistulas. Thus, this global analysis indicated that there are immune-system-wide differences in subset composition between peripheral blood and intestinal samples, and between duodenal samples from patients and controls.

t-SNE-ACCENCE analysis identifies 142 phenotypically distinct immune subsets

While SPADE analysis provides an overview of the heterogeneity and the relatedness of subsets within the major immune lineages it does not allow analysis at the single-cell level and consequently rare cells are difficult to visualize. Therefore, we applied t-Distributed Stochastic Neighbor Embedding (t-SNE) analysis^{16,17} which generates a two-dimensional map where cells with similar multidimensional phenotypes are placed close to each other, while maintaining single-cell resolution¹². To ensure a similar impact of the cells from PBMC and intestinal samples on the t-SNE analysis the number of cells incorporated from those two compartments were matched. We applied the t-SNE approach for every major lineage individually, here showing the CD4⁺ T cell compartment where over 440,000 cells were incorporated in the analysis (**Figure 2**).

The t-SNE analysis revealed expected types of marker distributions on the CD4⁺ T cells, such as broadly expressed markers (CD7, IL-7R α), markers that were expressed by

subpopulations of the cells (CD56, PD1, CD25) and markers that were co-expressed (CD45RA and CCR7), but also unanticipated distributions were revealed, like largely mutually exclusive marker expression patterns (i.e. CD27 and CD161) (**Figure 2A**). Next, we incorporated a kernel density-peak detection algorithm on the t-SNE map (ACCENSE)¹⁴ which automatically identified 28 CD4⁺ T cells subsets (**Figure 2B**) where each subset was defined by its marker expression profile (**Figure 2C**).

To reduce the complexity implied by the ACCENSE analysis we merged computationally-derived subsets with highly similar expression profiles, which resulted in 16 cell clusters that each express a distinct set of markers (**Figure 2D**). They fell within four major CD4⁺ T cell categories: naïve (CD45RA⁺CCR7⁺), CD27⁺IL-7R α ⁻ effector memory (EM; CD45RA⁻CCR7⁻), CD27⁻IL-7R α ⁺ EM and central memory (CM; CD45RA⁻CCR7⁺), and within those categories additional heterogeneity was present. For example, the highly similar CD161⁺CD27⁻IL-7R α ⁺ EM cell subsets 4 and 11 were distinguished from each other by the expression of CD56 (**Figure 2D**). We next analyzed the subset distribution of the CD4⁺ T cells in the various tissues included in the analysis by plotting the relative frequencies of the subsets for all samples analyzed (**Figures 2E** and **2F**). In line with the SPADE analysis, the CD4⁺ T cell subsets of the duodenum, rectum and PBMC samples clustered to distinct locations in the cell frequency heatmap, also when examining the 102 samples individually (**Figure S4**). Thus, we could effectively delineate cell populations in a data-driven manner, and this approach revealed distinct signatures in the cellular composition of the CD4⁺ T cells in biopsy material and peripheral blood.

By applying the t-SNE-ACCENSE analysis to all 6 major cell lineages individually we identified 142 subsets in the entire immune system (**Figure 3A**), 23 of which contained rare cells that did not fulfill lineage phenotypic criteria (data not shown). The distinct phenotypes of the remaining 119 subsets are summarized in a heatmap (**Figure 3B**) where the subsets are clustered according to their phenotypic hierarchy within their lineage and clustered based on marker expression. The analysis identifies relatively few subsets within the B cell and myeloid compartments, likely due to the composition of the antibody panel which was designed to capture the heterogeneity of the CD7⁺ lymphoid cells. In this context, our antibody panel

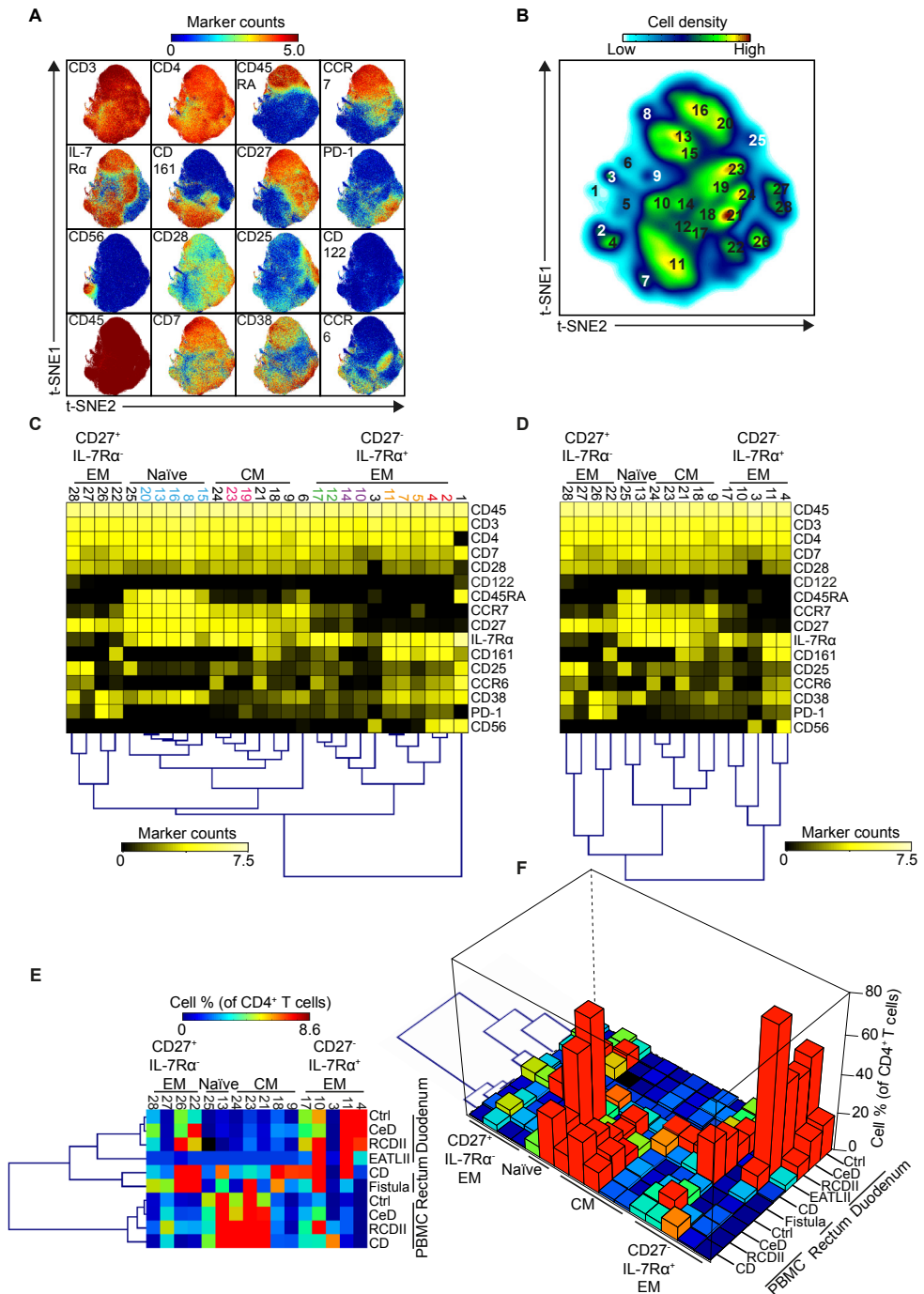


Figure 2. t-SNE-ACCENSE analysis pipeline identifies tissue-specific CD4⁺ T cell subsets

(A) Collective t-SNE dimensionality reduced CD4⁺ T cell single-cell data (4.7×10^5 cells) derived from 102 samples analyzed are plotted. Every dot represents a single cell and the color of the cells indicates ArcSinh5-transformed expression values for a given marker analyzed. (B) A density map depicting the local probability density of cells as embedded in panel A, computed using a kernel based transformation. Numbers in this map represents centers of phenotypic subsets and were identified using a peak detection algorithm. (C) A heatmap summary of median ArcSinh5-transformed expression values of T cell markers expressed by 16 CD4⁺ T cell subsets identified and hierarchical clustering of subsets with description of four categories. (D) A heatmap summary of average subset frequencies across tissues and disease states. Mean frequencies obtained from 102 samples analyzed. (E) A 3D heatmap as described in panel D. EM = effectormemory and CM = central memory. A detailed heatmap showing 102 samples is described in **Figure S4**.

the samples included. Collectively, the combined t-SNE-ACCENSE approach on high-dimensional cytometry data can effectively identify phenotypic distinct subsets in an unbiased and data-driven manner, and the analysis indicates that the heterogeneity of the immune system is far greater than previously appreciated.

Visualization of cellular ‘finger-print’ signatures across tissues and disease states

To visualize the distribution of immune cells based on tissue-origin and disease state we used the t-SNE maps to deduce cellular ‘finger-print-like’ signatures of immune cells in the 6 major immune lineages (**Figure 4A**). The ‘finger-print’ gives a visual representation of the position of a collection of cells from particular (tissue) samples in the t-SNE map of the collective dataset. As such it gives a unified overview of the distinctness of cells within the samples analyzed stratified for tissues and disease states. In all 6 immune lineages, the duodenum, rectum and PBMC samples displayed a distinct cellular signature (**Figure 4A**). Moreover, on the basis of these signature maps, we were able to identify phenotypically distinct cell clusters that were either specifically present or abundant in certain diseases (highlighted by red boxes and arrows in **Figure 4A**). For example, the lineage (Lin)⁻ CD3⁻CD7⁺ cells that expanded monoclonally in patients with RCDII (purple arrow; **Figure 4A**) were distinguished by the expression of CD45RA in 6 out of 7 patients (**Figures 4B** and **4C**). Moreover, these aberrant Lin⁻ CD3⁻CD7⁺ cells were also detectable in PBMC samples of 3 out of 6 patients (**Figures 4A** and **4D**), indicating a systemic spread of the pre-malignant cells. Similarly, a massive expansion of CD56⁺CD161⁺ CD8⁺ T cells was observed in a patient with an established lymphoma of EATL-type 2 (green arrow; **Figure**

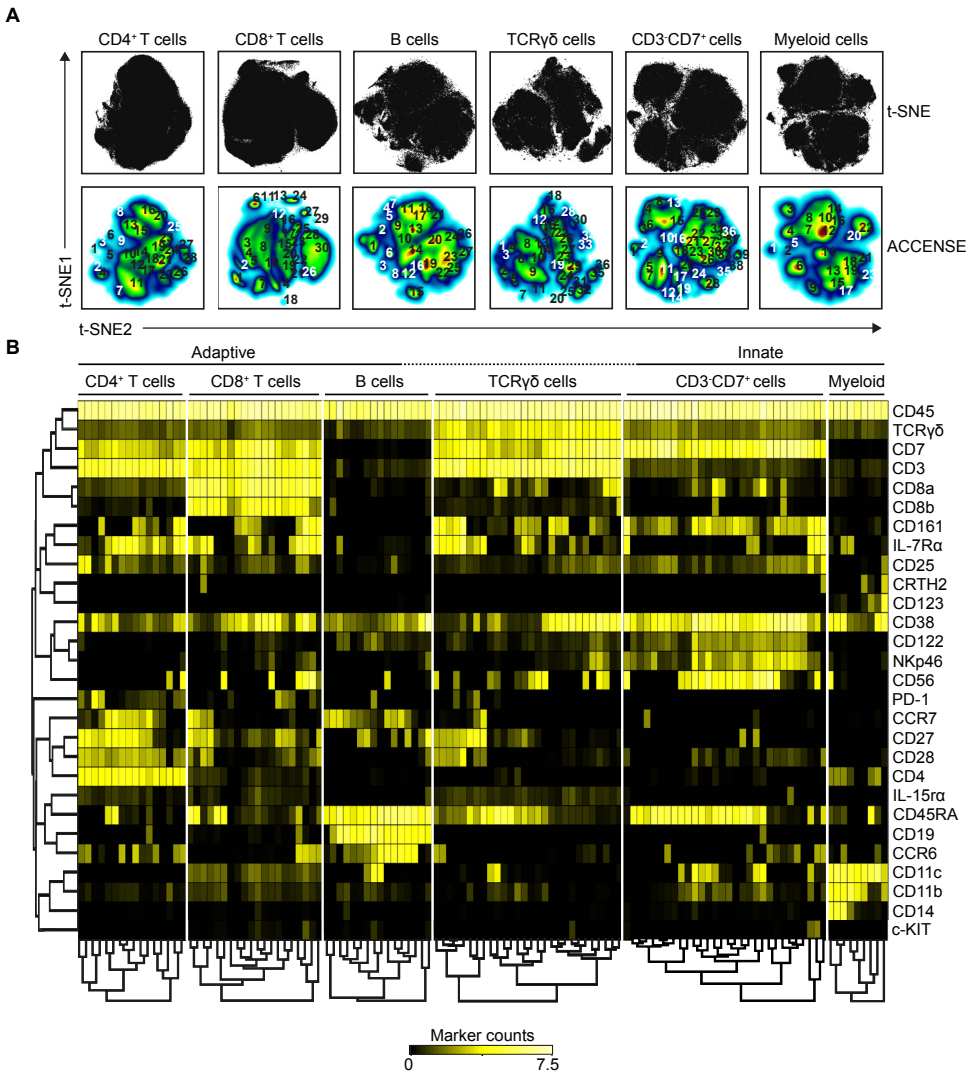


Figure 3. t-SNE-ACCENSE analysis delineates phenotypic distinct immune subsets in peripheral blood and intestine

(A) Identification of 142 cell subsets within the six major immune lineages through t-SNE-ACCENSE analysis. Cells from PBMCs were randomly sampled to match cell numbers to those from intestinal biopsies for each immune lineage individually. t-SNE plots are showing 4.7×10^5 CD4⁺ T cells, 9.3×10^5 CD8⁺ T cells, 1.8×10^5 B cells, 1.8×10^5 TCRγδ cells, 1.9×10^5 CD3-CD7⁺ cells and 2.2×10^5 myeloid cells of the combined 102 sample dataset. (B) Heatmap showing characterization of 119 cell clusters (16 CD4⁺ T cell subsets, 20 CD8⁺ T cell subsets, 16 B cell subsets, 28 TCRγδ cell subsets, 30 CD3-CD7⁺ cell subsets and 9 myeloid cell subsets). Shown are median ArcSinh5-transformed values of marker expression (black-to-yellow scale) and hierarchical clustering of markers and subsets within their major immune lineage.

4A). Rare cells (0.1-0.2% of CD8⁺ T cells) displaying an identical phenotype were detected in 25% of the other duodenum samples and these may therefore represent the precursor from which the lymphoma arose. In addition, two distinct IL-7R α ⁺ innate lymphoid cell type 3-like (ILC3-like)¹⁸ cell clusters were identified that were either chemokine receptor CCR6⁺ or CCR6⁻ (blue arrow; **Figures 4A** and **4B**). While the CCR6⁺ ILC3-like cells represented 50% of the CD3⁺CD7⁺ cells in the rectum of CD patients, its CCR6⁻ ILC3-like counterpart, which is associated with an inflammatory phenotype in CD¹⁹, was more abundant in the fistulas (**Figure 4C**). Also, 94% of the myeloid cells within the inflammatory perianal fistulas (red arrow; **Figure 4A**) displayed a CD11b⁺CD11c⁺ dendritic cell-like phenotype (**Figure 4B**) and they comprised 50% of the accumulated immune infiltrate (**Figure 4C**).

We next used the Jensen-Shannon (JS) divergence to quantify similarities and dissimilarities between pairs of t-SNE maps (**Figure 4E**). In these plots the JS divergences between samples from the intestine and peripheral blood were high for every major lineage (**Figure 4E**), indicative of dissimilarity of cellular signatures. In addition, the JS divergences reveal disease-associated cellular profiles exemplified by similarity of RCDII and CeD duodenal myeloid cells compared with those in duodenal controls, distinct CD8⁺ T cells in RCDII patient blood and distinct B cells, CD3⁺CD7⁺ cells and myeloid cells in CD patient blood compared with other blood samples.

Furthermore, we visualized the immune composition as an immune landscape where the distribution of the subsets in the various tissue and blood samples is shown (**Figure 5**). A 2-dimensional representation of the immune landscape along with the phenotypes of the associated immune subsets is shown in **Figure S5**, visualizing the distinct cellular phenotypes of the immune subsets and their occurrence in the various tissues. Together these findings illustrate that in most of the major immune lineages, cellular subsets could be identified that were exclusively present or enriched in defined tissue samples only. In peripheral blood, cells were mainly defined by expression of interleukin 7 receptor α (IL-7R α), CCR7, CD27 and CD28 for CD4⁺ and CD8⁺ T cells, CCR6 for B cells, CD56 for CD3⁺CD7⁺ cells and CD14 for myeloid cells. Similarly, many mucosal cells were defined by expression of CD161 for CD4⁺ and CD8⁺ T cells, CD38 for TCR $\gamma\delta$ cells and IL-7R α for CD3⁺CD7⁺ cells. Together these analyses demonstrate that by deducing cellular ‘finger-print’ signatures of immune cells we were able to visualize and quantify the immune subset distribution in the samples analyzed. In addition, we were able to identify immune subsets that are associated with disease states.

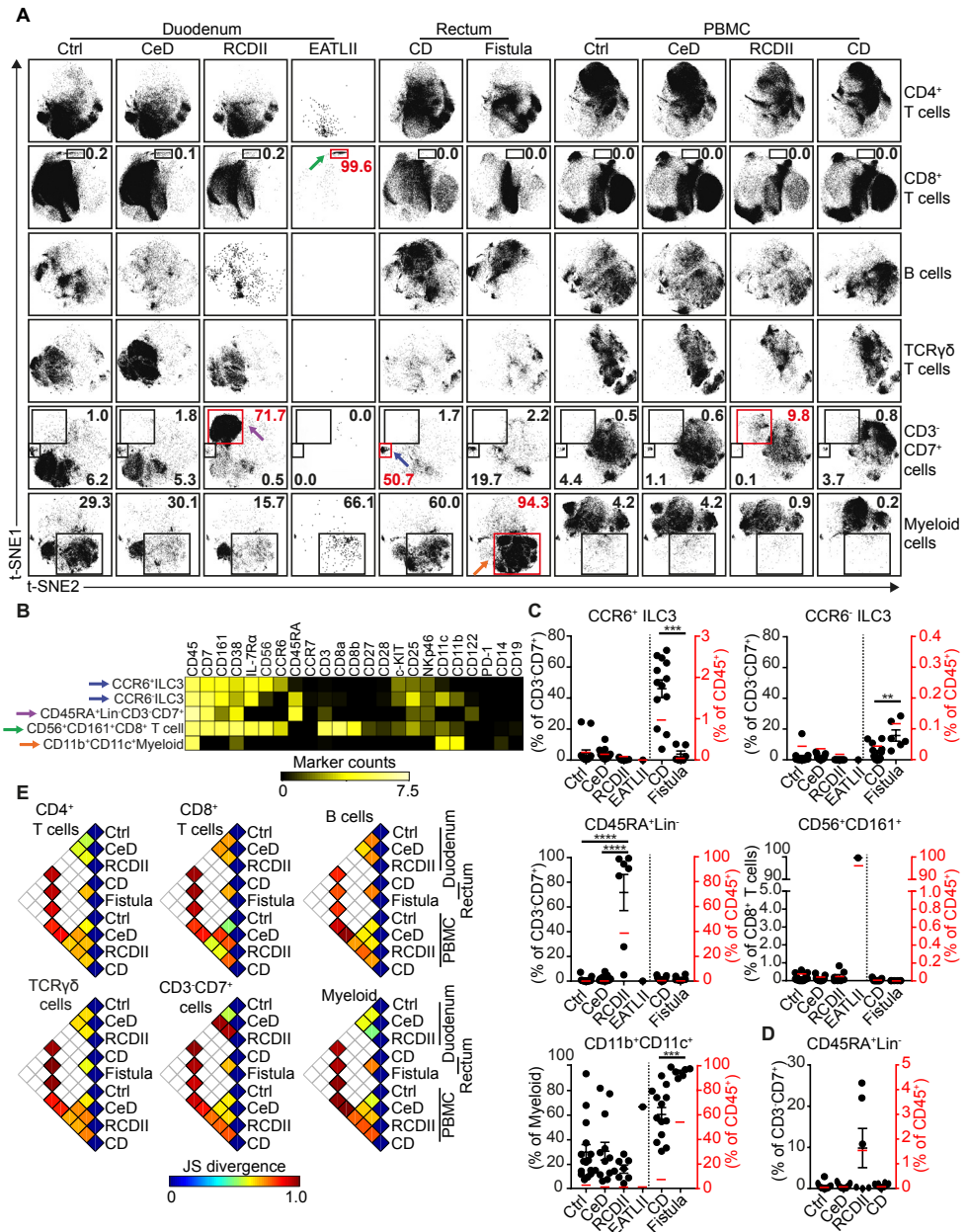


Figure 4. Stratified t-SNE plots identify distinct cellular ‘finger-print’ signatures across tissues and disease states
 (A) Collective t-SNE dimensionality reduced single-cell data from all 102 samples analyzed are plotted showing six major immune lineages stratified for tissues and disease states. Red boxes and arrows indicate t-SNE location of phenotypically distinct disease-associated clusters of cells (B) Heatmap summary of median ArcSinh5-transformed expression values of cellular markers expressed by gated subsets and annotation for each subset. Arrows as in panel A. (C) Comparisons of cellular frequencies

for subsets from intestinal biopsies. (D) Comparisons of cellular frequencies for the CD45RA⁺Lin⁻CD3⁻CD7⁺ subset from PBMC samples. (E) Pairwise Jensen-Shannon (JS) divergence plots of the collective t-SNE maps from all 102 samples analyzed showing six major immune lineages. A higher JS divergence value indicates more dissimilarity between a pair of t-SNE maps as shown in panel A. White squares indicate invalid comparisons. Data are plotted as single values. Red lines indicate mean value as % of CD45⁺ cells. (each data point represents an individual sample). *P <0.05; **P <0.01; ***P <0.001; ****P <0.0001, using Mann-Whitney U test. Error bars show means ± s.e.m.

An integrated system-wide view of the immune system reveals disease-associated networks of immune subsets

Finally, we investigated whether the identified immune-system-wide cellular patterns could be integrated collectively and used to characterize samples according to tissue location or disease state by visualizing them in relation to several clinical variables. For this purpose we visualized the immune composition of all identified subsets from all included biological samples in a single graph by applying the t-SNE algorithm on cell frequency values. As expected, the PBMC and intestinal biopsy samples formed two distinct clusters (**Figure 6A**). In addition, the rectum and perianal fistula biopsies separated from the duodenal biopsies (**Figures 6A** and **6B**) and the duodenal biopsies from patients with CeD and RCDII clustered away from the duodenal control biopsies (**Figures 6A** and **6B**). Also, the duodenal biopsies of the four RCDII patients with the most severe inflammation (**Table S2**) mapped far from the other duodenum samples (**Figures 6B** and **6C**). Furthermore, three RCDII biopsies, two of which were from patients in remission, clustered with the other CeD biopsies, suggesting a persisting CeD immune profile. The inflammation state of the biopsies was reflected in the cluster structure of intestinal samples in general (**Figure 6C**), while this was not the case for gender (**Figure 6D**). Moreover, the age of the patients and controls from which the samples were derived is reflected in the clustering of the samples, particularly in peripheral blood (**Figure 6E**). The PBMC and intestinal samples from six patients that were biopsied twice, with a 3- to 6-months time interval, clustered tightly together (**Figure 6F**) highlighting the reproducibility and robustness of this unbiased approach.

In order to reveal which cellular subsets were associated with the disease-associated patterns (**Figure 6G**), we performed a second t-SNE analysis on the subsets of the same dataset (instead of the samples) visualizing networks of cellular subsets that determine disease-specificity (**Figures 6H** and **6I**) and identified the top 5 ranked subsets contributing to these clustering patterns (**Figure 6J**). In this context, expected types of health- and disease-associated subsets were identified in the intestinal mucosa, such as CD45RA⁺Lin⁻CD3⁻CD7⁺ cells in control individuals,

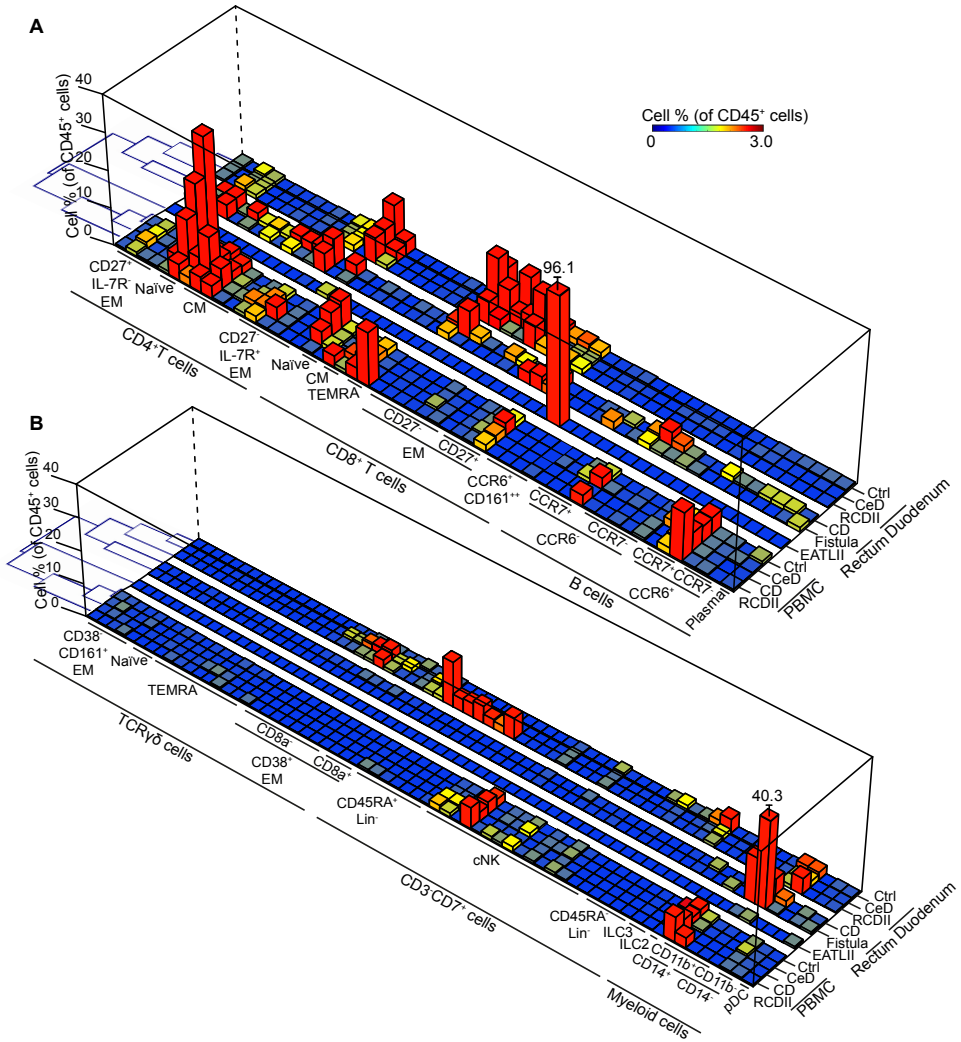


Figure 5. Immune system landscape visualizes subset composition

A 3-dimensional heatmap summary showing average frequencies of 119 immune subsets in the 102 biological samples combined with hierarchical clustering of samples and description of tissue type, disease state and biological assignment of the subsets. Color scale and z-axis indicate percentage of CD45⁺ cells. EM = effector memory, CM = central memory, TEMRA = terminally differentiated, Lin = lineage, cNK = conventional NK cells, ILC = innate lymphoid cells and pDC = plasmacytoid dendritic cells.

CD8a⁺ and CD8a⁻ TCRγδ cells in CeD, CD45RA⁺Lin⁻ CD3⁻CD7⁺ cells in RCDII, CCR6⁺ILC3 in CD and CD14⁻CD11b⁺ myeloid cells in fistulas. In addition, previously unidentified subset associations were revealed as well, such as CD45RA⁻ cNK cells and CD56⁻CD27⁻EM CD4⁺ T cells in controls, CD27⁻EM CD8⁺ T cells in CeD, CRTH2⁺ myeloid cells in RCDII (ranked 6), CCR6⁻CM and PD-1⁺CD27⁺EM CD4⁺ T

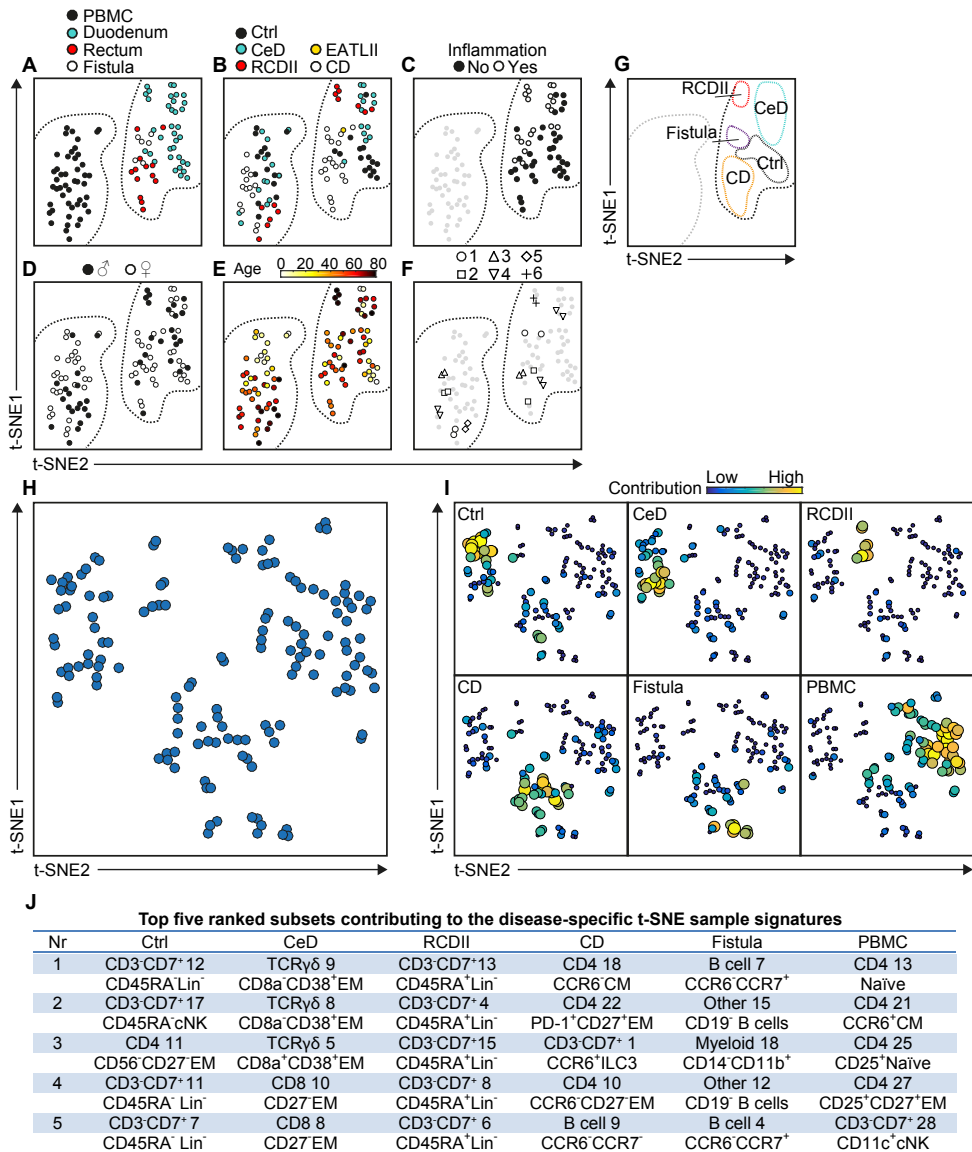


Figure 6. Integrated analysis of immune subset composition reveals tissue- and disease-associated clustering of biological samples

Collective t-SNE dimensionality reduced cell percentage data (as % of CD45⁺ cells) of 142 subsets for 102 samples analyzed are plotted. Every dot represents a single sample and the color of the samples shows the corresponding clinical information: (A) tissue, (B) disease, (C) biopsy inflammation, (D) gender, (E) age in years, (F) samples from six patients that were sampled twice. The left dashed border represents the PBMC cluster and the right dashed border represents the intestinal cluster. (G) Deducing disease-specific signatures in the t-SNE map based on the clustering patterns of the samples. (H) Collective t-SNE dimensionality reduced cell percentage data (as % of CD45⁺ cells) of 142 subsets for 102 samples analyzed are plotted. Every dot represents a single immune subset. The

closer the subsets are together the more similar the cell frequency values are across the samples. (I) Disease-specific subset signatures (average subset values per disease cluster in panel G, encoded with varying dot color and size). (J) Table showing top five ranked subsets contributing to the disease-specific t-SNE sample signatures (as shown in panel I) displaying both major lineage subset number and biological assignment. Lineage (Lin), conventional NK cell (cNK), effector memory (EM), central memory (CM) and innate lymphoid cells (ILC). Average cell frequency values are shown in **Figure 5**.

cells in CD, and CCR6⁺CCR7⁺ B cells in the fistulas. Thus, by integrating data-driven approaches highly specific disease-associated immune signatures across innate and adaptive major lineages in the intestine were readily identified. Figure S6 gives an overview of the developed integrated analysis pipeline developed in the current study.

DISCUSSION

Mass cytometry offers the opportunity to simultaneously analyze dozens of single-cell markers on complex cellular samples resulting in highly complex datasets. Conventional approaches for flow cytometry data analysis are not suitable for such datasets, suffer from individual user bias, and require prior knowledge of the cell type of interest. SPADE¹³ was originally applied to handle mass cytometric data. More recently, an unbiased analysis pipeline has been developed combining t-SNE^{12,16} and ACCENSE¹⁴ with mass cytometry to visualize and delineate phenotypically distinct subsets²⁰. In the current study we used a 32 antibody panel that was specifically designed to detect heterogeneity within the major adaptive and innate cell lineages. We applied this antibody panel to a variety of PBMC and intestinal biopsy samples and combined this with the newly available unbiased computational approaches to unravel the complexity of the human mucosal immune system. We used the Barnes-Hut implementation of t-SNE, a recently developed, computationally efficient t-SNE optimization algorithm¹⁷ to accommodate the large datasets. In addition, we provide novel applications of the t-SNE-based analysis allowing the visualization of cellular ‘finger-print’ signatures of immune cells, and by clustering samples based on their immune composition while visualizing the cluster-contributing subsets in parallel to highlight tissue- and disease-associated patterns.

Our results demonstrate that the mass cytometry-based analysis was robust and reproducible as identical control PBMC samples that were included during the entire 9 month study period provided highly similar results. Moreover, we obtained biopsy and PBMC specimens from a number of patients twice with a time interval between 3 to 6 months and in the final sample visualization analysis these specimens clustered close together, demonstrating a high degree of reproducibility. Also, we

readily observed changes in the composition of the immune compartment that are known to correlate with disease such as the increase in TCR $\gamma\delta$ cells in CeD²¹.

Both the SPADE and the combined t-SNE-ACCENSE analysis demonstrate that duodenal, rectal and PBMC samples grouped into different clusters, to a large extent due to substantial differences in the CD4⁺ and CD8⁺ T cell compartments. In total, 142 subsets in the immune system were defined of which 120 displayed distinct marker expression profiles on the basis of which these subsets were delineated. Compared to the CD4⁺ and CD8⁺T cell lineages, a larger degree of heterogeneity was detected in the TCR $\gamma\delta$ and CD3⁺CD7⁺ immune lineages. While we cannot exclude the possibility that by the use of another antibody panel additional heterogeneity within the CD4⁺ and CD8⁺ lineages may be revealed, the distinct marker expression profiles of the TCR $\gamma\delta$ and CD3⁺CD7⁺ subsets may correlate with distinct and potentially location-specific functional properties. This will be the subject of future investigations. Thus, based on 28 markers mass cytometry visualized system-wide cellular differences in subset composition in the samples obtained from the various anatomical locations. Further studies including control rectum samples are required to determine how these differences relate to the anatomical site and/or disease state.

Recent studies have described a crucial role for ILCs in CD²². They reside mainly in mucosal tissues and are functionally specialized cells characterized by the expression of lineage-defining transcription factors. Even without these markers in our antibody panel we were able to distinguish ILC-like subsets on the basis of cell surface phenotype through machine-learning cell cluster detection approaches. We identified a CRTH2⁺ ILC2-like subset in PBMC samples and in line with previous reports such cells were not found in intestinal samples²². Moreover, we detected an ILC3-like subset that was exclusively present in rectum biopsies of CD patients in remission. This subset corresponds with the IL-22-producing anti-inflammatory CD25⁺CD56⁺ ILC subset previously found in the intestine of CD patients^{19, 22}. Moreover, we observed that their CD56⁻ ILC counterpart was enriched in fistulas, and these cells were previously shown to produce the inflammatory cytokine IL-17A¹⁹. The CD56⁻-ILC3-like cells in fistulas unexpectedly showed expression of CD11c, a marker that has been used as 'dump channel' in the ILC field. Those cells may thus have been discarded from datasets of previous studies, highlighting the importance of unbiased data-driven approaches as used in the current study. In addition, the CD4⁺ T cell compartment in the CD biopsies was highly heterogeneous. Further studies are required to determine a possible relationship with the highly variable disease symptoms in CD.

Mucosal lymphoid malignancies were readily detected in patients with RCDII and in a patient with an EATL-type 2 lymphoma, along with the distinct cellular phenotypes that distinguish these lymphomas. The latter information could be used to identify the potential precursor cells in the healthy mucosa from which these malignancies are likely to originate. In the case of RCDII these precursors are Lin⁻CD3⁻CD7⁺ cells, confirming previous results²³. Moreover, our current analysis indicates that these precursors can be distinguished from their malignant counterpart by the lack of expression of CD45RA. Conversion of this subset to a CD45RA positive phenotype may thus predict development of RCDII and could constitute a novel prognostic marker. Also, extremely low numbers of CD56⁺CD161⁺CD8a⁺CD8b⁺ T cells were found in mucosal biopsies of healthy individuals, a phenotype which matches that of the CD8⁺ T cell malignancy in a patient with EATLII. Thus, the t-SNE analysis is highly suitable for the identification of mucosal malignancies and their likely precursors in healthy individuals, information that may be used to develop therapeutic approaches based on cellular characteristics.

Compared to control duodenal samples we observed the disappearance of CD3⁻CD7⁺ cells and the increase in TCR $\gamma\delta$ cells in CeD, both well-described disease hallmarks^{21, 23}. In the global analysis of the entire cell frequency dataset this resulted in the formation of clusters that distinguish duodenal biopsies derived from CeD patients from those of controls. By transposing the cell frequency dataset the disease cluster-associated subsets and their relative contribution to the clustering could be visualized and quantified. This tSNE application thus provided detailed information on the disease-associated networks of immune subsets. The identification of mucosal immune signatures that correlated with health and disease may potentially lead to the development of unbiased diagnostic procedures based on a single mass cytometric analysis.

Perianal fistulas in CD remain a substantial clinical challenge, causing pain, discharge, and abscess formation²⁴. Achieving complete fistula healing is difficult and accompanied by multiple relapses, and despite the best available therapies durable remission rates of perianal fistulas remain disappointingly low⁷. In this respect it will be important to unravel the function of the CD11b⁺CD11c⁺ myeloid cells that dominate in the fistula, where the immune composition is distinct from that in the adjacent rectum biopsies. This will be addressed in future studies.

In such follow-up studies our approach can be further refined as four antibodies

included in the original 32 antibody panel (CD103, IL21-R, CD34 and TCR $\alpha\beta$) were not informative. In particular the inclusion of antibodies specific for lineage-defining transcription factors and cytokines may provide further insight into the relationship between cell lineages and their function in the mucosal immune system. Moreover, the inclusion of an alternative metal reporter for the CD103-specific antibody in future studies may allow discrimination between cells derived from the epithelium and the lamina propria. Also, with regard to CD and perianal fistula we could not draw definitive conclusions regarding disease-specific changes as we lacked healthy control rectum samples. It would thus be highly valuable to characterize mucosal biopsies obtained from various intestinal locations within the same patients and controls, allowing direct comparisons. Finally, by combining the analysis of the mucosal immune system with an analysis of the stromal cell compartment a more integrated view of disease-specific changes may be obtained, optimizing opportunities to develop more effective personalized treatment modalities.

In conclusion, the mass cytometric analysis of the mucosal immune system revealed heterogeneity that was greater than previously appreciated. Also, our results indicate that disease-specific leukocytes reside mainly in the affected organ and are much less readily detectable in PBMC. The identification of disease-associated changes in immune composition offers opportunities to determine cellular parameters that correlate with disease and predict response to treatment, an important step towards personalized and cost-effective treatment.

EXPERIMENTAL PROCEDURES

Human Samples

Samples were collected from patients who were undergoing routine diagnostic endoscopies, and the curettage material of perianal fistulas were obtained at surgical intervention. The clinical characteristics of the patients are shown in **Table S2**. All samples were obtained after informed consent, medical ethical commission approval, in accordance with the local ethical guidelines of the VU Medical Center in Amsterdam (adult duodenal biopsies) and the Leiden University Medical Center (pediatric duodenal biopsies, CD rectum biopsies, and perianal fistulas), and in accordance with the declaration of Helsinki.

Isolation of cells from intestinal and PBMC samples

Cells from the epithelium were isolated from two or three intestinal biopsies by

treatment with 10 mL of HBSS (Sigma-Aldrich, St. Louis, United States) containing 1 mM EDTA (Merck, Darmstadt, Germany) under rotation for 2 hr at 37°C. To obtain cells from the lamina propria, the biopsies were washed with PBS containing 0.5% fetal calf serum (FCS) and incubated with 5 mL of a collagenase mix containing IMDM culture medium (Lonza, Basel, Switzerland) with 20% FCS, 1,000 U/mL collagenase IV (Worthington, Lakewood, United States) and 10 mg/mL DNaseI grade II (Roche Diagnostics, Basel, Switzerland) for 2 hr at 37°C. The cell suspension was then filtered through a 70 µm nylon cell strainer and centrifuged in 0.5% FCS/PBS. Curettage material of perianal fistulas obtained at surgical intervention were minced with fine scissors and incubated with 10 mL of HBSS containing 1 mM EDTA under rotation for 2 hr at 37°C. Peripheral blood mononuclear cells (PBMC) were isolated from up to 5 mL of freshly drawn heparin anticoagulated blood using Ficoll-Paque™ density-gradient centrifugation. PBMC samples from CD patients were cryopreserved and stained after thawing. Cell suspensions were washed with 0.5% FCS/PBS and kept at 4°C until antibody staining.

Antibodies

Antibodies, manufacturers, and concentrations are listed in **Table SI**. Primary antibody metal-conjugates were either purchased or conjugated using a total of 100 µg of carrier-free formulations of purified antibody combined with the MaxPar X8 antibody labeling kit (Fluidigm Sciences, Toronto, Canada) according to the manufacturer's instruction. Following conjugation, antibodies were diluted to 200 µL in Candor PBS Antibody Stabilization Buffer (Candor Bioscience GmbH, Wangen, Germany) and stored at 4°C.

Antibody staining and data acquisition

Procedures for mass cytometry antibody staining and data acquisition were carried out as previously described¹³. Briefly, directly after biopsy processing cells were resuspended in cell staining buffer (CSM; 1x PBS with 0.5% bovine serum albumin and 0.02% sodium azide, Fluidigm Sciences) and incubated with 1 mL of 1:500 diluted 500 µM rhodium DNA intercalator (Fluidigm Sciences) for 15 min to stain dead cells at room temperature (rT). Cells were washed with CSM and surface stained for 45 min at rT with a mixture of metal isotope-conjugated antibodies using predetermined concentrations (**Table SI**). Antibody staining reactions were performed in 100 µL final volume. After staining, cells were washed twice with CSM and then resuspended in 1 mL of 1:1000 diluted 125 µM iridium DNA intercalator (DVS Sciences) in Fix and Perm Buffer (PBS with 1.6% paraformaldehyde, Fluidigm Sciences) for 45 min at rT to discriminate single cells. Cells were stored overnight at

4°C. Finally, cells were washed twice in CSM and once in distilled water at rT. Prior to data acquisition, cell pellets were diluted in distilled water containing 1:10 diluted EQ Four Element Calibration Beads (Fluidigm Sciences) to the concentration of 0.4×10^6 cells/mL to achieve an acquisition rate of 500 events/s on the CyTOF 2™ mass cytometer (Fluidigm Sciences)²⁵. CyTOF data were acquired and analyzed on-the-fly, using dual-count mode and noise-reduction on. All other settings were either default settings or optimized with tuning solution, as instructed by Fluidigm Sciences. After data acquisition, the mass bead signal was used to normalize the short term signal fluctuations with the reference EQ passport P13H2302 during the course of each experiment and the bead events were removed²⁶.

Data analysis

SPADE analyses were performed as described¹⁵ with 500 target number of nodes and 10% of target down-sampled events using the implementation in Cytobank²⁷. Data from exported FCS files of major immune lineages as delineated by SPADE (**Figure 1**) were transformed using hyperbolic arcsin with a cofactor of 5. Because the number of cell events varied greatly between PBMC and intestinal biopsies, the contribution of intestinal and PBMC cells were normalized to a 1:1 ratio for each immune lineage and up to 10,000 events per sample was used. After down-sampling, the cumulative dataset per immune lineage was subjected to t-SNE dimensionality reduction. t-SNE was carried out using the Barnes-Hut implementation of t-SNE, a recent developed, computationally efficient t-SNE optimization algorithm (obtained from L.J.P. van der Maaten)¹⁷ to accommodate the large volumes of our clinical data. t-SNE was run with a default perplexity of 30. Cellular ‘finger-print’ signatures of immune cells and marker expression color overlays of t-SNE maps were generated with Cyt¹². We used the Jensen-Shannon (JS) divergence to quantify the similarity between t-SNE maps. After converting t-SNE maps into 2-dimensional probability density functions, the similarity between two maps is quantified as the JS divergence between their corresponding probability density functions. We used the base 2 logarithm in the JS divergence computation, which results in a continuous range of JS divergence values between 0 (for identical distributions) and 1 (for fully disjoint distributions). The density-peak detection algorithm to identify phenotypically distinct subsets was carried out with ACCENSE¹⁴, using the two coordinates of the t-SNE map for each cell as input. The density-based clustering first searches for the optimal bandwidth, followed by estimating the kernel density that allows the detection of density peaks. The respective amount of subpopulations identified per major lineage was based on the calculated optimal kernel bandwidth. Two-

dimensional gating analysis was done using Cytobank²⁷. Median intensity values of markers were calculated and visualized via plotting heatmaps. Hierarchical clustering dendrograms of heatmaps were produced using Pearson Correlation and average linkage clustering with MultiExperiment Viewer (www.tm4.org). Numbers of cells in different immune subsets were counted for each sample and percentages of each subset were calculated. t-SNE coordinates, ACCENSE subset number, and sample coding tags were added to FCS files as additional parameters to allow aggregate data analysis and visualization. The sample t-SNE map (**Figure 5**) was computed with the fractions of the total cell count per subtype (as % of CD45⁺ cells) as input variables. Standard t-SNE pre-processing was applied: the data matrix was normalized by centering each variable to zero mean, and scaling to unit vector length. In the sample map, a reprojection of the data on a reduced set of high-variance principal components (PCs) was performed. The component scores of the 10 highest variance PCs were used as input to the t-SNE. To reduce sensitivity to local optima, map construction was repeated 100 times with different randomly generated initial maps and the map with the minimal t-SNE error metric (Kullback Leibler divergence per data point) was selected. The subset t-SNE map in **Figures 6H** and **6I** was computed by transposing the normalized datamatrix. This switches the role of samples and variables, hence subsets with similar profiles across the population end up close together in the map. The t-SNE perplexity parameter was set to 10% of the number of data points in each map, i.e. 10 for the sample maps in **Figures 6A-6F**, and 15 for the subset map in **Figure 6G**. Average subset values were computed per disease subgroup as identified in the sample t-SNE map in **Figure 5G**, and displayed per subgroup.

REFERENCES

1. Kappelman, M.D., Moore, K.R., Allen, J.K. & Cook, S.F. Recent trends in the prevalence of Crohn's disease and ulcerative colitis in a commercially insured US population. *Dig Dis Sci* **58**, 519-525 (2013).
2. Rubio-Tapia, A., Ludvigsson, J.F., Brantner, T.L., Murray, J.A. & Everhart, J.E. The prevalence of celiac disease in the United States. *Am J Gastroenterol* **107**, 1538-1544; quiz 1537, 1545 (2012).
3. Al-Toma, A., Verbeek, W.H., Hadithi, M., von Blomberg, B.M. & Mulder, C.J. Survival in refractory coeliac disease and enteropathy-associated T-cell lymphoma: retrospective evaluation of single-centre experience. *Gut* **56**, 1373-1378 (2007).
4. Pascual, V. et al. Inflammatory bowel disease and celiac disease: overlaps and differences. *World J Gastroenterol* **20**, 4846-4856 (2014).
5. Randall, C.W. et al. From historical perspectives to modern therapy: a review of current and future biological treatments for Crohn's disease. *Therap Adv Gastroenterol* **8**, 143-159 (2015).
6. Schwartz, D.A. et al. The natural history of fistulizing Crohn's disease in Olmsted County, Minnesota. *Gastroenterology* **122**, 875-880 (2002).

7. Molendijk, I., Nuij, V.J., van der Meulen-de Jong, A.E. & van der Woude, C.J. Disappointing durable remission rates in complex Crohn's disease fistula. *Inflamm Bowel Dis* **20**, 2022-2028 (2014).
8. Jabri, B. & Sollid, L.M. Tissue-mediated control of immunopathology in coeliac disease. *Nat Rev Immunol* **9**, 858-870 (2009).
9. Verbeek, W.H. et al. Flow cytometric determination of aberrant intra-epithelial lymphocytes predicts T-cell lymphoma development more accurately than T-cell clonality analysis in Refractory Celiac Disease. *Clin Immunol* **126**, 48-56 (2008).
10. Geremia, A., Biancheri, P., Allan, P., Corazza, G.R. & Di Sabatino, A. Innate and adaptive immunity in inflammatory bowel disease. *Autoimmun Rev* **13**, 3-10 (2014).
11. Bandura, D.R. et al. Mass cytometry: technique for real time single cell multitarget immunoassay based on inductively coupled plasma time-of-flight mass spectrometry. *Anal Chem* **81**, 6813-6822 (2009).
12. Amir el, A.D. et al. viSNE enables visualization of high dimensional single-cell data and reveals phenotypic heterogeneity of leukemia. *Nat Biotechnol* **31**, 545-552 (2013).
13. Bendall, S.C. et al. Single-cell mass cytometry of differential immune and drug responses across a human hematopoietic continuum. *Science* **332**, 687-696 (2011).
14. Shekhar, K., Brodin, P., Davis, M.M. & Chakraborty, A.K. Automatic Classification of Cellular Expression by Nonlinear Stochastic Embedding (ACCENSE). *Proceedings of the National Academy of Sciences of the United States of America* **111**, 202-207 (2014).
15. Qiu, P. et al. Extracting a cellular hierarchy from high-dimensional cytometry data with SPADE. *Nature biotechnology* **29**, 886-891 (2011).
16. van der Maaten, L. & Hinton, G. Visualizing Data using t-SNE. *Journal of Machine Learning Research* **9**, 2579-2605 (2008).
17. van der Maaten, L. Accelerating t-SNE using Tree-Based Algorithms. *Journal of Machine Learning Research* **15**, 3221-3245 (2014).
18. Spits, H. & Cupedo, T. Innate lymphoid cells: emerging insights in development, lineage relationships, and function. *Annu Rev Immunol* **30**, 647-675 (2012).
19. Geremia, A. et al. IL-23-responsive innate lymphoid cells are increased in inflammatory bowel disease. *J Exp Med* **208**, 1127-1133 (2011).
20. Becher, B. et al. High-dimensional analysis of the murine myeloid cell system. *Nat Immunol* **15**, 1181-1189 (2014).
21. Spencer, J., Isaacson, P.G., Diss, T.C. & MacDonald, T.T. Expression of disulfide-linked and non-disulfide-linked forms of the T cell receptor gamma/delta heterodimer in human intestinal intraepithelial lymphocytes. *Eur J Immunol* **19**, 1335-1338 (1989).
22. Hazenberg, M.D. & Spits, H. Human innate lymphoid cells. *Blood* **124**, 700-709 (2014).
23. Schmitz, F. et al. Identification of a potential physiological precursor of aberrant cells in refractory coeliac disease type II. *Gut* **62**, 509-519 (2013).
24. Kamm, M.A. & Ng, S.C. Perianal fistulizing Crohn's disease: a call to action. *Clin Gastroenterol Hepatol* **6**, 7-10 (2008).
25. Ornatsky, O.I. et al. Development of analytical methods for multiplex bio-assay with inductively coupled plasma mass spectrometry. *J Anal At Spectrom* **23**, 463-469 (2008).
26. Finck, R. et al. Normalization of mass cytometry data with bead standards. *Cytometry A* **83**, 483-494 (2013).
27. Kotecha, N., Krutzik, P.O. & Irish, J.M. Web-based analysis and publication of flow cytometry experiments. *Curr Protoc Cytom* **Chapter 10**, Unit 10.17 (2010).

SUPPLEMENTAL INFORMATION

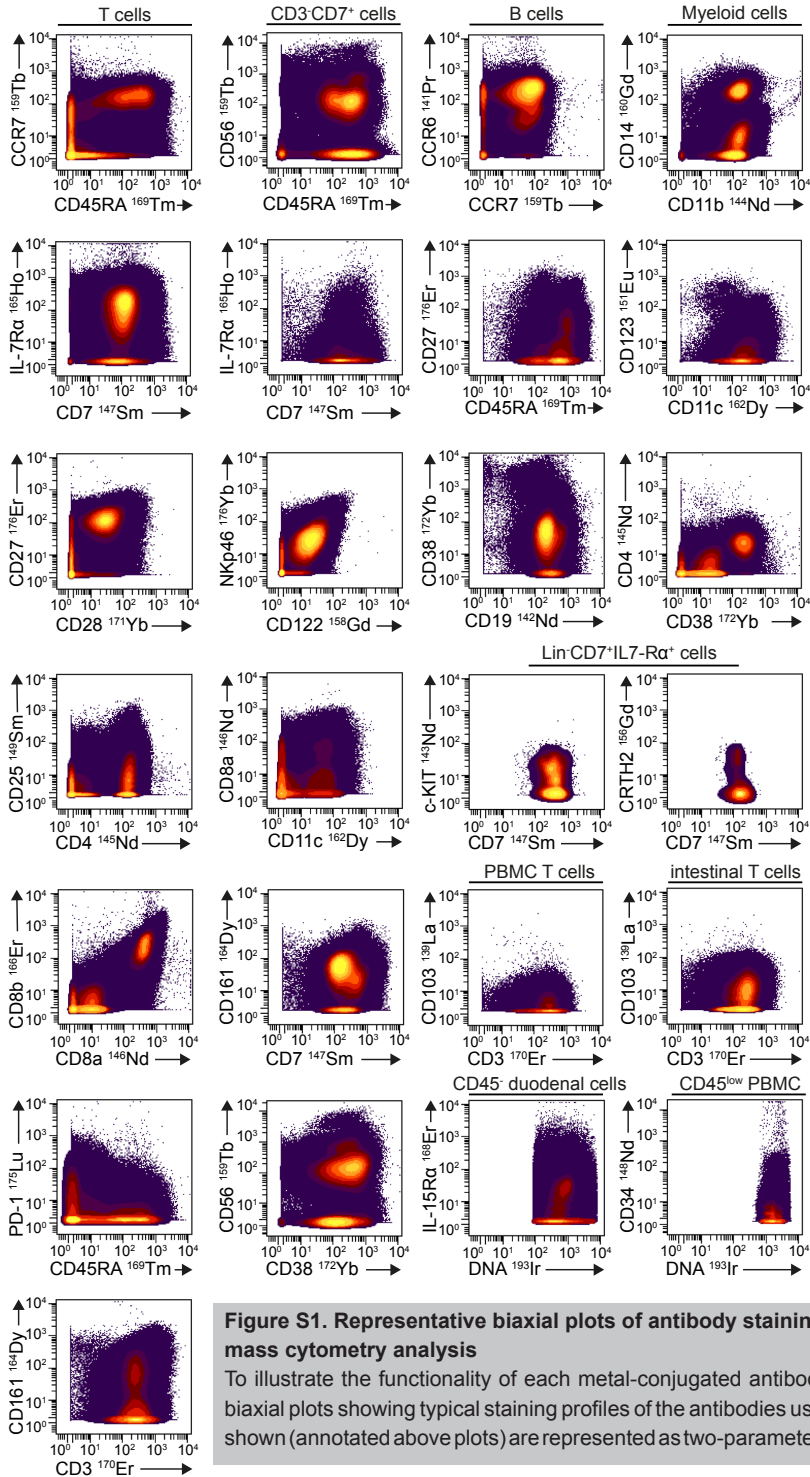


Figure S1. Representative biaxial plots of antibody stainings used for the mass cytometry analysis
 To illustrate the functionality of each metal-conjugated antibody, representative biaxial plots showing typical staining profiles of the antibodies used. Cells gated as shown (annotated above plots) are represented as two-parameter density dot plots.

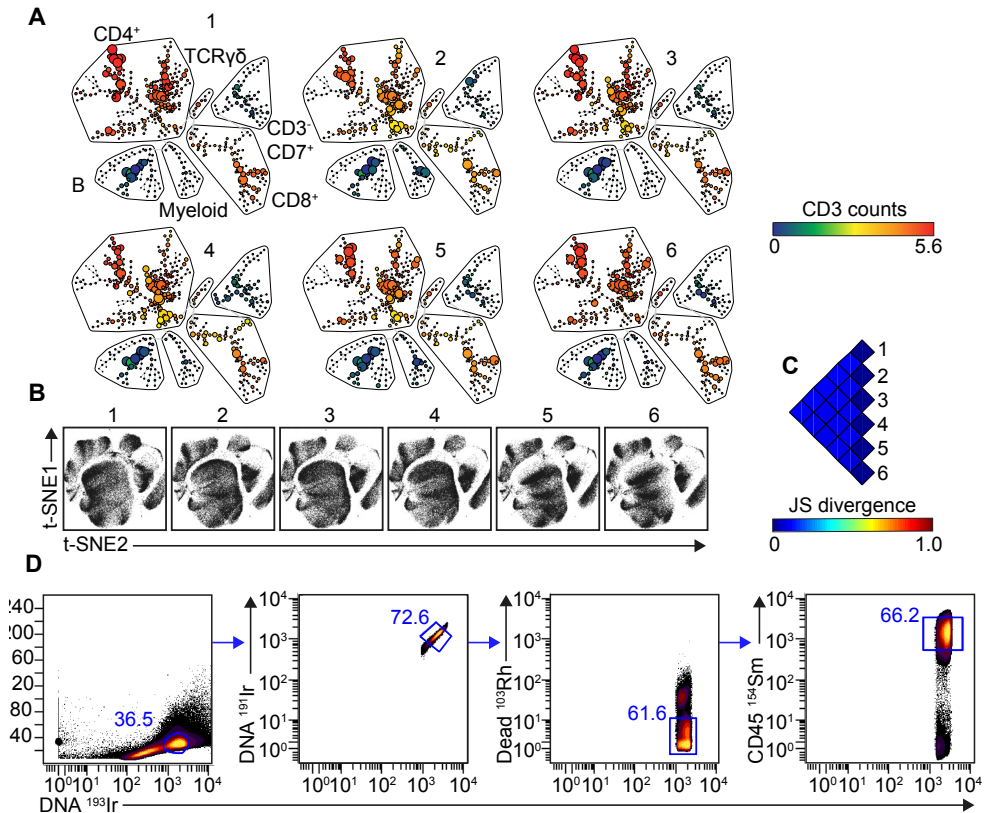


Figure S2. SPADE and t-SNE analysis of the internal peripheral blood control

(A) Six PBMC samples from the same individual taken at different time points during the entire study period are shown after collective SPADE analysis of live single CD45⁺ cells. Size of the nodes is proportional to the respective number of clustered cells. Color bars represent ArcSinh5 transformed values for CD3 marker expression. The identities of major immune lineages are annotated on the basis of lineage marker expression (CD4⁺ = CD4⁺ T cells, CD8⁺ = CD8⁺ T cells and B = B cells) (for details SPADE analysis see Figure 1) (B) Collective t-SNE dimensionality reduced single-cell data containing live single CD45⁺ cells from 6 PBMC samples as described in panel a analyzed are plotted. Each sample was down-sampled to 50,000 events prior to the t-SNE analysis. (for details t-SNE analysis see Figures 2 and 4) (C) Pairwise Jensen-Shannon (JS) divergence plot of the collective t-SNE maps from the 6 PBMC samples analyzed. A lower JS divergence value indicates more similarity between a pair of t-SNE maps as shown in panel b. (D) Live, single CD45⁺ cells gating strategy. Representative mass cytometry plots of a duodenum biopsy showing sequential gates with percentages. Event length is a mass cytometric measurement for the amount of scans it took to acquire a given ion cloud.

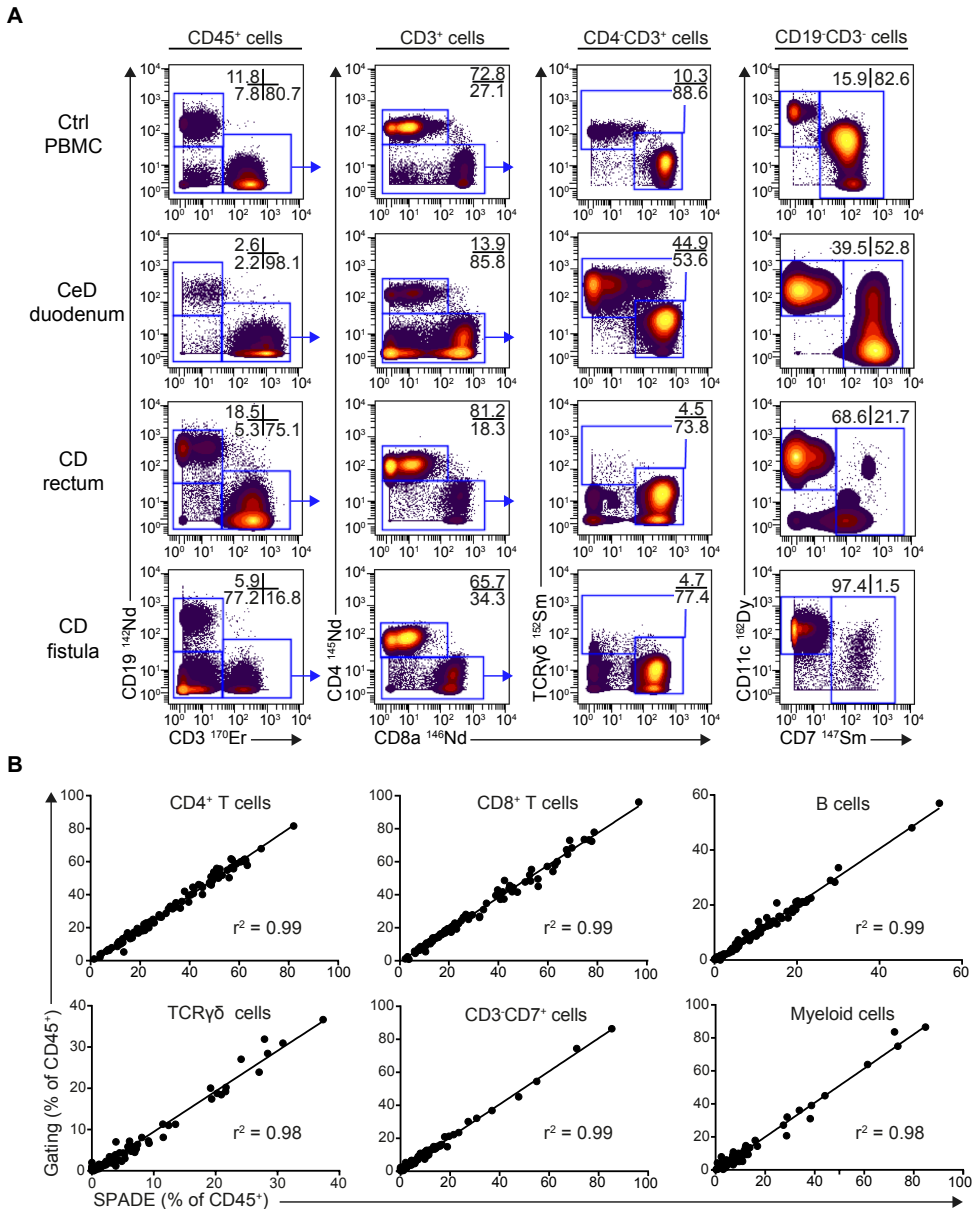


Figure S3. Traditional gating yields similar frequencies of major immune lineage cells as with SPADE analysis

(A) Representative samples are shown to demonstrate the gating strategy applied to identify the major immune lineages: CD4⁺ T cells, CD8⁺ T cells, B cells, TCRγδ cells, CD3-CD7⁺ cells and myeloid cells. Cells gated as shown (annotated above plots) are represented as two parameter density dot plots. (B) Correlation of cell frequencies obtained through traditional gating and with SPADE analysis are shown for the 102 samples as analyzed with linear regression. A dot represents a single sample.

Mass Cytometry of the Human Mucosal Immune System Reveals Tissue- and Disease-Associated Immune Subsets

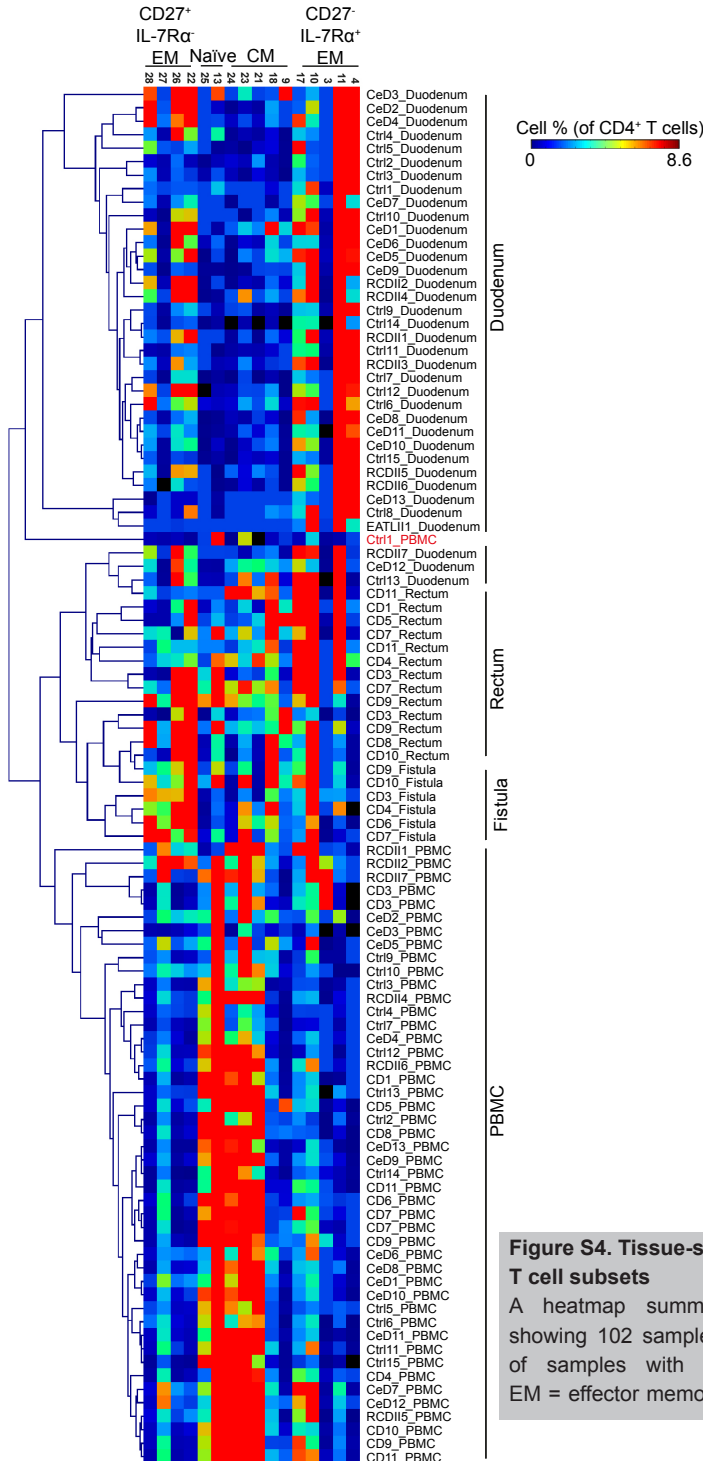


Figure S4. Tissue-specific composition of CD4⁺ T cell subsets

A heatmap summary of subset frequencies showing 102 samples and hierarchical clustering of samples with description of tissue type. EM = effector memory and CM = central memory.

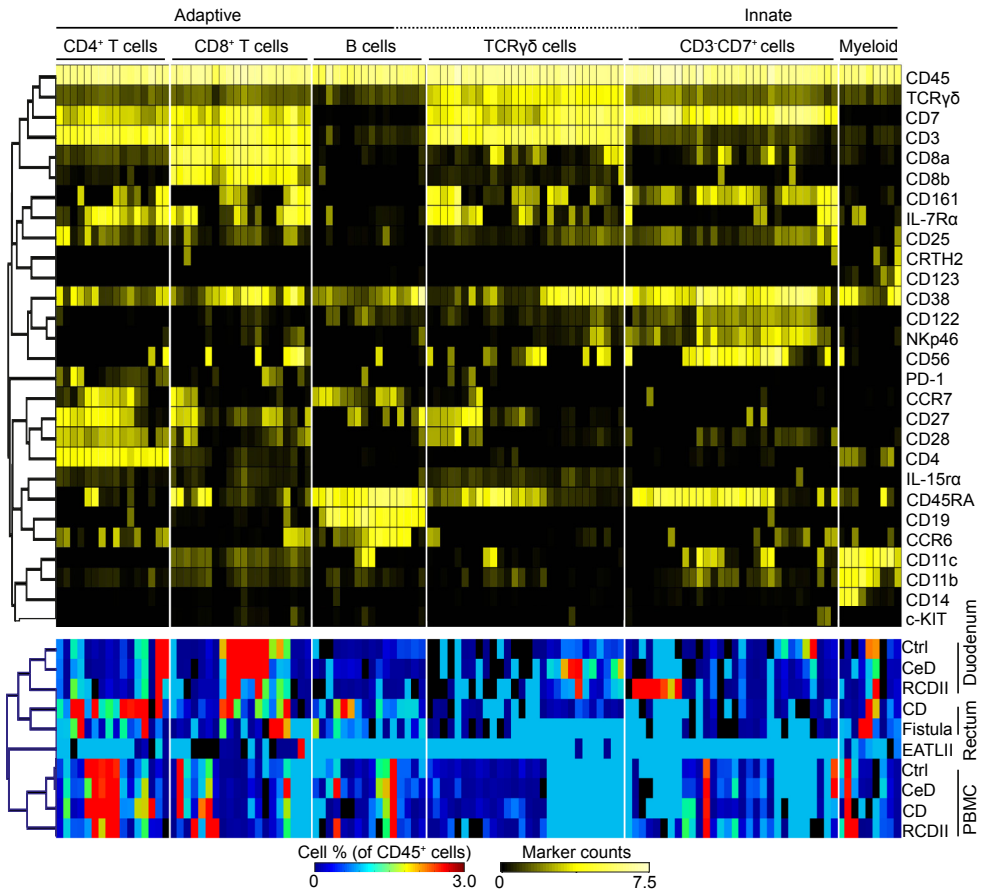


Figure S5. Marker expression profiles and composition of immune subsets in peripheral blood and intestine
 Heatmaps showing characterization of cell populations (median ArcSinh5-transformed values of marker expression; black-to-yellow scale), composition (average cell percentages; rainbow scale) and hierarchical clustering of markers and samples.

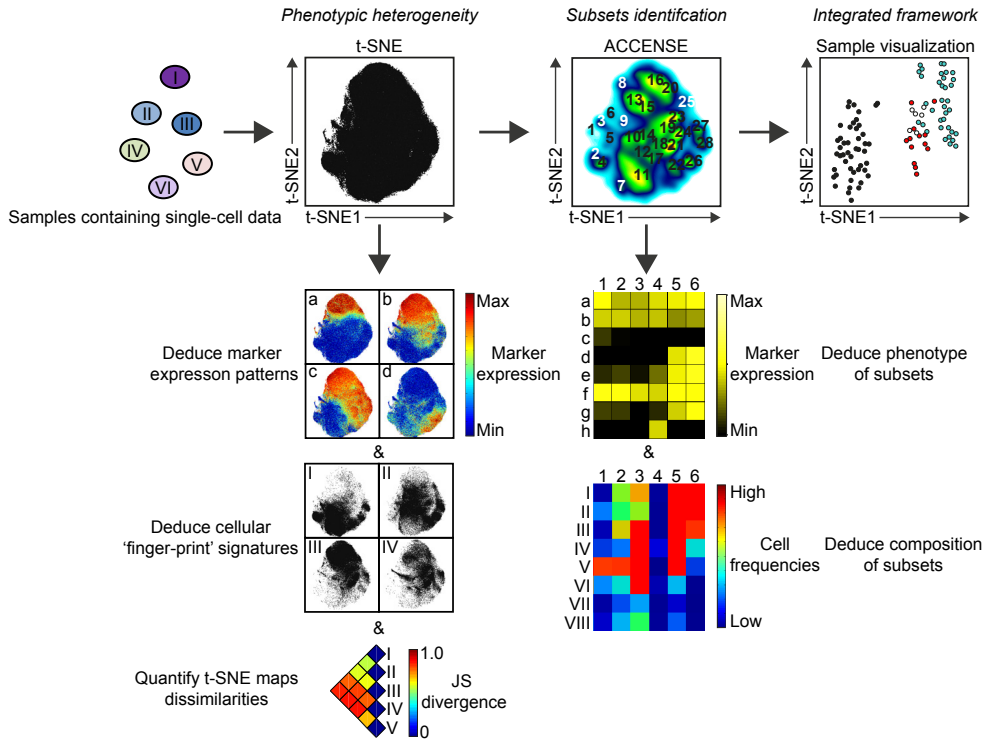


Figure S6. High-dimensional mass cytometry analysis pipeline

Samples containing single-cell data of cell populations of interest (e.g. based on SPADE analysis or gated subsets) are tagged with integer sample identification values, marker expression values are transformed using hyperbolic arcsin with a cofactor of 5, and cells are downsampled to match sample cell number. Collective t-SNE dimensionality reduction was performed on the single-cell data derived from all the samples. A dot represents a single cell and color overlays illustrate marker expression values to deduce marker expression patterns. t-SNE maps are stratified for tissues and disease states to illustrate cellular 'finger-print' signatures. Pairwise Jensen-Shannon (JS) divergence analysis quantifies dissimilarity between a pair of t-SNE maps. On the basis of the map created by t-SNE, a machine-learning cell cluster detection approach (ACCENSE) delineates cell subsets. Heatmaps illustrate the phenotypic signature of the identified immune subsets and illustrate the composition of subsets within the samples. The cell frequency data of all the identified immune subsets are used to visualize samples in an integrated framework using the t-SNE algorithm, where a dot represents a single sample and the color overlay illustrates clinical information. Markers are indicated in letters, samples in roman letters and cell subsets in numbers.

Table S1. CyTOF antibody panel

Antigen	Tag	Clone	Com.	Cat#	Conc.
CD56	¹⁷⁶ Yb	NCAM16.2	DVS	3176008B	1:100
CD4	¹⁴⁵ Nd	RPA-T4	DVS	3145001B	1:100
CD8a	¹⁴⁶ Nd	RPA-T8	DVS	3146001B	1:100
CD3	¹⁷⁰ Er	UCHT1	DVS	3170001B	1:100
CD14	¹⁶⁰ Gd	M5E2	DVS	3160001B	1:100
CD19	¹⁴² Nd	HIB19	DVS	3142001B	1:100
TCRgd	¹⁵² Sm	11F2	DVS	3152008B	1:100
CD45	¹⁵⁴ Sm	HI30	DVS	3154001B	1:100
CD45RA	¹⁶⁹ Tm	HI100	DVS	3169008B	1:100
CD27	¹⁶⁷ Er	O323	DVS	3167002B	1:100
CD38	¹⁷² Yb	HIT2	DVS	3172007B	1:100
CD127	¹⁶⁵ Ho	AO19D5	DVS	3165008B	1:100
CD11b	¹⁴⁴ Nd	ICRF44	DVS	3144001B	1:100
CD7	¹⁴⁷ Sm	CD7-6B7	DVS	3147006B	1:100
CD34	¹⁴⁸ Nd	581	DVS	3148001B	1:100
C-Kit	¹⁴³ Nd	104D2	DVS	3143001B	1:100
CD161	¹⁶⁴ Dy	HP-3G10	DVS	3164009B	1:100
CD123	¹⁵¹ Eu	6H6	DVS	3151001B	1:100
CCR6	¹⁴¹ Pr	G034E3	DVS	3141003A	1:100
CD25	¹⁴⁹ Sm	2A3	DVS	3149010B	1:100
CCR7	¹⁵⁹ Tb	G043H7	DVS	3159003A	1:100
PD-1	¹⁷⁵ Lu	EH 12.2H7	DVS	3175008B	1:100
CD11c	¹⁶² Dy	Bu15	DVS	3162005B	1:100
CD8b	¹⁶⁶ Er	SID18BEE	eBio	14-5273	1:50
CRTH2	¹⁵⁶ Gd	BM16	BioL	350102	1:50
TCRab	¹⁵⁰ Nd	1P26	BioL	306702	1:50
IL-21R	¹⁵³ Eu	2G1-K12	BioL	347802	1:50
IL-15Ra	¹⁶⁸ Er	eBioJM7A4	eBio	14-7159-82	1:50
CD103	¹³⁹ La	Ber-ACT8	BioL	350202	1:100
CD28	¹⁷¹ Yb	CD28.2	BioL	302902	1:100
NKp46	¹⁷⁴ Yb	9E2	BioL	331902	1:100
CD122	¹⁵⁸ Gd	TU27	BioL	339002	1:200

DVS Sciences (DVS), eBioscience (eBio), and Biolegend (BioL).

The antibody panel was designed to obtain a global overview of the heterogeneity of the immune system. For this purpose, the panel included markers that distinguish the major immune cell lineages, i.e. CD4⁺ T cells, CD8⁺ T cells, TCRγδ cells, B cells, innate lymphocytes (CD3⁺CD7⁺) and myeloid cells. In addition, markers were included that allow the identification of phenotypically distinct subsets within those immune cell lineages, like naïve and memory cells, resting and activated cells. In addition, markers were included that provide information on additional differentiation stages of cells, homing properties of cells, and their potential responsiveness to humoral factors like cytokines and chemokines. Our choice in markers was biased towards phenotyping CD7⁺-expressing lymphoid cells (T cells and CD3⁺CD7⁺ cells) rather than B cells and myeloid cells.

Table S2. Characteristics of control and patients with inflammatory intestinal diseases

Characteristics	Ctrl (N=15)	CeD (N=13)	RCDII ^a (N=5)	EATLII (N=1)	CD ^b (N=10)
AgeBiop , (mean, ±SEM)	33.1±5.6	34.5±6.5	74.8±1.6	66	37.3±2.9
Gender , N (%)					
Male	5 (33.3)	6 (46.2)	5 (100.0)	0 (0.0)	3 (30.0)
Female	10 (66.6)	7 (53.8)	0 (0.0)	1(100.0)	7 (70.0)
GFD , N (%)					NA
No	13 (86.7)	5 (38.5)	0 (0.0)	0 (0.0)	-
Yes	2 (13.3)	8 (61.5)	5 (100.0)	1 (100.0)	-
Type of Biopsy					
Duodenum	15	13	7	1	-
Rectum	-	-	-	-	13
Fistula	-	-	-	-	6
PBMC ^d	14	13	6	-	14
Inflamed gut biopsy^c , N (%)					
No	14 (93.3)	6 (46.2)	2 (28.6)	0 (0.0)	12 (66.7)
Yes	1 (6.7)	7 (53.8)	5 (71.4)	1 (100.0)	6 (33.3)
Marsh score biopsy N (%)				NA	NA
M0	14 (93.3)	6 (46.2)	2 (28.6)	-	-
M1	0 (0.0)	1 (7.7)	0 (0.0)	-	-
M2	0 (0.0)	0 (0.0)	0 (0.0)	-	-
M3a	1 (6.7)	1 (7.7)	2 (28.6)	-	-
M3b	0 (0.0)	4 (30.8)	1 (14.3)	-	-
M3c	0 (0.0)	1 (7.7)	2 (28.6)	-	-

^aTwo RCDII patients were biopsied twice at different time points.

^bFour CD patients were rectally biopsied twice at different time points.

^cAll 13 rectum biopsies of CD patients were non-inflamed, whereas all 6 fistula samples were inflamed.

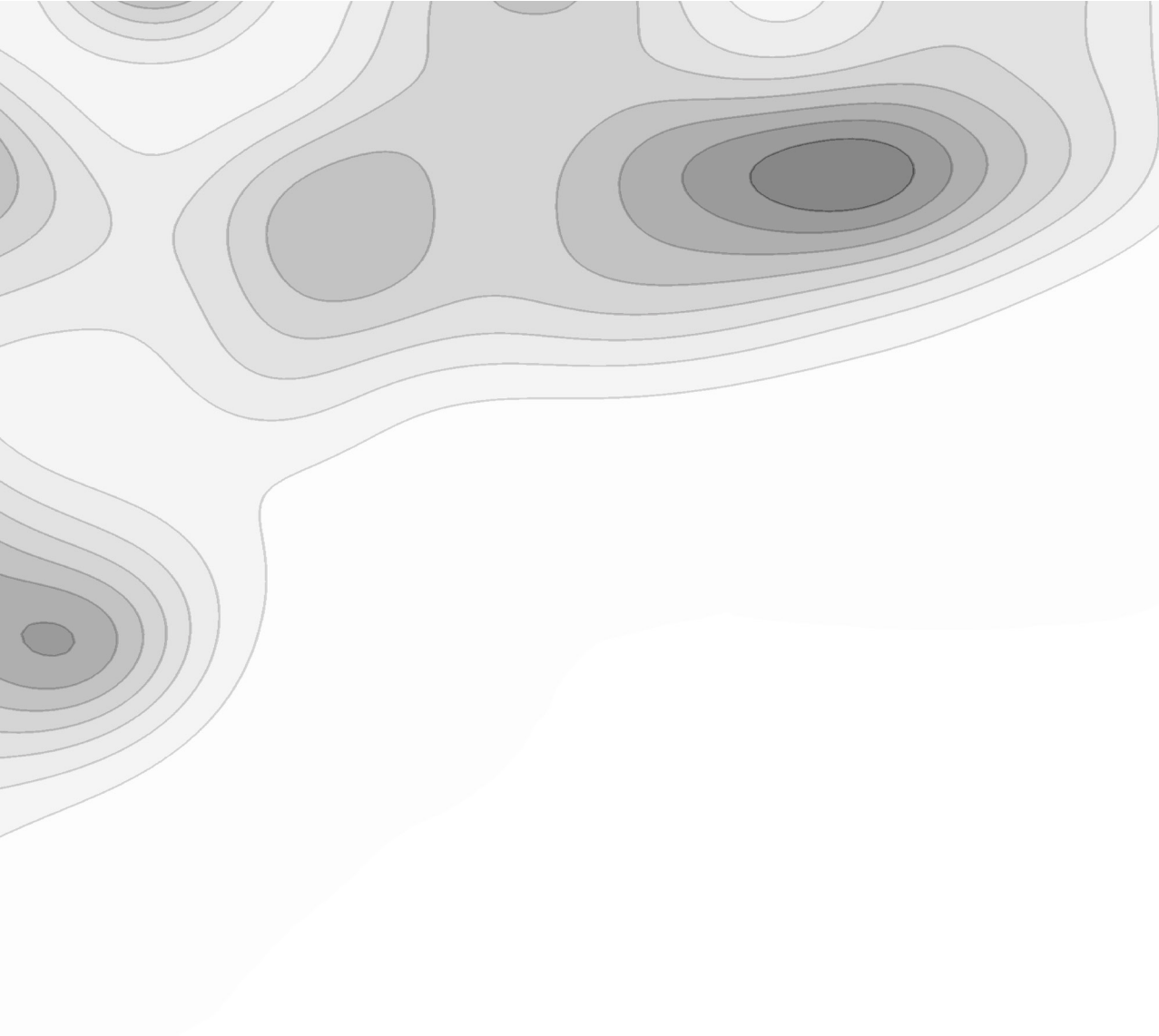
^dPBMC of CD patients were analyzed cryopreserved, whereas all other PBMC samples were analyzed fresh.

Celiac disease (CeD), refractory celiac disease type II (RCDII), enteropathy-associated T cell lymphoma type II (EATLII), Crohn's Disease (CD), age at biopsy time point (AgeBiop), glutenfree diet (GFD), and peripheral blood mononuclear cells (PBMC).

A contour plot in the top-left corner showing several nested, vertically elongated contours, with the innermost being the darkest. The contours are roughly oval-shaped and centered around a vertical axis.

CHAPTER 3

Cytosplore: Interactive Immune Cell Phenotyping for Large Single-Cell Datasets



CHAPTER 3

Cytosplore: Interactive Immune Cell Phenotyping for Large Single-Cell Datasets

Thomas Höllt¹, Nicola Pezzotti¹, Vincent van Unen², Frits Koning², Boudewijn P. F. Lelieveldt^{1,2}, Anna Vilanova¹.

¹Delft University of Technology, Delft, The Netherlands

²Leiden University Medical Center, Leiden, The Netherlands.

Computer Graphics Forum 35:3, 171-180 (2016)

www.cytosplore.org

ABSTRACT

To understand how the immune system works, one needs to have a clear picture of its cellular composition and the cells' corresponding properties and functionality. Mass cytometry is a novel technique to determine the properties of single-cells with unprecedented detail. This amount of detail allows for much finer differentiation but also comes at the cost of more complex analysis. In this work, we present Cytosplore, implementing an interactive workflow to analyze mass cytometry data in an integrated system, providing multiple linked views, showing different levels of detail and enabling the rapid definition of known and unknown cell types. Cytosplore handles millions of cells, each represented as a high-dimensional data point, facilitates hypothesis generation and confirmation, and provides a significant speed up of the current workflow. We show the effectiveness of Cytosplore in a case study evaluation.

I. INTRODUCTION

The immune system primarily protects our body against bacterial, viral and parasitic infections. However, it may respond to harmless self antigens, leading to auto-immune diseases, e.g., type 1 diabetes or rheumatoid arthritis. Detailed knowledge of the immune system's functioning is required to understand the cause of immune-mediated diseases, which is an important step towards preventive or therapeutic measures. To mediate its function, the immune system utilizes both; humoral (soluble) and cellular constituents. The cellular immune compartment consists of a variety of cellular subsets, each with a distinct function and associated phenotype. The phenotype describes "the observable physical or biochemical characteristics of an organism, as determined by both genetic makeup and environmental influences"² [AHD06]. For immune cells, the functionality mostly relates to a set of proteins expressed on the cells surface.

Recently introduced mass cytometry [OKB08] at the moment allows the observation of 36 of these proteins at the same time, three times as many as the clinical standard. However, this number is still orders of magnitude smaller than the estimated 10,000 immune-system-wide available proteins, providing phenotypic information. Hence, specific panels of markers, corresponding to proteins of interest, need to be designed for each study. The composition of these panels is often unique to a study and it is not known beforehand, which combinations of proteins can be expected. Therefore, the identification of different phenotypes largely needs to be carried out in a data-driven fashion by studying data heterogeneity rather than applying prior knowledge. The fine granularity of mass cytometry is usually not only used to increase detail but also to increase breadth, i.e., markers for different cell lineages can be tested simultaneously. A cell lineage describes a group of subsets, all derived from the same ancestry and sharing certain characteristics. Consequently, the data inherently provides multi-scale information; major lineages form clusters on a large scale, while small scale clusters correspond to phenotypical subsets.

To ensure comparability of measurements of multiple blood or tissue samples the same marker panel needs to be applied. In addition, different batches of the same marker can produce different results. Therefore, experiments are usually run in large cohort studies, resulting in hundreds of samples containing millions of cells. These large sizes pose significant challenges during the analysis process. We worked closely with immunohaematology experts to design a data-driven workflow for phenotype specification of cytometry data that we present in this paper. We are the first to

specifically tackle the multi-scale properties of the data. To this extent, we combine and link two proven techniques for the analysis of single-cell data on different levels of detail. For both steps, we provide in-place and linked visualizations of the feature space to interact with and refine the automatically-generated classifications.

The major contributions of this paper are:

- Cytosplore: an integrated system to interactively explore large high-dimensional single-cell datasets and identify phenotypically distinct subsets in a data-driven fashion.
- An analysis workflow, supporting linking of multiple levels of detail to enable
 - rapid, data-driven phenotype specification (including for unknown cell types)
 - the discovery, pinpointing and fixing of mistakes over multiple levels of detail

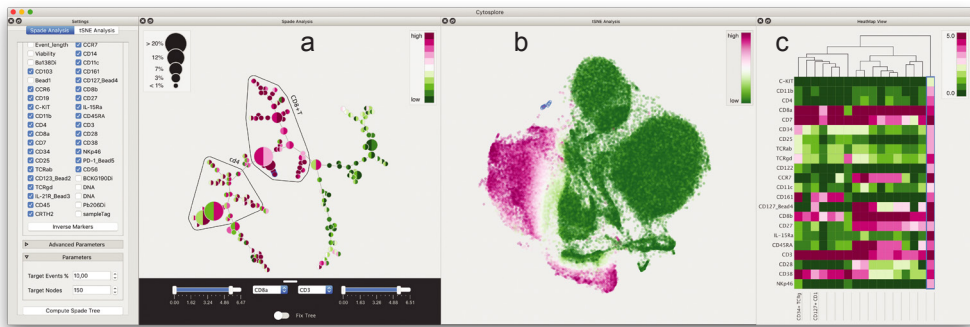


Figure 1: Cytosplore. Screenshot of our system with four widgets (adaptive settings, overview (a), embedding (b) and heatmap (c)), representing the workflow. Views can be rearranged or additional views of these types added.

2. BIOLOGICAL BACKGROUND

To analyze heterogeneity of immune cell subsets, multiparameter analysis of immune cells at single-cell level is required. Flow cytometry has been the method of choice for this purpose, however, suffers from a limitation; it is restricted by the number of cellular markers that can be simultaneously analyzed, usually 10 to 12. This limitation has been overcome by the introduction of mass cytometry.

Mass cytometry is a novel, mass spectrometry-based, technique for characterizing protein expression on cells (cytometry) at single-cell resolution. In short, antibodies, selected to bind to specific proteins of interest on the cell membrane,

are conjugated with heavy-metal reporters. After staining, the cells are vaporized, atomized and ionized one by one and the remaining metals in the ion cloud can be measured in a mass spectrometer to quantify the selected proteins on a per-cell basis. Mass cytometry currently allows the simultaneous analysis of 36 markers, a number which is expected to rise to 100 in the near future.

2.1. Data

Our partners use a prototypical non-integrated version of the workflow presented in this paper in a real world study of tissue- and disease-associated signatures of the human mucosal immune system [vULM16]. They acquired a cohort data set consisting of 102 samples from 44 donors. During preprocessing, the acquired dataset was filtered for live cells, with a strong expression of the CD45 marker (indicating immune cells), resulting in 5.2 million high-dimensional data points. 32 markers were selected for the study to provide information regarding six expected major lineages.

The resulting data is a table of cells and their expression profiles over all available markers. Each row in the table corresponds to a single cell and can be interpreted as a single high-dimensional data point. In abstract terms our input data consists of a large number of high-dimensional data points forming clusters on multiple scales (Section 1).

2.2. Tasks

In this work we aim to tackle the first step of the data analysis process, namely the definition of the phenotype of every cell. In this process our collaborators need to

- Group similar cells, where similarity is defined based on the protein expression for each cell.
- Define for each group the type of cell, which can be unknown beforehand, and annotate the cells.

We provide an abstraction of these tasks, following Brehmer and Munzner's multi-level task typology [BM13] in **Figure 2a** and make use of their adaptations for the visualization of high-dimensional data [BSIM14]. We use a monospaced font throughout the paper, when we use their typology.

3. RELATED WORK

Recent years brought many computer-aided solutions for cytometry-data analysis.

SPADE [QSB11] visualizes high-dimensional data and was developed for (and is commonly used in) single-cell analysis [BSQ11,BZF12,LZN15]. It clusters data in the high-dimensional space and then builds a minimum spanning tree. Flow MAP [ZLG15] follows SPADE, but replaces the spanning tree by a k-nearest neighbour graph, which is laid out via a force-directed layout. The approach avoids SPADE's problem of placing similar nodes far apart, but creates visual clutter. Scaffold Maps [SGF15] enable the user to drive the layout by defining landmarks of cell-type prototypes and by placing them in the visual space to build a scaffold in which similar clusters will be placed.

viSNE [ADT13] introduces t-Distributed Stochastic Neighbor Embedding (tSNE) [vdMH08] to mass cytometry data and ACCENSE [SBDC14] uses tSNE as the basis for automatic clustering. Classification in viSNE is performed by manually gating on the scatterplot, while ACCENSE performs automatic clustering of the embedded data. The tSNE-based techniques perform exceptionally well in embedding cytometry data and provide single-cell resolution. Nonetheless, due to a large computational cost, only limited interactivity is reached. In fact viSNE and ACCENSE both propose downsampling of large data for increased speed. Recently, Pezzotti et al. [PLvdM15] introduced A-tSNE, a tSNE variant, which aims at minimizing precomputation times for high-dimensional neighborhoods. While the cluster-based techniques are reasonably fast, they do not allow inspection on a single-cell level, and overall do not retain the high-dimensional structure as well as tSNE. A standard system for single-cell data analysis is the webbased service Cytobank [KKI10]. It offers SPADE and tSNE computations in a reasonably-easy way. However, it lacks integration and interactivity. As computations are queuebased, significant wait times of several hours can occur.

A multitude of visual analysis tools for *omics*-data have been proposed recently. The focus of the vast majority of these tools is on genomic data. Generally, these data are similar in structure, e.g., a cell can be represented by a high-dimensional expression vector. However, usually the goal of the analysis of these data are quite different. StratomeX [LSS12] allows exploration of genomics data for cancer subtype characterization. They allow comparison of multiple groups using a ribbon-based visualization. The presented case study data consists of a few thousand data points, consisting of up to 6,000 genes (dimensions), each. MizBee [MMP09] is targeted at the exploration of syntenic blocks, blocks of features that appear in the same form on the same or multiple chromosomes. While the data only consists of dozens of chromosomes, the number of features reaches hundreds of thousands. invis [DHHH13] allows exploration of RNA sequences.

Among others, the authors use dimensionality reduction, by means of PCA, and two-dimensional scatterplots to visualize the data. The presented data consist of 19,000 sequences with 186 dimensions. MulteeSum [MMDPI0] is a tool for the visual analysis of gene expression data in cells, with the addition of spatial and temporal information. Here, a typical dataset consists of thousands of cells with 50 dimensions over 6 time points. For all these tools it becomes apparent that besides different analysis questions, the data differs in key properties, compared to cytometry data; instead of millions of data points a typical genomics dataset only consists of thousands of data points, but sometimes with thousands of dimensions

4. MULTILEVEL PHENOTYPE SPECIFICATION WORKFLOW

We introduce a high-level task description in Section 2.2. In short, we need to *derive* groups of similar highdimensional data points and *annotate* these groups. In Section 3, we present a number of tools that are available and commonly used for these tasks in single-cell analysis. However, none of these tools performs optimally on large cohort studies (Section 2.1) consisting of millions of cells. The de facto standard in terms of quality is a combination of tSNE [vdMH08] (i.e., viSNE [ADT13]) with manual or automatic clustering in the embedding [SBDC14]. However, the computational complexity severely limits the applicability of tSNE for large data. Other tools, like SPADE [QSB11] work with larger data but do not produce cluster separation of the same quality.

In this work, we propose a multilevel workflow that effectively reduces these problems; we use SPADE clustering to create a high-level partitioning of the data, coupled with a detail analysis of each partition via A-tSNE, reducing the input size of each embedding and making it feasible. The partitioning is a means to deal with large data sizes but also has a biological justification. The amount of markers in mass cytometry enables the design of marker panels covering multiple cell lineages at the same time. In this case, the expression of markers strongly vary between lineages, but are more subtle within a lineage. Using the increased number of markers to create breadth inherently creates multiple scales within the data, which we separate in our multilevel workflow.

In the following, we present an abstraction of the two levels of this workflow, following Brehmer and Munzner's multi-level task typology [BM13]. Similar

to their extension for the visualization of high-dimensional data [BSIM14], we focus on the `why` and `what` in this section. We describe the `how` in Section 5.

4.1. Major Lineage Delineation

A major lineage of cells corresponds to a high-level cluster in the data (see Section 2.1). While we do expect tens to hundreds of different cell types, the number of major lineages is limited. Since the marker panel is designed specifically to cover a set of lineages of interest, their number, as well as their discerning markers, are known beforehand. However, the boundaries between the clusters are not fixed and the discerning markers are not always unique for a single lineage. Therefore, we propose an interactive approach to defining the high-level clustering.

We present an abstraction of the major lineage delineation in **Figure 2b**. We propose a two step approach. In **T1a** we group points, `deriving` a set of clusters in the highdimensional space. Even though we do know the number of expected high-level clusters, we propose to create more clusters here and combine them to high-level meta-clusters in **T1b**, to find the optimal boundaries. For **T1b**, we propose an interactive approach; since the target is known (based on the discerning markers) the user needs to `locate` the corresponding groups of clusters, `summarize` them to `derive` meta-clusters, and finally `annotate` those meta-clusters.

In summary, we need to provide the user with effective tools and visual encodings to:

- `derive` a predefined number of clusters, while preserving high-dimensional structures.
- `locate`, `summarize` and `derive` major lineages by their discerning markers using prior knowledge.

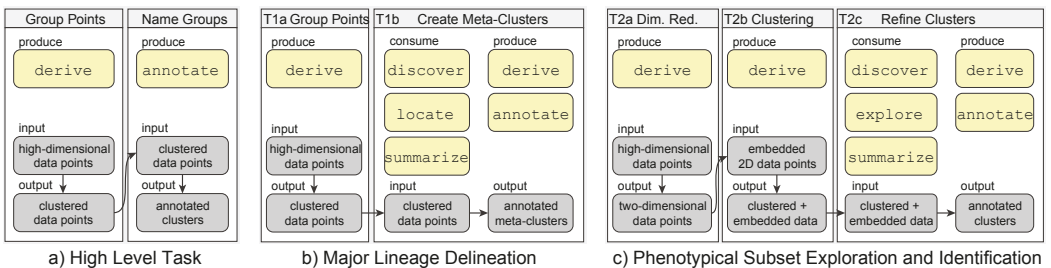


Figure 2: Abstraction of the identified high-level tasks as well as the detailed subtasks

4.2. Phenotypical Subset Exploration and Identification

Exploration and identification of phenotypically-distinct subsets happens in the second step of our workflow. We define a phenotypically-distinct subset as a group of cells with similar marker expression profiles. The subsets can greatly vary in size, in fact small subsets, corresponding to rare cells, are often of major interest and must not be lost during the analysis. Since the high-dimensional space, corresponding to the marker panel, varies from study to study, subsets need to be created in a data-driven fashion. Other than with the discerning markers in the lineage delineation, here, all markers can be of interest. We also expect to find subsets not known before requiring an explorative analysis.

We propose an approach consisting of three steps as presented in abstract form in **Figure 2c**. We use dimensionality reduction in **T2a** to *derive* two-dimensional data points for visual inspection of the complete data, without clustering or downsampling. This assures that small subsets do not get lost in a larger cluster or during downsampling. For creating the subsets (**T2b**), we propose to *derive* clusters based on the structure of the dimensionality reduced data. Finally, for **T2c**, we propose to re-introduce the original high-dimensional data to *explore* and verify the clusters. If the clustering is too coarse, the user can go back to the previous step and *derive* a new set of clusters. If the clustering is too fine, she can *derive* new clusters in this step by merging. Once the user is satisfied with the clustering she can *annotate* the clusters based on the complete expression profile.

To recapitulate; the proposed system needs to provide effective means to:

- *derive* two-dimensional coordinates, based on the high-dimensional expression.
- *derive* clusters, based on the two-dimensional structure.
- *explore and summarize* the data at single-cell resolution and *derive* subsets with similar marker expression.

5. CYTOSPLORE

We implemented a complete system for our workflow respecting the identified tasks (**Figure 1**). It provides a configurable environment with multiple linked views for the analysis. Here, we describe the implementation details, reasoning, and how we map the different workflow tasks presented in Section 4 to the actual visualization and analysis tools. **Figure 3** shows the complete workflow, as implemented.

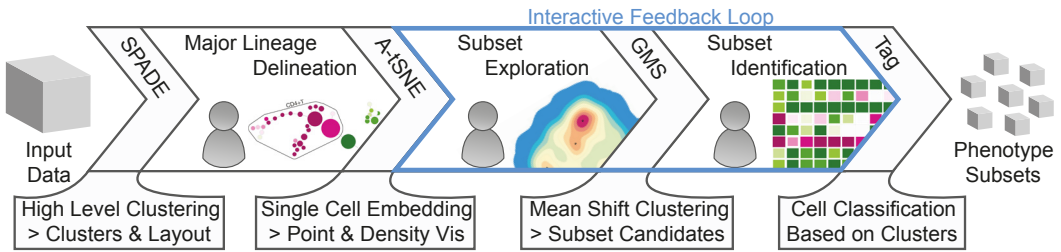


Figure 3: Phenotype Specification Workflow and its three major user-facing blocks; major-lineage delineation, subset exploration and identification. SPADE, A-tSNE, GMS and Tag-labeled blocks form the computational glue between user-driven parts. GMS requires a kernel-bandwidth definition, but is computed in real time, merging subset exploration and identification.

5.1. Major Lineage Delineation

Figure 2b shows a the abstraction of the major lineage delineation. We identified two major tasks, described in Section 4.1: **T1a**: grouping of points to clusters of similar expression and **T1b**: the creation of meta-clusters, clusters of clusters, that correspond to the major lineages. In the following, we describe *how* we support these tasks in our visual analysis tool.

T1a: Group Points. We use SPADE [QSBI1] for automatically grouping points to clusters of similar expression. In short, SPADE clusters data points based on their similarity in the high-dimensional space. It does so by downsampling the data, based on local densities, to avoid removing small distinctive groups. The downsampled data is then clustered and the data points, removed during downsampling, are added to the most similar cluster. The number of clusters needs to be predefined and should be set about an order of magnitude larger than the expected lineages to compensate for SPADE's lack of precision. Finally, a minimum spanning tree is constructed using the clusters' median expressions. We chose SPADE, as it is well known in the domain and has been proven to be a valuable tool for single-cell analysis [BSQ11, BZF12, LZNI5]. Its lack of precision and the need to predefine the number of clusters are not an issue for the major lineage delineation. Here, we are only interested in high-level structures and, in case points are mis-classified, these can be fixed later in the pipeline. The number of major lineages expected in the data is inherently defined by the design of the marker panel and as such known beforehand. To minimize the risk of clusters containing data points that belong to multiple lineages, the user simply selects a much larger number of clusters than expected as major lineages. These clusters are then grouped manually into *meta-clusters*, defining the major lineages.

T1b: Create Meta-Clusters. We visualize the SPADE tree using a node link diagram, where nodes correspond to the clusters and the links to the edges in the minimum spanning tree. The nodes are initially laid out using a force-directed layout but the user can `arrange` the layout as needed. Our partners are familiar with these types of diagrams and used them before to inspect the results of SPADE clustering, hence, we decided not to change this basic encoding of the data and rather focused on optimizing it for the task at hand. The experts need to `locate` branches of the tree with a similar expression in a few markers (usually no more than three), corresponding to the known major lineages. To help the user `navigate` to and `select` these branches, we color code the nodes to show the median expression of one or more markers of the corresponding cluster. To show two or three different markers, we divide the node into segments of equal size. By default, we use the pink-to-green diverging color map from colorbrewer, as the expression is usually classified in low or high values, which here correspond to the ends of the diverging spectrum. Once the user has identified a group of clusters with similar expression in the selected markers, she can simply brush in the diagram to `select` and `annotate` the selection via the context menu. A permanent meta-cluster is automatically `derived` from the annotated selection (**Figure 4**). The described steps are usually sufficient to define the major lineages. In case the user wants to inspect the complete expression of a cluster, we provide a circular heatmap that opens around the node of interest by double-clicking.

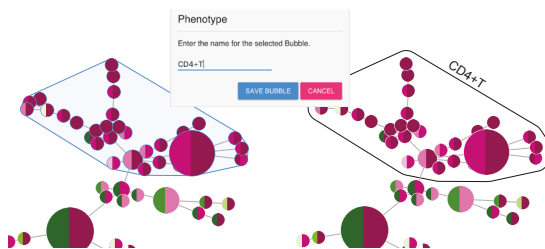


Figure 4: SPADE Detail. Meta-clusters can be selected by brushing (left) and annotated (dialog-box and right).

5.2. Phenotypical Subset Exploration and Identification

We show the abstraction for the phenotypical subset exploration and identification in **Figure 2c**. The process is divided into three major parts, as presented in Section 4.2; T2a: dimensionality reduction, T2b: clustering and T2c: cluster refinement, as described below.

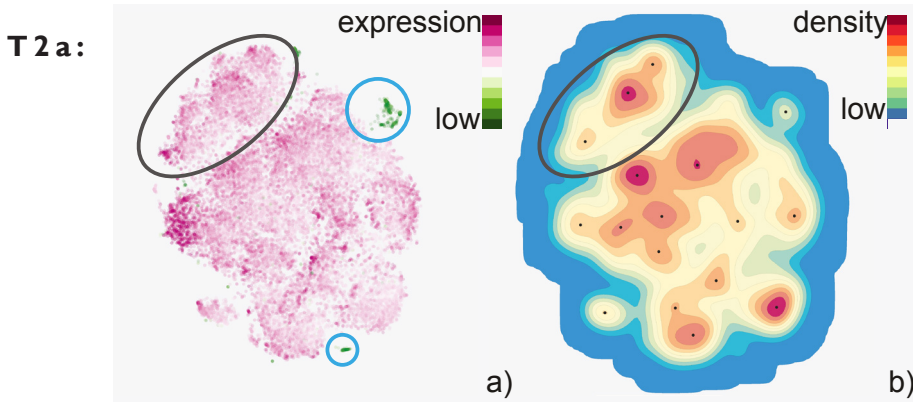


Figure 5: tSNE Visualization of a single lineage, as scatterplot (a) and as density plot (b). Erroneous selections can be identified in the scatterplot (blue circles) due to the low expression in the discerning marker for this lineage. Visual clusters can easily be distinguished in the density plot.

Dimensionality Reduction. Sedlmair et al. [SMT13] conclude that “*there is no one-and-only Dimensionality Reduction solution*”. A-tSNE [PLvdM15] is a variant of tSNE [vdMH08], which is designed to preserve local structure (i.e., clusters) in the high-dimensional space and is optimized to target two- or three-dimensional spaces for visualization [vdM09] and, therefore, fits our task very well. However, standard tSNE suffers from long computation times. We aim at fast computation of the detail visualization, as it will allow us to go back and forth between the high level and detail visualizations to iron out mistakes in the high level selection. Therefore, we chose A-tSNE to derive two-dimensional data points. A-tSNE is specifically designed for such interactive settings. By approximating the high-dimensional neighborhoods the startup time can be reduced by up to two orders of magnitude, when compared to the original implementation of tSNE. We use a conservative approximation parameterization, as described by Pezzotti et al. [PLvdM15] to make sure that the resulting embedding faithfully represents the data without user interaction.

T2b: Clustering. Manual selection of visual clusters in the embedding to derive subsets is a tedious task. Previous work proposes to use automatic clustering of the embedding to specify the phenotypical subsets. In their work on ACCENSE [SBDC14], Shekhar et al. propose a technique for density-based clustering of tSNE maps in the context of cytometry. However, ACCENSE suffers from several problems. Most importantly, they use a proprietary clustering algorithm that typically clusters only around 50% of the data.

We decided to use Gaussian Mean Shift (GMS) clustering to create the subsets. GMS has proven to be a reliable tool for the analysis of complex data, is capable of creating arbitrarily-shaped clusters [CM02], will cluster all available data, and corresponds well with the visually-identified clusters. Similar to ACCENSE, GMS does rely on density computations and a kernel bandwidth needs to be specified. ACCENSE tries to find an optimal size automatically by inspecting the number of resulting peaks for a range of different values. In our tests, the results of this approach were questionable. Instead, we expose this parameter to the user, in combination with a linked feature-space view of the resulting clusters. Hereby we allow the user to make an informed decision on the kernel bandwidth. For an effective visual exploration, the data needs to be clustered at interactive rates. GMS is a rather complex algorithm and is therefore usually not employed in interactive settings. In Section 6.1, we describe a GPU-based, discrete GMS implementation that allows for interactive clustering of hundreds of thousands of data points.

T2c: Cluster Refinement. We support the user in the process of exploring the created clusters and deriving new clusters with three visual encodings. We use a scatterplot (**Figure 5a**) or a density plot (**Figure 5b**) to show the dimensionality-reduced data. In the scatterplot (**Figure 5a**), subsets can be identified best by inspecting the actual marker expressions. Therefore, we use color coding to represent a single user-defined marker, using the same diverging colormap as described in Section 5.1. E.g., the user selects a discerning marker for the defined lineage from a dropdown menu to use for the color coding. Cells that show a high expression of the marker when low is required (or vice versa) can easily be identified in the scatterplot (see the blue circles in **Figure 5a**). The user can then go back and remove them from the defined lineage using the SPADE visualization, or simply handle them as outliers and create the correct annotation in the following steps. The density plot (**Figure 5b**) shows more detail within the groups. E.g., the group in the top left of the embedding (black highlight) seems relatively homogeneous in the scatterplot but shows three peaks in the density plot. However, in the density plot, we lose single-cell resolution and the marker expression. We couple the GMS clustering to the density plot and each cluster is represented by a black dot on the corresponding density peak for easy discovery.

The third visual encoding is a heatmap view (**Figure 6**), showing the median marker expression of the created clusters. A phenotypically-distinct subset is defined by a homogeneous unique marker expression of the contained cells. Consequently, we

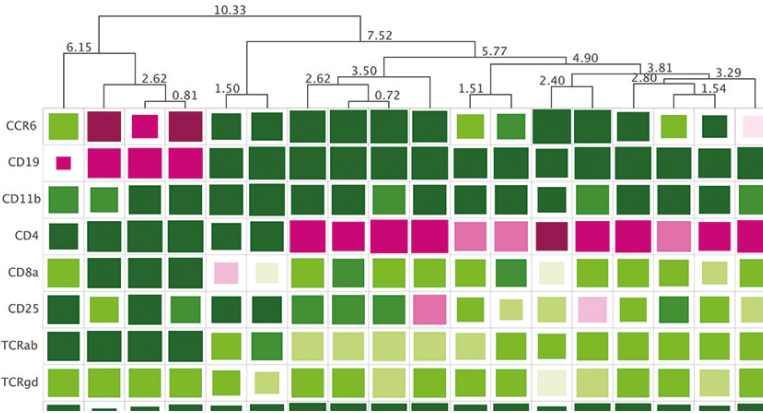


Figure 6: Detail of the Heatmap View showing marker expressions and variation. Variation is encoded in the amount of paint in each box. Columns are ordered by similarity as indicated by the dendrogram on top

propose to use the homogeneity of the resulting clusters as a quality measure. We provide the standard deviation as a measure for the homogeneity. Inspired by Gove and Herzog's work [GH13], we `encode` the standard deviation in the amount of paint in each box in the heatmap. Here, a filled box means little standard deviation, whereas a box with a lot of white corresponds to large heterogeneity inside the cluster for the corresponding marker. The combination of the interactive clustering and the linked heatmap view, including information on the homogeneity of clusters allows the user to make an informed decision on when the automatic clustering is satisfactory.

Once the user has defined a suitable kernel bandwidth, she proceeds to refine the created clusters, i.e., by merging clusters with a similar expression. We provide quick interactions (directly in the heatmap view) to merge multiple clusters that belong to the same phenotypical subset. The user can select one or more clusters by clicking on the corresponding column in the heatmap. The cluster will be highlighted in the heatmap view and the embedding to indicate the correspondence to the spatial location. We provide different ways to `arrange` the heatmap for easy comparison. To organize columns by their overall similarity, we compute hierarchical clustering using the median cluster expressions and visualize the columns as leaves of the resulting dendrogram. Thus, similar columns are automatically placed next to each other, allowing fast `exploration` of the clusters and the corresponding feature space. In addition, the user can also sort the columns based on the values of a single row. To derive new clusters, the user can simply select multiple columns and merge them to a single cluster via the context menu. The dendrogram and sorting are automatically updated on such interaction. Finally,

the refined clusters can be annotated directly in the heatmap and exported to separate files for further inspection and quantitative analysis in external tools.

6. IMPLEMENTATION

We implemented the core system of Cytosplore using C++ and Qt. For the visualization components, we use a combination of different rendering techniques, including D3 [BOH11] and hardware accelerated OpenGL with custom GLSL shaders, depending on the amount of objects on screen. Even though we mix and match hardware accelerated OpenGL-based visualization with slower webbased techniques, we would like to note that we strictly divide between pure visualization and intensive computational tasks. All heavy lifting, such as clustering, gradient descent and computation for A-tSNE is implemented in C++ or, if possible, on the GPU for maximum performance. When applicable, we only use a thin web layer for visualization.

6.1. GPU-based, Discrete Mean-Shift Clustering

One of the main drawbacks of the mean-shift algorithm is its computational complexity, making it not applicable in interactive scenarios with millions of data points. Therefore, we implemented a grid-based streaming version of the Gaussian Mean Shift algorithm based on work by Sirotkovic et al. [SDP13] for image segmentation. Instead of using the Improved Fast Gauss Transform [YDGD03], however, we use fast density estimation on the GPU [LH11] reducing the shift operation to a single lookup in a gradient table. In general, the mean-shift algorithm is a mode-seeking algorithm, taking each input data point and iteratively shifting it to the average of the data points in its neighbourhood until convergence to a fixed location. To increase the performance, we map the clustering problem to a segmentation problem of the visual space used for the embedding, to be able to apply the algorithm presented by Sirotkovic et al. [SDP13]. As a result, the cost of the shift operation is dependent on the resolution of the visual space, rather than the number of input points. Additionally this approach maps nicely to the GPU, further increasing performance.

We use three render passes to compute the segmentation of the visual space. In the first pass, we compute the density profile (**Figure 7a**) in image space [LH11]. Based on the density, we compute the first derivative via central differences, resulting in the gradient at each grid position in the second render pass (**Figure 7b**). In the third pass, we follow the gradient map upwards until we find a local peak for each pixel with a non-zero density. We inscribe the found

position as a color to the starting pixel, resulting in a map of constant colored

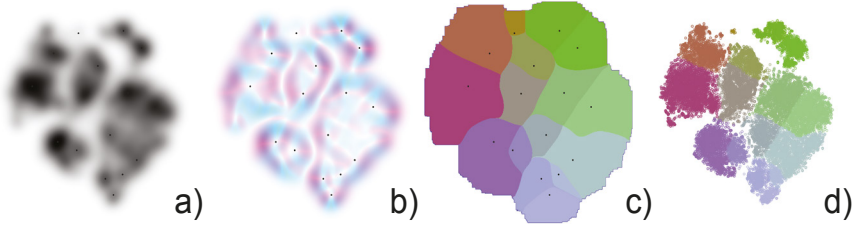


Figure 7: GPU Mean-Shift Steps. a shows the density map, with increasing density from white to black. b shows the corresponding (absolute) gradients, using the m and c channels of the cmyk color space to indicate the x and y components of the gradient vectors, respectively. c shows the final segmentation using unique colors for each partition. d shows the clustered points using the same coloring as in c.

partitions (**Figure 7c**). Finally, on the CPU, we set a unique id for each of these partitions. Assigning this id to each data point is then a simple look up in the resulting map using the points position. **Figure 7d** shows the final clustered points.

Performance. **Figure 8** shows computation times of the GPU mean-shift algorithm for different numbers of points, different grid sizes, and different kernel sizes from 10% to 40% of the image size. The computations were carried out using a 4 core intel core i7 processor, clocked at 4Ghz and an AMD Radeon R9 M295X with 4GB of GPU memory. Blue columns show measured times for 10,000 data points, green columns for 50,000 points and orange columns correspond to tests using 100,000 data points. It can be seen that the

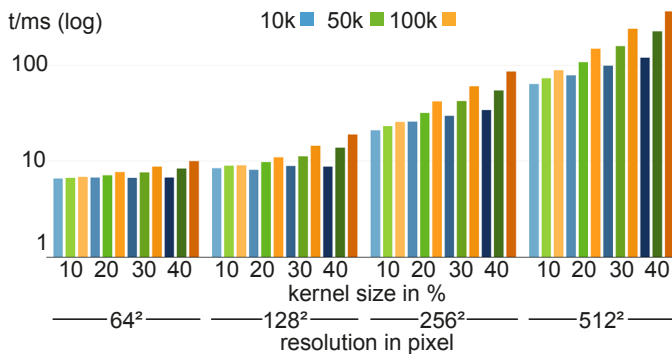


Figure 8: Performance of our Mean-Shift Clustering.

performance mostly depends on the resolution of the grid, while kernel size and number of points have a smaller effect. However, for larger resolutions, the impact of these two factors is visible. Overall, it can be seen that for the 128^2 resolution, we easily achieve real-time update rates for all tested kernel and data sizes. We can keep interactivity even at 512^2 resolution and 100,000 data points.

7. RESULTS

As described in Section 5, we focused on improving existing visual encodings and designing an integrated interactive workflow with the goal to improve efficiency. We conducted interviews with three experts from our collaborating institute to validate the choices we made to improve the visual encodings (Section 7.1). A prototypical version of the presented workflow, using separate tools, such as Cytobank, Matlab and custom R-scripts, is the basis for our collaborators complete study as presented in [vULM16]. For detailed information on specific findings, especially how the workflow supports hypothesis generation, we refer to that work. In our case study (Section 7.2), we focus on how we improve the effectiveness of the analysis by creating an integrated interactive system.

The participants in our evaluation had different exposure to Cytosplore before the study. Participant A was our main partner when developing the workflow and had strong influence on the design process of the system. He tested the system since its inception and can be considered an expert user. Participant B is a close collaborator but was less involved in creating the system. She tests the system frequently but for her daily routine still relies on other tools. Participant C was presented with the final system just for this study and only had brief exposure to a very early prototype before. All participants are familiar with the available computational tools.

7.1. User Evaluation

We demonstrated the tool to the participants in a group session and installed it on their lab computers, including a short document, describing the most important features and how to access them. The participants had as much time as needed to familiarize themselves with the system. We followed this up with a structured interview, to find out which parts of the proposed system work and which could be improved. The integrated nature of Cytosplore provides a strong improvement. Participant C specifically mentions the linking: “to see which clusters in the heatmap are which cells in the tSNE [...] makes it easy to make adjustments in the beginning of the pipeline” and

“makes it more reliable”. All participants agree that showing two markers at once in the SPADE visualization “saves time” (Participant B). Participant C mentions that she is fine with using a single marker in Cytobank, “*but with two markers, it is a lot faster to find subsets*”. Without knowledge that we tested more markers in an early design phase, she also states that “*more than two markers would probably [...] make me lose the overview*”. The circular heatmap received mixed reactions. Participant C states that “*it is not very helpful when a lot of markers are used in the panel*”. Participant A sums it up to “*looking at high detail for one node is a luxury but not a necessity*”, validating our choice to make it optional. Participant B works with data that sometimes produces very small lineages (i.e., consisting of a few hundred cells). During testing, she was able to successfully define the subsets with this kind of data. With such small data, where the differences in the density of the embedding are rather subtle, “*we need the heatmap to combine our immune knowledge to define the kernel bandwidth*”. Before, this process completely failed with her standard workflow. Interactively defining the kernel density made Participant C much more confident in the results of the density-based clustering: “*Yes, this [the linked heatmap view] is very helpful. The variation display shows even more clearly whether more subsets need to be created*.” Participant A praises the linking between clustering and the heatmap visualization of marker expressions: “*It immediately feedbacks the signatures revealing overall heterogeneity and homogeneity that often is the unknown for your data. It gives so much valuable simultaneous information and you are flexible in changing parameters without having to do hours of computations again. I am really happy with it*.” He does not, however, use the visualization of the standard deviation since markers without a clear low or high expression are hard to discern from the background due to the diverging colormap with a white center. We since changed the available colormaps in the heatmap view by removing the very light colored blocks, but did not conduct an updated evaluation.

7.2. Case Study

To measure the efficiency of our proposed system, we set up a small case study. The study consists of a single blood sample which was downsampled to 50,000 cells. The task was to specify the phenotypically distinct subsets within the dominant major lineage (CD4+T) within the sample. We asked Participant A to create the subsets using his traditional workflow

Table 1: Case Study Performance. Time in minutes needed for the different steps in the workflow.

	Total	T1: Lineage Delineation	T2a/b: Subset Computation*	T2c: Subset Postprocessing
Traditional	108	27	29	52
Ours	39	13	11	15

*completely automatic in the traditional and interactive in our workflow

[vULM16] as a benchmark, as well as our workflow for comparison. We chose Participant A because he is the most experienced user among our three participants. **Table I** shows the time it took to create the subsets with the traditional workflow compared to the time with our integrated solution. It can be seen that Cytosplore outperforms the traditional workflow roughly threefold. It should be noted that this small test case cannot completely capture the details of the workflow. E.g., as shown in Section 6.1, our implementation of the clustering for T2b scales very well with increasing data sizes, whereas the automatic clustering within ACCENSE often takes hours with real-world data sizes. However, it was necessary to use such a simple example, to allow the subset definition within a reasonable time frame. SPADE and tSNE computations in Cytobank are done in the cloud. We assume they use distributed computing, as their conventional tSNE was computed in the same time as our A-tSNE. However, since Cytobank runs on shared hardware, SPADE and tSNE computations are queued for all users and wait times easily reach hours during peak times. We measured the time only after the job was started to make sure the comparison is fair. With our tool, clusters can be merged with a few clicks and be verified immediately. The most time is needed for the biological interpretation of the heatmap itself. We can see a large speed up in this step, due to the fact that this is the least integrated part in the original workflow and requires several different tools and sometimes multiple iterations for verification of the results.

Finally, we compared the subsets that were assigned to each cell, to make sure our results are comparable to the traditional workflow. In the SPADE tree 27,172 cells were assigned to the created CD4+T lineage with the traditional workflow, 26,591 with ours. Within the lineage, in all tests, the same 14 subsets were identified after merging 16 automatically-generated subsets in the traditional workflow and 19 with ours. The results are not directly comparable on a single-cell level, because ACCENSE only clustered 14;643 of the original 27;172 cells. **Figure 9** shows the composition of the cells according to the subset specification during the evaluation. Except for the groups labeled I and II, where we found more cells using Cytosplore, the results were very similar; overall 14 subsets, 6 CD4+T Naïve

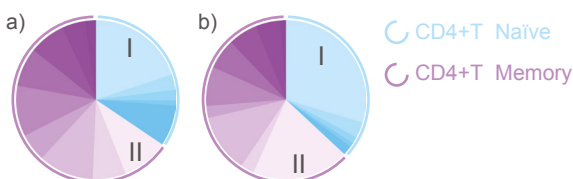


Figure 9: Subsets Created in the Evaluation by Participant A with the traditional workflow (a) and using Cytosplore (b). Note that a consists of only 54% of the cells assigned to the lineage, due to incomplete clustering using ACCENSE.

(different shades of blue) and 8 CD4+T Memory (different shades of purple) were defined in all tests. After further investigation, we found out that the additional cells in group I and II were mostly from the regions that were not clustered using ACCENSE. It needs to be investigated further, whether the difference is due to a bias introduced by the incomplete clustering in ACCENSE, or if the greedy clustering using mean shift introduces cells into the subsets where the phenotype is uncertain.

To summarize, we were able to achieve comparable results using our interactive workflow, when compared to previous work [vULMI 6]. Therefore, we assume that our framework allows for generating hypotheses in a similar fashion. However, it has the main advantage of significantly higher efficiency, when compared to the previous approach.

8. CONCLUSION AND FUTURE WORK

We presented Cytosplore, an interactive integrated system and workflow for the specification of phenotypical subsets in large high-dimensional cytometry data sets. We have shown the benefits of our approach in a case study evaluation. Participants found our integrated workflow useful and it allows them to produce results considerably faster than with their traditional workflow. The integrated nature of Cytosplore leads to much faster iteration during the subset specification.

Cytosplore allows us to go beyond data sizes currently possible to handle with other tools by effectively partitioning the input. However, scalability (in terms of data points) is still limited by the input size for A-tSNE. In our tests, tSNE is not only a limiting factor in terms of computational performance, but the embedding quality also quickly degenerates when going beyond a few million data points. We expect the number of dimensions to rise to around a hundred. For the computational tools presented in this work this will not be an issue. Cytosplore is also flexible enough to be employed in a basic clinical setting, e.g., to analyze the lower-dimensional flow cytometry data. If data are small enough, e.g., when analysing a single blood sample, the overview generation using SPADE can be skipped entirely and the data can be analysed using the embedding and heatmap, immediately. For the analysis of the immune system as a whole, the specification of cell types is only the first step, followed by a quantitative analysis of the found subsets. In future work, we would like to integrate the quantitative analysis within Cytosplore.

REFERENCES

1. [ADT13] AMIR E.-A. D., DAVIS K. L., TADMOR M. D., SIMONDS E. F., LEVINE J. H., BENDALL S. C., SHENFELD D. K., KRISHNASWAMY S., NOLAN G. P., PE'ER D.: viSNE enables visualization of high dimensional single-cell data and reveals phenotypic heterogeneity of leukemia. *Nature Biotechnology* 31 (2013), 545–552.
2. [AHD06] *The American Heritage Dictionary of the English Language*, 4 ed. Houghton Mifflin Harcourt, 2006.
3. [BM13] BREHMER M., MUNZNER T.: A multi-level typology of abstract visualization tasks. *IEEE Transactions on Visualization and Computer Graphics* 19, 12 (2013), 2376–2385.
4. [BOH11] BOSTOCK M., OGIEVETSKY V., HEER J.: D3: Datadriven documents. *IEEE Transactions on Visualization and Computer Graphics* 17, 12 (2011), 2301–2309.
5. [BSIM14] BREHMER M., SEDLMAIR M., INGRAM S., MUNZNER T.: Visualizing dimensionally-reduced data: Interviews with analysts and a characterization of task sequences. In *Proceedings of ACM BELIV Workshop* (2014), pp. 1–8
6. [BSQ11] BENDALL S. C., SIMONDS E. F., QIU P., AMIR E.-A. D., KRUTZIK P. O., FINCK R., BRUGGNER R. V., MELAMED R., TREJO A., ORNATSKY O. I., BALDERAS R. S., PLEVITIS S. K., SACHS K., PE'ER D., TANNER S. D., NOLAN G. P.: Single-cell mass cytometry of differential immune and drug responses across a human hematopoietic continuum. *Science* 332, 6030 (2011), 687–696.
7. [BZF12] BODENMILLER B., ZUNDER E. R., FINCK R., CHEN T. J., SAVIG E. S., BRUGGNER R. V., SIMONDS E. F., BENDALL S. C., SACHS K., KRUTZIK P. O., NOLAN G. P.: Multiplexed mass cytometry profiling of cellular states perturbed by small-molecule regulators. *Nature Biotechnology* 30 (2012), 858–867.
8. [CM02] COMANICIU D., MEER P.: Mean shift: a robust approach toward feature space analysis. *IEEE Transactions on Pattern Analysis and Machine Intelligence* 24, 5 (2002), 603–619.
9. [DHHH13] DEMIRALP C., HAYDEN E., HAMMERBACHER J., HEER J.: invis: Exploring high-dimensional RNA sequences from in vitro selection. In *IEEE Biological Data Visualization (BioVis)* (2013), pp. 1–8.
10. [GH13] GOVE R., HERZOG B.: Visualizing uncertain critical paths in schedule management. Poster at the *IEEE Conference on Visualization (VIS)*, 2013.
11. [KK10] KOTECHA N., KRUTZIK P. O., IRISH J. M.: *Current Protocols in Cytometry*. 2010, ch. 10, Web-Based Analysis and Publication of Flow Cytometry Experiments.
12. [LH11] LAMPE O. D., HAUSER H.: Interactive visualization of streaming data with kernel density estimation. In *Proceedings of the IEEE Pacific Visualization Symposium* (2011), pp. 171–178.
13. [LSS12] LEX A., STREIT M., SCHULZ H., PARTL C., SCHMALSTIEG D., PARK P. J., GEHLENBORG N.: StratomeX: visual analysis of large-scale heterogeneous genomics data for cancer subtype characterization. *Computer Graphics Forum* 31, 3 (2012), 1175–1184.
14. [LZN15] LUJAN E., ZUNDER E. R., NG Y. H., GORONZY I. N., NOLAN G. P., WERNIG M.: Early reprogramming regulators identified by prospective isolation and mass cytometry. *Nature* 521 (2015), 352–356.
15. [MMDP10] MEYER, MUNZNER T., DEPACE A., PFISTER H.: MulteeSum: A tool for comparative spatial and temporal gene expression data. *IEEE Transactions on Visualization and Computer Graphics* 16, 6 (2010), 908–917.

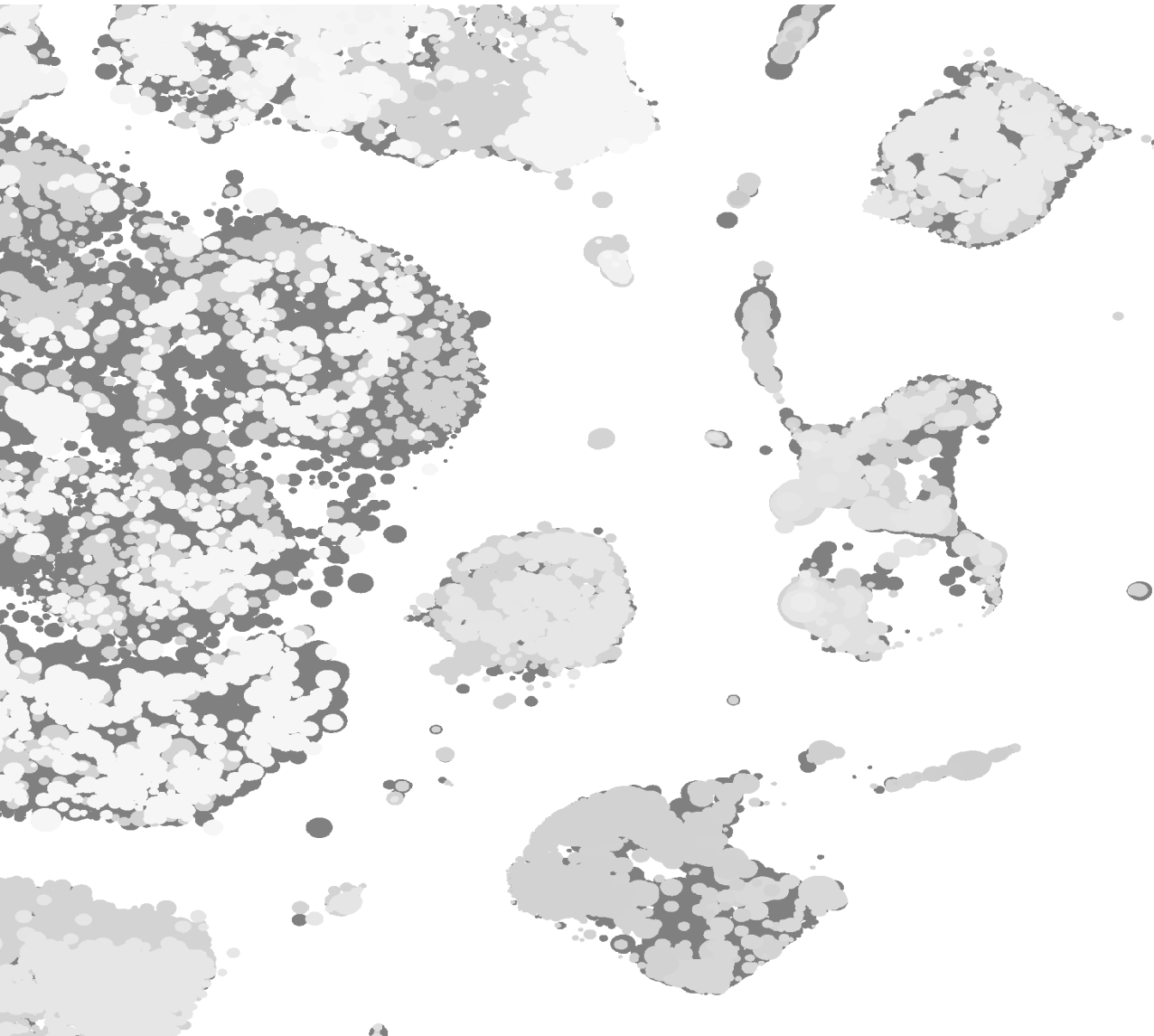
16. [MMP09] MEYER M., MUNZNER T., PFISTER H.: MizBee: A multiscale synteny browser. *IEEE Transactions on Visualization and Computer Graphics* 15, 6 (2009), 897–904.
17. [OKB08] ORNATSKY O. I., KINACH R., BANDURA D. R., LOU X., TANNER S. D., BARANOV V. I., NITZ M., WINNIK M. A.: Development of analytical methods for multiplex bio-assay with inductively coupled plasma mass spectrometry. *Journal of Analytical Atomic Spectrometry* 23 (2008), 463–469.
18. [PLvdM15] PEZZOTTI N., LELIEVELDT B. P. F., VAN DER MAATEN L., HÖLLT T., EISEMANN E., VILANOVA A.: Approximated and user steerable tSNE for progressive visual analytics. *ArXiv* (2015).
19. [QSB11] QIU P., SIMONDS E. F., BENDALL S. C., GIBBS JR K. D., BRUGGNER R. V., LINDERMAN M. D., SACHS K., NOLAN G. P., PLEVRITIS S. K.: Extracting a cellular hierarchy from high-dimensional cytometry data with SPADE. *Nature Biotechnology* 29 (2011), 886–891.
20. [SBDC14] SHEKHAR K., BRODIN P., DAVIS M. M., CHAKRABORTY A. K.: Automatic classification of cellular expression by nonlinear stochastic embedding (ACCENSE). *Proceedings of the National Academy of Sciences* 111, 1 (2014), 202–207.
21. [SDP13] SIROTKOVIC J., DUJMIC H., PAPIĆ V.: Accelerating mean shift image segmentation with IFGT on massively parallel GPU. In *36th International Convention on Information Communication Technology Electronics Microelectronics (MIPRO)* (2013), pp. 279–285.
22. [SGF15] SPITZER M. H., GHERARDINI P. F., FRAGIADAKIS G. K., BHATTACHARYA N., YUAN R. T., HOTSON A. N., FINCK R., CARMİY., ZUNDER E. R., FANTL W. J., BENDALL S. C., ENGLEMAN E. G., NOLAN G. P.: An interactive reference framework for modeling a dynamic immune system. *Science* 349, 6244 (2015).
23. [SMT13] SEDLMAIR M., MUNZNER T., TORY M.: Empirical guidance on scatterplot and dimension reduction technique choices. *IEEE Transactions on Visualization and Computer Graphics* 19, 12 (2013), 2634–2643.
24. [vdM09] VAN DER MAATEN L.: Learning a parametric embedding by preserving local structure. In *Proceedings of the Twelfth International Conference on Artificial Intelligence and Statistics (AISTATS)* (2009), vol. 5, pp. 384–391.
25. [vdMH08] VAN DER MAATEN L., HINTON G.: Visualizing data using t-SNE. *Journal of Machine Learning Research* 9 (2008), 2579–2605.
26. [vULM16] VAN UNENV., LI N., MOLENDIJK I., TEMURHAN M., HÖLLT T., VAN DER MEULEN-DE JONG A. E., VERSPAGET H. W., MEARIN M. L., MULDER C. J., VAN BERGEN J., LELIEVELDT B. P. F., KONING F.: Mass Cytometry of the Human Mucosal Immune System Identifies Tissue- and Disease-Associated Immune Subsets. *Immunity*, in press (2016).
27. [YDGD03] YANG C., DURAISWAMI R., GUMEROV N., DAVIS L.: Improved fast Gauss transform and efficient kernel density estimation. In *Proceedings of Ninth IEEE International Conference on Computer Vision* (2003), pp. 664–671 vol.1.
28. [ZLG15] ZUNDER E. R., LUJAN E., GOLTSEVY., WERNIG M., NOLAN G. P.: A continuous molecular roadmap to iPSC reprogramming through progression analysis of single-cell mass cytometry. *Cell Stem Cell* 16, 3 (2015), 323–337.





CHAPTER 4

Visual Analysis of Mass Cytometry Data by Hierarchical Stochastic Neighbor Embedding Reveals Rare Cell Types



CHAPTER 4

Visual Analysis of Mass Cytometry Data by Hierarchical Stochastic Neighbour Embedding Reveals Rare Cell Types

Vincent van Unen,^{1*} Thomas Höllt,^{2,3*} Nicola Pezzotti,^{2*} Na Li,¹ Marcel J.T. Reinders,⁴ Elmar Eisemann,² Frits Koning,^{1‡} Anna Vilanova,^{2‡} Boudewijn P. F. Lelieveldt.^{4,5‡}

¹Department of Immunohematology and Blood Transfusion, ³Computational Biology Center, ⁵Department of LKEB Radiology, Leiden University Medical Center, The Netherlands. ²Computer Graphics and Visualization Group, ⁴Pattern Recognition and Bioinformatics Group, Delft University of Technology, The Netherlands

* = Equal contribution

‡ = Joint supervision

Nature Communications 8:1, 1740 (2017)

ABSTRACT

Mass cytometry allows high-resolution dissection of the cellular composition of the immune system. However, the high-dimensionality, large size, and non-linear structure of the data poses considerable challenges for the data analysis. In particular, dimensionality reduction-based techniques like t-SNE offer single-cell resolution but are limited in the number of cells that can be analyzed. Here we introduce Hierarchical Stochastic Neighbor Embedding (HSNE) for the analysis of mass cytometry data sets. HSNE constructs a hierarchy of non-linear similarities that can be interactively explored with a stepwise increase in detail up to the single-cell level. We apply HSNE to a study on gastrointestinal disorders and three other available mass cytometry data sets. We find that HSNE efficiently replicates previous observations and identifies rare cell populations that were previously missed due to downsampling. Thus, HSNE removes the scalability limit of conventional t-SNE analysis, a feature that makes it highly suitable for the analysis of massive high-dimensional data sets.

INTRODUCTION

Mass cytometry (cytometry by time-of-flight; CyTOF) allows the simultaneous analysis of multiple cellular markers (>30) present on biological samples consisting of millions of cells. Computational tools for the analysis of such data sets can be divided into clustering-based and dimensionality reduction-based techniques¹, each having distinctive advantages and disadvantages. The clustering-based techniques, including SPADE², FlowMaps³, Phenograph⁴, Vortex⁵ and Scaffold maps⁶, allow the analysis of data sets consisting of millions of cells but only provide aggregate information on generated cell clusters at the expense of local data structure (i.e., single-cell resolution). Dimensionality reduction-based techniques, such as PCA⁷, t-SNE⁸ (implemented in viSNE⁹), and Diffusion maps¹⁰, do allow analysis at the single-cell level. However, the linear nature of PCA renders it unsuitable to dissect the non-linear relationships in the mass cytometry data, while the nonlinear methods (t-SNE⁸ and Diffusion maps¹⁰) do retain local data structure, but are limited by the number of cells that can be analyzed. This limit is imposed by a computational burden but, more importantly, by local neighborhoods becoming too crowded in the high-dimensional space, resulting in overplotting and presenting misleading information in the visualization. In cytometry studies, this poses a problem, as a significant number of cells needs to be removed by random downsampling to make dimensionality reduction computationally feasible and reliable. Future increases in acquisition rate and dimensionality in mass- and flow cytometry are expected to amplify this problem significantly^{11,12}.

Here we adapted Hierarchical stochastic neighbor embedding (HSNE)¹³ that was recently introduced for the analysis of hyperspectral satellite imaging data to the analysis of mass cytometry data sets to visually explore millions of cells while avoiding downsampling. HSNE builds a hierarchical representation of the complete data that preserves the non-linear high-dimensional relationships between cells. We implemented HSNE in an integrated single-cell analysis framework called Cytosplore^{+HSNE}. This framework allows interactive exploration of the hierarchy by a set of embeddings, two-dimensional scatter plots where cells are positioned based on the similarity of all marker expressions simultaneously, and used for subsequent analysis such as clustering of cells at different levels of the hierarchy. We found that Cytosplore^{+HSNE} replicates the previously identified hierarchy in the immune-system-wide single-cell data^{4,5,14}, i.e., we can immediately identify major lineages at the highest overview level, while acquiring more information by dissecting the immune system at the deeper levels of the hierarchy on demand. Additionally,

Cytosplore^{+HSNE} does so in a fraction of the time required by other analysis tools. Furthermore, we identified rare cell populations specifically associating to diseases in both the innate and adaptive immune compartments that were previously missed due to downsampling. We highlight scalability and generalizability of Cytosplore^{+HSNE} using three other data sets, consisting of up to 15 million cells. Thus, Cytosplore^{+HSNE} combines the scalability of clustering-based methods with the local single-cell detail preservation of non-linear dimensionality reduction-based methods. Finally, Cytosplore^{+HSNE} is not only applicable to mass cytometry data sets, but can be used for the other high-dimensional data like single-cell transcriptomic data sets.

RESULTS

Hierarchical exploration of massive single-cell data

For a given high-dimensional data set such as the three-dimensional illustrative example in **Fig. 1a**, HSNE¹³ builds a hierarchy of local neighborhoods in this high-dimensional space, starting with the raw data that, subsequently, is aggregated at more abstract hierarchical levels. The hierarchy is then explored in reverse order, by embedding the neighborhoods using the similarity-based embedding technique, Barnes–Hut (BH)-SNE¹⁵. To allow for more detail and faster computation, each level can be partitioned in part or completely, by manual gating or unsupervised clustering, and partitions are embedded separately on the next, more detailed level (compare **Fig. 1b**). HSNE works particularly well for the analysis of the mass cytometry data because the local neighborhood information of the data level is propagated through the complete hierarchy. Groups of cells that are close in the Euclidian sense (**Fig. 1a**, grey arrow), but not on the non-linear manifold (**Fig. 1a**, dashed black line), are well separated even at higher aggregation levels (**Fig. 1b**). The power of HSNE lies in its scalability to tens of millions of cells, while the possibility to continuously explore the hierarchy allows the identification of rare cell populations at the more detailed levels. Next follows a general description of how the hierarchy is built and explored through embeddings. More details can be found in the **Methods** section

The left panels of **Fig. 1c** give an overview of the HSNE-hierarchy construction. We show the hierarchy from the fine-grained data level to an overview level from the top to bottom panels. The number of levels is defined by the user and depends mostly on the input-data size. While the data aggregation is completely data-driven, for a typical mass cytometry data set, every additional level reduces the number of landmarks by roughly one order of magnitude. Therefore, we recommend to use

Visual Analysis of Mass Cytometry Data by Hierarchical Stochastic Neighbor Embedding Reveals Rare Cell Types

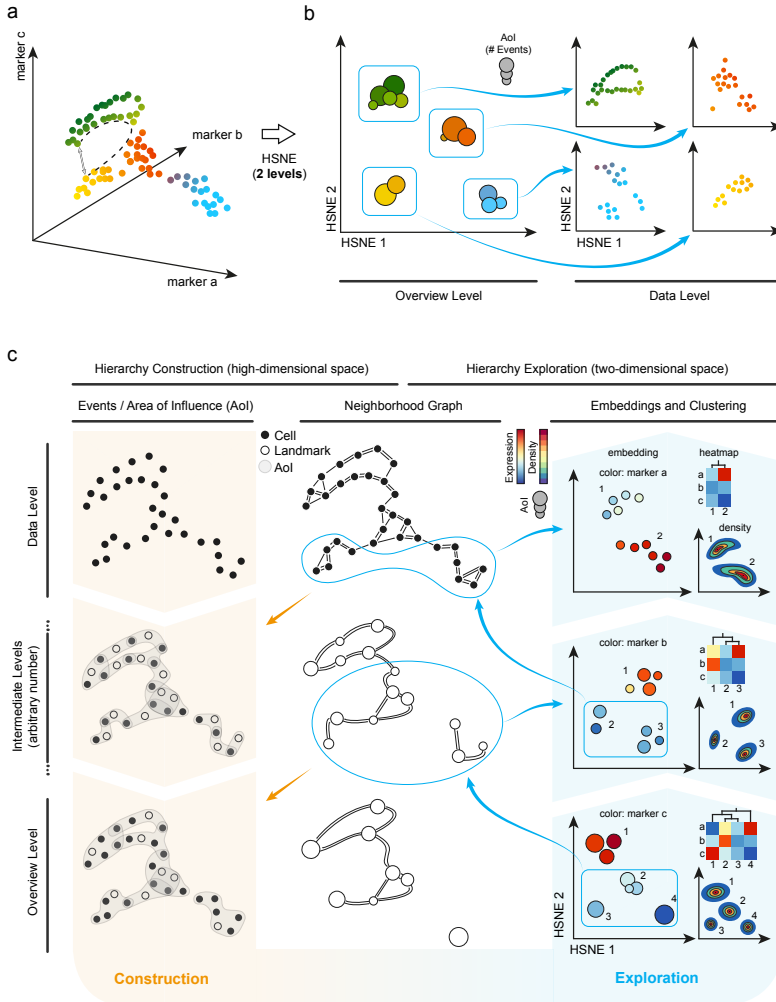


Fig. 1. Schematic overview of Cytosplore^{+HSNE} for exploring the mass cytometry data

By creating a multi-level hierarchy of an illustrative 3D data set (a), we achieve a clear separation of different cell groups in an overview embedding (left panel b) that conserves non-linear relationships (i.e., follows the distance indicated by the dashed line in a, instead of the grey arrow) and more detail within the separate groups on the data level (right panel b). c Construction and exploration of the hierarchy. The hierarchy is constructed starting with the data level (left two columns). On the basis of the high-dimensional expression patterns of the cells, a weighted kNN graph is constructed, which is used to find representative cells used as landmarks in the next coarser level. By administering the area of influence (Aoi) of the landmarks, cells/landmarks can be aggregated without losing the global structure of the underlying data or creating shortcuts. The exploration of the hierarchy is shown in the two rightmost columns. At the bottom, we see the overview level (in this example the 3rd level in the hierarchy), which shows that a group of landmarks has low expression in marker c (bottom-right panel). Selecting this group of landmarks for further exploration results in a look-up of the landmarks in the preceding level (neighborhood graph, intermediate level) that are in the Aoi, with which a new embedding can be created at the 2nd level of the hierarchy (middle-right panel). Marker b shows a strong separation between the upper and lower landmarks at this level. Zooming-in on the landmarks with low expression of marker b reveals further separation in marker a at the lowest level, the full data level (top-right panel).

$\log_{10}(N/100)$ levels, with N being the number of cells: this generally results in at most few thousands of landmarks at the highest level of the hierarchy. The foundation of the hierarchy is constructed using the original input data. Each dot represents a single cell (**Fig. 1c**, data level). Similarities between cells on the data level are defined by building an approximated, weighted k -nearest neighbor (kNN) graph¹⁶ using the Euclidian distances based on the complete marker expression (**Fig. 1c**, top-center panel). The weights of this graph can directly be used as input to embed the data into a two-dimensional space (**Fig. 1c**, top-right panel). With the BH-SNE the two-dimensional embedding is generated such that the layout of the points indicates similarities between the cells in the high-dimensional space according to the neighborhood graph.

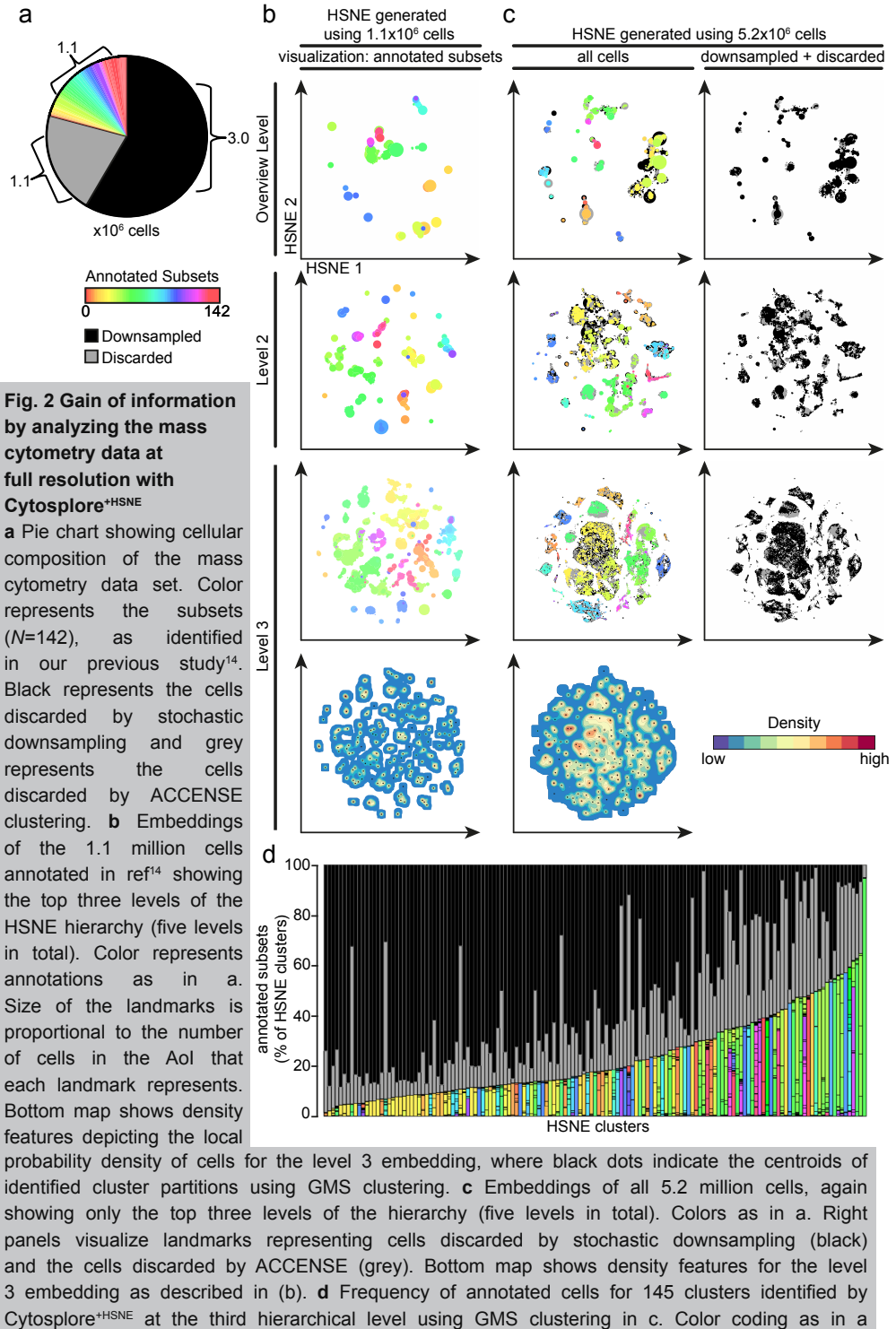
To aggregate the data into the next level (**Fig. 1c**, intermediate levels), we identify representative cells to use as landmarks (**Fig. 1c**, white circles). For that, the weighted kNN graph is interpreted as a Finite Markov Chain and the most influential (i.e., best-connected) nodes are chosen as landmarks, using a Monte Carlo process. The landmarks are then embedded into a two-dimensional space based on their similarities. However, simply repeating the kNN construction with Euclidian distances for the selected landmarks in the high-dimensional space would eventually eliminate non-linear structures by creating undesired “shortcuts” in the graph (a problem reported by Setty et al.¹⁷ in a different setting). Instead, we define the area of influence (Aoi) of each landmark, indicated by the grey hulls (**Fig. 1c**, left panels), as the cells that are well represented by the landmark according to the kNN graph. Different landmarks can have overlapping regions of locally-similar cells. Therefore, we define the similarity of two landmarks as the overlap of their respective Aois. Furthermore, we construct a neighborhood graph, based on these similarities. Here, two nodes are connected if they have overlapping Aois. The strength of the connection is defined by the number of data points within the overlapping region. This graph replaces the kNN graph as input for levels subsequent to the data level. Hereby, we effectively maintain the non-linear structure of the data to the top of the hierarchy and avoid shortcuts (**Fig. 1c**, bottom panels). We show that the preservation of non-linear neighborhoods by HSNE indeed conserves structure that is otherwise lost by random downsampling (**Supplementary Note I**. Cytosplore^{+HSNE} is reproducible and robust. and **Supplementary Fig. 1**).

The data exploration in Cytosplore^{+HSNE} starts with the visualization of the embedding at the highest level, the overview level (**Fig. 1c**, bottom-right panel).

Similar to other embedding techniques for visualizing the single-cell data^{4,9}, the layout of the landmarks indicates similarity in the high-dimensional space according to the level's neighborhood graph. Color is used to represent additional traits, such as marker expressions. The landmark size reflects its Aoi. While it is possible to continuously select all landmarks and compute a complete embedding of the next, more detailed level, this strategy would eventually embed all the data and suffer from the same scalability problems as a t-SNE embedding, i.e., overcrowding (**Supplementary Note 2**. Millions of cells cause performance issues and overcrowding in t-SNE. and **Supplementary Fig. 2**) and slow performance. Instead, we envision that the user selects a group of landmarks, by manual gating based on visual cues such as patterns found in marker expression, or by performing unsupervised Gaussian mean shift (GMS) clustering¹⁸ of the landmarks based on the density representation of the embedding (**Fig. 1c**, right panels). Then, the user can zoom into this selection by means of a more detailed embedding. This means that, all landmarks/cells in the combined Aoi on the preceding level are retrieved from the neighborhood graph (**Fig. 1c**, blue encirclements), embedded, and visualized in a new view. Moreover, interactively linked heatmap visualizations of clusters (**Fig. 1c**, right panels) and descriptive statistics of markers within a selection can be used to guide the exploration. For example, these tools allow to inspect the heterogeneity of cells within individual clusters, including the cells associated to individual landmarks. Importantly, all of the described tools are available at every level of the hierarchy and linked interactively. Selections in the embedding and heatmap at one level of the hierarchy can thus be highlighted in the embeddings of other levels (**Supplementary Fig. 3**). All these aspects are further demonstrated using a typical exploration workflow with Cytosplore^{+HSNE} in the **Supplementary Movie I**. With this strategy, tens of millions of cells can be explored, providing both global visualizations up to single-cell resolution visualizations, while preserving non-linear relationships between landmarks/cells at all levels of the hierarchy.

HSNE eliminates the need for downsampling

In a previous study¹⁴, a mass cytometry data set on 5.2 million cells derived from intestinal biopsies and paired blood samples was analyzed using a SPADE-t-SNE-ACCENSE pipeline. Due to t-SNE limitations, the data set had to be downsampled by 57.7% (**Fig. 2a**), where it was decided to equal the number of cells from blood and intestinal samples for a balanced comparison, which led to the exclusion of more cells from the blood samples. Moreover, ACCENSE clustered only 50% of the t-SNE-embedded data into subsets (**Fig. 2a**). Together,



this excluded 78.8% of the cells from the analysis. The remaining 1.1 million cells were annotated into 142 phenotypically distinct immune subsets¹⁴ (**Fig. 2a**).

To determine whether Cytosplore^{+HSNE} could identify similar subsets, we embedded the 1.1 million annotated cells (**Fig. 2b**). Computation time was in the order of minutes and the analysis was finished within an hour, compared to 8 weeks of computation in the original study. Color coding shows the grouping of subsets at all hierarchical levels. GMS clustering at the third level embedding (**Fig. 2b**, bottom panel) reveals that 75.5% of cells were assigned to a single subset by both methods (**Supplementary Fig. 4**). Hence, to reach similar results it was not necessary to explore the data at lower (more detailed) levels.

Next, we utilized Cytosplore^{+HSNE} to analyze the complete dataset on 5.2 million cells, thus including the cells that were discarded in the SPADE-t-SNE-ACCENSE pipeline. The embeddings show by color coding that subsets of the same immune lineage clustered at all three levels (**Fig. 2c**). More interestingly, the cells removed during downsampling (shown in black) and cells ignored during the ACCENSE clustering (shown in grey) were positioned throughout the entire map (**Fig. 2c**). We selected 145 clusters using GMS clustering at the third level and observed that the identified clusters contained variable numbers of downsampled and non-classified cells (**Fig. 2d**). These findings indicate that both the non-uniform downsampling and the cell losses during the ACCENSE clustering introduce a potential bias in observed heterogeneity in the immune system. Cytosplore^{+HSNE} overcomes this problem as it analyzes all cells and does so efficiently.

HSNE identifies rare subsets in the ILC compartment

We illustrate an exploration workflow with Cytosplore^{+HSNE} using the data set of 5.2 million cells¹⁴ (**Fig. 3**). At the overview level, 4,090 landmarks depict the general composition of the immune system (**Fig. 3a**) and color coding is applied to reveal CD-marker expression patterns on the basis of which the major immune lineages are identified (**Fig. 3b**). Next the CD7⁺CD3⁻ cell clusters were selected as indicated and a new higher resolution embedding was generated at level 3 of the hierarchy (**Fig. 3c**). Here, coloring of the landmarks based on marker expression (**Fig. 3c**, top panels) and a density plot of the embedding is shown (**Fig. 3d**) alongside the clinical features of the subjects from which the samples were obtained and the tissue-origin of the landmarks (**Fig. 3c**, bottom panels). This reveals a cluster of cells abundantly present in the intestine of patients with refractory celiac disease (RCDII). In addition,

a large cluster of CD45RA⁺CD56⁺ NK cells and three distinct innate lymphoid cell (ILC) clusters with a characteristic lineage⁻CD7⁺CD161⁺CD127⁺ marker expression profile^{19,20} are visualized. Strikingly, a distinct population of CD7⁺CD127⁻CD45RA⁺ and partly CD56⁺ cells is found in between the NK, RCD11 and ILC cell clusters.

To uncover the phenotypes of these ILC-related clusters, we next embedded the ILC and ILC-like clusters (**Fig. 3c**, selection) at the full single-cell data level (59,775 cells; 1.2% of total) (**Fig. 3e**). The marker expression overlays revealed that the majority of cells are CD7⁺ and displayed variable expression levels for CD127, CD45RA, and CD56 (**Fig. 3e**). In addition, and in line with previous reports^{21,22}, (co-)expression of CD127 with CD27, CRTH2, and c-KIT revealed the phenotypes corresponding to helper-like ILC type 1, 2 and 3, respectively (indicated by arrows in **Fig. 3e**). Moreover, by visualizing the tissue-origin in the Cytosplore^{+HSNE} embedding the tissue-specific location of ILC and ILC-related phenotypes became evident (**Fig. 3e**).

Next, we performed GMS clustering on the full data level embedding, which resulted in 19 phenotypically distinct clusters (**Fig. 3e**, right plots) based on marker expression profiles (**Fig. 3f**). The cell surface phenotypes of 8 out of the 19 clusters (**Fig. 3f**) matched previously described²¹ biological annotations (**Fig. 4**, black annotations) including the CRTH2⁺ILC2 (cluster 16), c-KIT⁺ILC3 (cluster 5) and CD56⁻CD127⁻ lineage⁻ IELs (cluster 19, 13, 18, 14, 6, and 8), the latter representing innate type of lymphocytes with dual T-cell precursor and NK/ILC traits^{23,24,25}. Remarkably, the remaining 11 clusters strongly resembled distinct ILC types, but did not fulfil the complete phenotypic requirements according to

Fig. 3 Analysis of the CD7⁺CD3⁻ innate lymphocyte compartment in inflammatory intestinal diseases **a** First HSNE level embedding of 5.2 million cells. Color represents arcsin5-transformed marker expression as indicated. Size of the landmarks represents AoI. Blue encirclement indicates selection of landmarks representing CD7⁺CD3⁻ innate lymphocytes and CD4⁺ T cells further discussed in **Fig. 5**. **b** The major immune lineages, annotated on the basis of lineage marker expression. **c** Third HSNE level embedding of the CD7⁺CD3⁻ innate lymphocytes (5.0 × 10 cells). Color represents arcsin5-transformed marker expression in top panels, and tissue-origin and clinical features in bottom panels. Blue encirclement indicates selection of landmarks representing CD127⁺ ILC and ILC-like cells. **d** Third HSNE level embedding shows density features depicting the local probability density of cells, where black dots indicate the centroids of identified cluster partitions using GMS clustering. **e** Embedding of the CD127⁺ ILC and ILC-like cells (6.0 × 10 cells) at single-cell resolution. Arrows indicate ILC1 (blue), ILC2 (orange) and ILC3 (green) Bottomright panel shows corresponding cluster partitions using GMS clustering based on density features (top-right panel). **f** A heatmap summary of median expression values (same color coding as for the embeddings) of cell markers expressed by CD127⁺ ILC and ILC-like clusters identified in **b** and hierarchical clustering thereof. **g** Composition of cells for each cluster is represented graphically by a horizontal bar in which segment lengths represent the proportion of cells with: (left tissue-of-origin, (middle) disease status and (right) sampling status.

Subset	Phenotype	Annotation
16	CD127 ⁺ CD161 ⁺ CD25 ⁺ CD122 ⁺ CRTH2 ⁺	ILC2
15	CD127 ⁺ CD161 ⁺ CD25 ⁺ CD122 ⁺ CRTH2 ⁻	ILC2-like
4	CD56 ⁺ NKp46 ⁺ CD127 ⁻ CD161 ⁻ c-KIT ⁻	NK-like
17	CD56 ⁺ NKp46 ⁺ CD127 ⁺ CD161 ⁻ c-KIT ⁻	ILC1-like
9	CD56 ⁺ NKp46 ⁺ CD127 ⁺ CD161 ⁻ c-KIT ⁻	ILC1-like
11	CD56 ⁺ NKp46 ⁺ CD127 ⁺ CD161 ⁻ c-KIT ⁻	ILC1-like
10	CD56 ⁺ NKp46 ⁺ CD127 ⁻ CD161 ⁻ c-KIT ⁻	NK-like
1	CD7 ⁻ CD127 ⁺ CD161 ⁺ c-KIT ⁺	ILC3-like
5	CD7 ⁺ CD127 ⁺ CD161 ⁺ c-KIT ⁺	ILC3
12	CD56 ⁺ CD127 ⁺ CD161 ⁺ c-KIT ⁻ CD27 ⁻	ILC1-like
19	CD56 ⁻ CD127 ⁻ NKp46 ⁻ CD161 ^{dim}	Lin- cells
13	CD56 ⁻ CD127 ⁻ NKp46 ⁻ CD161 ^{dim}	Lin- cells
18	CD56 ⁻ CD127 ⁻ NKp46 ⁺ CD161 ⁻	Lin- cells
14	CD56 ⁻ CD127 ⁻ NKp46 ⁺ CD161 ⁻	Lin- cells
6	CD56 ⁻ CD127 ⁻ NKp46 ⁺ CD161 ⁺	Lin- cells
8	CD56 ⁻ CD127 ⁻ NKp46 ⁺ CD161 ⁺	Lin- cells
7	CD56 ⁺ CD127 ⁻ CD45RA ⁻ CD161 ⁻	NK-like
2	CD56 ⁺ CD127 ⁻ CD45RA ⁺ CD161 ⁺	NK-like
3	CD56 ⁺ CD127 ⁻ CD45RA ⁺ CD161 ⁺	NK-like

Fig. 4 CD127⁺ ILC and ILC-like subsets identified by Cytosplore^{+HSNE}

Table showing cluster number, distinguishing phenotypic marker expression profiles and biological annotation for the clusters identified in Fig. 3e. Black color indicates clusters described in previous reports and red color additional unknown clusters. Hierarchical clustering of clusters based on marker expression profile shown in the heatmap depicted in Fig. 3f

established nomenclature²¹ (**Fig. 4**, red annotations). For example, cluster 15 is highly similar to ILC2 (cluster 16) based on the expression of CD7, CD127, CD161, and CD25, but lacks the ILC2-defining marker CRTH2. Also, clusters 17, 9 and 11 bear close resemblance to ILC1 based on CD7⁺CD127⁺c-KIT⁺ marker expression profile, but lack the ILC-defining CD161 marker. Finally, cluster 1 is very similar to ILC3 (cluster 5) based on CD127, CD161 and c-KIT positivity, but lacks the lymphoid marker CD7. Interestingly, the ILC3 (cluster 5) and ILC3-like (cluster 1) populations resided mainly in intestinal biopsies of patient with Crohn's disease (**Fig. 3f**) and may be related. Cluster 4 was mainly present in peripheral blood of patients with RCDII, suggesting a possible association with this pre-malignant disease state. Importantly, three clusters (4, 17, and 19) (**Fig. 3f**) were essentially missed in our previous study¹⁴ due to the downsampling. Finally, all identified cell clusters consist to a variable extent of cells that were downsampled in the original

analysis (**Fig. 3g**). Thus, the analysis of the full data set provides increased detail and confidence in establishing the phenotypes of these low abundance innate cell subsets.

HSNE identifies rare CD4⁺ T-cell subsets in blood

Next, we selected the CD4⁺ T-cell lineage (**Fig. 3a**) and show the distribution of the landmarks at the third level, revealing several clusters within the CD4⁺ T-cell compartment (**Fig. 5a**), including a small CD28⁺CD4⁺ T-cell memory population (25,398 cells; 0.5% of total), most likely representing terminally differentiated cells²⁶. Subsequent analysis at the single-cell level (**Fig. 5b**) identified a CD56⁺ population within the CD28⁺CD4⁺T cells that is enriched in blood of patients with Crohn's disease (**Fig. 5b**, bottom panels, dashed black circle), as well as a CD56⁻ population of CD28⁺CD4⁺T cells (**Fig. 5b**, bottom panels, dashed yellow circle) present in blood samples of both patients and controls. Importantly, this latter cell population was not identified in our previous publication due to the non-uniform downsampling of cells (**Fig. 5b**).

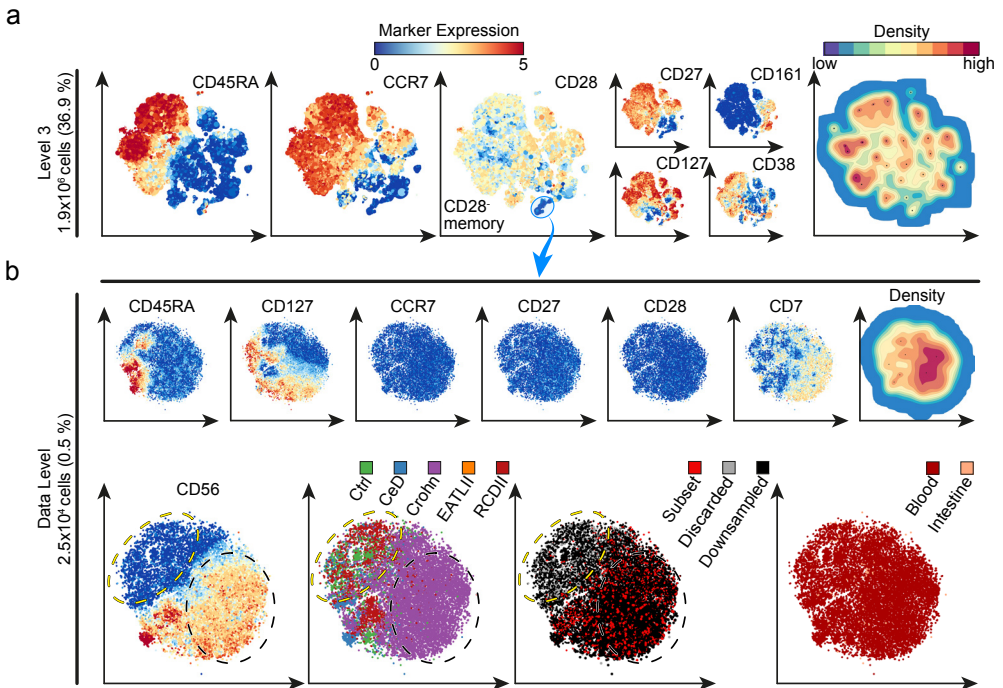


Fig. 5 Analysis of the CD4⁺ T-cell compartment in inflammatory intestinal diseases **a** Third HSNE level embedding of the CD4⁺ T cells (1.4×10⁶ cells, selected in Fig. 3). Color and size of landmarks as described in Fig. 3. Right panel shows density features for the level 3 embedding. Blue encirclement indicates selection of landmarks representing CD28⁺CD4⁺ T cells. **b** Embedding of the CD28⁺CD4⁺ T cells (2.6×10⁶ cells) at single-cell resolution. Bottom-left panel shows yellow and black dashed encirclements based on CD56⁻ and CD56⁺ expression, respectively. Three bottom-right panels show cells colored according to: (left) from subjects with different disease status (CeD, Crohn, EATLII, RCDII, and controls), (middle) sampling status (annotated subset, discarded and downsampled) and (right) tissue-of-origin.

Together, these findings emphasize that Cytosplore^{+HSNE} is highly efficient in unbiased analysis of both abundant and rare cell populations in health and disease by permitting full single-cell resolution. It enables the simultaneous identification and visualization of known cell subsets and provides evidence for additional heterogeneity in the immune system, as it reveals the presence of cell clusters that were missed in a previous analysis due to downsampling of the input data. These currently unspecified cell clusters might represent intermediate stages of differentiation or novel rare cell types with presently unknown function.

HSNE is robust and outperforms current single-cell methods

While the exploration of the hierarchy requires analysis at multiple levels, the workflow is robust and reproducible as shown in **Supplementary Fig. 5**. In this exemplary analysis, we obtained the same Cytosplore^{+HSNE} clusters at the single-cell level upon reconstructing the hierarchy and embeddings in a matter of minutes (**Methods** section). In addition, we tested the Cytosplore^{+HSNE} applicability to three different public mass cytometry data sets. First, we analyzed a well-characterized bone marrow data set²⁷ containing 81,747 cells as a benchmark case (**Supplementary Fig. 6**) and demonstrated that the landmarks in the overview level (2,632; 3.2% of total) that were selected by the HSNE algorithm were distributed across almost all of the manually gated cell types (**Supplementary Fig. 6a**), indicating that the global data heterogeneity was accurately preserved. Also, GMS clustering resulted in HSNE clusters that were phenotypically similar to the manually gated cell types and displayed additional diversity within those subsets (**Supplementary Fig. 6b**). However, as the power of Cytosplore^{+HSNE} lies in its scalability to data sets exceeding millions of cells, we also tested the versatility of Cytosplore^{+HSNE} by comparing it to other state-of-the-art scalable single-cell analysis methods and accompanying large data sets (**Supplementary Note 3**. Cytosplore^{+HSNE} offers advantages over current scalable single-cell analysis methods, **Supplementary Figs. 7 and 8**). Here Cytosplore^{+HSNE} computed the analyses of the Vortex data set⁵ containing 0.8 million cells in 4 min compared to 22 h, using the publicly available Vortex implementation on the same computer. Similarly, analysis of the Phenograph data set⁴ containing 15 million cells was computed in 3.5 h compared to 40 h, using the publicly available Phenograph implementation on the same computer. Both analyses show that Cytosplore^{+HSNE} reproduces the main findings as presented in the original publications. More importantly, Cytosplore^{+HSNE} provides the distinct advantage of visualizing all cells and intracluster heterogeneity at subsequent levels of detail up to the single-cell level, even for the 15 million of cell data set, without a need for

downsampling. Also, Vortex failed computing the 5.2 million cell gastrointestinal data set within 3 days of clustering (regardless of using Euclidian or Angular distance), where Cytosplore^{+HSNE} accomplished this within 29 min. Moreover, while Phenograph did identify rare clusters that largely consisted of CD56⁺ cells within the CD28⁻CD4⁺ memory T cells (**Fig. 5b**), these clusters did not accurately correspond to the total number of CD56⁺ cells, obscuring the association with Crohn's disease, further highlighting the advantages of Cytosplore^{+HSNE} over these other computational tools.

Finally, we investigated whether a density-based downsampling as implemented for instance by SPADE², could provide better results compared to random downsampling. However, solely applying density-based downsampling does not allow for quantitative analysis of the resulting sample, as different types of cells will be reduced by different amounts. To mitigate this problem, SPADE implements an elaborate pipeline of downsampling, clustering and subsequent upsampling to enable for such a comparison, while this is an inherent part of HSNE. Therefore, we made a direct comparison between density-based downsampling used in the SPADE pipeline² and HSNE of the same 5.2 million cells gastrointestinal data set. On the basis of the expression of major lineage markers (**Fig. 3a**), HSNE created six large clusters (**Fig. 3b**) in the two-dimensional space at the overview level where similar landmark cells group closely, laying out all the cells of one cluster very close to any other cell of the same cluster, but distant from the cells of the other clusters. The SPADE analysis on the same data (**Supplementary Fig. 9**) created a dendrogram where cells of one cluster are close to cells of other clusters, while in high-dimensional space, they could be dissimilar and far apart. Importantly, we compared the ability of the SPADE analysis to preserve rare cellular subsets with HSNE. Despite density-based downsampling, several SPADE nodes that were created displayed a mixture of different phenotypes (underclustering) as revealed by the single resolution of a linked t-SNE analysis that we show for the CD56⁺CD4⁺ T-cell node as an example (**Supplementary Fig. 9b**, node #1), while other SPADE nodes contained cells with overlapping phenotypes (overclustering) such as several myeloid cell populations (**Supplementary Fig. 9c**, nodes #2–5). In addition, rare subsets such as the CD28⁻subpopulations of CD4⁺ memory T cells (**Supplementary Fig. 9d**) or the ILC-like clusters (**Supplementary Fig. 9e**) that we could identify with HSNE (**Figs. 3 and 5**) were in the resulting SPADE tree indistinguishable from other CD4⁺ T cells or innate lymphocytes, respectively (shown by the overlapping distributions of cells from different nodes); this indicates that SPADE is less suitable for rare cell analysis. A similar problem was reported by Amir et al., where leukemic cells were not separated from

healthy cells in the SPADE tree⁹. Thus, combining the single-cell resolution with the enhanced scalability may be critical for the success of HSNE in preserving rare cells.

DISCUSSION

Mass cytometry data sets generally consist of millions of cells. Current tools can either extract global information with no single-cell resolution or provide single-cell resolution but at the expense of the number of cells that can be analyzed. Consequently, when single-cell resolution is of interest, most current tools require downsampling of the data sets. However, reducing the number of included cells in the analysis pipeline may hamper the identification of rare subsets.

To overcome this problem, we introduce Cytosplore^{+HSNE}. On the basis of a novel hierarchical embedding of the data (HSNE), Cytosplore^{+HSNE} enables the analysis of tens of millions of cells using the whole data in a fraction of the time required by currently available tools. The power of the hierarchical embedding strategy is that Cytosplore^{+HSNE} provides visualizations of the data at different levels of resolution, while preserving the non-linear phenotypic similarities of the single cells at each level. Cytosplore^{+HSNE} enables the user to interactively select the groups of data points at each resolution level, either hand-picked or guided by density-based clustering, to further zoom-in on the underlying data points in the hierarchy up to the single-cell resolution. Using a data set of 5.2 million cells, we demonstrate that Cytosplore^{+HSNE} allows a rapid analysis of the composition of the cells in the data set that, at all levels of the hierarchy, the representation of these cells preserve phenotypic relationships, and that one can zoom-in on rare cell populations that were missed with other analysis tools. The identification of such rare immune subsets offers opportunities to determine cellular parameters that correlate with disease.

There is an ongoing scientific debate on the validity of clustering in t-SNE maps versus direct clustering on the high-dimensional space. However, it has been shown that stochastic neighbor embedding (SNE) preserves and separates clusters in the high-dimensional space²⁸. While clustering the data points on highly non-linear manifolds is possible with complex models, we argue that the presented approach simplifies clustering considerably. We show that HSNE efficiently unfolds the non-linearity in the high-dimensional data, as other SNE approaches do and therefore simpler clustering methods based on locality in the map suffice to partition the data faithfully (e.g., the density-based GMS clustering, implemented in Cytosplore^{+HSNE}).

Especially when combined with an interactive quality control mechanism to visually inspect residual variance within each cluster, the kernel size can be selected such that within-cluster variance is minimized, and thereby supports the validity of the cluster with respect to potential underclustering. This is indeed confirmed by comparisons to other scalable tools (i.e., Phenograph and Vortex), showing that Cytosplore^{+HSNE} provides a superior discriminatory ability to identify and visualize rare phenotypically distinct cell clusters in large data sets in a very short time span. However, depending on user preference, Cytosplore^{+HSNE} can be used in conjunction with such direct clustering approaches. This allows the user to identify additional heterogeneity that is potentially missed by direct clustering, and provides the tools for an informed merging and splitting of clusters as the user deems appropriate. The recent application of mass cytometry and other high-dimensional single-cell analysis techniques has greatly increased the number of phenotypically distinct cell clusters within the immune system. This raises obvious questions about the true distinctiveness and function of such cell clusters in health and disease, an issue that is beyond the scope of the present study but needs to be addressed in future studies.

In conclusion, Cytosplore^{+HSNE} allows an interactive and fast analysis of large high-dimensional mass cytometry data sets from a global overview to the single-cell level and is coupled to patient-specific features. This may provide crucial information for the identification of disease-associated changes in the adaptive and innate immune system which may aid in the development of disease- and patient-specific treatment protocols. Finally, Cytosplore^{+HSNE} applicability goes beyond analyzing mass cytometry data sets as it is able to analyze any high-dimensional single-cell data set.

METHODS

HSNE algorithm

HSNE builds a hierarchy of local and non-linear similarities of high-dimensional data points¹³, where landmarks on a coarser level of the hierarchy represent a set of similar points or landmarks of the preceding more detailed level. To represent the non-linear structures of the data, the similarity of these landmarks is not described by Euclidian distance, but by the concept of Aol on landmarks of the preceding level. The similarities described in every level of the hierarchy are then used as input for an adapted version of the similarity-based embedding technique BH-SNE¹⁵ for visualization.

The algorithm works as follows: First, a weighted k-nearest neighbor (kNN) graph

is computed from the raw input data. For optimal performance and scalability, the neighborhoods are approximated as described in ref.¹⁶. The weight of the link between the two data points in the kNN graph describes the similarity of the connected data points.

In the subsequent steps, the hierarchy is built based on the similarities of the data level. To this extent, a number of random walks of predefined length is carried out starting from every node in the kNN graph, using the similarities as probability for the next jump; similar nodes to the current node are more likely to be the target of the next jump. Nodes in the graph that are reached more often are considered more important and selected as landmarks for the next coarser level. The number of landmarks is selected in a data-driven manner, based on this importance. The Aol of a landmark is defined by a second set of random walks started from all nodes (data points or landmarks on the preceding level). Here, the length is not predefined. Rather, once a landmark is reached, the random walk terminates. The influence on the node is then defined for every reached landmark as the fraction of walks that terminated in that landmark. Inversely, the Aol for each landmark is defined as the set of all nodes that reached this landmark at least once in this second set of random walks. Consequently, since multiple random walks initiated at the same node can end in different nodes, the Aols of different landmarks can overlap.

We use this overlap to define a new neighborhood graph at the levels above the data level. Here, two nodes in the graph corresponding to landmarks at this level are connected if they have overlapping Aols, where the link between the nodes is weighted by the number of data points in the overlapping area. This process is carried out iteratively, until a predefined number of hierarchical levels has been constructed. For the full technical details, we refer to our previous work¹³.

HSNE implementation in Cytosplore

We implemented our integrated analysis tool Cytosplore^{+HSNE} using a combination of C++, javascript and OpenGL. All computationally demanding parts are implemented in C++ and make use of parallelization, where possible. The density estimation and GMS clustering make use of the graphics processing unit (GPU), as described in our original publication on Cytosplore²⁹, if possible, allowing clustering of millions of points in less than a second. We implemented the visualizations of the embedding in OpenGL on the GPU, for optimal performance, and less computational demanding visualizations, such as the heatmap, in javascript. We implemented the HSNE algorithm in C++ , as

presented in ref. ¹³. Since we use the sparse data structures, memory consumption strongly depends on the data complexity. Maximum memory consumption during the construction of a four level hierarchy plus overview embedding of the 841,644 cell Vortex data set was 1,684 MB, construction of a five-level hierarchy of our human inflammatory intestinal diseases data set, consisting of 5,220,347 cells required a maximum of 9,357 MB of main memory, and finally, the 15,299,616 cell Phenograph data set required a maximum of 24.3 GB of memory during the computation of a five-level hierarchy plus the overview embedding. Computation times for the described hierarchies plus the first level embedding after 1,000 iterations were 4 min, 29 min, and, 3 h and 37 min, respectively, on a HP Z440 workstation with a single intel Xeon E5-1620 v3 CPU (4 cores) clocked at 3.5 Ghz, 64 GB of main memory and an nVidia Geforce GTX 980 GPU with 4 GB of memory, running Windows 7.

Human gastrointestinal disorders mass cytometry data set

Detailed description of the mass cytometry data set on human gastrointestinal disorders can be found in our previous work¹⁴. In brief, samples ($N = 102$) were collected from patients who were undergoing routine diagnostic endoscopies. The cells from the epithelium and lamina propria were isolated from two or three intestinal biopsies by treatment with EDTA followed by a collagenase mix under rotation at 37 °C. We analyzed single-cell suspensions from biological samples including duodenum biopsies ($N = 36$), rectum biopsies ($N = 13$), perianal fistulas ($N = 6$), and PBMC from control individuals ($N = 15$) and from patients with inflammatory intestinal diseases (celiac disease (CeD), $N = 13$; RCD type II (RCDII), $N = 5$; enteropathy-associated T-cell lymphoma type II (EATLII), $N = 1$ and Crohn's disease (Crohn), $N = 10$). A CyTOF panel of 32 metal isotope-tagged monoclonal antibodies was designed to obtain a global overview of the heterogeneity of the innate and adaptive immune system. Primary antibody metal-conjugates were either purchased or conjugated in-house. Procedures for mass cytometry antibody staining and data acquisition were carried out as previously described²⁷. CyTOF data were acquired and analyzed on-the-fly, using dual-count mode and noise-reduction on. All other settings were either default settings or optimized with a tuning solution. After data acquisition, the mass bead signal was used to normalize the short-term signal fluctuations with the reference EQ passport PI3H2302 during the course of each experiment and the bead events were removed³⁰.

Processing of mass cytometry data

We transformed data from the human inflammatory intestinal diseases data set

using hyperbolic arcsin with a cofactor of 5 directly within Cytosplore^{+HSNE}. We discriminated live, single CD45⁺ immune cells with DNA stains and event length for the human inflammatory intestinal diseases study. We analyzed other data (Phenograph and Vortex data sets) as was available, except the transformation using hyperbolic arcsin with a cofactor of 5.

Cytosplore^{+HSNE} analysis

Cytosplore^{+HSNE} facilitates the complete exploration pipeline in an integrated manner (see **Supplementary Movie I**). All presented tools are available for every step of the exploration and every level of the hierarchy. Data analysis in Cytosplore^{+HSNE} included the following steps: We applied the arcsin transform with a cofactor of five upon loading the data sets. After that, we started a new HSNE analysis and defined the markers that should be used for the similarity computation. We used markers CD3, CD4, CD7, CD8a, CD8b, CD11b, CD11c, CD14, CD19, CD25, CD27, CD28, CD34, CD38, CD45, CD45RA, CD56, CD103, CD122, CD123, CD127, CD161, CCR6, CCR7, c-KIT, CRTH2, IL-15Ra, IL-21R, NKp46, PD-1, TCRab, and TCRgd for the human inflammatory intestinal diseases data set, all available markers for the bone marrow benchmark dataset, surface markers CD3, CD7, CD11b, CD15, CD19, CD33, CD34, CD38, CD41, CD44, CD45, CD47, CD64, CD117, CD123 and HLA-DR for the Phenograph dataset, and markers CD3, CD4, CD5, CD8, CD11b, CD11c, CD16/32, CD19, CD23, CD25, CD27, CD34, CD43, CD44, CD45.2, CD49b, CD64, CD103, CD115, CD138, CD150, I20g8, B220, CCR7, c-KIT, F4/80, FcεR1a, Foxp3, IgD, IgM, Ly6C, Ly6G, MHCII, NKp46, Sca1, SiglecF, TCRb, TCRgd and Ter119 to construct the hierarchy for the Vortex data set. We used the standard parameters for the hierarchy construction; number of random walks for landmark selection: $N = 100$, random walk length: $L = 15$, number of random walks for influence computation: $N = 15$. For any clustering that occurred the GMS grid size was set to $S = 256$ ref.² The reduction factor from one level in the hierarchy to the next coarser level is completely data-driven. In our experiments with mass cytometry data, the number of landmarks was consistently reduced by roughly one order of magnitude from one level to the next. Embeddings consisting of only a few hundred points usually provide little insight. Therefore, we defined the number of levels such that the overview level could be expected to consist of in the order of 1,000 landmarks meaning $N = 5$ for the human inflammatory intestinal diseases data set and Phenograph data set, $N = 3$ for the bone marrow benchmark data set, and $N = 4$ for the Vortex data set. Building the hierarchy automatically creates a visualization of the overview level using BH-SNE. Cytosplore^{+HSNE} enables color coding of the landmarks using expression

(e.g., **Fig. 3a**) of any provided markers or by sample. For example, we created the clinical feature (e.g., **Fig. 3c**, bottom-left panel) and blood/intestine (e.g., **Fig. 3c**, bottom-right panel) color schemes based on samples for the human inflammatory intestinal diseases data set within Cytosplore^{+HSNE}, and for the Phenograph data set, we created a color scheme that represented the sample coloring as provided in ref.⁴ (**Supplementary Fig. 7**). For zooming into the data, we generally selected cells based on visible clusters, either using manual selection or by selecting clusters derived by using the GMS clustering. For the Vortex data set, we clustered the third level embedding (**Supplementary Fig. 8**). We specified a kernel size of 0.18 of the embedding size, to match the 48 clusters created by the X-shift clustering described in ref.⁵, resulting in 50 clusters. For subset classification, we first cluster the embedding at a given level using the GMS clustering. Next, we inspect the clustering by using the integrated descriptive marker statistics and heatmap visualization. If there is still meaningful variation of the marker expression within clusters, we zoom further into these clusters. If clusters are phenotypically homogeneous, the corresponding cell types are defined by inspecting the full marker expression profile in the heatmap and then the cluster is exported from any level in the hierarchy.

Data availability

The gastrointestinal mass cytometry data set that supports the findings of this study is publicly available on Cytobank, experiment no 60564. <https://community.cytobank.org/cytobank/experiments/60564>. The source code of the HSNE library, written in C++, is available at <https://github.com/NicolaI7/High-Dimensional-Inspector>. Furthermore, we provide a Cytosplore^{+HSNE} installer for Windows, allowing exploration of several million cells, for academic use at <https://www.cytosplore.org>.

REFERENCES

1. Saeys, Y., Gassen, S.V. & Lambrecht, B. N. Computational flow cytometry: helping to make sense of high-dimensional immunology data. *Nat. Rev. Immunol.* 16, 449–462 (2016).
2. Qiu, P. et al. Extracting a cellular hierarchy from high-dimensional cytometry data with SPADE. *Nat. Biotechnol.* 29, 886–891 (2011).
3. Zunder, E. R., Lujan, E., Goltsev, Y., Wernig, M. & Nolan, G. P. A continuous molecular roadmap to iPSC reprogramming through progression analysis of single-cell mass cytometry. *Cell Stem Cell* 16, 323–337 (2015).
4. Levine, J. H. et al. Data-Driven phenotypic dissection of AML reveals progenitor-like cells that correlate with prognosis. *Cell* 162, 184–197 (2015).
5. Samusik, N., Good, Z., Spitzer, M. H., Davis, K. L. & Nolan, G. P. Automated mapping of phenotype space with single-cell data. *Nat. Methods* 13, 493–496 (2016).
6. Spitzer, M. H. et al. IMMUNOLOGY. An interactive reference framework for modeling a dynamic immune system. *Science* 349, 1259425 (2015).

7. Hotelling, H. Analysis of a complex of statistical variables into principal components. *J. Ed. Psychol.* 24, 417–441 (1933).
8. van der Maaten, L. J. P. & Hinton, G. E. Visualizing high-dimensional data using t-SNE. *J. Mach. Learn. Res.* 9, 2579–2605 (2008).
9. Amir, E.-A. D. et al. viSNE enables visualization of high dimensional single-cell data and reveals phenotypic heterogeneity of leukemia. *Nat. Biotechnol.* 31, 545–552 (2013).
10. Haghverdi, L., Buettner, F. & Theis, F. J. Diffusion maps for high-dimensional single-cell analysis of differentiation data. *Bioinformatics* 31, 2989–2998 (2015).
11. Bendall, S. C., Nolan, G. P., Roederer, M. & Chattopadhyay, P. K. A deep profiler's guide to cytometry. *Trends Immunol.* 33, 323–332 (2012).
12. Chattopadhyay, P. K., Gierahn, T. M., Roederer, M. & Love, J. C. Single-cell technologies for monitoring immune systems. *Nat. Immunol.* 15, 128–135 (2014).
13. Pezzotti, N., Höllt, T., Lelieveldt, B., Eisemann, E. & Vilanova, A. Hierarchical Stochastic Neighbor Embedding. *Comput. Graph. Forum* 35, 21–30 (2016).
14. van Unen, V. et al. Mass cytometry of the human mucosal immune system identifies tissue- and disease-associated immune subsets. *Immunity* 44, 1227–1239 (2016).
15. van der Maaten, L. Accelerating t-SNE using tree-based algorithms. *J. Mach. Learn. Res.* 3221–3245 (2014).
16. Pezzotti, N. et al. Approximated and user steerable tSNE for progressive visual analytics. *IEEE. Trans. Vis. Comput. Graph.* 23, 1739–1752 (2016).
17. Setty, M. et al. Wishbone identifies bifurcating developmental trajectories from single-cell data. *Nat. Biotechnol.* 34, 637–645 (2016).
18. Comaniciu, D. & Meer, P. Mean shift: a robust approach toward feature space analysis. *IEEE. Trans. Pattern Anal. Mach. Intell.* 24, 603–619 (2002).
19. Spits, H. & Cupedo, T. Innate lymphoid cells: emerging insights in development, lineage relationships, and function. *Annu. Rev. Immunol.* 30, 647–675 (2012).
20. McKenzie, A. N. J., Spits, H. & Eberl, G. Innate lymphoid cells in inflammation and immunity. *Immunity* 41, 366–374 (2014).
21. Spits, H. et al. Innate lymphoid cells--a proposal for uniform nomenclature. *Nat. Rev. Immunol.* 13, 145–149 (2013).
22. Robinette, M. L. et al. Transcriptional programs define molecular characteristics of innate lymphoid cell classes and subsets. *Nat. Immunol.* 16, 306–317 (2015).
23. Schmitz, F. et al. Identification of a potential physiological precursor of aberrant cells in refractory coeliac disease type II. *Gut.* 62, 509–519 (2013).
24. Schmitz, F. et al. The composition and differentiation potential of the duodenal intraepithelial innate lymphocyte compartment is altered in coeliac disease. *Gut.* 65, 1269–1278 (2016).
25. Ettersperger, J. et al. Interleukin-15-dependent T-cell-like innate intraepithelial lymphocytes develop in the intestine and transform into lymphomas in coeliac disease. *Immunity* 45, 610–625 (2016).
26. Mou, D., Espinosa, J., Lo, D. J. & Kirk, A. D. CD28 negative T cells: is their loss our gain? *Am. J. Transplant.* 14, 2460–2466 (2014).
27. Bendall, S. C. et al. Single-cell mass cytometry of differential immune and drug responses across a human hematopoietic continuum. *Science* 332, 687–696 (2011).
28. Shaham, U. & Steinerberger, S. Stochastic neighbor embedding separates well-separated clusters. *arXiv [stat.ML]* (2017).
29. Höllt, T. et al. Cytosplore: Interactive immune cell phenotyping for large singlecell datasets. *Comput. Graph. Forum* 35, 171–180 (2016).
30. Finck, R. et al. Normalization of mass cytometry data with bead standards. *Cytometry A* 83, 483–494 (2013).

SUPPLEMENTAL INFORMATION

Supplementary Note 1. Cytosplore^{+HSNE} is reproducible and robust

Cytosplore^{+HSNE} allows significant user interaction during the exploration of the HSNE hierarchy, where the embedding visualizations and integrated clustering provide strong guidance. Independent explorations of the 5.2 million dataset, following the same zooming-in strategy are shown in **Supplementary Figure 5**. While the embeddings slightly vary at all levels, (mostly in rotation and reflection of the map), the same high level structure is found in all explorations. The robust separation of these structures guides the user in the selection and zooming-in process, resulting in highly similar embeddings down to the data level.

Focusing on separate regions of the data and interactively zooming into these separately provides significantly more detail than is possible by direct dimensionality reduction or clustering of the complete dataset (**Figs. 3 and 4**). However, Cytosplore^{+HSNE} does provide the possibility to visualize the complete dataset at the data level (**Supplementary Fig. 1a**). A dataset consisting of 1 million cells created by randomly sampling the 5.2 million cell dataset presented in the main text and three smaller ones derived from this were analysed with HSNE and t-SNE resulting in highly similar embeddings (**Supplementary Fig. 1a**).

Supplementary Figure 1b shows the robustness of HSNE with regard to downsampling as well as the superiority of the HSNE data reduction towards the overview level, compared to random downsampling. Here the embeddings within each column are similar, indicating that HSNE captures similar features even with downsampled data. However, detail increases with growing data sizes even if the number of landmarks are comparable between datasets. Thus the HSNE hierarchy preserves the non-linear structures in the data when reducing the data for visualization at the more abstract levels, while these structures can be lost during random downsampling. The difference in detail is especially striking when comparing the complete HSNE hierarchy of 1 million cells (**Supplementary Fig. 1b**, top row) to the t-SNE embeddings of randomly sampled datasets of similar sizes as the HSNE levels (**Supplementary Fig. 1a**, bottom row).

Supplementary Note 2. Millions of cells cause performance issues and overcrowding in t-SNE

Although feasible with a strong computational infrastructure, t-SNE suffers from several problems when analyzing datasets exceeding hundreds of thousands of cells.

Three main parameters influence the result of a t-SNE embedding: the number of iterations for the gradient descent i , perplexity p and theta t (the latter only for BH-SNE). Cytobank provides a brief analysis of the parameters^a that shows diminishing returns for p and t , beyond certain values, which can sensibly be used as defaults and do not significantly change with the input data size. In contrast, i needs to be adjusted with increasing data sizes. We show that the commonly used default value of $i=1,000$ is not enough to properly embed millions of cells (**Supplementary Fig. 2**). All embeddings were created using A-tSNE, implemented in Cytosplore, using the default parameters of $p=30$ and $t=0.01$. Supplementary Figure 2a-c show embeddings of 1 million, 2 million and 5 million cells, respectively, randomly sampled from the 5.2 million cell dataset presented in the main text after 1,000 iterations. Computation time for the embeddings were (a) 5.5 h, (b) 13 h, and (c) 54 h. **Supplementary Figure 2d-f** show the same embeddings after 4,000 further iterations. Total computation time for the embeddings were (d) 19.5 h, (e) 45.5 h, and (f) 252 h.

While **Supplementary Figure 2a** seems to provide a good separation for some high level clusters **Supplementary Figure 2b and c** show typical artifacts of a non-converged embedding, i.e. the cells concentrate strongly in the center of the visualization, often forming a cross shape along the two axes as is clearly visible in the density plots.

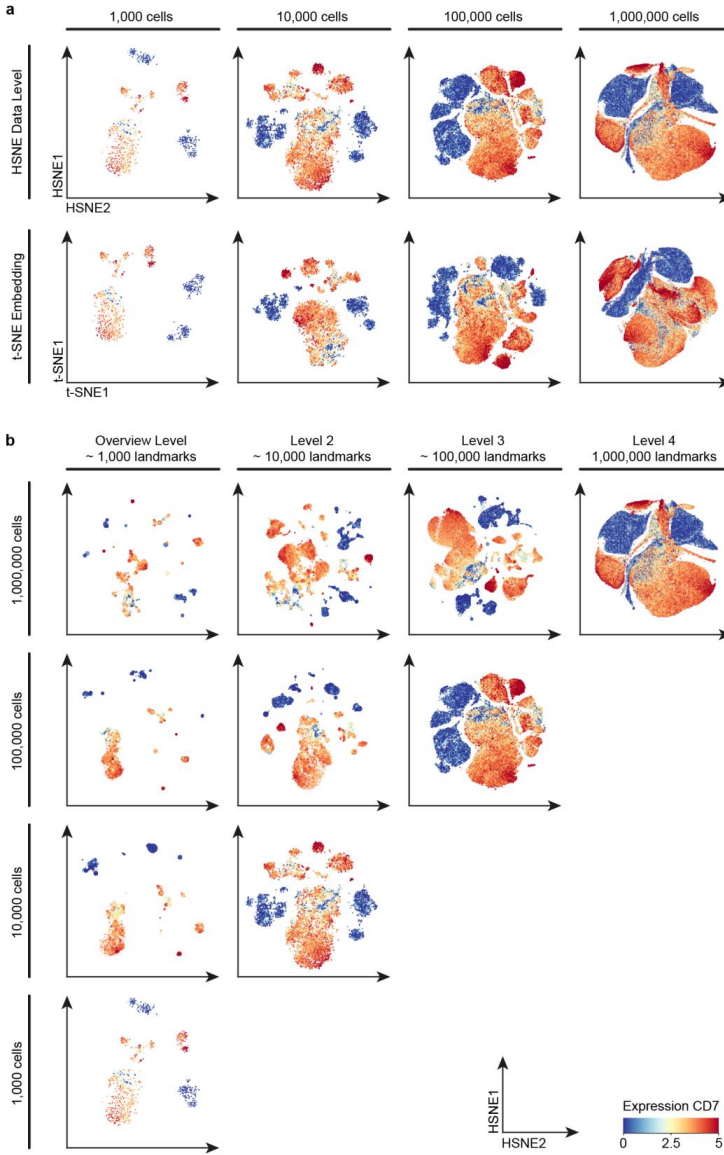
All embeddings evolved significantly after 4,000 additional iterations (**Supplementary Fig. 2d-f**), indicating that 1,000 iterations are not enough to fully converge for these large data sizes. Even after 5,000 iterations and 252 h of computation **Supplementary Figure 2f** still shows similar artifacts. Another problem of computing t-SNE for such large datasets is overcrowding. All embeddings show signs of overcrowding. Only large scale neighborhoods can be identified in **Supplementary Figure 2d**, while structure within these neighborhoods is hard to identify due to the large number of cells, even in the density plot. Also, in **Supplementary Figure 2e and f** some 'color smear' is present in the single-cell plots indicating that local neighborhoods were not resolved properly by the t-SNE algorithm. Intuitively, t-SNE accounts for small neighborhoods. By increasing the size of the input data local neighborhoods will often become less strongly connected and can tear, resulting in the displacement of cells in the plot. These effects might be reduced by increasing the perplexity value^b. Increasing p will help in the separation of high level clusters, however, at the cost of intracluster separation, as there will be less visual space for each cluster. A detailed analysis of the neighborhood conservation of different dimensionality reduction techniques, including t-SNE, can be found in our previous work¹³.

Supplementary Note 3. Cytosplore^{+HSNE} offers advantages over current scalable single-cell analysis methods

We investigated the generalizability as well the scalability of Cytosplore^{+HSNE} by comparison to two other-of-the-art scalable single-cell analysis methods and accompanying public datasets (Phenograph and Vortex). Both techniques use a clustering method followed by visualization of the generated clusters.

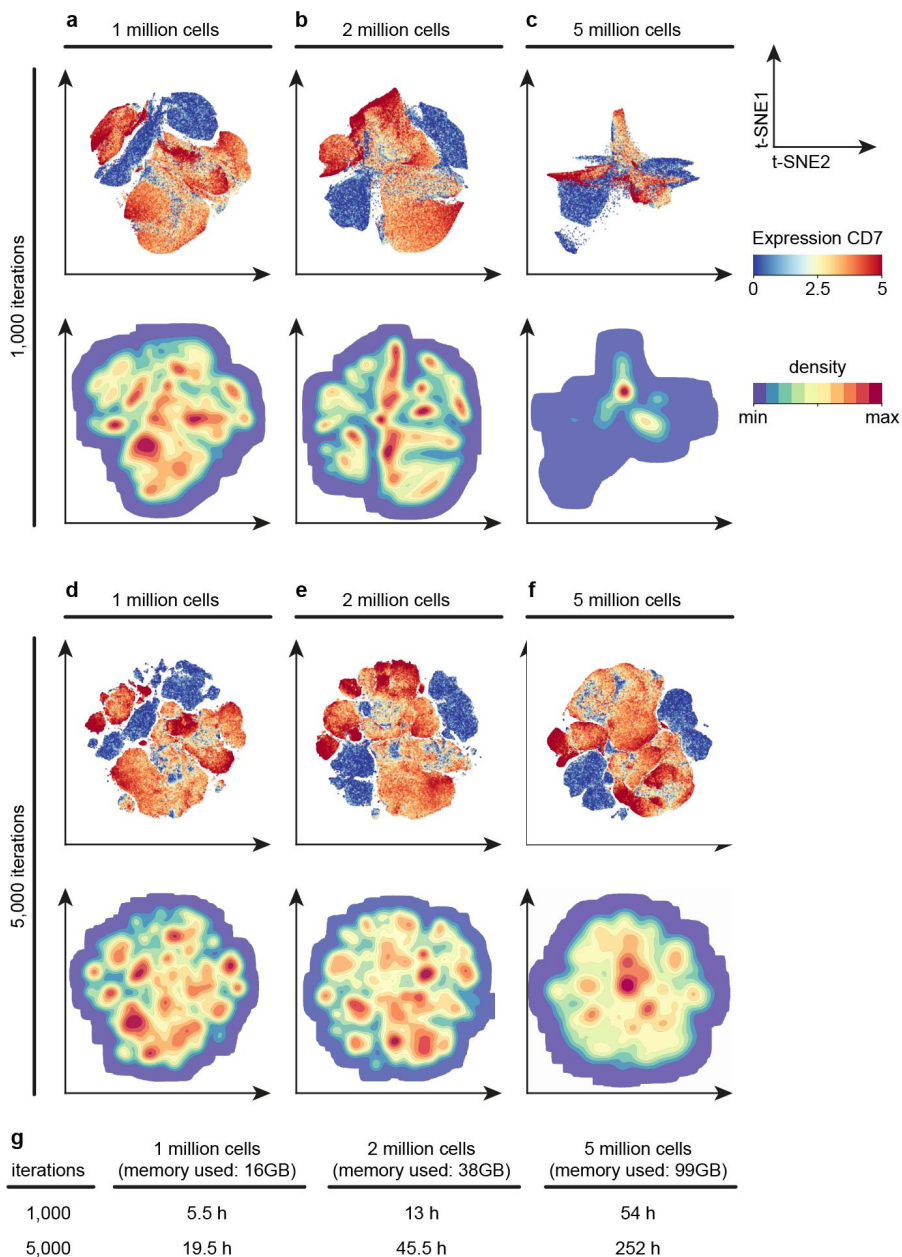
Phenograph achieves this by the Louvain community detection method for partitioning of the kNN graph, followed by a t-SNE embedding of the communities based on their median values. The resulting embedding places the communities in a global context, but cannot display the details of the single-cell complexity within the communities. Using Cytosplore^{+HSNE} we were able to reproduce the clusters of the Phenograph bone marrow dataset, consisting of 15 million cells, after 3.5 hours of computation, compared to 40 hours with the Phenograph algorithm (clustering per individual samples) on the same computer. Also, Cytosplore^{+HSNE} only required 29 minutes to compute the 5.2 million cell gastrointestinal dataset, while Phenograph required 4 hours. In addition to the significantly faster computation, Cytosplore^{+HSNE} provides the distinct advantage of visualizing all cells and intracluster heterogeneity at subsequent levels of detail (**Supplementary Fig. 7**)

Vortex first clusters the data using the X-shift algorithm, and then visualizes the result by random sampling of cells from the clusters for visualization in a single-cell force-directed layout. The sampling is necessary, as the force-directed layout can computationally handle 30,000 cells only. Therefore, the resulting single-cell visualization shows only 3.6 % of the original dataset. Although the technique allows for more detailed cellular visualization compared to Phenograph, a time-consuming second computation is required for every additional analysis on individual immune lineages. In a direct comparison Cytosplore^{+HSNE} recapitulated the murine bone marrow clusters at the second level of a 4 level hierarchy in minutes while Vortex required 22 hours (**Supplementary Fig. 8a,b**). In addition, by applying the zooming-in approach, we obtained the single-cell details for the plasmacytoid dendritic cell lineage within seconds (Supplementary Fig. 8c). Finally, Vortex failed computing the 5.2 million cell gastrointestinal dataset within 3 days of clustering (regardless of using Euclidian or Angular distance).



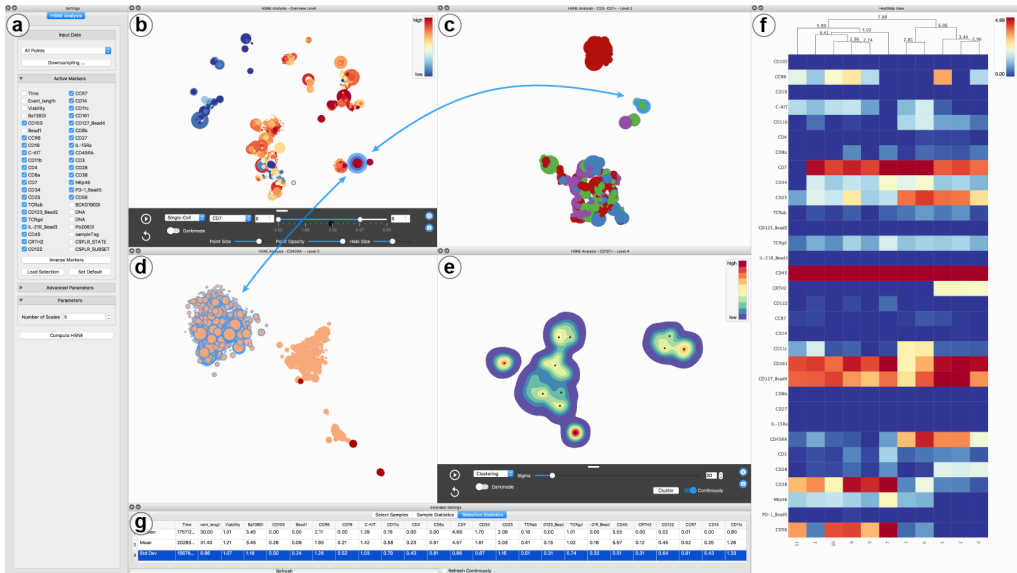
Supplementary Figure 1 Comparison of robustness with regard to downsampling between t-SNE and HSNE (a) Comparison of t-SNE (bottom row) and HSNE (top row) data level embeddings for datasets of different sizes (columns). First, 1 million cells were randomly sampled from the 5.2 million cell dataset, the smaller datasets were then created by randomly sampling the next largest one. All plots were created after 1,000 iterations. The 1 million cell embeddings were not fully converged. Color indicates CD7 expression. (b) Robustness of the HSNE hierarchy with regard to downsampling. Each row shows the datasets as described above. Embeddings for the complete hierarchy of $\log_{10}(N/100)$ levels, with N being the number of cells, are shown in the columns. Color as in panel a. Numbers of landmarks are approximated, indicating a reduction of one order of magnitude per level. In all columns the amount of detail increases towards the top (larger datasets), even though all embeddings in a column consist of roughly the same number of points. This implies that the preservation of non-linear neighborhoods by HSNE conserves structure that is lost by random downsampling

Visual Analysis of Mass Cytometry Data by Hierarchical Stochastic Neighbor Embedding Reveals Rare Cell Types



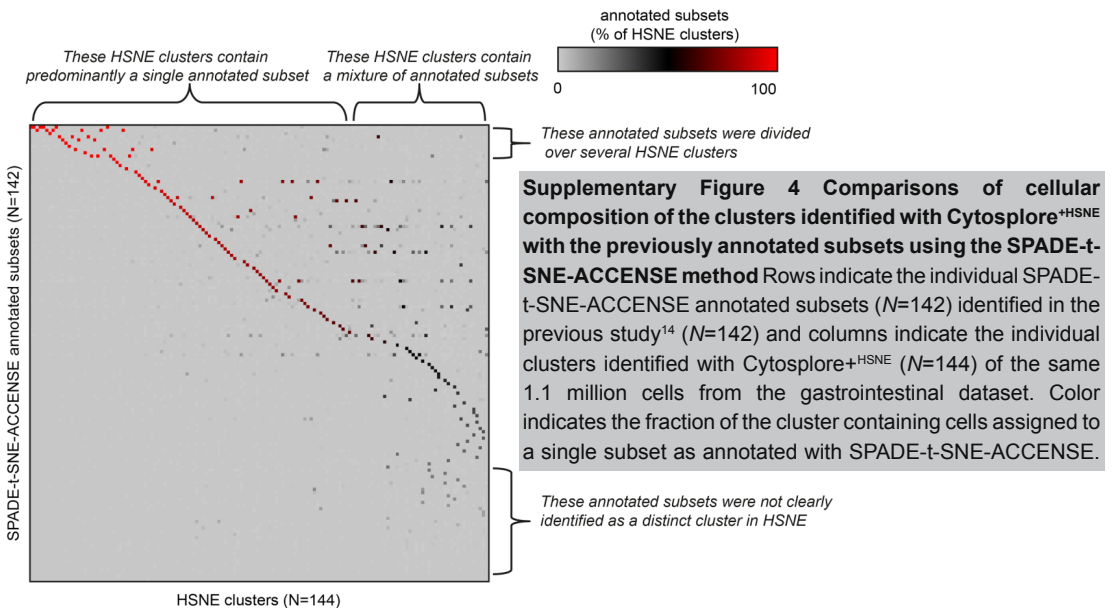
Supplementary Figure 2 t-SNE embeddings of millions of cells show overcrowding and artifacts caused by insufficient optimization

(a-c) Single-cell (top row) and density-based (bottom row) visualizations of t-SNE embeddings of (a) 1, (b) 2 and (c) 5 million cells, respectively, after 1,000 iterations, the standard setting used in many t-SNE applications. Color in the single-cell visualization corresponds to the CD7 marker expression; in the density visualization to the cell density in the t-SNE plot. (d-f) The same embeddings, consisting of (d) 1, (e) 2 and (f) 5 million cells, respectively, after 4,000 additional iterations, resulting in a total of 5,000 iterations. Colors as above. (g) Computation times for the different t-SNE computations.

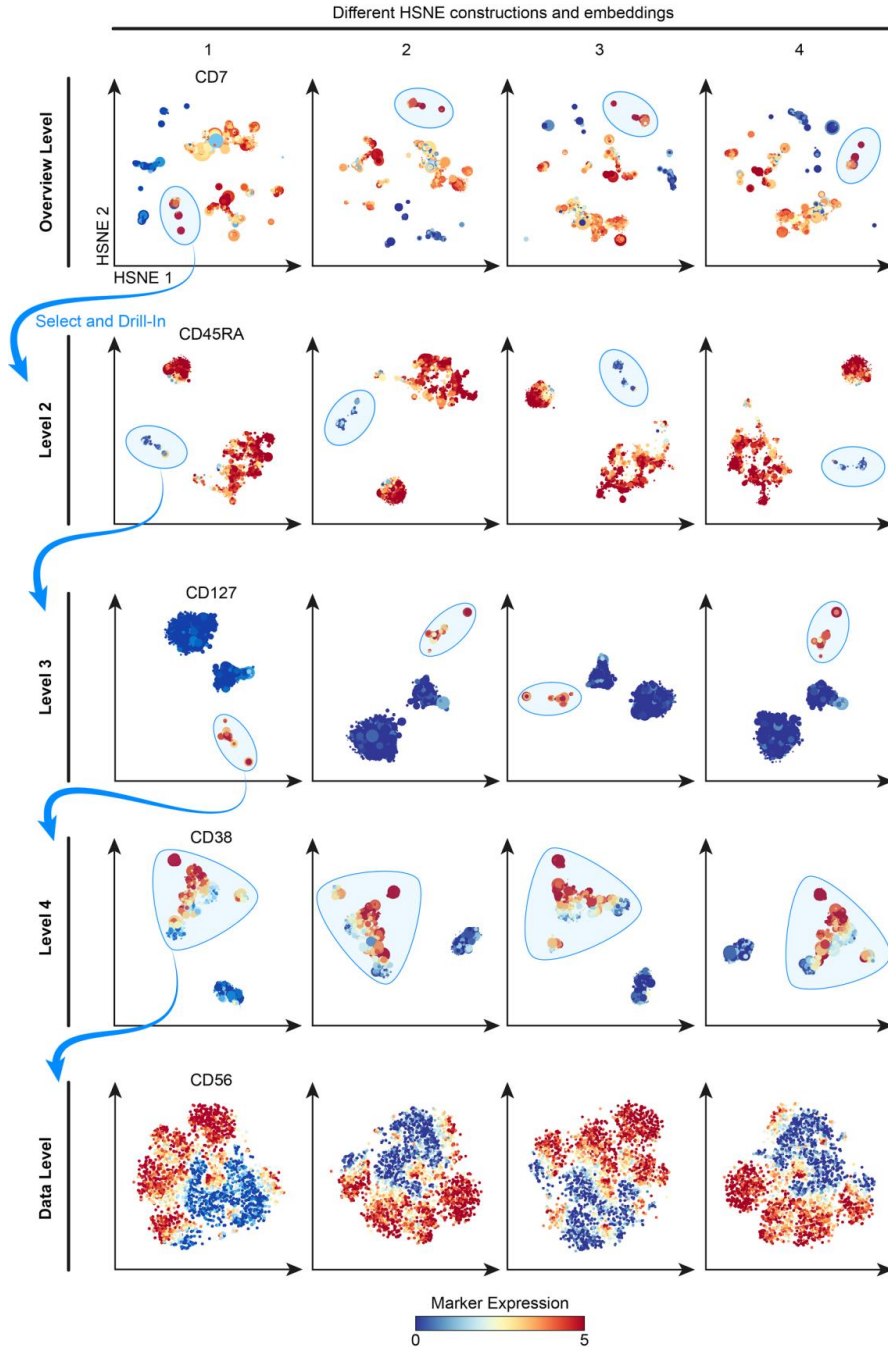


Supplementary Figure 3 The Cytosplere⁺HSNE software

(a) Settings panel for the HSNE analysis. (b-e) Zoom into the Innate Lymphocytes as shown in Figure 3 (b) overview level, (c) level 2, (d) level 3, (e) level 4. Color shows; (b) CD7 marker expression, (c) clinical features, (d) tissue origin, (e) cell density. A selection in panel d is highlighted in panel b,c, and d by blue halos around circles and arrows. Note, arrows added for clarity only and are not part of the software. (f) heatmap visualization of the median values of the clusters generated by GMS clustering based on the density visualization in panel e. Color shows marker expression. (g) Statistics of the selection shown in panel b-d.

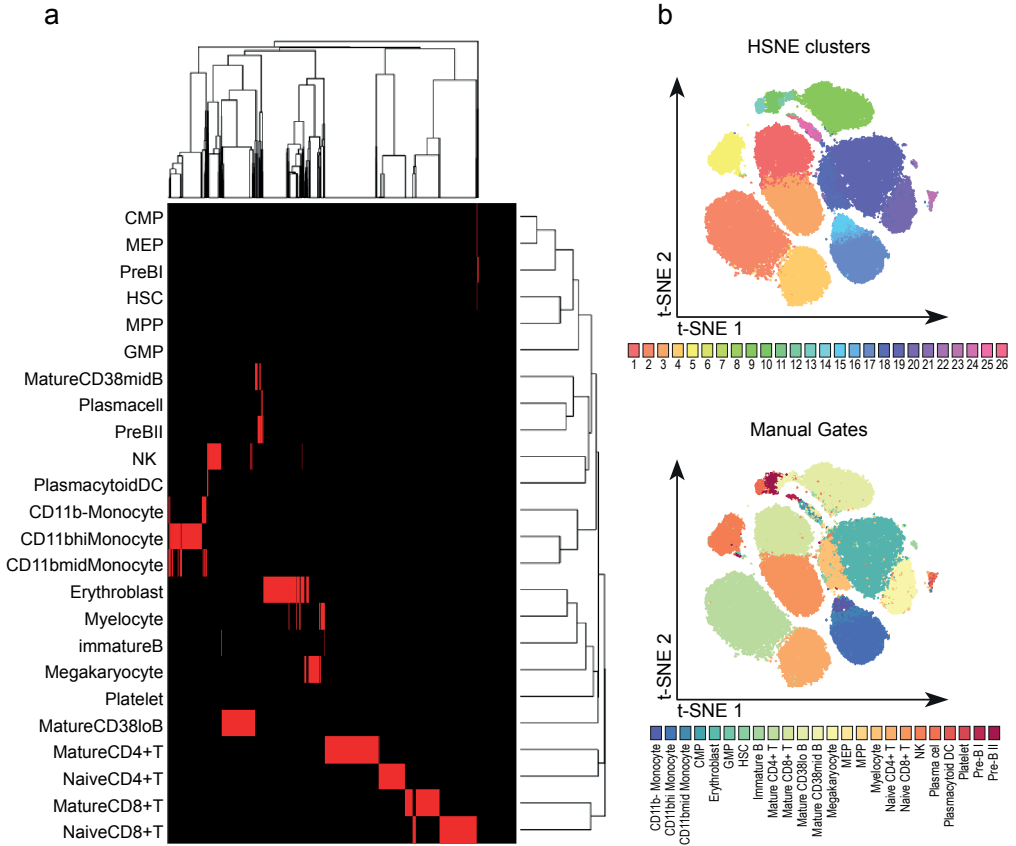


Supplementary Figure 4 Comparisons of cellular composition of the clusters identified with Cytosplere⁺HSNE with the previously annotated subsets using the SPADE-t-SNE-ACCENSE method Rows indicate the individual SPADE-t-SNE-ACCENSE annotated subsets (N=142) identified in the previous study¹⁴ (N=142) and columns indicate the individual clusters identified with Cytosplere⁺HSNE (N=144) of the same 1.1 million cells from the gastrointestinal dataset. Color indicates the fraction of the cluster containing cells assigned to a single subset as annotated with SPADE-t-SNE-ACCENSE.



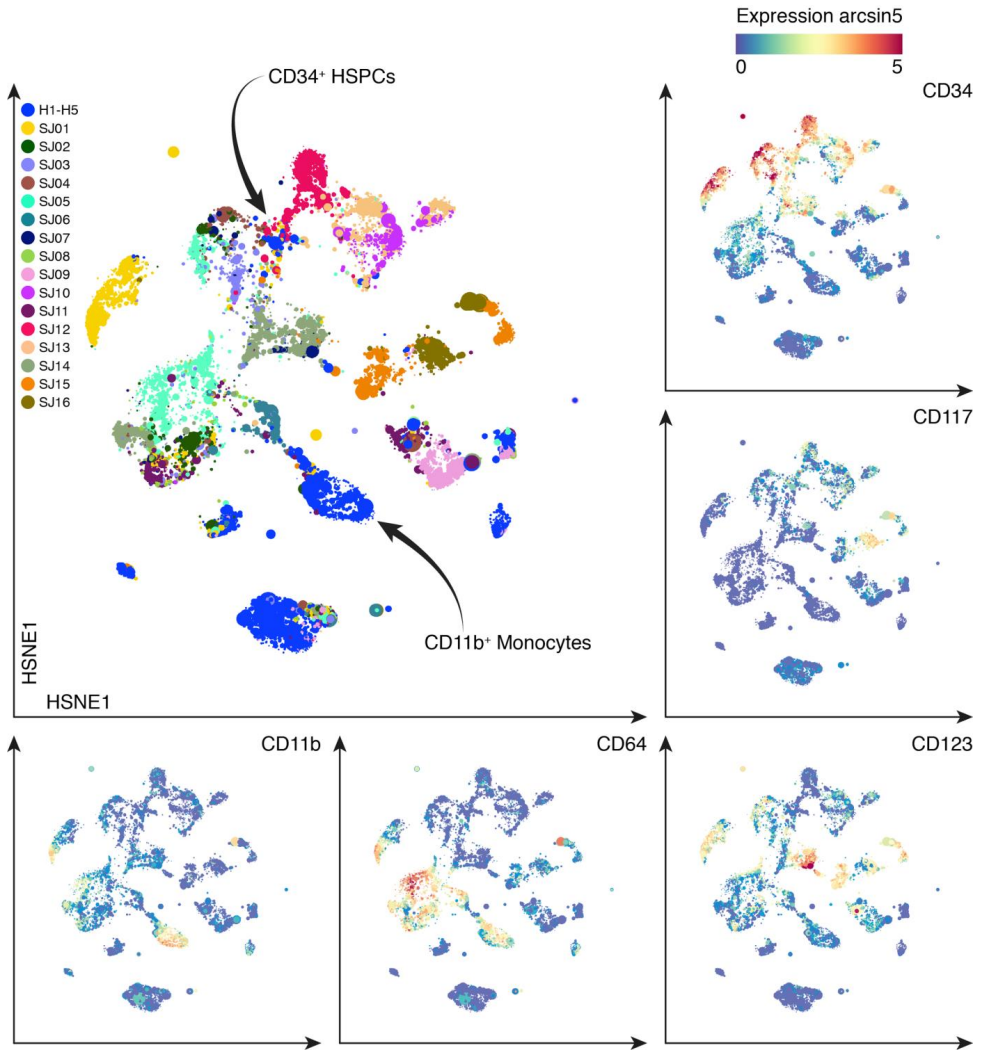
Supplementary Figure 5 Reproducibility of the hierarchy and the embeddings

Four independent Cytosplore^{+HSNE} analyses are shown (columns) reproducing the hierarchy construction and exploration of the data with the same zooming-in strategy (blue encirclements). Color-coding indicates arcsin5-transformed marker expression.



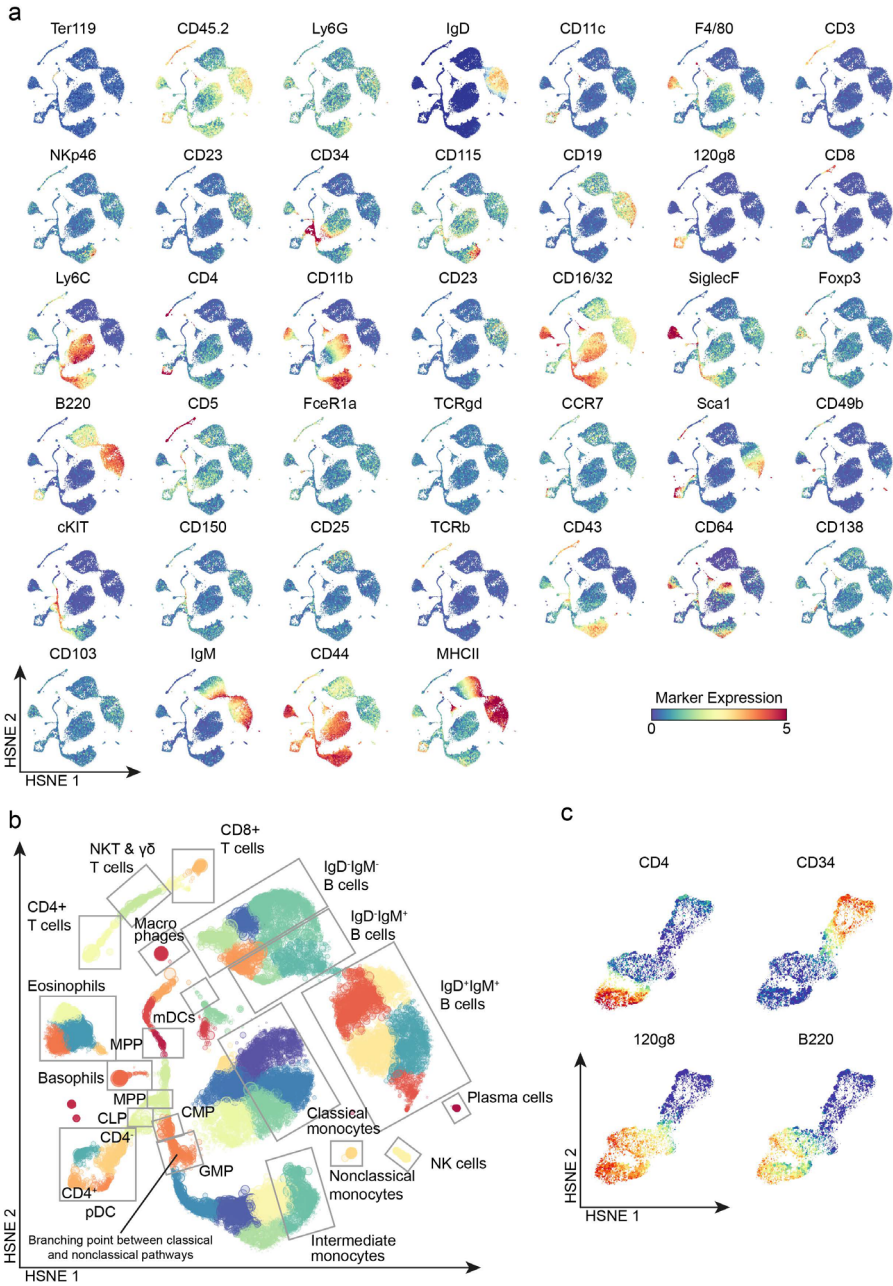
Supplementary Figure 6 Cytosplore^{+HSNE} analysis of the manual gated bone marrow benchmark dataset

(a) Heatmap depicting the distributions of the landmarks in the overview level (N=2,632; 1st hierarchical level of 3 in total) across the manual gated subsets of the bone marrow benchmark dataset²⁷ (N=81,747 cells) and hierarchical clustering thereof. (b) t-SNE embedding of the bone marrow benchmark dataset color-coded for cell clusters identified with Cytosplore^{+HSNE} (top panel) or by cell type assignments established by manual gating (bottom panel).



Supplementary Figure 7 Cytosplere^{+HSNE} analysis of the Phenograph bone marrow dataset.

Cytosplere^{+HSNE} embeddings of the full 15.0 million cells of the Phenograph human bone marrow dataset (overview level of a 5 level hierarchy). Color coding of main panel (top left) by patient identity. In additional panels, color coding indicates arcsin5-transformed marker expression. The above shows a comparison with Figure 3 of the original study⁴.

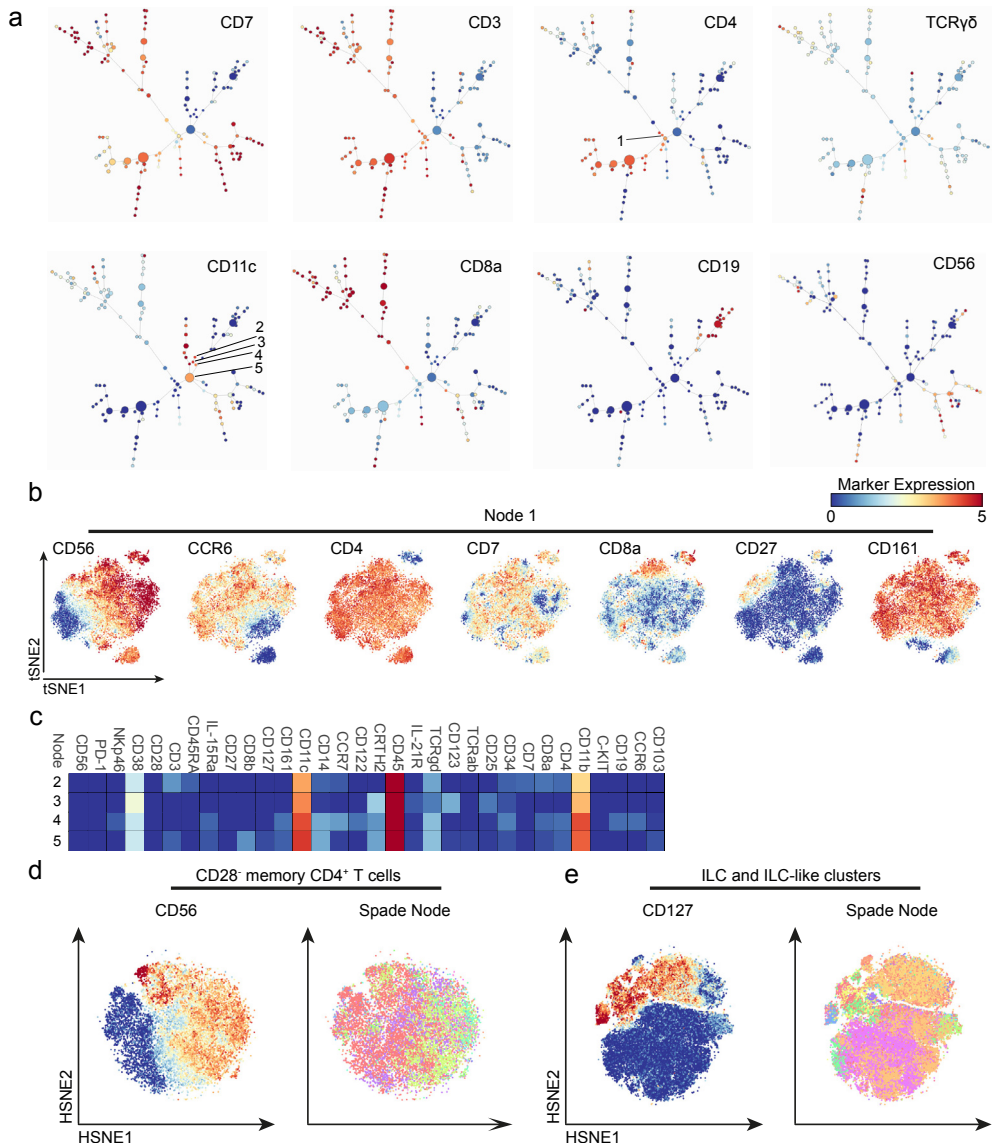


Supplementary Figure 8 Cytosplere^{+HSNE} analysis of the Vortex bone marrow dataset

(a) Cytosplere^{+HSNE} embeddings of the full 0.8 million cells of the Vortex mouse bone marrow dataset (2nd hierarchical level of 4 in total). Color coding indicates arcsin5-transformed marker expression. (b) Embedding as in panel a. Color coded for 50 clusters identified with Cytosplere^{+HSNE}. Shaded boxes show locations of hand-gated cell populations. (c) Embeddings of zoomed-in populations related to pDC development (3rd hierarchical level of 4 in total). The above shows a comparison with Figure 2 of the original study⁵.

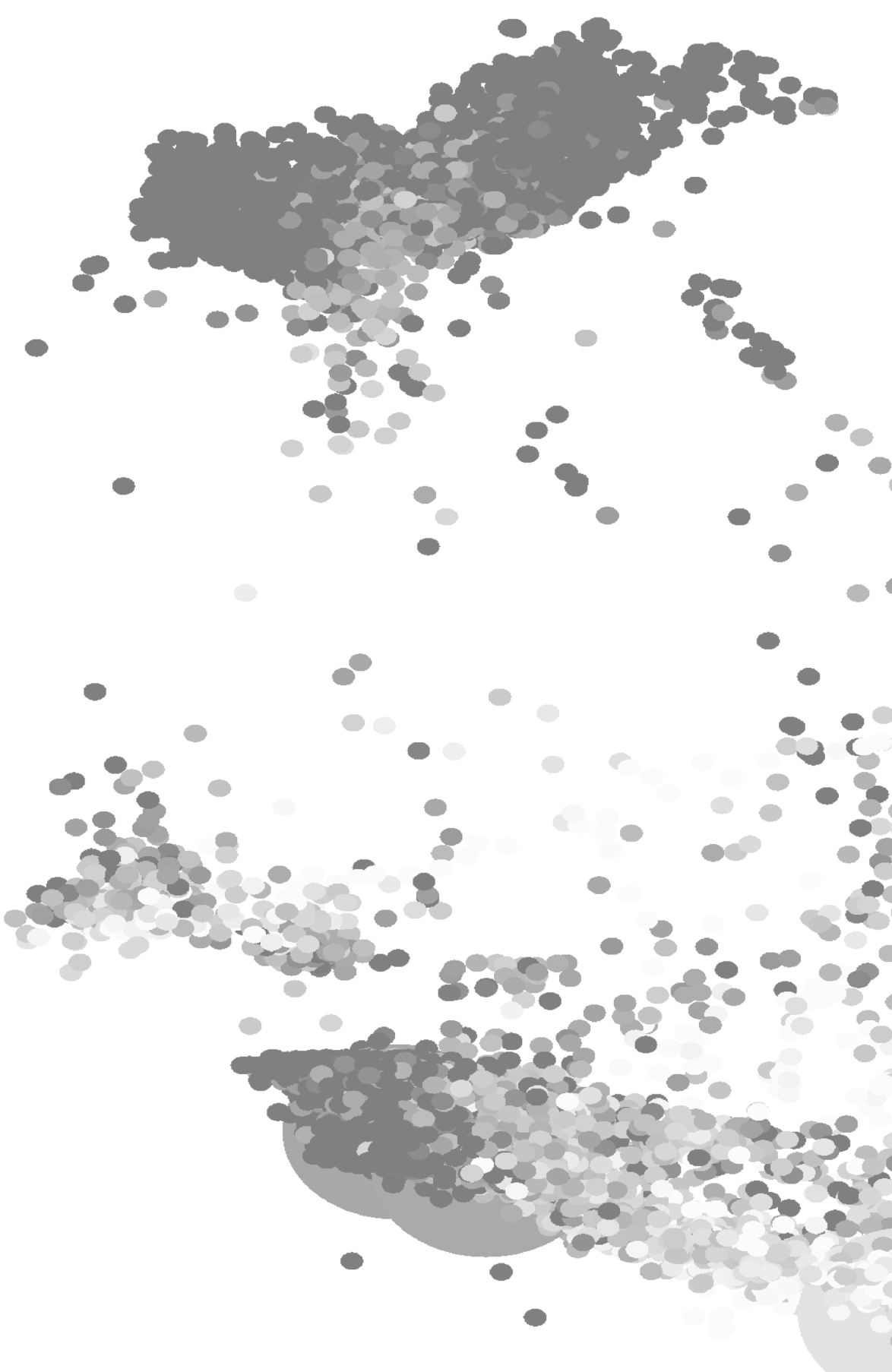
Visual Analysis of Mass Cytometry Data by Hierarchical Stochastic Neighbor Embedding Reveals Rare Cell Types

4



Supplementary Figure 9 SPADE analysis of the gastrointestinal dataset

The 5.2 million cell gastrointestinal dataset was analyzed by SPADE using 10% target events for density-based downsampling and 142 target nodes as settings. (a) SPADE tree colored with arcsin5-transformed marker expression as indicated. Size of the nodes represents cell size. Five nodes are indicated for further analysis. (b) t-SNE embedding of node 1 (panel a) at single-cell resolution. Color of cells as in panel a. (c) A heatmap summary of median expression values of cell markers expressed by nodes 2-5 (panel a). Coloring as in panel a. (d) HSNE data level of CD28⁺ memory CD4⁺ T cells after clustering with SPADE. Colors indicate marker expression (left) and SPADE node identity (right) (e) HSNE data level of ILC and ILC-like clusters after clustering with SPADE.



CHAPTER 5

Stratification of immune cell infiltrates in inflammatory bowel disease by high-dimensional mass cytometry



CHAPTER 5

Stratification of immune cell infiltrates in inflammatory bowel disease by high-dimensional mass cytometry

Vincent van Unen¹, Na Li¹, Tamin Abdelaal^{2,3}, Yvonne Kooy-Winkelaar¹, Laura F. Ouboter¹, Thomas Höllt^{3,4}, M. Luisa Mearin⁵, Anne M.C. Witte⁶, Cees Clemens⁶, Sunje Abraham⁶, Hankje C. Escher⁷, Boudewijn P.F. Lelieveldt^{8,9}, Andrea E. van der Meulen-de Jong¹⁰, Frits Koning¹.

¹Department of Immunohematology and Blood Transfusion, Leiden University Medical Center. ²Delft Bioinformatics Lab, Delft University of Technology. ³Leiden Computational Biology Center, Leiden University Medical Center. ⁴Computer Graphics and Visualization, Delft University of Technology. ⁵Department of Paediatrics, Leiden University Medical Center. ⁶Department of Gastroenterology, Alrijne Hospital. ⁷Department of Paediatric Gastroenterology, Erasmus University Medical Center. ⁸Pattern Recognition and Bioinformatics Group, Delft University of Technology. ⁹Department of LKEB Radiology, Leiden University Medical Center. ¹⁰Department of Gastroenterology, Leiden University Medical Center.

In preparation

ABSTRACT

Inflammatory bowel disease (IBD) is characterized by chronic inflammation of the intestine. Studies on individual immune lineages have shown alterations in the innate and adaptive intestinal immune system implicated in IBD. However, a comprehensive analysis of the cell composition in intestinal biopsies from IBD patients across all major immune lineages simultaneously was lacking. Here, we applied mass cytometry with a 36-antibody panel to the analysis of specimens along the intestinal tract paired with and/or without inflammation (N=118) and peripheral blood mononuclear cells (N=46) in non-diseased controls (N=15) and untreated, newly diagnosed IBD patients (N=23). Utilizing HSNE, we identified 309 distinct cell clusters from the collective intestinal dataset containing 3.4 million cells in a data-driven manner. We identified a large interindividual variation as compared to intraindividual variation in immune cell composition in the intestine. The CD4⁺ and CD8⁺ T cell adaptive compartment, and the TCR $\gamma\delta$, innate lymphoid cell and

myeloid cell innate compartment display alterations in composition with distinct cellular profiles in IBD-affected specimens compared with unaffected specimens from patients and controls. The integration of all lineages into an immune-system-wide analysis resulted in six types of intestinal samples based on respective cell compositions. Distribution of the samples demonstrated that infiltrate type 1, type 2 and type 3 were present in biopsies from both control and IBD patients, while infiltrate type 3, type 4 and type 5 were exclusively present in biopsies from patients. The stratification of immune cell infiltrates in the intestine sheds new light on the involvement of the immune system in IBD, an important step towards personalized and cost-effective patient care.

INTRODUCTION

Inflammatory bowel disease (IBD) is an expanding global health problem characterized by chronic, idiopathic inflammation of the intestine, where disruption of intestinal homeostasis is key. The incidence and prevalence of IBD are steadily rising worldwide¹ with nearly 1.4 million Americans and 2.2 million Europeans affected.²⁻³ IBD aetiology is multifactorial, and depends upon host's genetics, dysregulated immune responses and environmental triggers.⁴ The two main forms are Crohn's disease (Crohn) and ulcerative colitis (UC). In 10%-15% of cases, however, a clear assignment is not possible, a condition termed undeterminate colitis (IBD-U). In addition, perianal fistulas occur in 25% of Crohn cases and this is accompanied by multiple relapses and a poor prognosis.⁵ Endoscopic evaluation with gastro- or ileocolonoscopy is the gold standard to diagnose and monitor IBD, but is invasive, costly, and time-consuming. For unknown reasons the incidence of paediatric IBD is rising, and in comparison with adult onset IBD, paediatric onset tends to be more extensive and associated with severe exacerbations and worse prognosis.⁶ The treatment for IBD is usually lifelong pharmacotherapy including biologicals (anti-TNF) with an estimated cost 36,000 dollars per patient per year,⁷ yet remission is often difficult to maintain.⁸ Also, the clinical response to immune suppression-based therapies is variable and unpredictable.⁹ Consequently, thirty percent of patients undergo surgery within 5 years after diagnosis. This emphasizes, altogether, that there is a significant morbidity in many patients. Therefore, there is an urgent need for improved classification of IBD, biomarkers to predict response to treatment, and novel diagnostics and therapeutic approaches are highly desirable.

The immune characteristics of IBD involve abnormal responses by both the innate

and adaptive immune system. For example, it has been shown that IBD-associated chronic inflammation results from aberrant responses against the intestinal microbiota, by both innate dendritic cells¹⁰ and adaptive CD4⁺ T cells.^{11 12} While many more studies¹³ have investigated the role of the immune compartments in IBD, due to the scarcity of the available biopsy material it has been very challenging to delineate the role of all immune subsets simultaneously. High-dimensional mass cytometry (cytometry by time-of-flight, CyTOF) now offers a unique opportunity to gain such insight as it allows the analysis of many (>40) cellular markers simultaneously per single cell,¹⁴ providing an opportunity to analyze the mucosal immune system with unprecedented resolution. As such, we previously have applied mass cytometry on samples from a cohort of patients with inflammatory intestinal diseases.¹⁵ Here, we observed a high number of diverse immune cell types present in the intestine, with a large degree of both inter- and intraindividual variation specifically associated with Crohn,¹⁵ providing a basis for patient stratification. However, only a small number of IBD specimens were analysed in that study. Therefore, in the current study we applied mass cytometry to the analysis of the composition of immune cells in biopsies along the intestinal tract and paired peripheral blood mononuclear cell (PBMC) samples of patients with IBD and controls.

METHODS

Sample processing as described in Chapter 2 and data analysis using the computational tools we developed described in Chapter 3 and Chapter 4.

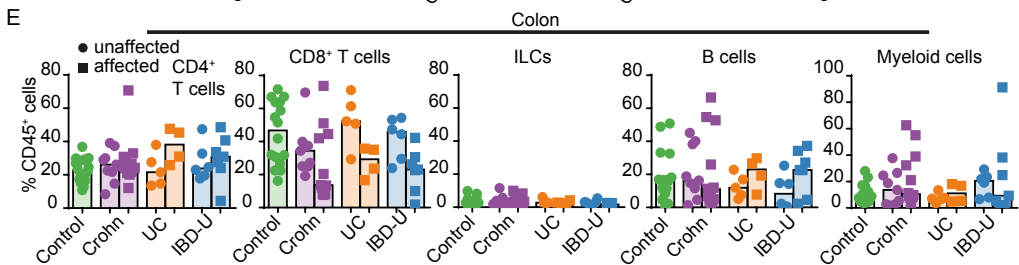
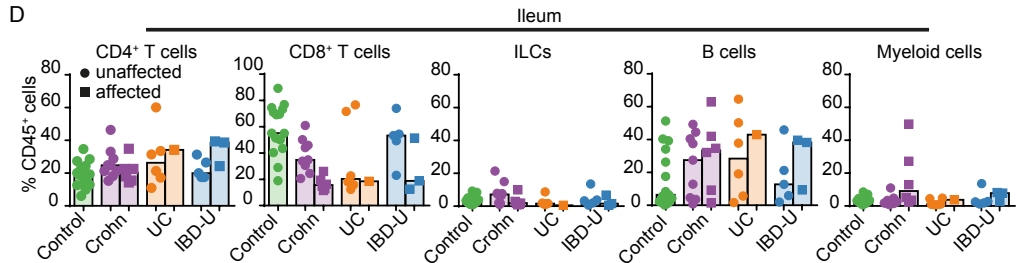
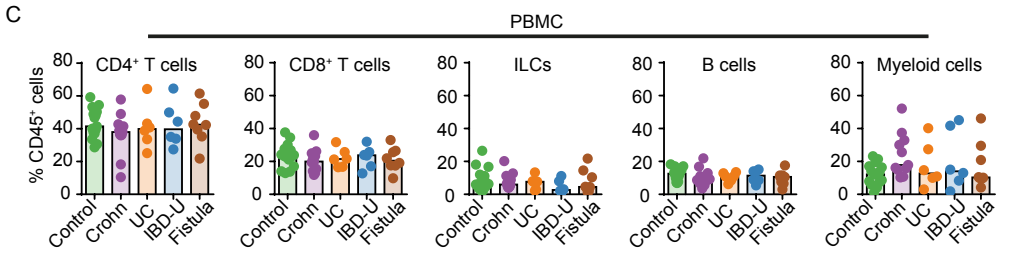
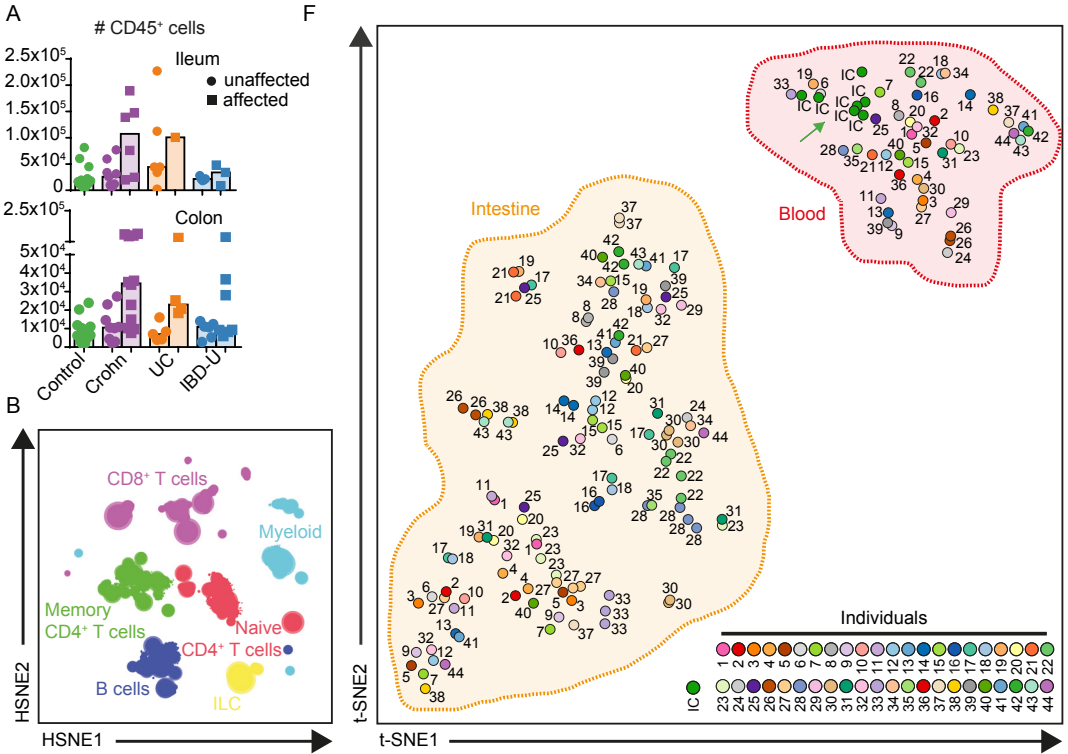
RESULTS

Identification of stable intraindividual immune profiles in the intestine

We designed a CyTOF panel of 36 metal isotope-tagged antibodies to obtain an overview of the heterogeneity of the innate and adaptive immune system (table S1). We incorporated markers that distinguished the six major immune lineages, different activation, maturation, and developmental stages, responsiveness to humoral and chemokine factors, and to separate naïve from memory cells. With this panel, single-cell suspensions derived from biological specimens were analysed including ileum biopsies (N=45), colon biopsies (N=59), rectum biopsies (N=14) and peripheral blood mononuclear cells (PBMC) from control individuals (N=15) and from IBD patients (Crohn, N=11; UC, N=6; IBD-U, N=6 and Fistula, N=6) (table S2). All samples (N=164) were taken in untreated condition with suspicion of IBD

diagnosis, except for the group of Fistula patients. They were previously diagnosed with Crohn and presented now with recurrent peri-anal fistulas of which we analysed the fistula-adjacent rectum biopsies. The control individuals were non-diseased and in complete absence of intestinal inflammation. In case of IBD diagnosis, according to the Montreal classification,^{19,20} biopsies were analysed from both a segment with active disease (affected; IBD-associated inflammation) and from an adjacent segment with endoscopic inactive disease (unaffected), next to two standard biopsies from the colon and terminal ileum. All antibodies displayed clear discrimination between antibody-positive and -negative cells (methods). Live, single, CD45⁺ immune cells were discriminated using DNA stains and the mass cytometry-parameter event length (**figure S1**). The mass cytometry dataset contained 5.5 million cells from the blood and 3.4 million from the intestine samples, respectively. We acquired 43,725 cells from the ileum and 20,266 cells from the colon samples on average (**figure 1A**), and 18,544 cells from the rectum and 118,910 cells from the PBMC samples (data not shown).

To facilitate the analysis of such a large data size, we utilized Hierarchical Stochastic Neighbour Embedding (HSNE),¹⁷ a computational approach that overcomes the scalability limits of t-SNE-type approaches, thus enabling the analysis of tens of millions of cells without the need for subsampling the data. The HSNE overview level depicted 7,468 landmark cells, representative data points, illustrating the global cellular heterogeneity of the entire dataset of 8.9 million cells (**figure 1B**). The landmark clustering patterns based on phenotypic similarity corresponded with the identification of the major immune lineages (**figure 1B**): CD4⁺ T cells (a memory and a naïve cluster), CD8⁺ T cells (including the TCR $\gamma\delta$ ⁺ lineage), innate lymphoid cells (ILC, here described as CD7⁺CD3⁻ cells, including CD127⁺ helper-ILCs and NK cells), B cells and myeloid cells. In general, the cell frequencies of these major cell lineages between PBMC samples from controls and patients were quite similar, although some variability in the number of CD4⁺ T cells and an increase in myeloid cells in several patient samples was detected (**figure 1C**). In contrast, the ileum and colon samples displayed substantial differences (**figure 1D,E**). For example, a high variation was present in the number of ileum CD8⁺ T cells among controls, but this was decreased in patient affected biopsies (**figure 1D**). Compared with controls, an increase in number of ileum and colon-derived B cells was observed in some patients, especially in Crohn. In addition, an increase in number of myeloid cells was observed in several patients and was most pronounced in the affected colon (**figure 1E**). Next, we clustered the cells into 343 global partitions using HSNE,



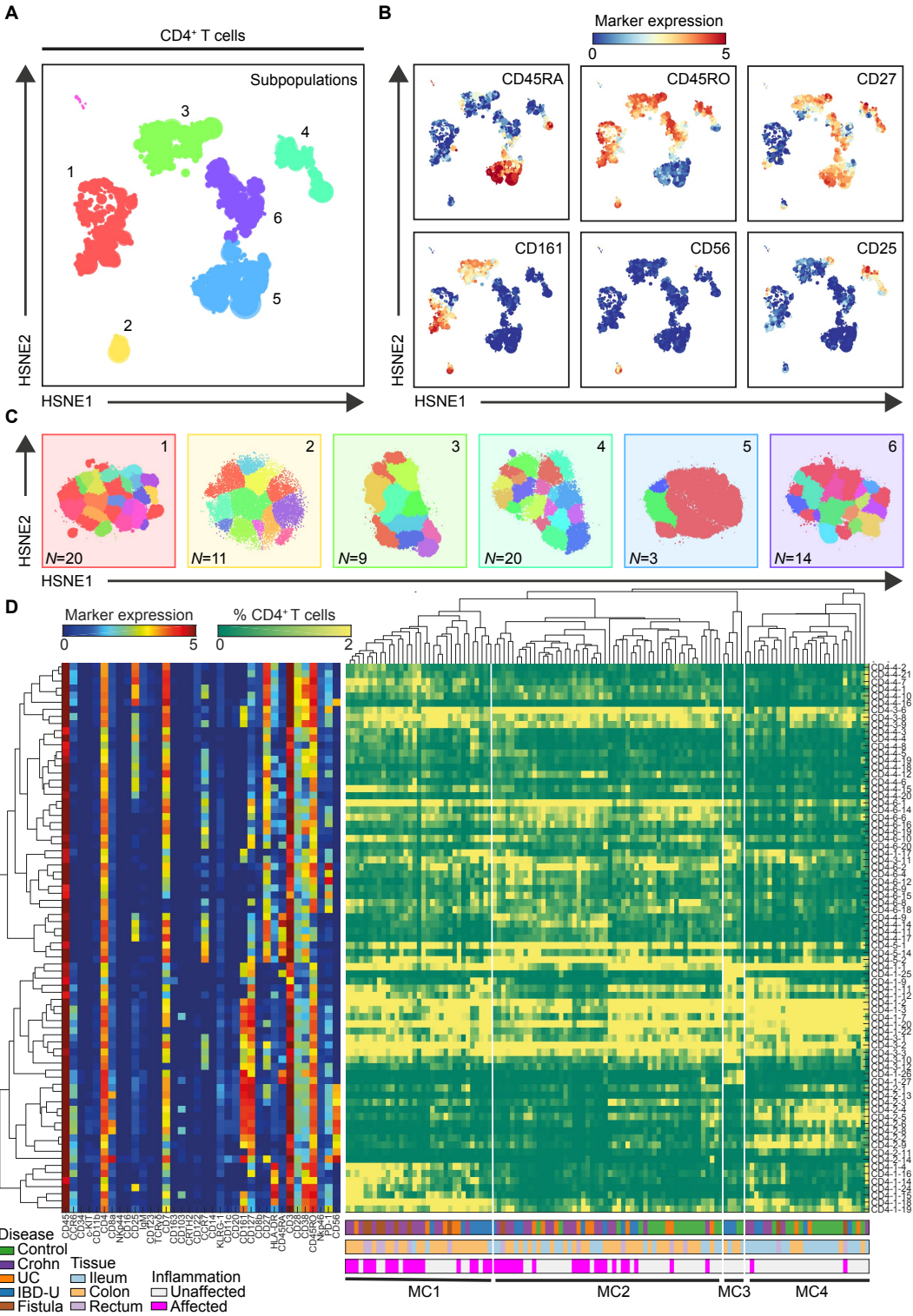
and visualized the immune compositions of these cell clusters from all included samples in a single graph by applying the t-SNE algorithm on cell frequency values. As expected, the PBMC and intestinal samples formed two distinct clusters (**figure 1F**), emphasizing the distinctness of immune phenotypes present in the peripheral blood and the intestine. To monitor the robustness of the measurements, we included a standardized PBMC sample as an internal control at seven intervals in the acquisition sessions during the entire 12-month study period, which all clustered together (**figure 1F**, green arrow), demonstrating the reproducibility of the data acquisition. When comparing the immune cell composition of intestinal biopsies from the same individual but at different intestinal location or inflammatory state, the large interindividual variation as compared to intraindividual variation was striking (**figure 1F**). In several cases, samples derived from the same individual clustered together suggestive of a unique immune ‘fingerprint’ along the intestinal tract (**figure 1F**).

Overall, there are large differences in major immune lineage composition between peripheral blood and intestinal samples, within and between intestinal samples from the different patient groups and controls, and there is a large amount of interindividual variation present.

Dissection of the major immune lineages into distinct cell populations

Because we observed in the global analysis that the immune cell compositions of the intestinal samples are highly distinct compared with blood (**figure 1F**), we next analysed those samples separately. To identify cell populations within the major immune lineages, we next zoomed-in on every lineage individually using HSNE. Here, we show the intestinal CD4⁺ T cell lineage that we selected at the HSNE overview level (**figure 1B**), and show the distribution of the landmarks at the second hierarchical level, revealing six large subpopulations within the CD4⁺ T cell compartment (**figure 2A**). These subpopulations could be distinguished based on differential expression patterns of several markers (**figure 2B**). For

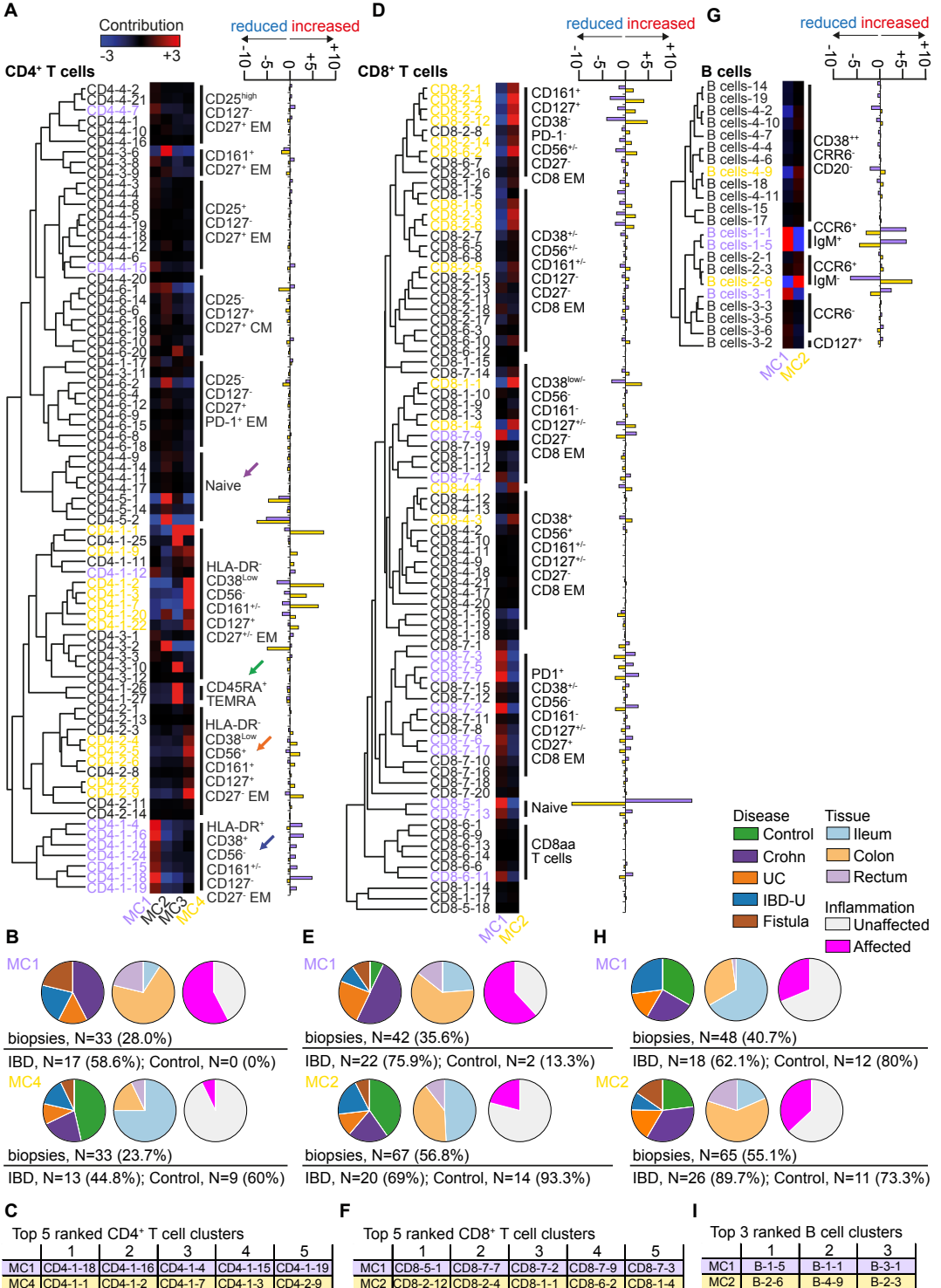
Fig. 1 HSNE analysis identifies major immune lineages in the peripheral blood and intestine (A) Live single CD45⁺ absolute cell number acquired for 45 ileum biopsies and 59 colon biopsies. **(B)** First HSNE level embedding of the collective 8.9 million cells. Color represents the major immune lineages, annotated on the basis of lineage marker expression. Comparisons of cellular frequencies for major immune lineages from **(C)** 46 PBMC samples, **(D)** 45 ileum biopsies and **(E)** 59 colon biopsies. **(F)** Collective t-SNE dimensionality-reduced cell percentage data (as percentage of CD45⁺ cells) of 343 cell clusters for 164 samples analyzed are plotted. Every dot represents a single sample and the color and number of the samples display the 44 individuals and the internal control (IC). The red dashed border represents the PBMC cluster and the orange dashed border represents the intestinal cluster.



example, subpopulation 1 expresses CD45RO while lacking the expression of CD45RA and CD27, indicative of a CD27⁻ memory phenotype. Subpopulations 2, 3 and 4 also displayed a memory phenotype (CD45RO⁺CD45RA⁻) and could be further distinguished by the expression of CD56, CD161 and CD25, respectively. In contrast, subpopulation 6 with a memory phenotype did not express those three markers. Subpopulation 5 represents naive T cells based on the expression of CD45RA and CD27 without expression of CD45RO. Next, we zoomed-in on every CD4⁺ T cell subpopulation individually using HSNE, and applied Gaussian mean-shift clustering which automatically identifies distinct cell clusters (**figure 2C**), where each cluster was defined by its unique marker expression profile (**figure 2D**, left panel in rainbow colour). In total, 77 distinct CD4⁺ T cell clusters were identified derived from all 118 intestinal samples included in the analysis. We next evaluated the samples quantitatively by analysing the cluster distribution of the CD4⁺ T cells by plotting the relative cell frequencies of the CD4⁺ T cell clusters for all intestinal samples analysed (**figure 2D**, right panel in green-to-yellow colour). Hierarchical clustering of the samples divided these into four metaclusters (MC) based on sample similarity in the composition of CD4⁺ T cells (**figure 2D**). Each MC had a mixed sample composition regarding clinical metadata, containing samples from different types of IBD patients or controls, intestinal segments and inflammation states (**figure 2D**, bottom three bars). Strikingly, MC1 was in complete absence of control samples, while MC4 was enriched for control and IBD-unaffected samples.

Thus, the HSNE analysis approach can effectively identify distinct cell populations in mass cytometry data in a data-driven manner, and the analysis reveals different types of CD4⁺ T cell compositions in the intestine associated with IBD.

Fig 2. The CD4⁺ T cell lineage dissected into distinct cell clusters (A) Second HSNE level embedding of the collective intestinal CD4⁺ T cells (1.0×10^6 cells). Color represents six major subpopulations. (B) HSNE embedding as in panel A, colored for arcsinh5-transformed expression of indicated markers. (C) Fourth HSNE level embedding of the CD4⁺ T cell subpopulations #1, #3, #4, #5 and #6, and fifth HSNE level embedding of subpopulation #2. Transparent square colors represent six subpopulations as in panel A and cell colors represent cell clusters (N=77). (D) Heatmaps showing characterization of cell clusters (left panel, median ArcSinh5-transformed values of marker expression; rainbow scale), cell cluster composition of samples (right panel, cell percentages; green-to-yellow scale), sample clinical metadata (bottom panel; disease, tissue and inflammation state) and hierarchical clustering of marker expression profiles and samples. Annotation of cell clusters represents their phenotypic hierarchy identified with HSNE. White lines indicate four metaclusters of samples based on cell cluster composition.



Intestinal CD4⁺ and CD8⁺T cell compositions are altered in inflammatory bowel disease

Next we asked which of the CD4⁺ T cell clusters were most differentially present in the four types of compositions by calculating for each cell cluster their contribution to the grouping of samples (**figure 3A**, blue-to-red colour). For example, MC1 was characterized by the specific presence of CD4⁺ effector memory (EM; CD45RA⁻CD45RO⁺CCR7⁻) T cells with an activated phenotype based on high expression of HLA-DR and CD38 while lacking CD27 and CD127 (**figure 3A**, blue arrow), MC2 by increased numbers of naive CD4⁺T cells (**figure 3A**, purple arrow) among others, MC3 by the specific presence of CD45RA⁺ terminally differentiated (TEMRA) cells (**figure 3A**, green arrow), and MC4 by the specific presence of NK-like CD56⁺ CD4⁺ T cells (**figure 3A**, orange arrow). Regarding clinical metadata, MC2 showed an intermixed sample composition and MC3 contained only few samples (**figure 2D**). However, MC1 contained samples from 17 out of 29 IBD patients without any controls (**figure 3B**). The majority of these was derived from the colon (69.7%) and more from affected segments (57.6%). In contrast, MC4 consisted almost entirely (92.9%) of unaffected biopsies from both patients and controls with a majority (75%) derived from the ileum. Therefore, we visualized the exact contribution values of the cell clusters associated with MC1 and MC4 in an additional graph (**figure 3A**, purple and yellow bars). The top 5 ranked CD4⁺ T cell clusters contributing to the sample clustering patterns of MC1 indeed shows that all these corresponded to the activated HLA-DR⁺CD38⁺ cell population (**figure 3A,C**), displaying additional diversity in the expression of CD25, CD161 and PD-1 (**figure 2D**). Next to the specific presence of innate NK-like CD56⁺ CD4⁺ T cells in MC4 (cluster CD4-2-9), the most upregulated cell clusters in this sample group were CD4⁺ EM T cells with low expression of CD38 and lacking HLA-DR (**figure 3A,C**). These findings suggest that the CD4⁺ T cell compartment is altered in a subgroup of IBD patients, where activated HLA-DR⁺CD38⁺ CD4⁺ T cells are upregulated (**figure 3A-C**, in purple) while innate NK-like CD56⁺ CD4⁺T cells are downregulated (**figure 3A-C**, in yellow).

Fig 3. The adaptive immune system is skewed in the IBD-affected intestine (A) Heatmap showing contributions of CD4⁺ T cell clusters in grouping of samples into four metaclusters and hierarchical clustering of marker expression profiles as in Figure 2D. Bar graphs showing contributions of CD4⁺ T cell clusters in grouping of samples into metacluster 1 in purple and metacluster 4 in yellow, and cell cluster labels contributing greater than value 1 are colored similarly. (B) Pie charts depicting clinical metadata for sample metacluster 1 (top panel) and metacluster 4 (bottom panel) (C) Table showing top five ranked CD4⁺ T cell clusters contributing to sample clustering into metacluster 1 and metacluster 4 (as shown in A). Similar visualizations for (D-F) CD8⁺ T cells and (G-I) B cells

Similarly, we identified 79 distinct cell clusters in the intestinal CD8⁺ T cell compartment and here the samples clustered into two large groups (**figure 3D** and **figure S2**). MCI samples were to a large extent clustered together due to the contribution of high numbers of naive CD8⁺ T cells (**figure 3D**, cluster CD8-5-1), and these were, surprisingly, in particular derived from IBD patients (**figure 3E**). In contrast, three other of the most MCI-contributing CD8⁺ T cell clusters (**figure 3D-F**, cluster CD8-7-7, -7-2 and -7-3) displayed an activated EM phenotype based on expression of PD-1. Conversely, MC2 samples displayed an upregulation of CD161⁺CD127⁺ CD8⁺ EMT cells with and without CD56 expression, but lacking PD-1, which were more (79.9%) derived from biopsies of patients and controls without inflammation (**figure 3D-F**).

Only 22 B cell clusters were identified (**figure S3**) due to the relative few B cell markers implemented in the antibody panel, and the samples clustered into two groups. This clustering was mainly attributed to differential expression of IgM in CCR6-expressing B cells, where IgM⁻ cells are suggestive of B cell isotype switching (**figure 3G**). However, there was no difference between patients and controls, tissue segments or inflammation states for the different frequencies observed within the B cell compartment (**figure 3G-I**).

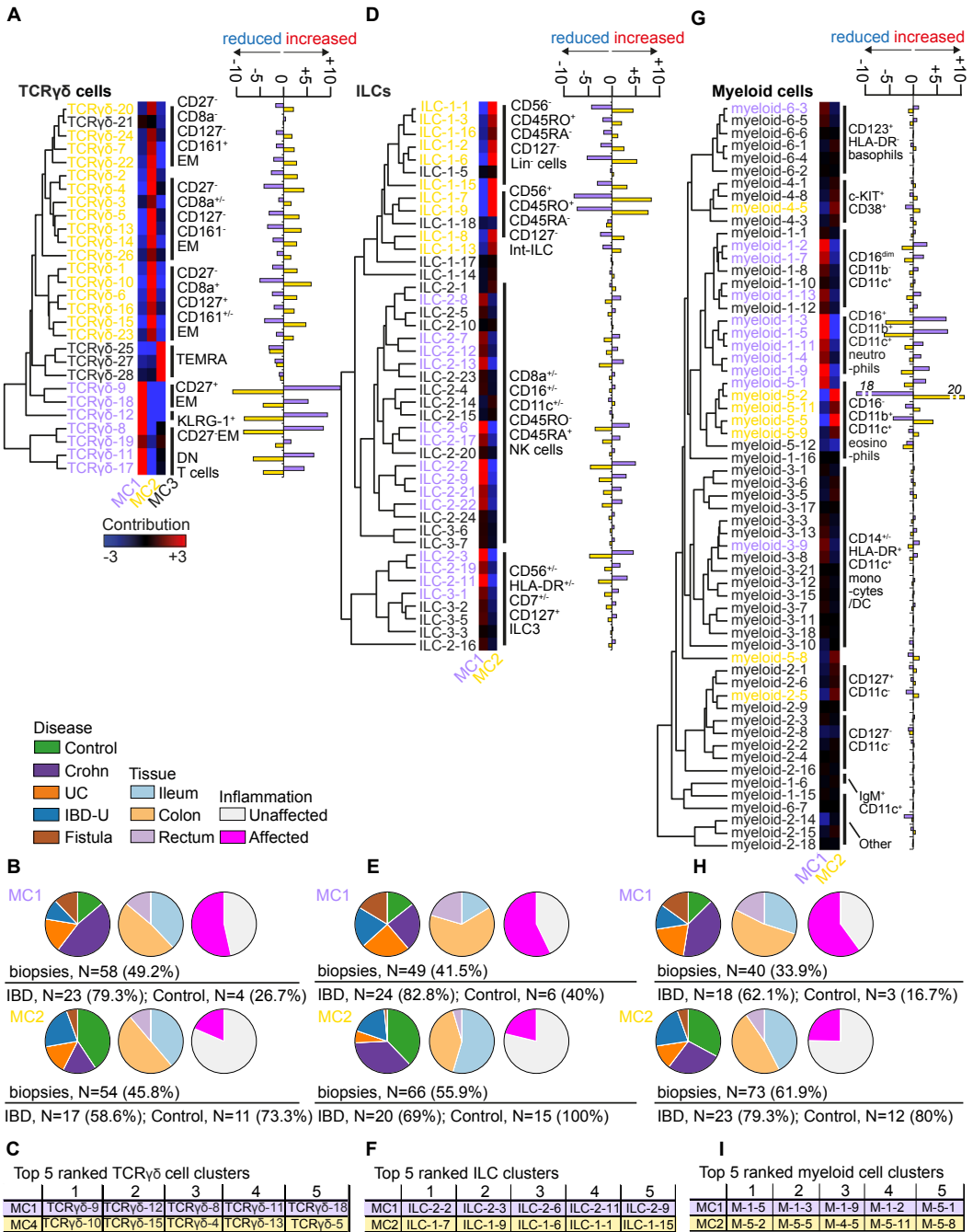
Thus, the CD4⁺ and CD8⁺ T cell adaptive immune compartment display a shift in phenotypic composition with distinct cellular profiles in IBD-affected specimens compared with unaffected specimens from both patients and controls.

The intestinal innate immune system is altered in inflammatory bowel disease

Next we assessed whether the innate immune system was also altered in IBD by analysing those cell clusters in more detail. We identified 28 distinct TCR $\gamma\delta$ cell clusters and hierarchical clustering of the samples resulted in three MCs (**figure 4A** and **figure S4**). MC3 contained only 6 samples and was characterized by

Fig 4. The innate immune system is skewed in the IBD-affected intestine (A) Heatmap showing contributions TCR $\gamma\delta$ cell clusters in grouping of samples into three metaclusters and hierarchical clustering of marker expression profile as in Figure S4. Bar graphs showing contribution of TCR $\gamma\delta$ cell clusters in grouping of samples into metacluster 1 in purple and metacluster 2 in yellow, and cell cluster labels contributing greater than value 1 are colored similarly. (B) Pie charts depicting clinical metadata for sample metacluster 1 (top panel) and metacluster 2 (bottom panel) (C) Table showing top five ranked TCR $\gamma\delta$ cell clusters contributing to sample clustering into metacluster 1 and metacluster 2 (as shown in A). Similar visualizations for (D-F) ILCs and (G-I) myeloid cells.

Stratification of immune cell infiltrates in inflammatory bowel disease by high-dimensional mass cytometry



upregulated numbers of TCR $\gamma\delta$ TEMRA cells. The remaining 112 samples fell either into MC1 or MC2, which was largely determined by differential presence of CD27⁺ and CD27⁻ TCR $\gamma\delta$ EM cell clusters, respectively (**figure 4A,C**) Of note, four

clusters corresponded with double-negative (DN) T cells based on the absence of CD4, CD8a and TCR $\gamma\delta$ expression yet clustered together with the TCR $\gamma\delta$ cell lineage in the HSNE analysis (**figure S4**), and these were also upregulated in MCI samples. Ranked second in contributing to MCI was the presence of a KLRG-1+ TCR $\gamma\delta$ cluster (**figure 4C**). Here we observed that MCI contained relatively more samples from IBD patients, while MC2 contained more samples from unaffected segments of patients and controls (**figure 4B**) suggesting a skewed TCR $\gamma\delta$ profile.

Despite their rare occurrence (**figure 1D,E**), we could distinguish 44 cell clusters within the ILC compartment (**figure S5**). These could be categorized into the well-described CD45RA⁺ NK cell and ILC3 populations, but also into the recently described Lin⁻CD56⁻CD127⁻ cell (Lin-ILC) and CD56⁺CD127⁻CD45RO⁺CD45RA⁻ intermediate ILC (int-ILC) populations. Lin⁻ ILCs represent innate type of lymphocytes with dual T cell precursor and NK/ILC traits,^{21 22 23 24} while int-ILCs represent an intermediate cell population that can differentiate into NK cells and ILC3.¹⁶ Hierarchical clustering of the samples resulted into two MC groups (**figure 4D** and **figure S5**). MCI profile was characterized by upregulated NK cell clusters expressing variable levels of CD8a, CD16, CD161 and CD11c, together with upregulated ILC3 clusters expressing variable levels of CD56, HLA-DR and NKp44 (**figure 4D,F**). In contrast, MC2 was characterized by upregulated Lin⁻ ILCs and int-ILCs with variable expression of CD161 (**figure 4D,F**). Here, MCI contained more samples from IBD patients with a majority (63.3%) derived from the colon, while MC2 contained more unaffected specimens with a majority (54.6%) derived from the ileum (**figure 4E**). These results suggest that there is a shift in balance of precursor/intermediate ILC populations (Lin⁻ ILC and int-ILC) relative to effector ILC populations (NK cells and ILC3) in unaffected compared with affected IBD and in the colon compared with the ileum.

Finally, we investigated the cellular composition of the myeloid cell lineage and identified 60 distinct clusters (**figure S6**). We could not directly phenotype cells as granulocytes due to the absence of the granulocyte-specific markers CD15 and CD66 in the antibody panel. However, we imputed cell clusters as CD15-expressing neutrophils indirectly by their expression of CD16, CD11b, CD11c, CD45RO, while lacking CD14 and HLA-DR, based on additional experiments we performed using a CD15 antibody (data not shown). The cytometry surface phenotype of eosinophils is similar to neutrophils but lacks the expression of CD16,^{25 26} which corresponded with several clusters we identified. In addition, we distinguished basophils based on CD123 expression and the lack of HLA-DR.²⁷ Moreover, we identified several

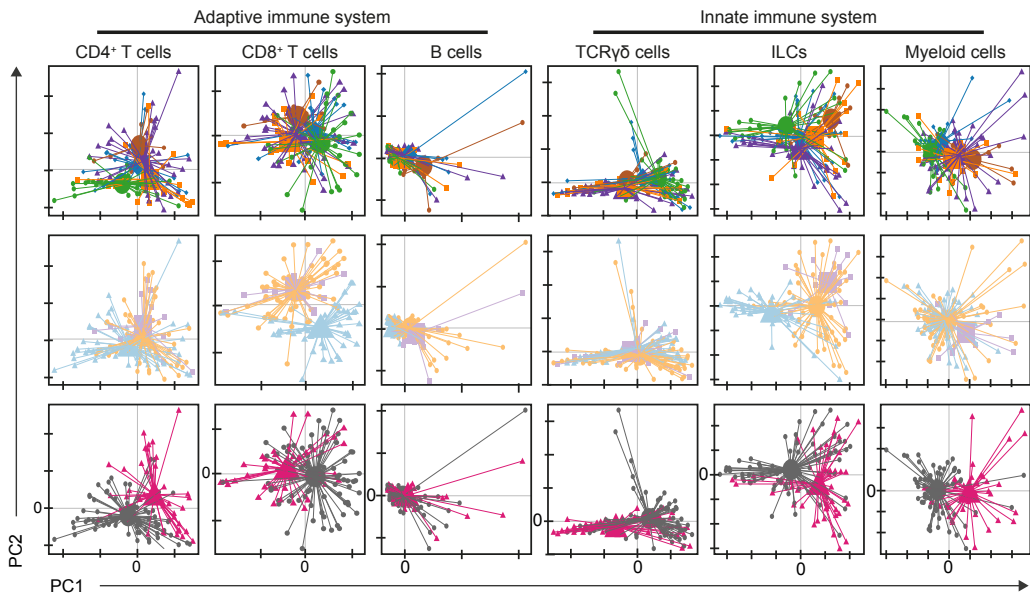
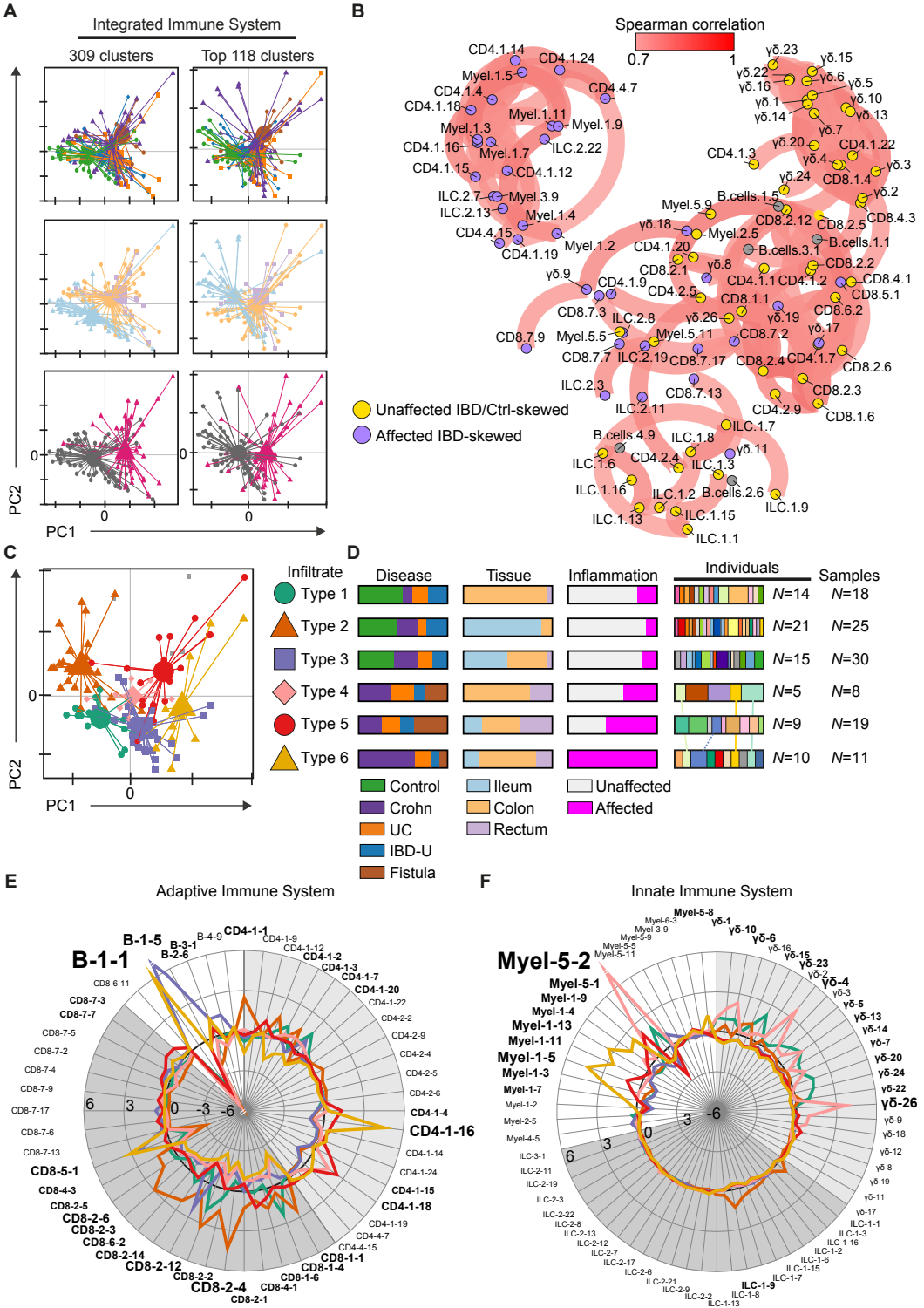


Fig 5. PCA reveals distinct clustering of IBD-affected samples stratified per immune lineage. Collective PCA dimensionality-reduced cell percentage data (as percentage of major immune lineage) of 77 CD4⁺ T cell clusters, 79 CD8⁺ T cell clusters, 22 B cell clusters, 28 TCRγδ cell clusters, 43 ILC clusters and 60 myeloid cell clusters for 118 intestinal samples analyzed are plotted. Every dot represents a single sample and colors show disease (top panel; green, control; purple, Crohn; orange, UC; blue, IBD-U and brown, Fistula), tissue (middle panel; light blue, Ileum; light orange, Colon and light purple, Rectum) and inflammation state (bottom panel; grey, Unaffected and pink, Affected). Lines connect samples to the centroid of each group.

CD14⁺ monocyte and CD14⁻ dendritic cell (DC) populations expressing high levels of HLA-DR and CD11c. Based on the hierarchical clustering of the samples we could distinguish 2 MC groups, of which the granulocyte compartment was contributing most to this separation (**figure 4G,I**). Specifically, CD16⁺ neutrophil-like cells were upregulated in MC1 and CD16⁻ eosinophil-like cells in MC2. Of note, a few cell clusters negative for CD11c expression clustered together with the CD11c⁺ myeloid lineage in the HSNE analysis, but these did not contribute to differential clustering of the samples. We observed again that MC1 contained more samples from IBD patients with a majority (60.0%) from affected segments, while MC2 contained samples with a majority (75.3%) from unaffected segments of patients and controls (**figure 4H**). This suggests that different populations of granulocytes are implicated in IBD.

To further substantiate these findings on alterations in the cellular compositions within the major immune lineages associated with affected IBD, we next performed a complimentary analysis approach by applying principal component analysis (PCA)



on the collective 118 intestinal samples analysed (**figure 5**). Except for the B cells, all lineages displayed a minor shift when comparing the clustering of control samples with patient samples (**figure 5**, top row). The samples from the different subgroups of IBD (Crohn, UC, IBD-U and Fistula) were, however, mostly intermixed consistent with the hierarchical clustering results (**figures 3 and 4**), suggesting similarities in immune profile. The PCA also revealed the differences between samples from the colon and the ileum (**figure 5**, middle row), which was most pronounced for the CD8⁺ T cells and ILCs. The latter also separated the rectum from the colon samples in addition, revealing specific ILC compositions along the intestinal tract. However, except for B cells, most of the variation per major immune lineage in the intestine was captured by the differences between cells from the IBD affected specimens compared to unaffected specimens of patients and controls (**figure 5**, bottom row).

Integrated immune system analysis in inflammatory bowel disease

Next, we integrated all the individual major lineages into a collective immune-system-wide analysis, by first applying PCA on the cell frequency values of all 309 identified immune clusters from all intestine samples in a single graph (**figure 6A**, left panel). These results show that controls clustered separate from patients, ileum samples separate from colon and rectum samples, and most strikingly was the separation of affected segments compared to unaffected segments. When we applied the PCA only on the 118 immune clusters that were differentially abundant in groups of samples by greater than 1 percent (marked purple and yellow in **figure 3 and 4**) we obtained similar results (**figure 6A**, right panel). Next we performed a correlation network analysis on the 118 cell clusters showing that

Fig. 6. Integrated immune system analysis identifies differential disease-associated immune infiltrate types. (A) Collective PCA dimensionality-reduced cell percentage data (as percentage of CD45⁺ cells) of (left panel) 309 cell clusters and (right panel) 118 top ranked cell clusters for 118 intestinal samples analyzed are plotted. Every dot represents a single sample and colors show the disease, tissue and inflammation state. Lines connect samples to the centroid of each sample group. (B) Network representation of correlations (Spearman's Rho) greater than coefficient value of 0.7 between 118 top ranked cell clusters. Every dot represents an immune cell cluster, colored for contributing to clustering of samples into metaclusters associated with unaffected-IBD and controls in yellow or with affected-IBD in purple as shown in Figures 3 and 4. The closer the cell clusters are together, the higher the correlation. Color shade and thickness of the line indicate the strength of the correlation. (C) PCA representation as in panel A, colored for six types of samples grouped by hierarchical clustering based on cell percentages of 118 top ranked cell clusters for 118 intestinal samples analyzed. (D) Pie charts of samples grouped into six types showing clinical metadata of disease, tissue, inflammation state, and individuals. (E) Radial graph depicting contributions of top 52 adaptive immune cell clusters in hierarchical grouping of samples into six metaclusters shown in panel C. Colored lines indicate the six types of samples. The peaks of lines and font size of cell cluster labels indicate the level of contribution. (F) Radial graph as in panel E depicting contributions of top 66 innate immune cell clusters.

85 clusters were strongly (spearman rank > 0.7) correlated (**figure 6B**). For example, a group of CD4⁺ T cell clusters, ILC clusters and myeloid cell clusters were correlated with each other (**figure 6B**, top-left network) and upregulated in affected segments of patients as assessed before (**figures 3 and 4**), while a group of TCR $\gamma\delta$ cell clusters, CD4⁺ and CD8⁺ T cell clusters (**figure 6B**, top-right network) and a group of ILC clusters (**figure 6B**, bottom network) were correlated with each other and upregulated in unaffected segments of patients and controls.

Hierarchical clustering of the samples based on the cell cluster frequencies of the integrated immune system resulted in six groups for 111 out of 118 samples (**figure 6C**), suggestive of different types of immune infiltrates across all major immune lineages. When we analysed the distribution of samples containing these different immune infiltrate types we observed that infiltrate type 1, type 2 and type 3 were present in biopsies from both control and IBD patients, while infiltrate type 3, type 4 and type 5 were exclusively present in biopsies from patients (**figure 6D**). In addition, infiltrate type 1 was strongly associated with an unaffected colon profile and infiltrate type 2 with an unaffected ileum profile, shared among many patients and controls. Infiltrate 3, however, represented a mixture of both unaffected colon and unaffected ileum samples. The IBD-associated type 4, type 5 and type 6 infiltrates were found in an increasingly abundance of affected specimens, respectively. All immune infiltrate types were present in more samples than unique individuals, suggesting that several biopsies were derived from the same individual emphasizing the unique individual fingerprint we identified before (**Figure 1F**). Immune infiltrate type 4 was identified in biopsies from 5 individuals, of which 3 also had a parallel biopsy containing infiltrate type 6 (**figure 6D**). Except for one, the IBD-associated immune infiltrates type 5 and type 6 were present in biopsies from different sets of IBD patients. Therefore, we looked at their clinical metadata in more detail. Notably, the median age at diagnosis for the patients with immune infiltrate type 5 was 28 years old and did not contain any paediatric patients, while that for patients with immune infiltrate type 6 was 18 years old and 5 out of 10 were paediatric patients (**figure S7**), suggesting that the affected intestine of paediatric patients may more frequently present with a type 6 immune infiltrate.

Finally, we analysed what combinations of immune cell clusters across all major lineages predominantly distinguished these six types of immune infiltrates by visualizing the contribution of each cell cluster to the clustering of samples in a graph (**figure 6E,F**). For example, the unaffected colon-associated infiltrate type 1

was characterized by the combinatorial presence of adaptive CD8⁺ T cell CD27⁻ EM (#1-4), CD161⁺CD127⁺ EM (#2-12) clusters and a CD4⁺ T cell HLA-DR⁻CD38^{low} EM (#1-20) cluster, together with the innate TCR $\gamma\delta$ cell CD27⁻ EM (#23, #13 and #20) clusters and a myeloid cell CD16⁻ eosinophil-like (#5-2) cluster. The unaffected ileum-associated infiltrate type 2 was defined by many adaptive CD8⁺ T cell CD27⁻ EM (#2-4, #2-12, #2-6, #2-3, #1-1, #6-2, #2-2 and #1-6) clusters displaying a variable expression for CD161, CD127 and CD56, together with CD4⁺ T cell HLA-DR⁻CD38^{low} EM (#1-1, 1-2 and 1-7) clusters. In addition, the innate int-ILC (#1-9) cluster was specifically present in the unaffected ileum-associated infiltrate type 2. Both the unaffected colon and ileum-associated immune infiltrate types 1 and 2 were showing an underrepresentation of the B cell IgM⁺CCR6⁺ (#1-5 and #1-1) clusters and a CD8⁺ T cell naïve (#5-1) cluster. In contrast, the unaffected intermixed colon-ileum infiltrate type 3 was characterized by the abundant presence of these latter cell cluster.

The IBD-associated infiltrate type 4 found in relatively more unaffected specimens was characterized by high numbers of innate CD16⁻ eosinophil-like (#5-2 and #5-1) clusters and TCR $\gamma\delta$ CD27⁻ EM (#26, #4, #6, #10 and #13) clusters, together with the adaptive CD161⁺ activated CD4⁺ T cell HLA-DR⁺CD38⁺ EM (#1-18) cluster, without the B cell IgM⁺CCR6⁺ (#1-5 and #1-1) clusters. The IBD-associated infiltrate type 5 found in relatively more affected specimens was characterized by the presence of several CD161⁺ and CD161⁻ activated CD4⁺ T cell HLA-DR⁺CD38⁺ EM (#1-18, #1-4 and #1-15) clusters and a CD56⁺ NK-like CD8⁺ T cell EM (4-1) cluster, together with both an innate CD16⁻ eosinophil-like (#5-1) cluster and a CD16⁺ neutrophil-like (#1-5) cluster, also with a downregulated B cell IgM⁺CCR6⁺ (#1-5) cluster. In contrast, the IBD-associated infiltrate type 6 found in only affected specimens was characterized by the highly abundant adaptive B cell IgM⁺CCR6⁺ (#1-1) cluster, the CD161⁻ activated CD4⁺ T cell HLA-DR⁺CD38⁺ EM (#1-16) cluster and the CD8⁺ T cell naïve (#5-1) cluster, while several CD8⁺ T cell CD161⁺CD127⁺ EM clusters (#2-12, #2-4 and #2-14) and a CD8⁺ T cell CD161⁻CD127⁺ EM (#1-1) cluster were downregulated. Of the innate immune system, not CD16⁻ eosinophil-like, but many CD16⁺ neutrophil-like cell (#1-5, #1-13, #1-11, #1-3, #1-9 and #1-4) clusters were implicated in addition to infiltrate type 6. Taken together, we could divide the intestinal immune infiltrates into six types characterized by different complex combinations of both adaptive and innate immune cell populations, which were associated with the location of the intestine and IBD-related inflammation.

DISCUSSION

Mass cytometry has proven to be a powerful tool for dissecting the cellular immune landscape in many studies²⁸. Here, we choose a mass cytometry approach with a broad coverage by analysing across all major immune lineages simultaneously to obtain an unbiased view of the role of immune cell subsets in tissue-specific inflammatory immune responses in IBD. For this we applied mass cytometry to the analysis of a variety of intestinal samples, from both inflamed and uninfamed intestinal locations, and peripheral blood samples of IBD patients and non-diseased controls. Mass cytometry data analysis is challenging due to its complexity in high-dimensionality and data size. Therefore, we utilized HSNE¹⁷, allowing unsupervised learning to identify phenotypically distinct cell clusters in datasets exceeding millions of cells in a t-SNE-based manner without the need for downsampling, a well-suited approach for the collective 8.9 million immune cells acquired in this cohort study.

Most of the observed variation in immune cell compositions between samples was explained by differences between immune cells from the blood as compared to the intestine, in line with a previous study¹⁵ and emphasizing the distinctness between these anatomical compartments. Next, the large interindividual variation as compared to intraindividual variation was striking, when comparing the immune cell composition of intestinal biopsies from the same individual but at different intestinal location. In several cases, samples derived from the same individual clustered together. Indeed, cell compositions and other immune markers have been described to be different between individuals in several reports investigating peripheral blood^{15 29 30 31 32}. In agreement, our results confirm the presence of a unique individual 'fingerprint' in immune cell composition in the periphery. In addition, we have provided evidence that the collective immune cell composition in the intestine is also individual-specific, emphasizing the need for personalized medicine. In addition, we could distinguish similarities among IBD-affected samples and among unaffected specimens of patients and controls for all individual immune lineages analysed, except for B cells. In addition, there was both an ileum-associated profile and a colon-associated profile detectable in immune cell composition, most pronounced for CD8⁺ T cells and ILCs.

Surprisingly, there was no separation of samples from Crohn's patients and samples from UC patients based on immune cell composition, as they were intermixed in every analysis performed. A recent study characterizing the enhancer and promotor

landscape of colon biopsies found that the IBD-specific transcription start sites are associated to genes with roles in both inflammatory cascades and gut epithelia while transcription start sites distinguishing UC and Crohn are associated to gut epithelial functions³³. This may suggest that the IBD-associated immune profiles described in the present study may not distinguish UC from Crohn, but rather, that the clinical phenotype of these diseases may be based on immune-unrelated aspects, such as characteristics of the gut epithelium.

The integrated analysis of the immune system revealed six types of immune infiltrates in the intestine, each defined by a specific combination of innate and adaptive immune cell clusters. Three infiltrate types were associated with an unaffected-IBD and control profile, of which two were mostly represented by either colon samples or ileum samples. The other three infiltrate types were specifically associated with IBD, where type 4 to type 5 to type 6 coincided with increasingly more abundance of inflamed samples. Here we have profiled immune cells within biopsies taken in the intestine of admitted IBD patients and controls. Such biopsies are identical to biopsies used in current diagnosis methods. This has the advantage that samples are highly clinically relevant, and that the changes in immune compositions in the disease states measured will be close to the *in vivo* reality. The six infiltrate types we identified may in the future provide a foundation for patient stratification based on immune profile at time of diagnosis. It would be interesting to determine in follow-up studies whether these different immune infiltrate types may correspond with a different severity of disease course, treatability or time-to-relapse.

By having characterized the similarities and differences between the intestinal immune system's cellular composition of patients and controls in a system-wide approach, it will allow the rational design of studies to gain mechanistic insight into how the distinct cellular components of the immune system interact in IBD pathology. This may provide insight crucial to the development of personalized medicine, rather than a one-size-fits-all remedy. In order to develop new approaches to manipulate the immune system in IBD pathology and treat or cure the disease, the next step must be to obtain an understanding of the origin of the stratifying intestinal immune signatures.

REFERENCES

1. M'Koma AE. Inflammatory bowel disease: an expanding global health problem. *Clin Med Insights Gastroenterol* 2013;6:33-47.
2. Loftus EV, Jr. Clinical epidemiology of inflammatory bowel disease: Incidence, prevalence, and environmental influences. *Gastroenterology* 2004;126(6):1504-17.
3. Matricon J. [Immunopathogenesis of inflammatory bowel disease]. *Med Sci (Paris)* 2010;26(4):405-10.
4. Danese S, Fiocchi C. Etiopathogenesis of inflammatory bowel diseases. *World J Gastroenterol* 2006;12(30):4807-12.
5. Molendijk I, Nuij VJ, van der Meulen-de Jong AE, et al. Disappointing durable remission rates in complex Crohn's disease fistula. *Inflamm Bowel Dis* 2014;20(11):2022-8.
6. Griffiths AM. Specificities of inflammatory bowel disease in childhood. *Best Pract Res Clin Gastroenterol* 2004;18(3):509-23.
7. Yu H, Maclsaac D, Wong JJ, et al. Market share and costs of biologic therapies for inflammatory bowel disease in the USA. *Aliment Pharmacol Ther* 2018;47(3):364-70.
8. Randall CW, Vizueté JA, Martínez N, et al. From historical perspectives to modern therapy: a review of current and future biological treatments for Crohn's disease. *Therap Adv Gastroenterol* 2015;8(3):143-59.
9. Sales-Campos H, Basso PJ, Alves VB, et al. Classical and recent advances in the treatment of inflammatory bowel diseases. *Braz J Med Biol Res* 2015;48(2):96-107.
10. Hart AL, Al-Hassi HO, Rigby RJ, et al. Characteristics of intestinal dendritic cells in inflammatory bowel diseases. *Gastroenterology* 2005;129(1):50-65.
11. Shale M, Schiering C, Powrie F. CD4(+) T-cell subsets in intestinal inflammation. *Immunol Rev* 2013;252(1):164-82.
12. Hegazy AN, West NR, Stubbington MJT, et al. Circulating and Tissue-Resident CD4(+) T Cells With Reactivity to Intestinal Microbiota Are Abundant in Healthy Individuals and Function Is Altered During Inflammation. *Gastroenterology* 2017;153(5):1320-37 e16.
13. Silva FA, Rodrigues BL, Ayrizono ML, et al. The Immunological Basis of Inflammatory Bowel Disease. *Gastroenterol Res Pract* 2016;2016:2097274.
14. Bandura DR, Baranov VI, Ornatsky OI, et al. Mass cytometry: technique for real time single cell multitarget immunoassay based on inductively coupled plasma time-of-flight mass spectrometry. *Anal Chem* 2009;81(16):6813-22.
15. van Unen V, Li N, Molendijk I, et al. Mass Cytometry of the Human Mucosal Immune System Identifies Tissue- and Disease-Associated Immune Subsets. *Immunity* 2016;44(5):1227-39.
16. Li N, van Unen V, Holt T, et al. Mass cytometry reveals innate lymphoid cell differentiation pathways in the human fetal intestine. *J Exp Med* 2018.
17. van Unen V, Holt T, Pezzotti N, et al. Visual analysis of mass cytometry data by hierarchical stochastic neighbour embedding reveals rare cell types. *Nat Commun* 2017;8(1):1740.
18. Holt T, Pezzotti N, van Unen V, et al. Cytosplore: Interactive Immune Cell Phenotyping for Large Single-Cell Datasets. *Comput Graph Forum* 2016;35(3):171-80.
19. Satsangi J, Silverberg MS, Vermeire S, et al. The Montreal classification of inflammatory bowel disease: controversies, consensus, and implications. *Gut* 2006;55(6):749-53.

20. Levine A, Griffiths A, Markowitz J, et al. Pediatric modification of the Montreal classification for inflammatory bowel disease: the Paris classification. *Inflamm Bowel Dis* 2011;17(6):1314-21.
21. Schmitz F, Kooy-Winkelaar Y, Wiekmeijer AS, et al. The composition and differentiation potential of the duodenal intraepithelial innate lymphocyte compartment is altered in coeliac disease. *Gut* 2016;65(8):1269-78.
22. Schmitz F, Tjon JM, Lai Y, et al. Identification of a potential physiological precursor of aberrant cells in refractory coeliac disease type II. *Gut* 2013;62(4):509-19.
23. Ettersperger J, Montcuquet N, Malamut G, et al. Interleukin-15-Dependent T-Cell-like Innate Intraepithelial Lymphocytes Develop in the Intestine and Transform into Lymphomas in Celiac Disease. *Immunity* 2016;45(3):610-25.
24. Kooy-Winkelaar YM, Bouwer D, Janssen GM, et al. CD4 T-cell cytokines synergize to induce proliferation of malignant and nonmalignant innate intraepithelial lymphocytes. *Proc Natl Acad Sci U S A* 2017;114(6):E980-E89.
25. Thureau AM, Schylz U, Wolf V, et al. Identification of eosinophils by flow cytometry. *Cytometry* 1996;23(2):150-8.
26. Ruhle PF, Fietkau R, Gaipl US, et al. Development of a Modular Assay for Detailed Immunophenotyping of Peripheral Human Whole Blood Samples by Multicolor Flow Cytometry. *Int J Mol Sci* 2016;17(8).
27. Han X, Jorgensen JL, Brahmandam A, et al. Immunophenotypic study of basophils by multiparameter flow cytometry. *Arch Pathol Lab Med* 2008;132(5):813-9.
28. Simoni Y, Chng MHY, Li S, et al. Mass cytometry: a powerful tool for dissecting the immune landscape. *Curr Opin Immunol* 2018;51:187-96.
29. Brodin P, Jovic V, Gao T, et al. Variation in the human immune system is largely driven by non-heritable influences. *Cell* 2015;160(1-2):37-47.
30. Carr EJ, Dooley J, Garcia-Perez JE, et al. The cellular composition of the human immune system is shaped by age and cohabitation. *Nat Immunol* 2016;17(4):461-68.
31. Tsang JS, Schwartzberg PL, Kotliarov Y, et al. Global analyses of human immune variation reveal baseline predictors of postvaccination responses. *Cell* 2014;157(2):499-513.
32. Kurioka A, Cosgrove C, Simoni Y, et al. CD161 Defines a Functionally Distinct Subset of Pro-Inflammatory Natural Killer Cells. *Front Immunol* 2018;9:486.
33. Al-Haddad S, Riddell RH. The role of eosinophils in inflammatory bowel disease. *Gut* 2005;54(12):1674-5.
34. Boyd M, Thodberg M, Vitezic M, et al. Characterization of the enhancer and promoter landscape of inflammatory bowel disease from human colon biopsies. *Nat Commun* 2018;9(1):1661.

SUPPLEMENTAL INFORMATION

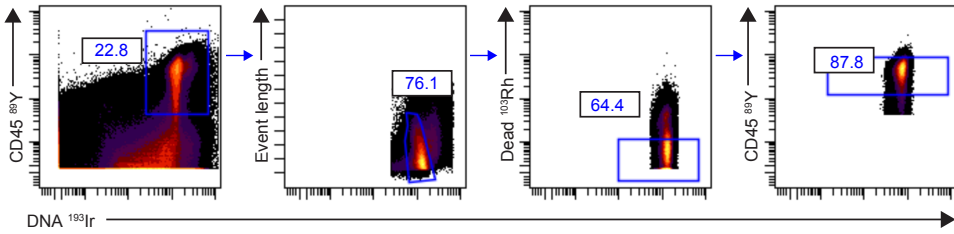


Fig. S1. Live single cell CD45+ gating strategy

Stratification of immune cell infiltrates in inflammatory bowel disease by high-dimensional mass cytometry

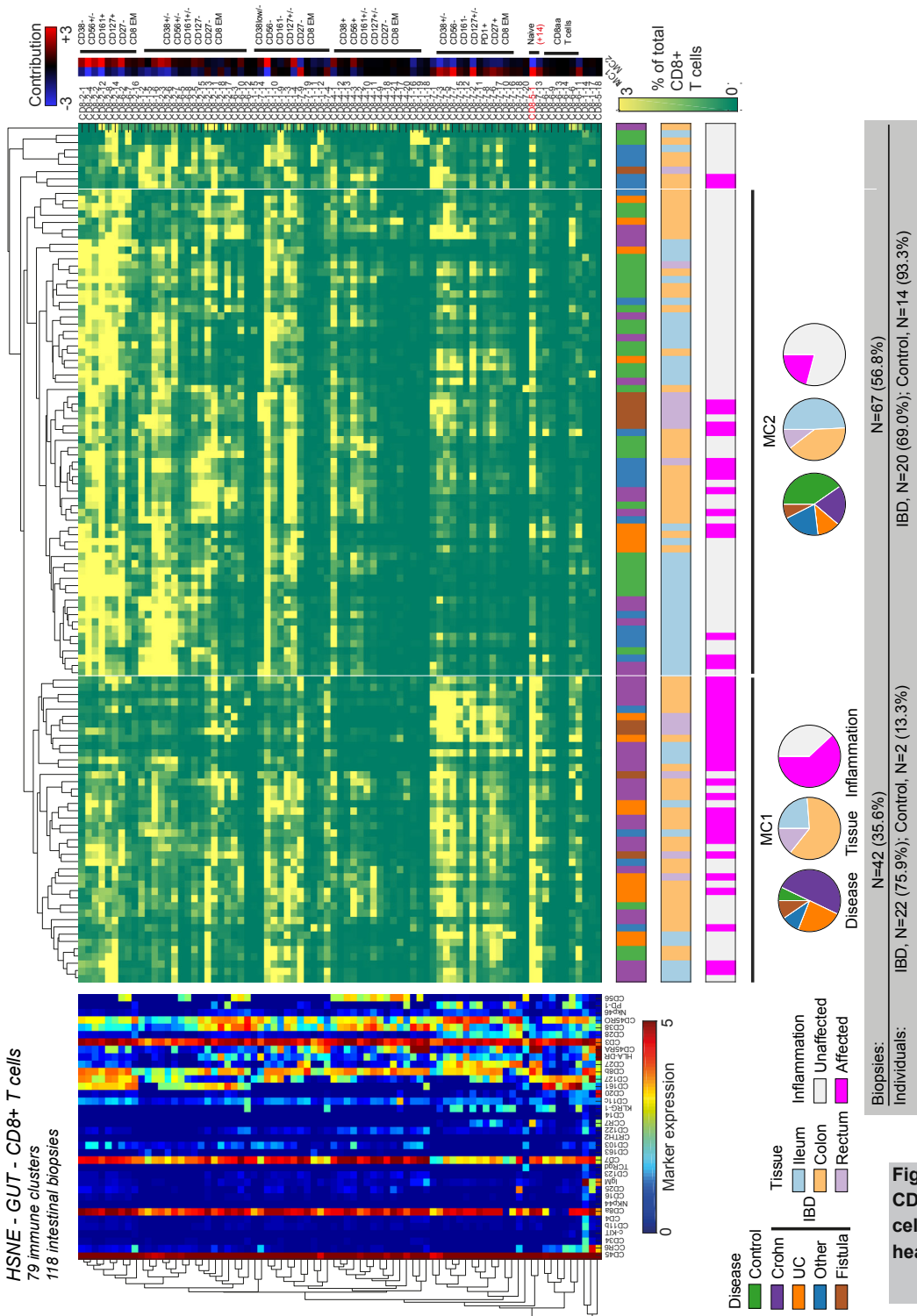
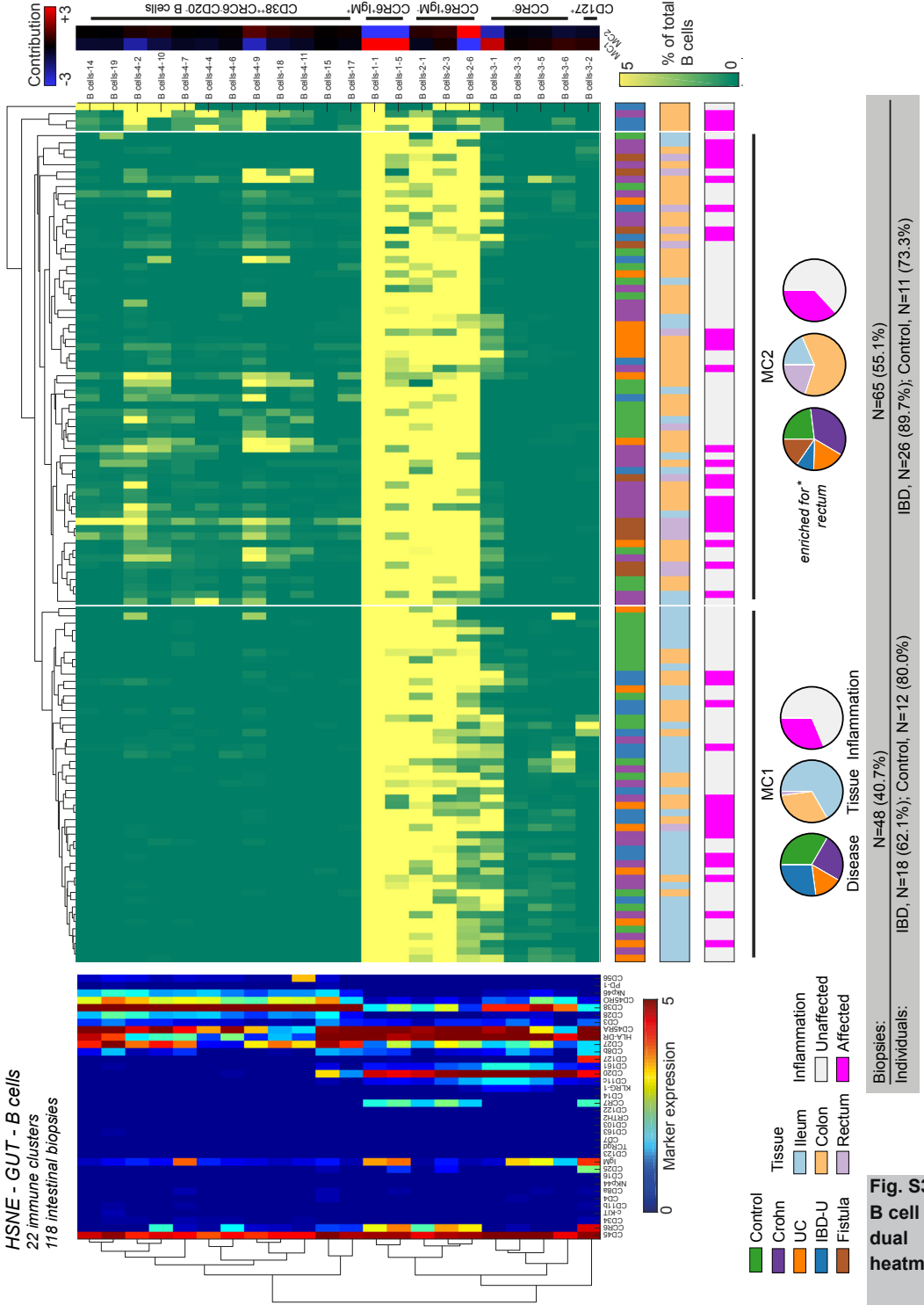


Fig. S2
CD8+ T
cell dual
heatmap



Stratification of immune cell infiltrates in inflammatory bowel disease by high-dimensional mass cytometry

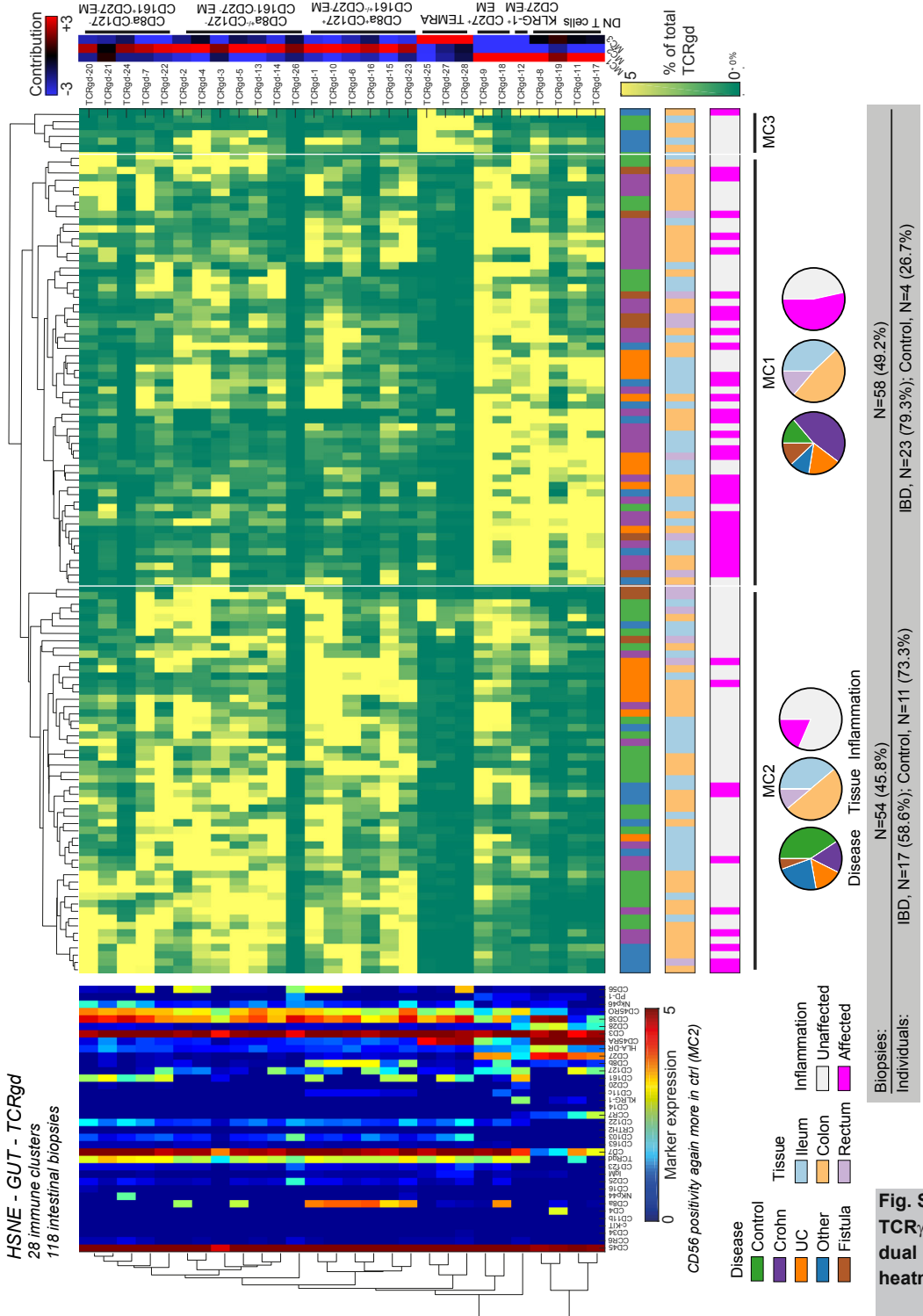
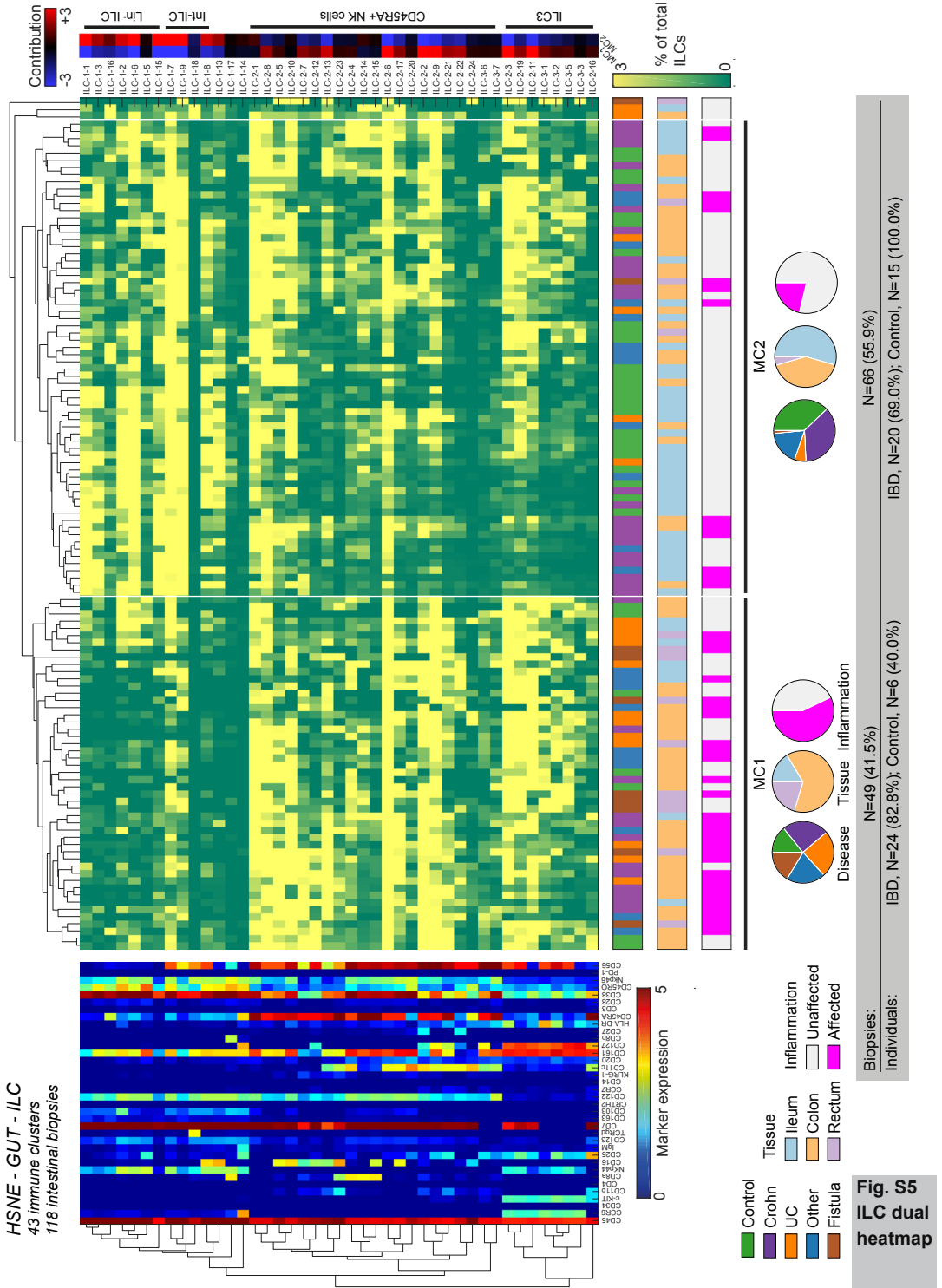
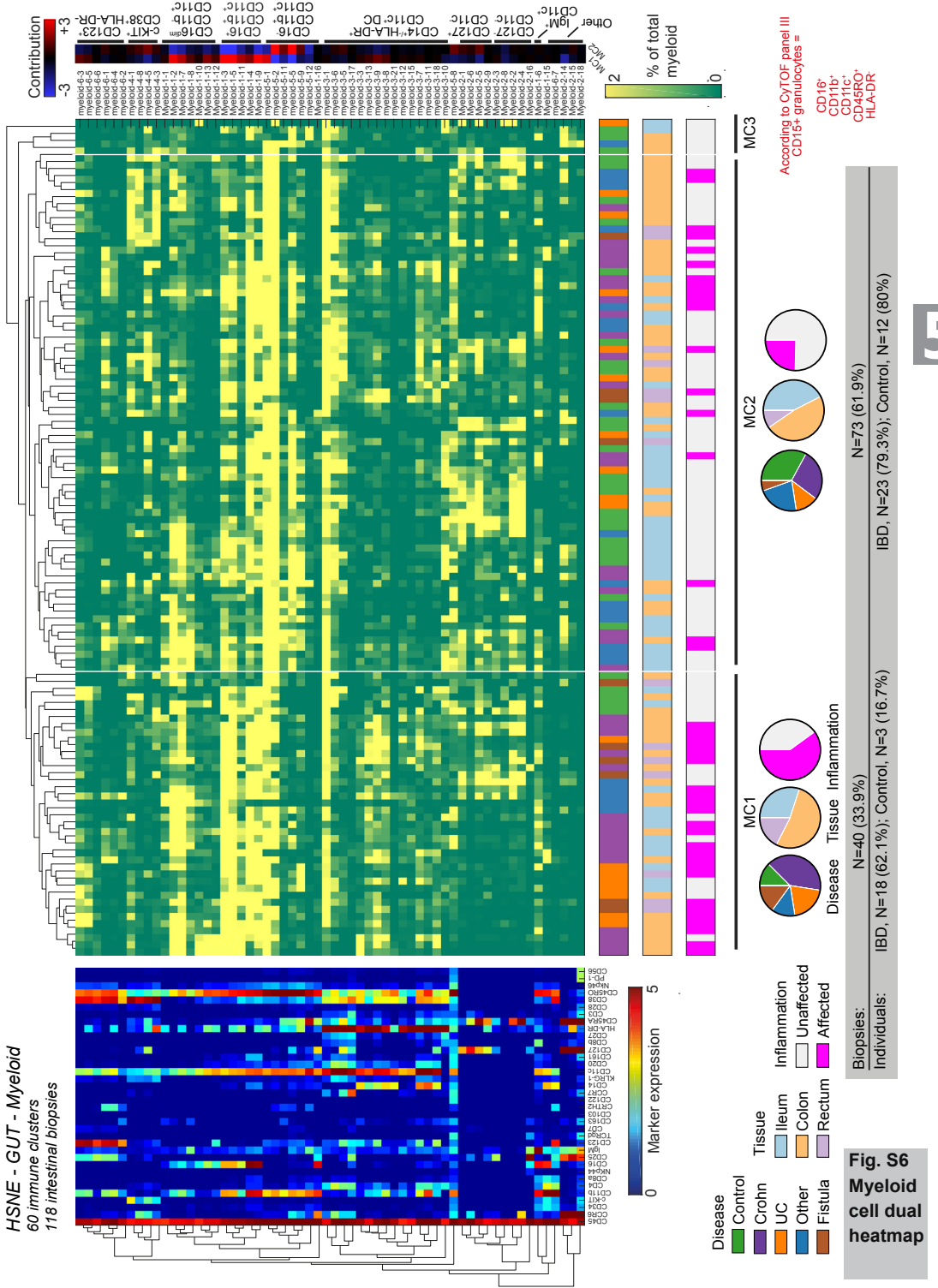


Fig. S4
TCR $\gamma\delta$
dual
heatmap



Stratification of immune cell infiltrates in inflammatory bowel disease by high-dimensional mass cytometry



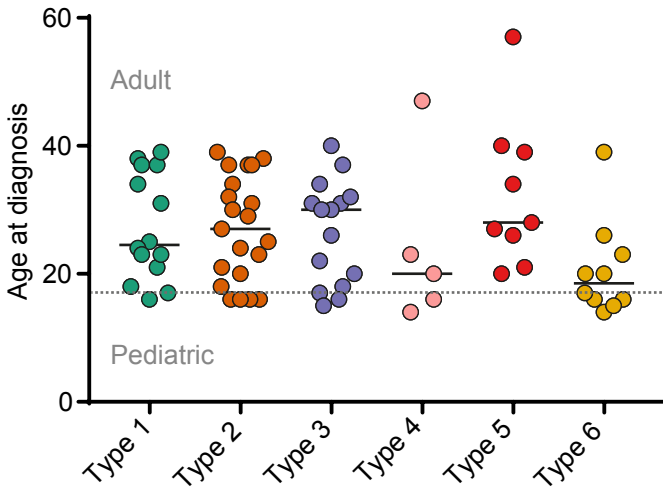


Fig. S7. Age distribution across the six identified immune infiltrate types



JEM

Journal of
Experimental
Medicine

Vol 215 - No 5 - MAY 2018

CHAPTER 6

Mass Cytometry Reveals Innate Lymphoid Cell Differentiation Pathways in the Human Fetal Intestine

ON THE COVER

Li et al. apply mass cytometry to delineate the fetal gut innate lymphoid cell (ILC) population and use a t-SNE-based approach to predict potential differentiation trajectories. This image represents the composition of the ILC compartment in the individual fetal intestines. The image was taken from the original manuscript and modified by the JEM editorial office. See page **77**

CHAPTER 6

Mass Cytometry Reveals Innate Lymphoid Cell Differentiation Pathways in the Human Fetal Intestine

Na Li,^{1*} Vincent van Unen,^{1*} Thomas Höllt,^{2,3} Allan Thompson,¹ Jeroen van Bergen,¹ Nicola Pezzotti,² Elmar Eisemann,² Anna Vilanova,² Susana M. Chuva de Sousa Lopes,⁴ Boudewijn P.F. Lelieveldt,^{5,6} Frits Koning.¹

¹Department of Immunohematology and Blood Transfusion, Leiden University Medical Center, Leiden, ²Computer Graphics and Visualization Group, Delft University of Technology, Delft. ³Computational Biology Center, Leiden University Medical Center, Leiden. ⁴Department of Anatomy and Embryology, Leiden University Medical Center, Leiden. ⁵Department of LKEB Radiology, Leiden University Medical Center, Leiden. ⁶Department of Pattern Recognition and Bioinformatics group, Delft University of Technology, Delft. The Netherlands.

* Equal contribution

Journal of Experimental Medicine 215:5, 1383-1396 (2018)

ABSTRACT

Innate lymphoid cells (ILCs) are abundant in mucosal tissues and involved in tissue homeostasis and barrier function. While several ILC subsets have been identified, it is unknown if additional heterogeneity exists and their differentiation pathways remain largely unclear. We applied mass cytometry to analyze ILCs in the human fetal intestine and distinguished 34 distinct clusters through a t-SNE-based analysis. A lineage (Lin)⁻CD7⁺CD127⁻CD45RO⁺CD56⁺ population clustered between the CD127⁺ ILC and natural killer (NK) cell subsets, and expressed diverse levels of Eomes, T-bet, GATA3 and ROR γ t. By visualizing the dynamics of the t-SNE computation, we identified smooth phenotypic transitions from cells within the Lin⁻CD7⁺CD127⁻CD45RO⁺CD56⁺ cluster to both the NK cells and CD127⁺ ILCs, revealing potential differentiation trajectories. In functional differentiation assays the Lin⁻CD7⁺CD127⁻CD45RO⁺CD56⁺CD8a⁻ cells could develop into CD45RA⁺ NK cells and CD127⁺ROR γ t⁺ ILC3-like cells. Thus, we identified a previously unknown intermediate innate subset that can differentiate into ILC3 and NK cells.

INTRODUCTION

Innate lymphoid cells (ILCs) lack expression of T cell receptors but otherwise are a functional counterpart of cytotoxic and helper T cell subsets. Helper ILCs are classified into 3 groups: ILC1, ILC2 and ILC3¹. ILC1s are mainly characterized as Lineage (Lin)⁻CD161⁺CD127⁺CRTH2⁻CD117⁻; express the transcription factor T-bet and produce T helper 1 (TH1) cell-associated cytokines. ILC2s are Lin⁻CD161⁺CD127⁺CRTH2⁺, express GATA3, and produce T helper 2 (TH2) cell-associated cytokines. ILC3s, including fetal lymphoid tissue-inducer (LTI) cells, are Lin⁻CD161⁺CD127⁺CRTH2⁻CD117⁺, ROR γ t⁺, and secrete TH17/TH22 helper T cell-associated cytokines^{1,2}. A fraction of human ILC3s expresses natural cytotoxicity receptors such as Nkp44, Nkp46 and Nkp30, and neural cell adhesion molecule CD56, similar to natural killer (NK) cells^{3,4}. NK cells are a cytotoxic subset of ILCs that express the transcription factor T-bet and/or Eomes and produce IFN- γ , granzymes and perforin¹. Also, ILCs are most abundant and reside in mucosal tissues such as the tonsil, lung and intestine, where they can expand locally⁵.

Several studies have reported the differentiation pathways of ILCs in a variety of tissues in both mice and humans^{6,7}. For example, in murine fetal liver and adult intestine, a CXCR6⁺ROR γ t⁺ α 4 β 7⁺ subset has been identified that can differentiate into ILC3s and NK cells⁸. As this subset was not found in adult bone marrow, it might migrate to the intestine during fetal development. In humans, ROR γ t⁺CD34⁺ progenitor cells were identified in the tonsil and intestine, but these were absent in peripheral blood, umbilical cord blood, bone marrow and thymus^{9,10}. Since these progenitors could differentiate into helper ILCs and NK cells, mucosal organs might be the preferential sites for ILC differentiation. In addition, a CD127⁺CD117⁺ ILC precursor has been identified in cord blood, peripheral blood and tissues, including fetal liver, adult lung and tonsil, which can generate all ILC subsets *in situ* and could represent an intermediate between precursor cells and mature ILCs¹¹. Also, previous studies have observed ILC plasticity mainly in mucosal tissues, such as the small intestine¹²⁻¹⁵, suggesting that environmental cues may play an important role in cell-fate decision. So far, most of the studies on human ILC differentiation used CD34⁺ progenitors and mature types of ILCs⁶, while the intermediates or transitional stages connecting the CD34⁺ populations to mature types of ILCs have not been fully identified.

High-dimensional mass cytometry provides an opportunity to analyze the heterogeneity and potential differentiation pathways of human ILCs in an unbiased

and data-driven fashion based on the simultaneous measurement of over 30 cellular markers at single-cell resolution¹⁶. Although the sensitivity of metal reporters in mass cytometry is not as sensitive as some of the brightest fluorochromes in flow cytometry, the advantage of including many more markers in a single antibody panel offers unique opportunities to evaluate the composition of the immune system with unprecedented resolution. Up to recently, analysis of flow cytometry data was mainly performed with gating strategies based on (primarily) bimodal expression patterns. The incorporation of over 30 markers in mass cytometry antibody panels is not well compatible with such an analysis approach. Instead, t-Distributed Stochastic Neighbor Embedding (t-SNE)-based approaches are currently becoming the standard in the field as they allow the simultaneous analysis of all marker expression profiles in an unbiased fashion. Hierarchical SNE, for example, allows efficient analysis of mass cytometry data sets on tens of millions of cells at the single-cell level¹⁷. Here, we applied mass cytometry to analyze the ILC compartment in the human fetal intestine and provide evidence for previously unrecognized heterogeneity within this compartment. Moreover, we utilized a t-SNE-based computational approach to predict potential differentiation trajectories *in silico*, and provide evidence for the existence of a previously unrecognized innate cell subset that can differentiate into both NK cells and ILC3 *in vitro*.

RESULTS

High-dimensional analysis reveals previously unrecognized heterogeneity in the ILC compartment

We developed a 35 metal isotope-tagged monoclonal antibody panel (**Table SI**) to identify the 6 major immune lineages (B cells, myeloid cells, CD4⁺, CD8⁺, $\gamma\delta$ T cells, and Lin⁻CD7⁺ cells; the latter hereafter referred to as ILCs) and heterogeneity within those lineages. For this purpose the panel included lineage markers and markers linked to cell differentiation, activation, trafficking and responsiveness to humoral factors. With this panel, single-cell suspensions prepared from 7 fetal intestines were analyzed individually. Single, live CD45⁺ cells were discriminated by event length, DNA stainings and CD45 antibody staining (**Fig. SI A**). All antibodies showed clear discrimination between antibody-positive and -negative cells (**Fig. SI B**). Similar to our previous study¹⁸, we applied a combined t-SNE¹⁹-ACCENSE²⁰ data analysis approach to the 6 major cell lineages (**Fig. SI C**) which revealed a large degree of heterogeneity within these lineages.

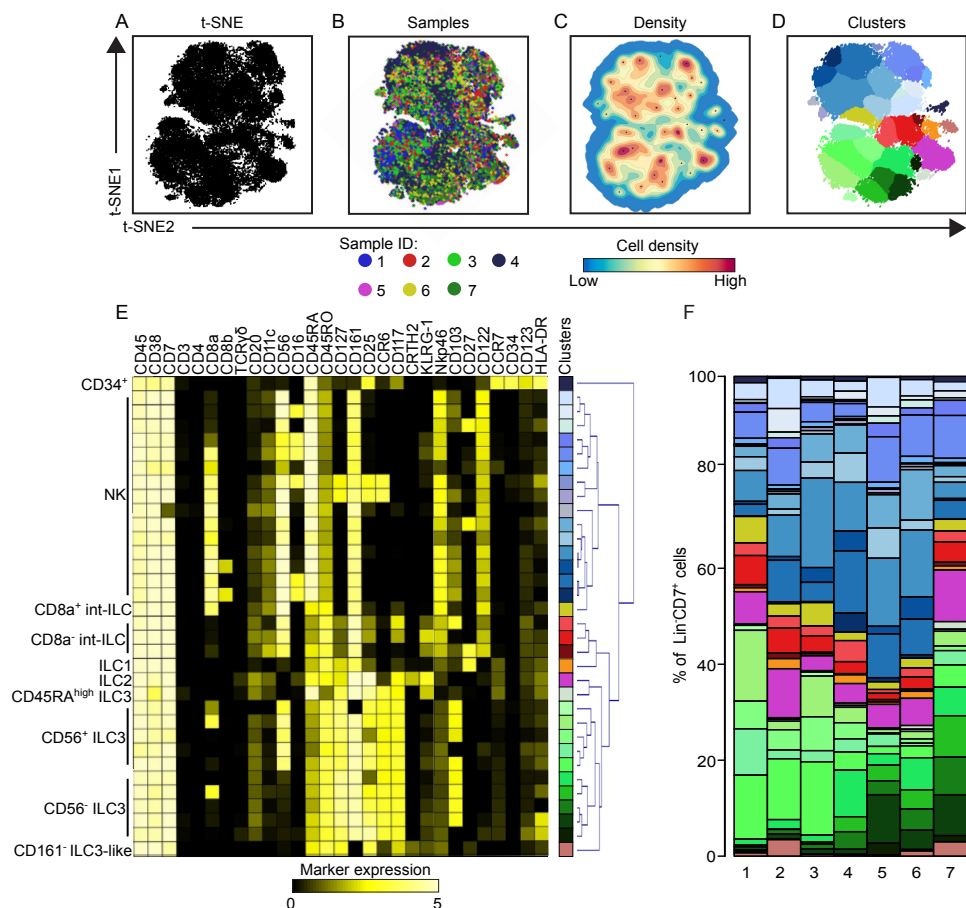
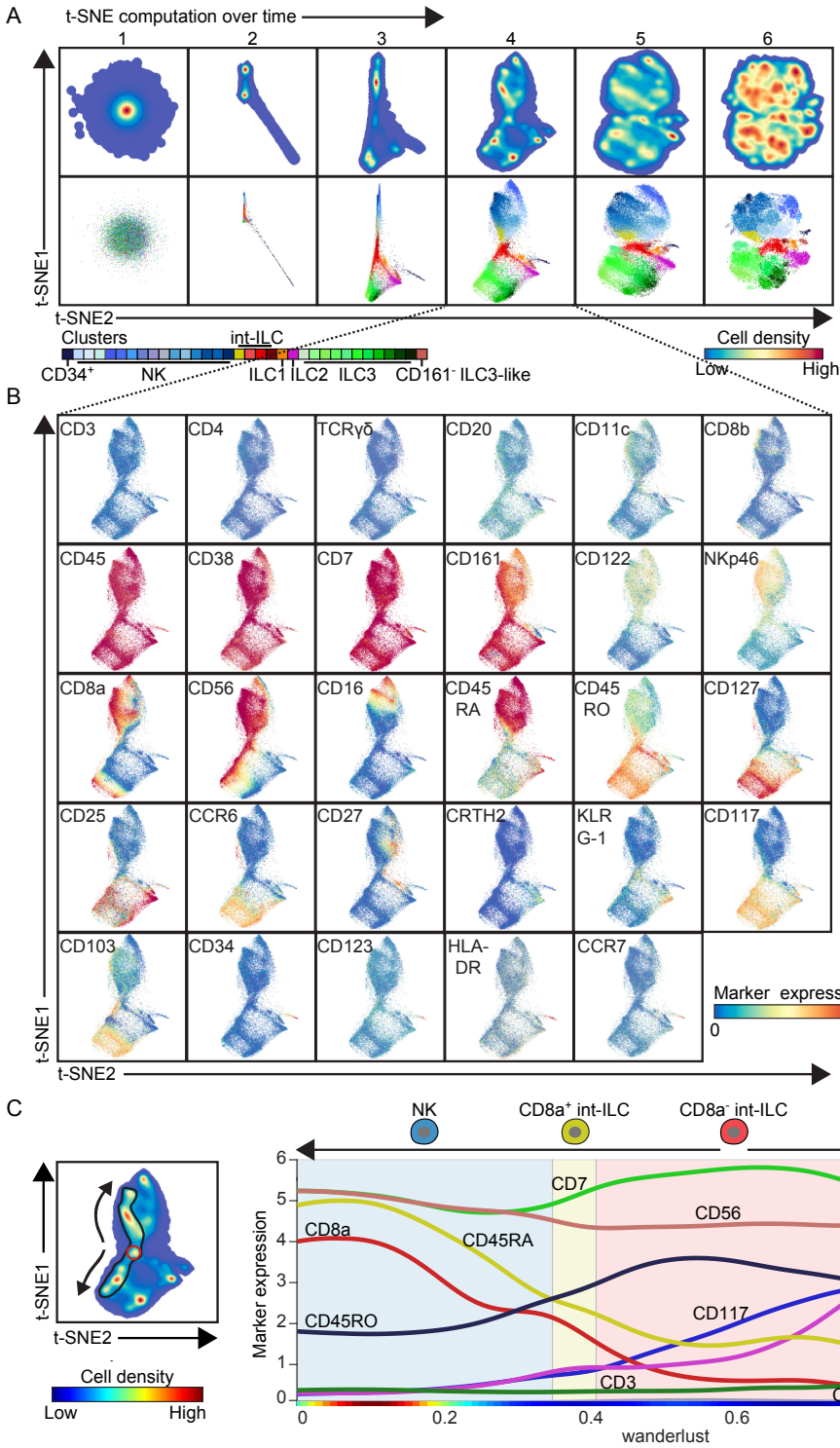


Fig. 1. High-dimensional mass cytometry analysis reveals previously unrecognized heterogeneity in the fetal intestinal ILC compartment

(A) A t-SNE embedding showing the collective ILCs (4.5×10^4 cells) derived from 7 fetal intestines, each black dot represents a single cell. (B) A t-SNE embedding as shown in panel A. Colors represent the different samples. (C) A density map describing the local probability density of t-SNE-embedded cells where black dots represent centroids of identified clusters using Gaussian Mean Shift clustering. (D) A t-SNE plot showing cluster partitions in different colors. (E) Heatmap showing the median ArcSinh5-transformed marker expression values (black-to-yellow scale) of the clusters identified in panel A with description of ten annotated categories based on pre-existing literature, and hierarchical clustering thereof. (F) Composition of the ILC compartment in the individual fetal intestines ($N=7$) represented in vertical bars where the size of the colored segments represents the proportion of cells as % of total ILC in the sample. Colors as in panel A.

We next focused on the ILC compartment (**Fig. S2 A**) which comprised $20.4\% \pm 7.8\%$ of the $CD45^+$ cells. We pooled the data from the 7 samples and performed a t-SNE analysis in Cytosplore²¹. This provided a two-dimensional map where cells are positioned based on the similarity in expression of all marker simultaneously (**Fig. 1 A and B**). Based on the density features of the t-SNE-embedded cells, we



identified 34 phenotypically distinct clusters (**Fig. I, C and D**) using the Gaussian Mean Shift clustering and generated a heatmap showing the distinct marker expression profiles for each cluster (**Fig. I E**). Unbiased hierarchical clustering revealed distinct clusters including a group of CD34⁺ cells expressing CD45RA and CD117, a larger cluster of several types of NK cells, and a CD127⁺ ILC cluster with cells expressing markers corresponding to ILC1, ILC2, CD45RA^{high} ILC3, subsets of several types of CD56⁺ and CD56⁻ ILC3^{2,22} and a CD161⁻ ILC3-like population²³. In addition, several unrecognized cell clusters with a Lin⁻CD7⁺CD127⁻CD45RO⁺CD56⁺ phenotype [referred to as intermediate ILC (int-ILC) hereafter] were identified which clustered between the NK cells and CD127⁺ ILCs (**Fig. I, C-E**). While the majority of these int-ILCs (6.6% of ILCs \pm 2.3%) were CD8a⁻, a smaller related population (3.0% \pm 1.6%) was CD8a⁺ (**Fig. I F**). Importantly, analysis of the composition of the cluster frequencies in the individual fetal samples demonstrated that even though quantitative differences exist, most of the identified clusters, including the int-ILCs were present in all 7 samples (**Fig. I F**). Together, these data indicate that all known NK and CD127⁺ ILC cell clusters could be identified simultaneously while evidence for the existence of previously unrecognized clusters was obtained as well.

Visualization of the t-SNE computation dynamics predicts potential differentiation trajectories in the ILC compartment

The cell surface phenotype of int-ILC (i.e. CD127⁻CD45RO⁺) places them in between the CD127⁺ ILCs and the NK cells (**Fig. I, C-E**), suggesting potential relationships with both. To investigate this in more detail, we sought to visualize potential relationships between cell populations without prior designation of a user-defined starting cell type *in silico*. To this end, we exploited the ability of Cytosplore to visualize the evolution of the t-SNE map²¹. Separating the computational modelling

Fig. 2. Monitoring t-SNE computation dynamics predicts potential differentiation trajectories of ILCs (A) t-SNE embeddings of the collective ILC single-cell data derived from 7 fetal intestines showing density features (upper row) and single cells (bottom row) at 6 stages over the course of the t-SNE computation. Colors represent the local probability density of t-SNE-embedded cells (upper row), or cluster partitions (bottom row), as described in Fig. 1 A. (B) t-SNE embeddings at stage 4 of the optimization phase as described in panel A. Colors of the cells represent ArcSinh5-transformed expression values of indicated markers. (C) Left panel: t-SNE embedding at stage 4 as in panel A. Colors represent density features and black encirclement indicates the trajectory of cells along the CD56 expression continuum shown in panel B. Right panel: Wanderlust graph (trajectory 0-1.0) of the CD56 positive cells in the left panel showing median ArcSinh5-transformed expression of CD8a, CD45RO, CD45RA, CD7, CD3, CD56, CD117, CD127 and CRTH2 from the CD8a⁻ int-ILCs (shaded red box) via the CD8a⁺ int-ILC (shaded yellow box) to NK cells (shaded blue box), and from the CD8a⁻ int-ILCs to ILC3s (shaded green box). The rainbow color bar indicates relative cell density.

into 6 stages revealed how distinct cell clusters were formed, while their high-dimensional similarities were projected onto a two-dimensional map, and linked to each other based on marker expression profiles (**Fig. 2 A**). Since the initial positions in the t-SNE map are assigned randomly, at the first stage of the t-SNE computation all cells were unordered around a single density peak. Shortly thereafter the CD34⁺ lymphoid precursor cells separated from the other cells (stage 2) and the first formation of the NK and CD127⁺ ILC clusters became apparent (stage 2 and 3). These early events were based on relatively large and highly discriminatory differences in the expression profiles between cell clusters, like the unique combination of CD34 and HLA-DR expression by CD34⁺ cells. At stage 4 of the t-SNE computation the int-ILC cluster was positioned in the center with several distinct strands of cells forming trajectories towards the NK, CD27⁺ ILC1, KLRG-1⁺ ILC2 and CD103⁺ ILC3 clusters. In addition, a trajectory between the ILC2 and ILC3 clusters was visible (stage 4). Furthermore, cells from the CD8a⁻ int-ILC population connected via the CD8a⁺ int-ILC population with NK cells, further supporting the notion that these two CD8a⁻ and CD8a⁺ int-ILC populations are highly related (**Fig. 2 A and Fig. S2 B**). At the final stage of the t-SNE computation the 34 clusters were defined while the connections between the individual clusters were less clear as the t-SNE algorithm eventually assigns cells in between two clusters to either one of the two. Individual marker expression patterns at stage 4 of the t-SNE computation gave insight into the separations of and the connections between clusters (**Fig. 2 B**). Here, the NK cluster was characterized by the co-expression of CD45RA, CD56, CD122 and NKp46 while the CD127⁺ ILC cluster expressed CD45RO, CD117, CD127, CD25 and to a lesser extent CCR6 and CD103. Similarly, connections between int-ILC to ILC1, ILC2, ILC3 and NK cells were marked by (gradients of) expression of CD27, KLRG-1, CD103 and CD56, respectively. The absence of CD45RA, CD127, and CCR6 in combination with the presence of CD45RO and CD56, and divergent expression of CD117, CD122 and CD25, positioned the int-ILC in between the NK cell and ILC clusters. Interestingly, CD56 expression linked the ILC3 to the CD8a⁻ int-ILC, and the CD8a⁺ int-ILC to the NK cells. We next applied Wanderlust²⁴ to determine changes in marker expression along this CD56 continuum (**Fig. 2 C**), which demonstrated that the expression of CD127, CD117 and CD45RO gradually decreased while that of CD45RA and CD8a increased moving from CD8a⁻ int-ILC to NK cells, via CD8a⁺ int-ILC; and the expression of CD127 and CD117 gradually increased from CD8a⁻ int-ILC to ILC3. Altogether, these results suggest that these t-SNE-based trajectories may reflect potential differentiation pathways.

Expression of cytokines, transcription factors and CD94 distinguish int-ILCs from mature CD127⁺ ILCs and NK Cells

To further characterize the int-ILC population, we used the mass cytometry data (Fig. S3 A) to design a minimal antibody panel to distinguish the CD127⁻CD45RO⁺ int-ILCs from CD45RA⁺ NK cells, and to identify the mature CD127⁺ ILC types through differential expression of CD117 and CRTH2 (Fig. 3 A). Subsequently, we analyzed the proliferative state and examined the capacity of the subsets to produce cytokines and express markers linked to cytolytic potential by flow cytometry. For the former we stained the cells with the proliferation marker Ki-67 *ex vivo*. The highest

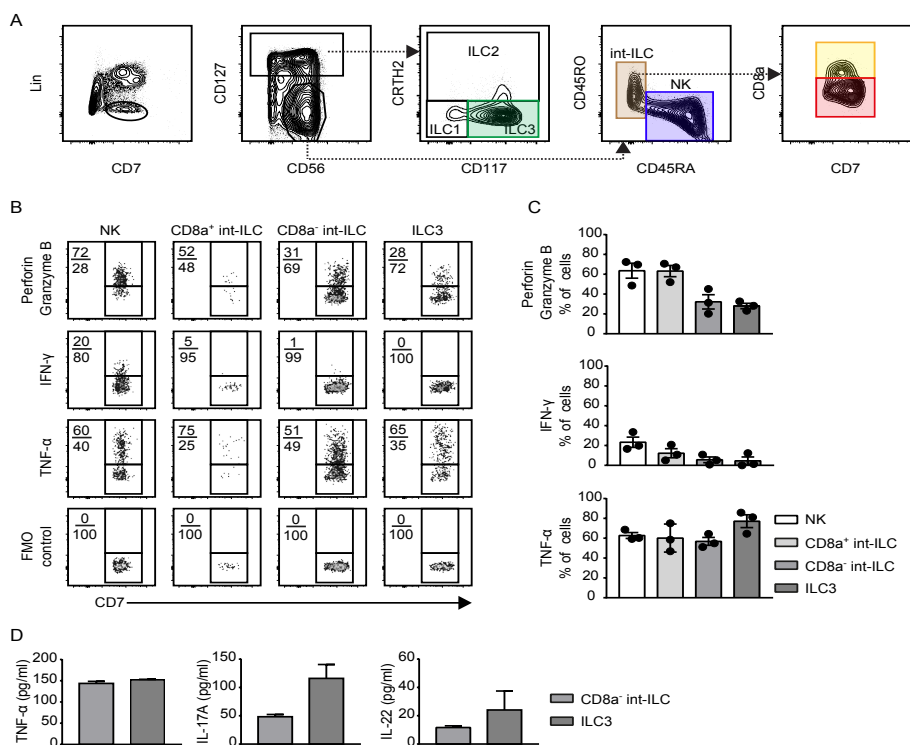


Fig. 3. Cytokine production profiles of fetal intestinal ILCs *ex vivo*. (A) Representative biaxial plots depicting the gating strategy for ILC1, ILC2, ILC3, NK and int-ILC subsets derived from a human fetal intestine analyzed by flow cytometry. The antibody cocktail contains lineage (Lin) markers (CD3, CD19, CD11c and CD14), and CD7, CD127, CD56, CRTH2, CD117, CD45RA, CD45RO and CD8a to allow distinction of the ILC subsets. (B and C) Expression of cytotoxic molecules (Perforin + Granzyme B) and cytokines (IFN- γ and TNF- α) by the indicated subsets defined in panel A after stimulation with PMA and ionomycin for 6 h. The biaxial plots (B) depict one representative experiment and the bar graphs (C) depict quantification of data obtained from 3 different human fetal intestines. Three independent experiments. FMO, fluorescence-minus-one control. Error bar shows mean \pm SEM. (D) Bar plots depict the secretion of TNF- α , IL-17A and IL-22 by CD8a⁺ int-ILC and ILC3, after stimulation with IL-2, IL-1 β and IL-23 for 4 days, using Luminex bead-based assay of an experiment with 3 intestines and duplicate wells. (Two independent experiments). Error bar shows mean \pm SD.

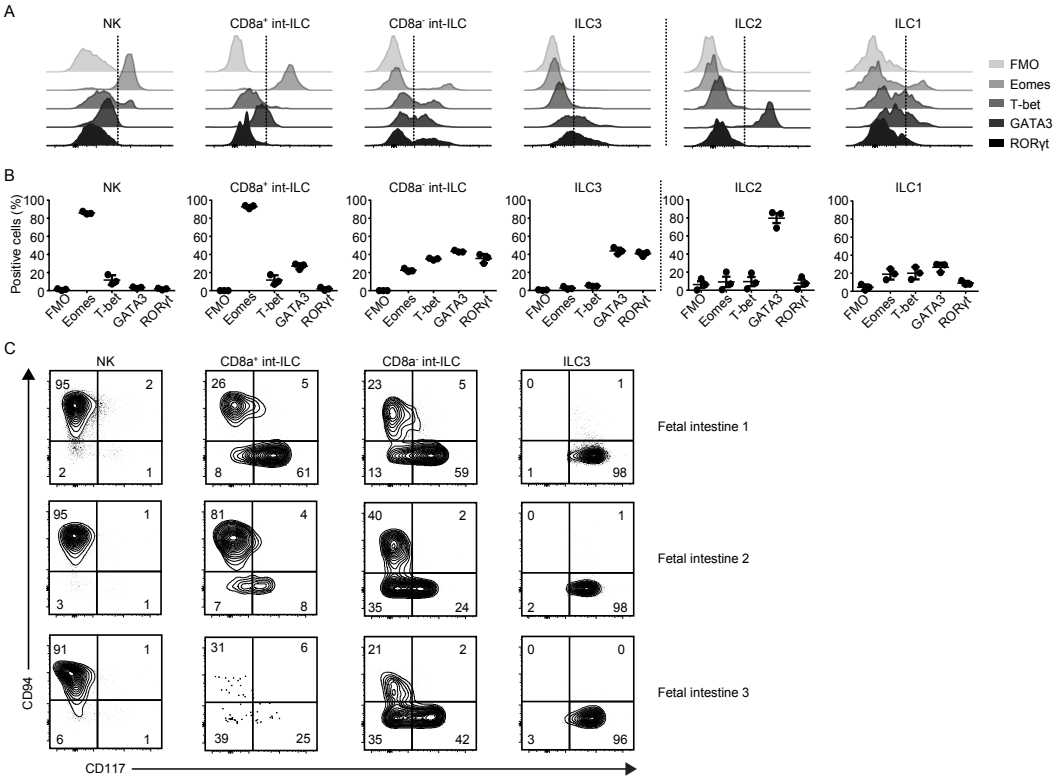


Fig. 4. Transcription factors and CD94 expression profiles of fetal intestinal ILCs *ex vivo*. (A and B) Flow cytometric determination of the expression of the transcription factors Eomes, T-bet, GATA3 and RORγt by the indicated ILC subsets as defined in Fig. 3 A. Histograms (A) depict the results with one representative human fetal intestine and the graphs (B) depict quantification of data obtained from 3 different human fetal intestines. (Three independent experiments). FMO, fluorescence-minus-one control. Error bar shows mean ± SD. (C) Biaxial plots showing the expression of CD94 and CD117 by the indicated subsets. Results on 3 human fetal intestines are shown. (Three independent experiments).

percentage of Ki-67 positive cells was present in the CD8a⁺ int-ILC population (43.9%) while on average 20% of cells in the other subsets were Ki-67 positive (Fig. S3 B). Upon stimulation with PMA and ionomycin Perforin/Granzyme B was detectable in all subsets, but more profoundly in the NK cells and CD8a⁺ int-ILCs compared with the CD8a⁻ int-ILCs and ILC3s (Fig. 3, B and C). Moreover, all subsets expressed high levels of TNF-α, while IFN-γ was detected mainly in the NK cells and CD8a⁺ int-ILCs but hardly in the CD8a⁻ int-ILCs and ILC3s (Fig. 3, B and C). ILC2s expressed IL-4, IL-5 and IL-13, but ILC1s very little IFN-γ (not shown). In contrast, IL-4, IL-5 and IL-13 was undetectable in any of the other subsets (not shown) while IL-17A and IL-22 expression was higher by ILC3s than CD8a⁻ int-ILCs (Fig. 3 D).

Next we determined the expression of key transcription factors associated with ILC development and phenotype. The expression of ID2, TCF7, AHR, NFIL3, ZBTB16 and TOX did not discriminate between the subsets (**Fig. S3 C**). In line with previous work²⁵, the ILC2 subset was strongly GATA3 positive and ROR γ t negative, while ILC3s were GATA3 and ROR γ t positive (**Fig. 4, A and B and Fig. S3 D**). However, we found only low levels of T-bet expression by ILC1 (**Fig. 4, A and B**). Notably, both mature NK cells and CD8a⁺ int-ILCs expressed high levels of Eomes (**Fig. 4, A and B and Fig. S3, E and F**). In contrast, the CD8a⁻ int-ILCs were heterogeneous with respect to the expression of the 4 transcription factors which were all expressed by a proportion of the cells (**Fig. 4, A and B**), an expression profile that does not correspond to those found in mature CD127⁺ ILCs. Furthermore, multiple lineage transcription factors could be simultaneously expressed by CD8a⁻ int-ILCs, such as T-bet and GATA3 (26.1% of CD8a⁻ int-ILCs) (**Fig. S3, G-I**). Finally, the frequency of cells expressing Eomes decreased along the potential differentiation trajectory linking the NK cells to CD8a⁺ int-ILCs, CD8a⁻ int-ILCs and ILC3s, while that of ROR γ t increased (**Fig. 4, A and B**).

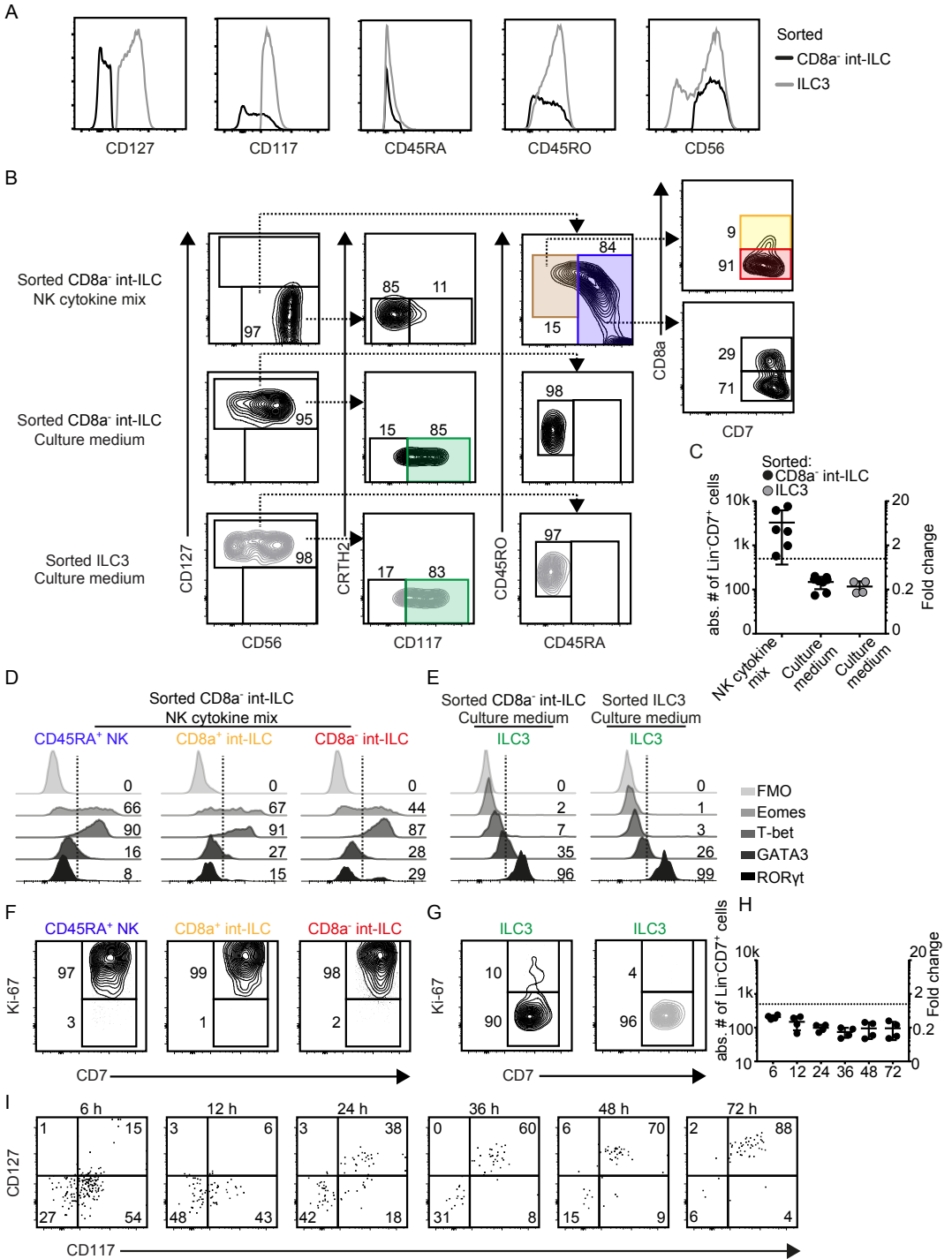
To investigate the relationship between the int-ILCs, NK cells and ILC3s further, we evaluated the expression of CD62L, CD57, CD5 and the NK cell-associated C-type lectin receptor CD94. Here, expression of CD62L, CD57 and CD5 was almost lacking and did not discriminate between the subsets (not shown) while CD94 expression was high on NK cells but virtually absent from ILC3s (**Fig. 4 C**), in agreement with previous studies^{2,10}. In contrast, only part of the int-ILCs were CD94 positive with a higher expression level of CD94 on CD8a⁺ int-ILCs compared to CD8a⁻ int-ILCs (**Fig. 4 C**), a result in line with the lower expression of Eomes in the latter. Furthermore, in contrast with CD94⁻ cells, CD94⁺ cells lacked the expression of CD117, similar to mature NK cells (**Fig. 4 C**).

Together, these data indicate that the int-ILC subset is distinct from mature ILCs, where the expression pattern of the cytokines, CD94 and transcription factors link the CD8a⁺ int-ILCs to NK cells and the CD8a⁻ int-ILCs to ILC3s.

int-ILC can differentiate into CD45RA⁺ NK cells

To test the hypothesis that the int-ILC subset may differentiate into CD127⁺ ILCs and/or NK cells, we first purified the CD8a⁻ int-ILCs by flow cytometry (**Fig. 5 A**) and performed functional differentiation assays by co-culturing these with OP9 stromal cells expressing the Notch ligand Delta-like 1 (OP9-DL1). After 7 days of culture in

Chapter 6



medium containing stem cell factor (SCF), IL-7, IL-2 and IL-15 (hereafter referred to as NK cytokine mix), the majority of the int-ILCs acquired a CD45RA⁺ phenotype (**Fig. 5 B**) and expanded substantially (**Fig. 5 C**). Also, these cells upregulated CD94 (42% positive) (**Fig. S4 A**) and displayed expression of Eomes and/or T-bet, but no ROR γ t or GATA3 (**Fig. 5 D**), all similar to mature NK cells. Furthermore, part of these cells expressed CD8a (**Fig. 5 B**), a marker expressed by most fetal NK cells *ex vivo* (**Fig. 2 B**), where most of the CD8a⁺ cells displayed the highest expression of Eomes (**Fig. S4 B**). Moreover, a small fraction of generated cells maintained the CD45RA⁻CD45RO⁺ int-ILC phenotype and a fraction of them also acquired CD8a (**Fig. 5 B**). In line with the suggested differentiation trajectory (**Fig. 2 C**), the expression of ILC3-associated ROR γ t decreased from the CD8a⁻ int-ILCs to CD8a⁺ int-ILCs to CD45RA⁺ NK cells while all populations expressed high levels of NK cell-associated Eomes and/or T-bet (**Fig. 5 D**). Also, the cells became uniformly Ki-67 positive (**Fig. 5 F**), consistent with the observed increase in cell numbers (**Fig. 5 C**). As similar results were obtained when purified CD8a⁻ int-ILCs were co-cultured with OP9 stromal cells without Delta-like 1, Notch signalling appears not to be involved (**Fig. S4 C**). In addition, upon culture on OP9-DL1 purified CD8a⁺ int-ILCs also acquired the CD45RA⁺ NK cell phenotype, maintained CD8a expression and expressed

Fig. 5. int-ILC can differentiate into CD45RA⁺ NK cells and ILC3. (A) Representative histograms depicting the expression of CD127, CD117, CD45RA, CD45RO, CD56 by flow cytometry-purified CD8a⁻ int-ILCs (black line) and ILC3s (grey line) from human fetal intestines. Data are representative of six independent experiments. (B-G) Purified CD8a⁻ int-ILCs and ILC3s were co-cultured in 96 well plates at 500 cells/well with irradiated OP9-DL1 stromal cells for 7 days with culture medium alone or supplemented with SCF, IL-7, IL-2, IL-15 (referred to as NK cytokine mix). Generated cells were analyzed by flow cytometry. Duplicated wells were included for each condition. Representative plots show a single duplicate. (B) Representative biaxial plots depict the phenotypes of generated Lin⁻CD7⁺ cells based on the gating strategy for ILC1, ILC2, ILC3, NK and int-ILC subsets as shown in Fig. 3 A, for three different combinations of sorted cell populations (int-ILC in black contours, ILC3 in grey contours) and culture conditions as indicated. (Three to five independent experiments). (C) Quantification of the generated Lin⁻CD7⁺ cells in panel B in absolute cell number (left axis) and fold change (right axis) compared to the number of initially sorted cells (dashed line). (Two to four independent experiments). Error bar shows mean \pm SD. (D and E) Histograms depict the expression of transcription factors Eomes, T-bet, GATA3 and ROR γ t by the indicated subsets generated from (D) sorted CD8a⁻ int-ILCs with NK cytokine mix and (E) sorted CD8a⁻ int-ILCs or ILC3s with culture medium. Numbers indicate the percentage of positive cells. FMO, fluorescence-minus-one control. Combined data on 5 human fetal intestines. (F and G) Biaxial plots depict the expression of Ki-67 by indicated subsets generated from the combinations of sorted cell populations (int-ILC in black contours, ILC3 in grey contours) and culture conditions as in panel D and E. Combined data on 5 human fetal intestines. (H-I) Purified CD8a⁻ int-ILCs were co-cultured at 500 cells/well with irradiated OP9-DL1 stromal cells in culture medium and harvested at the time points indicated in hours. Duplicated wells were included in each experiment. (Two independent experiments). (H) Quantification of the generated Lin⁻CD7⁺ cells in absolute cell number (left axis) and fold change (right axis) compared to the number of initially sorted cells (dashed line). (I) Representative biaxial plots show the expression of CD127 and CD117 by the generated Lin⁻CD7⁺ cells.

high levels of CD94 (84% positive) (**Fig. S4 D**). Finally, purified CD8a⁻ int-ILCs co-cultured with OP9-DLI and IL-15 cytokine only similarly expanded (not shown), acquired CD45RA, upregulated CD94 (41% positive), and became in part CD8a positive (**Fig. S4 E**). However, under these conditions approximately 60% of these generated cells remained CD117⁺ (**Fig. S4 E**), suggesting an incomplete conversion to the mature NK cell phenotype²⁶. Together these data indicate that in the presence of NK cytokines, proliferative CD45RA⁺ NK cells are generated from int-ILC.

CD8a⁻ int-ILC can differentiate into ILC3

In marked contrast, when purified CD8a⁻ int-ILCs and ILC3s (**Fig. 5 A**) were individually co-cultured with OP9-DLI in cytokine-free culture medium, the ILC3s retained their phenotype while the CD8a⁻ int-ILCs acquired an ILC3 phenotype as they became CD127⁺CD117⁺ (**Fig. 5 B**), remained CD45RA⁻CD45RO⁺ (**Fig. 5 B**) and CD8a⁻ (not shown), in the absence of cell expansion and proliferation (**Fig. 5, C and G**). This phenotype was also stable during prolonged culture (**Fig. S4 F**). In addition, these cells homogeneously expressed ROR γ t, but no Eomes or T-bet (**Fig. 5 E**), suggesting an established ILC3 population². As similar results were observed when we co-cultured the CD8a⁻ int-ILCs with OP9 stromal cells that lacked Notch ligand Delta-like 1, Notch signalling appears not to be involved (**Fig. S4, G and H**). Unlike CD8a⁻ int-ILCs and ILC3s, both purified CD45RA⁺ NK cells and CD8a⁺ int-ILCs did not survive under these conditions. To exclude that the generation of ILC3 by int-ILCs was due to outgrowth of contaminating ILC3s, we determined cell numbers and the acquisition of CD127 and CD117 at various time points during culture. After 24 and 72 h of culture, 38% and 88% of purified CD8a⁻ int-ILCs had acquired both CD127 and CD117, respectively, while no increase in cell numbers was observed (**Fig. 5, H and I**). Together with the observation that only a very small proportion of both the purified mature ILC3s and differentiated ILC3s from int-ILCs were Ki-67⁺ (**Fig. 5 G**), this indicates that it is highly unlikely that selective outgrowth of contaminating ILC3s could explain the appearance of cells with an ILC3 phenotype in the CD8a⁻ int-ILC/OP9 co-cultures. Thus, these results indicate that the CD8a⁻ int-ILC population can differentiate into ILC3 *in vitro*.

Differentiation properties of CD8a⁻ int-ILC subpopulations

By the differential expression of CD94 and CD117 three distinct CD8a⁻ int-ILC subpopulations could be distinguished: CD94⁺CD117⁻, CD94⁻CD117⁻ and CD94⁻CD117⁺ (**Fig. 4 C**). We therefore investigated whether these subsets could differentiate into either NK cells or ILC3s *in vitro*. For this purpose, we first

Mass Cytometry Reveals Innate Lymphoid Cell Differentiation Pathways in the Human Fetal Intestine

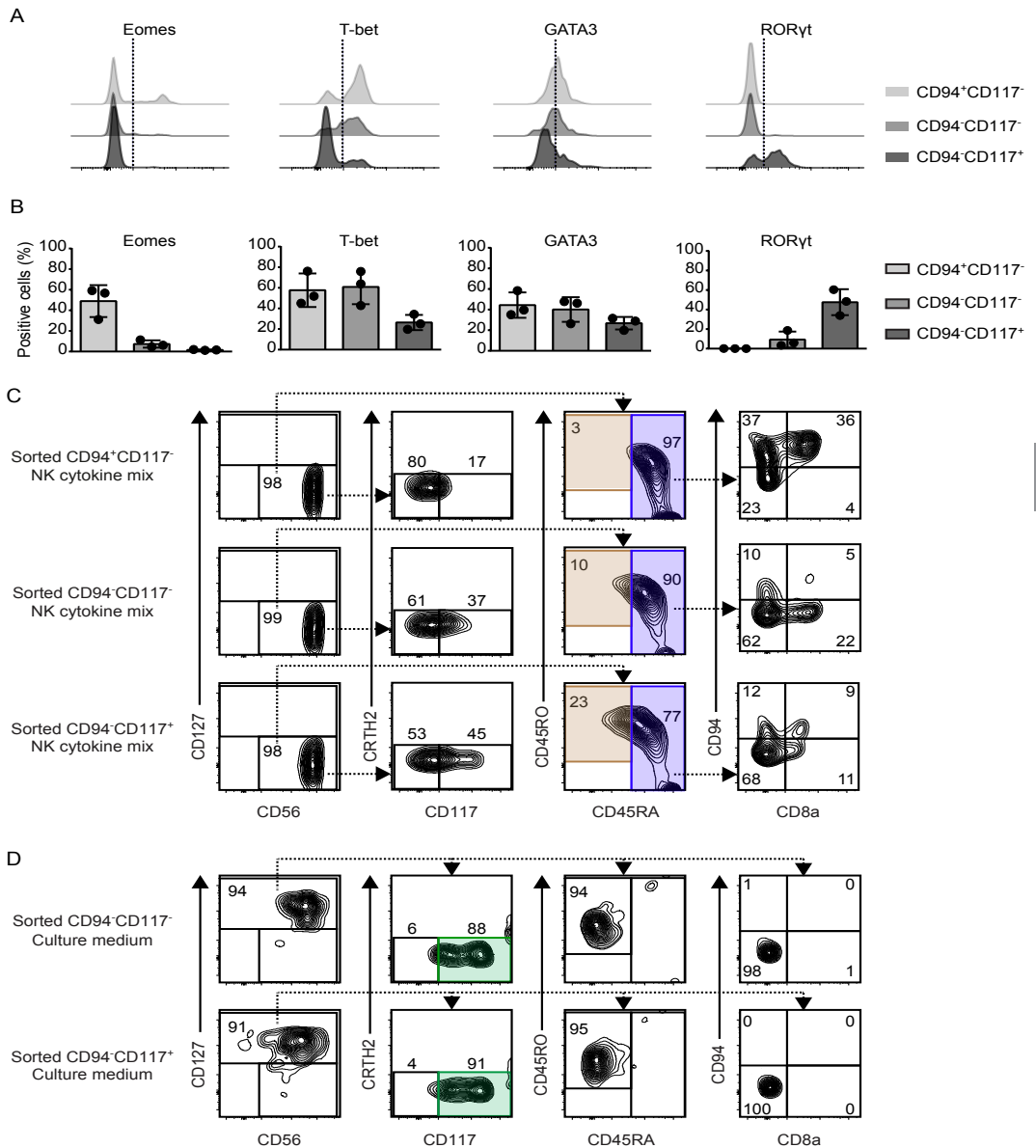


Fig. 6. Distinct differentiation properties of CD8a⁺ int-ILC subpopulations. (A and B) Expression of the transcription factors Eomes, T-bet, GATA3 and RORyt by the indicated subpopulations of CD8a⁺ int-ILC *ex vivo*. Histograms (A) depict the results with one fetal intestine and the graphs (B) depict quantification of data obtained from 3 intestines. (Two independent experiments). Error bar shows mean \pm SD. (C and D) Purified CD94⁺CD117⁻CD8a⁻ int-ILC, CD94⁺CD117⁺CD8a⁻ int-ILC and CD94⁻CD117⁺CD8a⁻ int-ILC populations were co-cultured in 96 well plates at 500 cells/well with irradiated OP9-DL1 stromal cells for 7 days with (C) culture medium supplemented with NK cytokine mix or (D) culture medium alone. Generated cells were analyzed by flow cytometry. Representative biaxial plots depict the phenotypes of the generated Lin⁺CD7⁺ cells based on the gating strategy for ILC1, ILC2, ILC3, NK and int-ILC subsets as shown in Fig. 3 A, for the five combinations of cell populations and culture conditions indicated. Duplicated wells were included in each condition. Representative plots show a single duplicate. (Three to four independent experiments).

examined the expression of transcription factors (**Fig. 6, A and B**). This revealed that Eomes was primarily present in the CD94⁺CD117⁻ subset while ROR γ t expression was most pronounced in the CD94⁻CD117⁺ subset. In addition, all subsets expressed GATA3 and T-bet, where T-bet expression was most pronounced by the CD117⁻ subsets. Together, these results explain the heterogeneity in the expression of transcription factors by CD8a⁻ int-ILCs and position the CD94⁻CD117⁻ subset in between the CD94⁺CD117⁻ and CD94⁻CD117⁺ subsets.

Next, we purified CD94⁺CD117⁻, CD94⁻CD117⁻, and CD94⁻CD117⁺ subsets individually and co-cultured them with OP9-DL1 stromal cells with either NK cytokine mix or cytokine-free medium. In the presence of NK cytokine mix (**Fig. 6 C**), virtually all of the CD94⁺CD117⁻ cells acquired the CD45RA⁺ NK cell phenotype, maintained expression of high levels of CD94 (76%), acquired CD8a expression (43%) and expanded substantially (12-fold; not shown). Similarly, most of the CD94⁻CD117⁻ cells and the majority of the CD94⁻CD117⁺ cells also acquired the CD45RA⁺ NK cell phenotype, acquired expression of CD94 (17% and 25%, respectively) and CD8a (24% and 16%, respectively), and expanded (9-fold and 7-fold, respectively; not shown). In contrast, in cytokine-free medium (**Fig. 6 D**) both the CD94⁻CD117⁻ and CD94⁻CD117⁺ int-ILCs acquired an ILC3 phenotype as they became CD127⁺, remained CD45RO⁺CD45RA⁻CD94⁻CD8a⁻ and acquired or increased the levels of CD117 expression, respectively (**Fig. 6 D**). Similar to CD8a⁺ int-ILCs and CD45RA⁺ NK cells the CD94⁺CD117⁻ int-ILCs did not survive under these conditions.

Taken together, in these *in vitro* experiments all three subpopulations of the CD8a⁻ int-ILCs can differentiate into NK cells, whereas the CD94⁻CD117⁻ and CD94⁻CD117⁺ cells, but not the CD94⁺CD117⁻ cells can differentiate into ILC3s.

DISCUSSION

Numerous studies have reported substantial heterogeneity in the ILC compartment^{2,22}. In our mass cytometry-based approach the NK, ILC1, ILC2 and ILC3 subsets could be readily identified in the human fetal intestine as well as substantial variability within those subsets, results that were highly consistent in several samples analyzed. Based on the marker expression profiles, we identified a large number of distinct NK cell clusters, whose biological significance needs to be investigated in the future studies. In addition, we found a small CD27⁺ ILC cluster that matches ILC1 criteria^{1,27}. However, in contrast to findings from Bernink

et al.¹², but in line with other studies^{22,23}, only few of these ILC1s expressed T-bet. Furthermore, two additional CD127⁺ ILC1-like clusters were identified which clustered with the NK cells due to the expression of several NK cell-associated markers, including CD45RA, CD56, CD8a and NKp46. Consistent with previous reports^{2,13,22} the ILC3 compartment was most frequent and heterogeneous, including CD45RO⁺ ILC3, CD45RA⁺ ILC3, HLA-DR⁺ ILC3 and CD56^{+/-} ILC3 clusters. Further studies will be required to clarify the potential functional significance of observed heterogeneity in the ILC3 lineage. We could not distinguish LTi cells from ILC3s as no specific cell surface marker for human LTi cells was available at the time we performed our analysis. Moreover, while most of the human ILCs described express CD161^{1,2}, we also detected a recently described CD161⁻CD117⁺ ILC3-like cluster that clustered with the CD127⁺ ILCs²³. In addition, we identified two previously unknown CD8a⁺ counterparts of ILC3s that warrants further investigation. We also observed a rare CD34⁺CD45RA⁺CD117⁺ population that resembles the CD34⁺ precursors recently described in human tonsils and intestines after birth^{9,10}.

Finally, we identified a Lin⁻CD7⁺CD127⁻CD45RO⁺CD56⁺ group of cells which by unbiased clustering were positioned between the CD45RA⁺ NK cells and CD127⁺ ILCs, and were termed int-ILC. While in previous studies^{1,2} such CD56⁺CD127⁻ cells were classified as NK cells, the simultaneous use of CD45RA and CD45RO allowed us to distinguish these CD45RO⁺ cells from the CD45RA⁺ NK cells. It is important to note that these int-ILCs display variable expression of several surface markers, including CD8a, CD94, CD117, CD122, CD25, CD27, KLRG-1 and CD103, indicating that they are not a homogenous group of cells. Their unique position in between the NK cells and CD127⁺ ILCs, however, prompted us to investigate potential relationships between these cell clusters.

In recent years, several studies have explored developmental pathways by applying computational approaches on mass cytometry datasets. Wanderlust, accurately predicted B cell lymphopoiesis²⁴ and Wishbone was found to recover the T cell developmental pathway²⁸ at single-cell resolution. However, Wanderlust is not suitable to predict multi-lineage differentiation trajectories. While Wishbone can be used to identify bifurcating developmental trajectories, it needs the designation of a user-defined precursor cell type. As we wished to investigate potential developmental relationships without pre-assumptions we developed a novel computational approach to visualize the evolution of the t-SNE map over the course of the optimization. t-SNE is a non-linear dimensionality reduction algorithm which projects the high-

dimensional similarities onto a two-dimensional map based on the concurrent marker expression profiles¹⁹. Here t-SNE not only employs bimodal distribution patterns but also incorporates gradients of the expression of cellular markers and therefore offers superior resolution. Importantly, the Cytosplore framework²¹ can visualize every iteration by making use of the A-tSNE²⁹. This allowed us to analyze potential relationships between the int-ILC, ILC1, ILC2, ILC3 and NK clusters through visualization of gradients along putative differentiation trajectories. Such gradients are clearly visible in our Cytosplore analysis (**Fig. 2**) and contribute to the generation of cell clusters. Our current results indicate that at least some of those gradual changes in marker expression profiles correlate with differentiation pathways of immune subsets. Consistent with the observed plasticity among ILCs^{13,15}, the analysis revealed a clear trajectory between the ILC2 and ILC3 clusters. This may imply that the CD103⁻ ILC2 can differentiate into CD103⁺ ILC3 locally depending on physiological or pathological conditions. Alternatively, the fetal ILC2s may leave the intestine, in line with previous reports that ILC2s can be found in the peripheral blood³⁰ but are virtually absent in the human intestine after birth¹³. In addition, a trajectory within the CD56⁺ cell compartment was revealed, where the CD8a⁻ int-ILC was connected with the CD56⁺ ILC3 on one side and with the CD8a⁺ int-ILC and the NK cells on the other. Importantly, while the above analysis was performed on the innate cell population present in the 7 fetal intestines collectively, similar relationships between cell populations were revealed when the innate cell compartment of each fetal sample was analyzed individually, attesting to the robustness of the approach (**Fig. S2 B**).

The putative link between the int-ILC and the mature ILC and NK cells is further strengthened by several other observations. First, both the cytokine production profiles and CD94 expression profile *ex vivo* link the CD8a⁺ int-ILCs to NK cells and the CD8a⁻ int-ILCs to the ILC3s. Second, the expression pattern of the transcription factors by int-ILCs is heterogeneous with features of both NK cells (Eomes and T-bet) and ILC3s (GATA3 and ROR γ t) where the CD8a⁺ int-ILCs resemble the NK cells while the CD8a⁻ int-ILCs are closer to CD127⁺ ILCs. Finally, in the OP9-based co-culture system, in the presence of NK cytokines purified int-ILC expanded and displayed a CD45RA⁺Eomes⁺/T-bet⁺ NK cell phenotype while in the absence of cytokines the cells did not expand but acquired a stable CD127⁺CD117⁺ROR γ t⁺ ILC3 phenotype.

Further dissection of the CD8a⁻ int-ILC compartment demonstrated the existence of three distinct subpopulations based on differential expression of CD94 and CD117: CD94⁺CD117⁻, CD94⁻CD117⁻ and CD94⁻CD117⁺. In our *in vitro* experiments both

the Eomes-expressing CD94⁺CD117⁻ and non-Eomes-expressing CD94⁻CD117⁻ and CD94⁻CD117⁺ subpopulations could differentiate into CD45RA⁺ NK cells when cultured with NK cytokine mix. Furthermore, the differentiation into CD45RA⁺ NK cells was most efficient in the case of the CD94⁺CD117⁻ cells and least for the CD94⁻CD117⁺ cells, compatible with a model where the CD94⁺CD117⁻ cells are positioned close to NK cells, the CD94⁻CD117⁺ cells most distant and the CD94⁻CD117⁻ cells in between. The acquisition of CD8a by the CD94⁻CD8a⁻ int-ILCs in these cultures indicates that the CD8a⁺ int-ILC may also be an intermediate stage towards NK cell differentiation. In the absence of cytokines CD117⁺CD127⁺ ILC3-like cells could be generated from both CD94⁻CD117⁺ and CD94⁻CD117⁻ cells but not from CD94⁺CD117⁻ cells. Together this indicates that CD94⁺CD117⁻ cells can exclusively differentiate into NK cells while the other two populations can differentiate into both NK cells and ILC3s, at least under the *in vitro* conditions employed.

In the absence of cytokines the int-ILC changed into ILC3-like cells without signs of cell expansion, cell division or cell death, arguing that the generation of ILC3 from the int-ILC is not due to selective outgrowth of contaminating ILC3s. In agreement, we did not observe any proliferative response of flow cytometry-purified ILC3 under the same experimental conditions.

In mice, it has been shown that developmental hierarchy of ILCs goes from the common lymphoid progenitor to mature ILCs via α 4 β 7-expressing lymphoid progenitor, early innate lymphoid progenitor, common helper ILC progenitor, and the ILC precursor⁷. Here the early innate lymphoid progenitor has been distinguished from other progenitors by the lack of CD127 and ILC lineage-specific transcription factors³¹, while the ILC precursor exhibits co-expression of transcription factors associated with ILC1, ILC2 and ILC3 subsets³². Finally, a murine fetal transitional CD127⁺ ILCP has been identified in the intestine which expresses varying amount of T-bet, GATA3 and ROR γ t³³. In humans, two studies have shown that ILC3s can be generated from ROR γ t⁺CD34⁺ progenitors from tonsils and intestines^{9,10} but little is known about the intermediate stages. Interestingly, Scoville et al.¹⁰ generated both NK cells and the three types of helper ILCs from these CD34⁺ progenitors *in vitro*, however, the generated cells did not express CD127 but rather CD161 and intracellular ILC-related cytokine profiles. Also, a NK cell lineage-restricted CD34⁺ progenitor was identified in the human fetal liver and bone marrow³⁴. In contrast, CD127⁻ int-ILC in our study express CD45RO and variable levels of Eomes, T-bet, GATA3 and ROR γ t, but no CD34 and CD45RA, markers expressed by most human

progenitors. Also, with our mass cytometry approach we have been unable to identify cells with an int-ILC phenotype in the human fetal liver and fetal spleen (not shown), indicating that the int-ILC may specifically reside in mucosal tissues. Together, the cell surface phenotype, tissue distribution and transcription factor profiles of CD127⁺ int-ILC suggests that these cells are distinct from previously identified ILC progenitors and may be in an intermediate differentiation stage among ILC lineages. Finally, we observed that the ILC3s and NK cells derived from the CD8a⁻ int-ILC could partly revert their phenotype upon prolonged culture indicating that the int-ILC may represent an intermediate between two plastic lineages (not shown).

It has been shown that environmental cues including OP9/OP9-DL1 stromal cells and cytokines such as IL-7 and SCF play an important role in driving ILC3 differentiation^{9,10,35}. While the addition of SCF and IL-7 did promote significant expansion of the CD8a⁻ int-ILCs, they did not differentiate into other types of cells (not shown). Instead, the differentiation of CD8a⁻ int-ILCs toward ILC3s occurred in cytokine-free medium. In mice, Notch signalling for ILC3 development is necessary in adults but not in fetuses⁸, while in humans, the differentiation of CD34⁺ progenitors to ILC3s can occur without Notch signalling^{9,10}. Consistent with these observations the generation of ILC3s from the CD8a⁻ int-ILCs was Notch independent.

In conclusion, we delineated the heterogeneity of ILCs in the human fetal intestine and developed a computational model to predict potential differentiation trajectories based on mass cytometry data. This allowed the identification of a previously unidentified innate cell cluster that harbors cells that can differentiate into NK cells and ILC3-like cells *in vitro*. This may provide plasticity in the human fetal intestine in response to external stimuli.

MATERIALS AND METHODS

Human fetal intestine and cell isolation

Human fetal intestines from elective abortions were collected after informed consent. Approval by the medical ethical commission of the LUMC (protocol P08.087) was obtained in accordance with the local ethical guidelines and the declaration of Helsinki. The gestational age ranged from 16 to 22 weeks. Single cell suspensions from fetal intestines were prepared as previously described¹⁸. Briefly, the mesentery, colon part and meconium were removed from the fetal intestine. The intestines were then cut into small fragments and treated with 1 mM 1,4-Dithiothreitol (Fluka) in 15 mL

of HBSS (Sigma-Aldrich) for 2 x 10 min (replacing buffer) at room temperature (rT) to dissolve the mucus and subsequently with 1 mM EDTA (Merck) in 15 mL of HBSS under rotation for 2 x 1 h (replacing buffer) at 37 °C to separate the epithelium from the lamina propria fraction. To obtain single-cell suspensions from the lamina propria, the intestines were rinsed with HBSS and incubated with 15 mL Iscove's Modified Dulbecco's Medium (IMDM; Lonza) supplemented with 10% FCS, 10 U/mL collagenase IV (Worthington), 200 µg/mL DNase I grade II (Roche Diagnostics), at 37 °C overnight, after which cell suspensions were filtered through a 70 µm nylon cell strainer. Finally, the immune cells were isolated with a Percoll (GE Healthcare) gradient and stored in liquid nitrogen.

Mass cytometry antibody staining and data acquisition

Details on antibodies used are listed in **Table S1**. Conjugation of the purified antibodies with metal reporters was performed with the MaxPar X8 antibody labeling kit (Fluidigm Sciences) according to the manufacturer's instruction. Procedures for mass cytometry antibody staining and data acquisition were carried out as previously described¹⁸. Briefly, cells from fetal intestinal lamina propria were thawed and incubated with 1 mL 500x diluted 500 µM Cell-ID intercalator-I03Rh (Fluidigm Sciences) for 15 min at rT to identify dead cells. Cells were then stained with metal-conjugated antibodies for 45 min at rT. After staining, cells were labeled with 1 mL 1,000x diluted 125 µM Cell-ID intercalator-Ir (Fluidigm Sciences) to stain all cells in MaxPar Fix and Perm Buffer (Fluidigm Sciences) overnight at 4 °C. Finally, cells were acquired by CyTOF 2TM mass cytometer (Fluidigm Sciences). Data were normalized by using EQ Four Element Calibration Beads (Fluidigm Sciences) with the reference EQ passport P13H2302 during the course of each experiment.

Mass cytometry data analysis

The biaxial plots showing antibody staining patterns in **Fig. S1** were generated in Cytobank³⁶. Data for single, live CD45⁺ cells gated from each fetal intestine individually using Cytobank 36 as shown in **Fig. S1 A**, were sample tagged and hyperbolic arcsinh transformed with a cofactor of 5 prior to t-SNE analysis. The 907 clusters shown in **Fig. S1 C** were identified by analyzing the entire immune system (CD45⁺ cells) using the t-SNE-ACCENSE analysis pipeline as described before¹⁸. Next, t-SNE was performed for the ILC dataset using A-tSNE²⁹ in Cytosplore²¹. t-SNE was carried out with default parameters (perplexity: 30; iterations: 1000). All t-SNE plots were generated in Cytosplore. Hierarchical clustering of the heatmap was created with Pearson Correlation and average linkage clustering in

MultiExperiment Viewer (<http://www.tm4.org>). Wanderlust analysis was performed on cells that were selected along the linear CD56 expression continuum at stage 4 of the t-SNE computation with the CD56⁺CD8a⁺ ILC3 cluster as starting point (as this cluster is located at the outer end of the CD56 trajectory), using Cyt in Matlab²⁴.

Antibodies and flow cytometry

FITC-conjugated anti-CD11c (3.9), PerCP-Cy5.5-conjugated anti-CD45RO (UCHL1), PE/Dazzle 594-conjugated anti-CD45RA (HI100), PE-Cy7-conjugated anti-CD127 (A019D5), Brilliant Violet 605-conjugated anti-CRTH2 (BM16), anti-T-bet (4B10), PE-conjugated anti-T-bet (4B10), anti-IFN- γ (4S.B3), anti-IL-5 (TRFK5), anti-IL-13 (JES10-5A2), anti-IL-17A (BL168) and anti-TNF- α (Mab11) were purchased from Biolegend. The following monoclonal antibodies were purchased from BD: FITC-conjugated anti-CD3 (SK7), anti-CD19 (4G7) and anti-CD14 (M \square P9), APC-conjugated anti-CD117 (YB5.B8), APC-R700-conjugated anti-CD56 (NCAM16.2), V450-conjugated anti-CD7 (M-T701), Brilliant Violet 605-conjugated anti-CD94 (HP-3D9), PE-conjugated anti-CD94 (HP-3D9), anti-ROR γ t (Q21-559), anti-Ki-67 (B56), anti-Perforin (δ G9), anti-IL-4 (3010.211). PE-conjugated anti-Eomes (WD1928), anti-GATA3 (TWAJ), anti-Granzyme B (GB11), and eFluor 660-conjugated anti-GATA3 (TWAJ) were purchased from eBioscience. PE-conjugated anti-IL-22 (IC7821P) was purchased from R&D systems. Pacific Orange-conjugated anti-CD8a (3B5) was purchased from Life technologies.

For the cell surface staining, cells were incubated with fluorochrome-conjugated antibodies and human FC block (Biolegend) for 30-45 min at 4 °C. The transcription factor staining was performed by using Foxp3 Staining Buffer Set (eBioscience) according to the manufacturer's instruction. For the intracellular cytokine staining/cytotoxic molecule, cells were stimulated with 0.1 mg/mL PMA (Sigma-Aldrich) and 1 μ g/mL Ionomycin (Sigma-Aldrich) for 6 h at 37 °C and GolgiPlug (BD Biosciences) was added for the final 4 h after which cells were stained by using Fixation Buffer and Intracellular Staining Perm Wash Buffer (Biolegend). Cells were acquired on an LSR II cytometer (BD Biosciences) or sorted on a FACSAriaTM III sorter (BD Biosciences) based on the gating strategy as shown in **Fig. 3 A**. Data were analyzed with FlowJo V10 software.

Quantitative Real-Time PCR (RT-PCR)

RNA extraction was performed with the NucleoSpin[®] RNA XS kit (Macherey-Nagel). cDNA was synthesized with the High Capacity cDNA Reverse Transcription kit (Applied Biosystems). RT-PCR was performed in a

StepOnePlus™ Real-Time PCR Systems (Applied Biosystems) with FastStart Universal SYBR Green Master Mix (Roche). ΔC_t values were calculated using GAPDH as reference gene. The sequences of RT-PCR primers are as follows: GAPDH, forward primer: 5'-GTCTCCTCTGACTTCAACAGCG-3'; reverse primer, 5'-ACCACCCTGTTGCTGTAGCCAA-3'; AHR, forward primer: 5'-CTTAGGCTCAGCGTCAGTTA-3'; reverse primer, 5'-GTAAGTTCAGGCCTTCTCTG-3'; ID2, forward primer: 5'-TTGTGAGCCTGCATCACCAGAG-3'; reverse primer, 5'-AGCCACACAGTGCTTTGCTGTC-3'; NFIL3, forward primer: 5'-TGGAGAAGACGAGCAACAGGTC-3'; reverse primer, 5'-CTTGTGTGGCAAGGCAGAGGAA-3'; ZBTB16, forward primer: 5'-GAGCTTCCTGATAACGAGGCTG-3'; reverse primer, 5'-AGCCGCAAACACTATCCAGGAACC-3'; TOX, forward primer: 5'-AGCATACAGAGCCAGCCTTG-3'; reverse primer, 5'-TGCATGGCAGTTAGGTGAGG-3'; and TCF1, forward primer: 5'-TGCAGCTATACCCAGGCTGG-3'; reverse primer, 5'-CCTCGACCGCCTCTTCTTC-3'.

Cell culture and differentiation assays

OP9-DLI or OP9 stromal cells were maintained in Minimum Essential Medium α (Lonza) supplemented with 10% FCS. Flow cytometry-purified CD8a⁻ int-ILCs or CD94⁺CD117⁻, CD94⁻CD117⁻ and CD94⁻CD117⁺ subpopulations (500 cells/well) or CD8a⁺ int-ILCs (100 cells/well) were co-cultured with irradiated OP9 or OP9-DLI stromal cells (1,500 RAD, 5,000 cells/well) in a 96 well plate (Corning) and maintained in culture medium (IMDM supplemented with 10% human serum or in culture medium containing 25 ng/mL SCF (Miltenyi Biotec), 25 ng/mL IL-7 (Peprotech), 10 U/mL IL-2 (Novartis) and 10 ng/mL IL-15 (R&D Systems) or only IL-15. The phenotype of generated progeny was determined by flow cytometry.

Cytokine secretion

CD8a⁻ int-ILCs and ILC3 (2,000 cells/well) were stimulated with 10 U/mL IL-2 (Novartis), 50 ng/mL IL-1 β (Peprotech) and 50 ng/mL IL-23 (Peprotech) for 4 days. TNF- α , IL-17A and IL-22 were measured by using Bio-Plex Pro™ human cytokine 17-plex panel kit and Bio-Plex Pro™ human Treg cytokine panel 12-plex kit (Bio-Rad).

REFERENCES

1. Spits, H. et al. Innate lymphoid cells--a proposal for uniform nomenclature. *Nat. Rev. Immunol.* 13, 145–149 (2013).
2. Hazenberg, M. D. & Spits, H. Human innate lymphoid cells. *Blood* 124, 700–709 (2014).
3. Cella, M. et al. A human natural killer cell subset provides an innate source of IL-22 for mucosal immunity. *Nature* 457, 722–725 (2009).
4. Cupedo, T. et al. Human fetal lymphoid tissue-inducer cells are interleukin 17-producing precursors to RORC+ CD127+ natural killer-like cells. *Nat. Immunol.* 10, 66–74 (2009).
5. Gasteiger, G., Fan, X., Dikiy, S., Lee, S. Y. & Rudensky, A. Y. Tissue residency of innate lymphoid cells in lymphoid and nonlymphoid organs. *Science* 350, 981–985 (2015).
6. Juelke, K. & Romagnani, C. Differentiation of human innate lymphoid cells (ILCs). *Curr. Opin. Immunol.* 38, 75–85 (2016).
7. Ishizuka, I. E., Constantinides, M. G., Gudjonson, H. & Bendelac, A. The Innate Lymphoid Cell Precursor. *Annu. Rev. Immunol.* 34, 299–316 (2016).
8. Possot, C. et al. Notch signaling is necessary for adult, but not fetal, development of ROR γ t(+) innate lymphoid cells. *Nat. Immunol.* 12, 949–958 (2011).
9. Montaldo, E. et al. Human ROR γ t CD34 Cells Are Lineage-Specified Progenitors of Group 3 ROR γ t Innate Lymphoid Cells. *Immunity* 41, 988–1000 (2014).
10. Scoville, S. D. et al. A Progenitor Cell Expressing Transcription Factor ROR γ t Generates All Human Innate Lymphoid Cell Subsets. *Immunity* 44, 1140–1150 (2016).
11. Lim, A. I. et al. Systemic Human ILC Precursors Provide a Substrate for Tissue ILC Differentiation. *Cell* 168, 1086–1100.e10 (2017).
12. Bernink, J. H. et al. Human type 1 innate lymphoid cells accumulate in inflamed mucosal tissues. *Nat. Immunol.* 14, 221–229 (2013).
13. Bernink, J. H. et al. Interleukin-12 and -23 Control Plasticity of CD127(+) Group 1 and Group 3 Innate Lymphoid Cells in the Intestinal Lamina Propria. *Immunity* 43, 146–160 (2015).
14. Lim, A. I. et al. IL-12 drives functional plasticity of human group 2 innate lymphoid cells. *J. Exp. Med.* 213, 569–583 (2016).
15. Bal, S. M. et al. IL-1 β , IL-4 and IL-12 control the fate of group 2 innate lymphoid cells in human airway inflammation in the lungs. *Nat. Immunol.* 17, 636–645 (2016).
16. Bandura, D. R. et al. Mass cytometry: technique for real time single cell multitarget immunoassay based on inductively coupled plasma time-of-flight mass spectrometry. *Anal. Chem.* 81, 6813–6822 (2009).
17. van Unen, V. et al. Visual analysis of mass cytometry data by hierarchical stochastic neighbour embedding reveals rare cell types. *Nat. Commun.* (2017).
18. van Unen, V. et al. Mass Cytometry of the Human Mucosal Immune System Identifies Tissue- and Disease-Associated Immune Subsets. *Immunity* 44, 1227–1239 (2016).
19. Maaten, L. van der & Hinton, G. Visualizing Data using t-SNE. *J. Mach. Learn. Res.* 9, 2579–2605 (2008).
20. Shekhar, K., Brodin, P., Davis, M. M. & Chakraborty, A. K. Automatic Classification of Cellular Expression by Nonlinear Stochastic Embedding (ACCENSE). *Proc. Natl. Acad. Sci. U. S. A.* 111, 202–207 (2014).
21. Höllt, T. et al. Cytosplore: Interactive Immune Cell Phenotyping for Large Single-Cell Datasets. *Comput. Graph. Forum* 35, 171–180 (2016).
22. Björklund, Å. K. et al. The heterogeneity of human CD127(+) innate lymphoid cells revealed by single-cell RNA sequencing. *Nat. Immunol.* 17, 451–460 (2016).
23. Simoni, Y. et al. Human Innate Lymphoid Cell Subsets Possess Tissue-Type Based Heterogeneity in Phenotype and Frequency. *Immunity* 46, 148–161 (2017).
24. Bendall, S. C. et al. Single-Cell Trajectory Detection Uncovers Progression and Regulatory Coordination in Human B Cell Development. *Cell* 157, 714–725 (2014).
25. Artis, D. & Spits, H. The biology of innate lymphoid cells. *Nature* 517, 293–301 (2015).
26. Freud, A. G. et al. Evidence for discrete stages of human natural killer cell

- differentiation in vivo. *J. Exp. Med.* 203, 1033–1043 (2006).
27. Klose, C. S. N. et al. Differentiation of type 1 ILCs from a common progenitor to all helper-like innate lymphoid cell lineages. *Cell* 157, 340–356 (2014).
 28. Setty, M. et al. Wishbone identifies bifurcating developmental trajectories from single-cell data. *Nat. Biotechnol.* 34, 637–645 (2016).
 29. Pezzotti, N. et al. Approximated and User Steerable tSNE for Progressive Visual Analytics. *IEEE Trans. Vis. Comput. Graph.* (2016). doi:10.1109/TVCG.2016.2570755
 30. Mjösberg, J. M. et al. Human IL-25- and IL-33-responsive type 2 innate lymphoid cells are defined by expression of CRTH2 and CD161. *Nat. Immunol.* 12, 1055–1062 (2011).
 31. Yang, Q. et al. TCF-1 upregulation identifies early innate lymphoid progenitors in the bone marrow. *Nat. Immunol.* 16, 1044–1050 (2015).
 32. Ishizuka, I. E. et al. Single-cell analysis defines the divergence between the innate lymphoid cell lineage and lymphoid tissue-inducer cell lineage. *Nat. Immunol.* 17, 269–276 (2016).
 33. Bando, J. K., Liang, H.-E. & Locksley, R. M. Identification and distribution of developing innate lymphoid cells in the fetal mouse intestine. *Nat. Immunol.* 16, 153–160 (2015).
 34. Renoux, V. M. et al. Identification of a Human Natural Killer Cell Lineage-Restricted Progenitor in Fetal and Adult Tissues. *Immunity* 43, 394–407 (2015).
 35. Satoh-Takayama, N. et al. IL-7 and IL-15 independently program the differentiation of intestinal CD3-NKp46+ cell subsets from Id2-dependent precursors. *J. Exp. Med.* 207, 273–280 (2010).
 36. Kotecha, N., Krutzik, P. O. & Irish, J. M. Web-based analysis and publication of flow cytometry experiments. *Curr. Protoc. Cytom.* Chapter 10, Unit 10.17 (2010).

SUPPLEMENTAL INFORMATION

	Antigen	Tag	Clone	Supplier	Cat.	Final dilution
1	CD127	¹⁶⁵ Ho	AO19D5	DVS	3165008B	1/800
2	CCR6	¹⁴¹ Pr	G034E3	DVS	3141003A	1/200
3	CD8a	¹⁴⁶ Nd	RPA-T8	DVS	3146001B	1/200
4	CD11c	¹⁶² Dy	Bu15	DVS	3162005B	1/200
5	CD38	¹⁷² Yb	HIT2	DVS	3172007B	1/200
6	CD45	⁸⁸ v	HI30	DVS	3089003B	1/100
7	CD117	¹⁴³ Nd	104D2	DVS	3143001B	1/100
8	CD4	¹⁴⁵ Nd	RPA-T4	DVS	3145001B	1/100
9	CD16	¹⁴⁸ Nd	3G8	DVS	3148004B	1/100
10	CD25	¹⁴⁹ Sm	2A3	DVS	3149010B	1/100
11	CD123	¹⁵¹ Eu	6H6	DVS	3151001B	1/100
12	CD7	¹⁵³ Eu	CD7-6B7	DVS	3153014B	1/100
13	CD163	¹⁵⁴ Sm	GHI161	DVS	3154007B	1/100
14	CCR7	¹⁵⁸ Tb	G043H7	DVS	3159003A	1/100
15	CD14	¹⁶⁰ Gd	M5E2	DVS	3160001B	1/100
16	CD161	¹⁶⁴ Dy	HP-3G10	DVS	3164009B	1/100
17	CD27	¹⁶⁷ Er	O323	DVS	3167002B	1/100
18	CD45RA	¹⁶⁹ Tm	HI100	DVS	3169008B	1/100
19	CD3	¹⁷⁰ Er	UCHT1	DVS	3170001B	1/100
20	PD-1	¹⁷² Lu	EH 12.2H7	DVS	3175008B	1/100
21	CD56	¹⁷⁸ Yb	NCAM16.2	DVS	3176008B	1/100
22	CD11b	¹⁴⁴ Nd	ICRF44	DVS	3144001B	1/100
23	TCRgd	¹⁵² Sm	11F2	DVS	3152008B	1/50
24	HLA-DR	¹⁵⁸ Er	L243	BioL	307651	1/200
25	CD20	¹⁶² Dy	2H7	BioL	302343	1/200
26	CD34	¹⁴² Nd	HIB19	BioL	343531	1/100
27	IgM	¹⁵⁰ Nd	MHM88	BioL	314527	1/100
28	CD103	¹⁵⁸ Gd	Ber-ACT8	BioL	350202	1/100
29	CRTH2	¹⁵⁸ Gd	BM16	BioL	350102	1/100
30	CD28	¹⁷¹ Yb	CD28.2	BioL	302902	1/100
31	CD45RO	¹⁷³ Yb	UCHL1	BioL	304239	1/100
32	CD122	¹⁵⁸ Gd	TU27	BioL	339002	1/50
33	KLRG-1	¹⁶¹ Dy	REA261	MACS	120-014-229	1/50
34	CD8b	¹⁶⁶ Er	SID8BEE	ebio	14-5273	1/50
35	NKp46	¹⁷⁴ Yb	9E2	BioL	331902	1/40

DVS Sciences (DVS), eBioscience (eBio) and Biologend (BioL).

Table S1. CyTOF antibody panel

The conjugation, validation and titration of all the antibodies which were not bought from DVS were done in house.

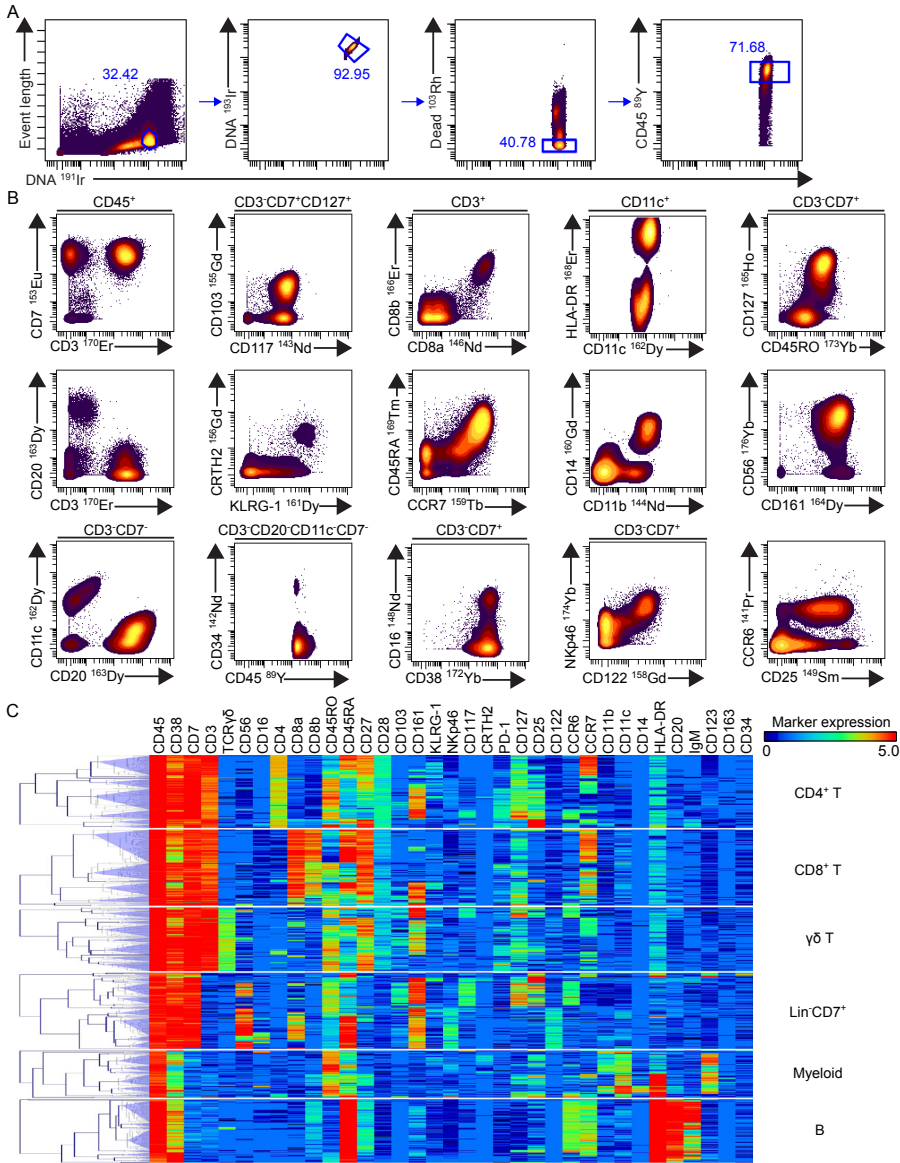
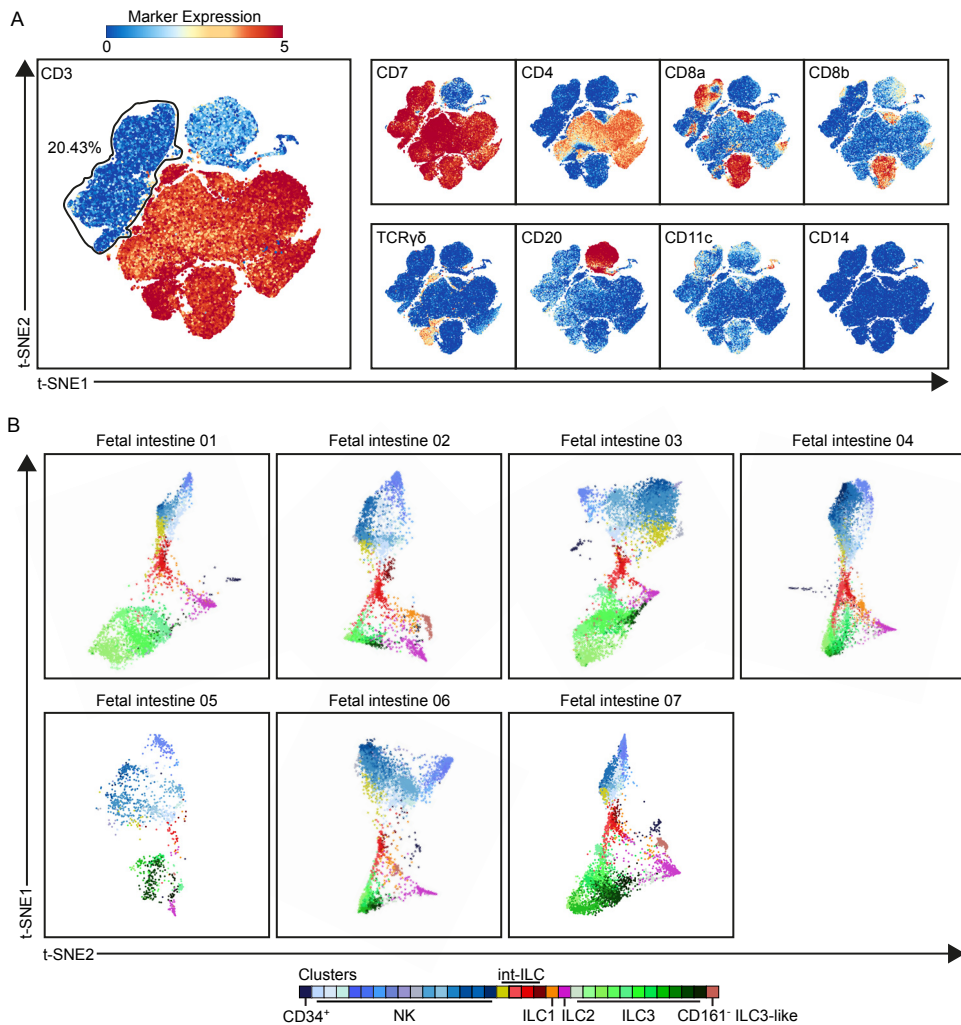


Fig. S1. Analysis of the entire immune system in the human fetal intestine using mass cytometry. (A) Representative biaxial density dot plots from one fetal intestine showing the gating strategy for single, live CD45+ cells with percentages analysed by mass cytometry (N=7). Event length is a mass cytometry parameter defined as signal duration for the number of scans taken to acquire a given ion cloud. (B) Representative biaxial density dot plots from one fetal intestine showing the typical cell staining profiles of the antibodies used in mass cytometry after gating as shown in panel A (N=7). Gated cell populations are annotated above the plots. (C) A heatmap showing the median ArcSinh5-transformed marker expression values of the total 907 clusters identified by analyzing the entire immune system (CD45+ cells) from 7 fetal intestines using the t-SNE-ACCENSE analysis pipeline (clustering per individual sample) for each of the 6 major immune lineages individually, as described before¹⁸, and hierarchical clustering thereof. four independent experiments).

Mass Cytometry Reveals Innate Lymphoid Cell Differentiation Pathways in the Human Fetal Intestine



6

Fig. S2. t-SNE-based analysis of the LinCD7⁺ innate immune compartment in the human fetal intestine.

(A) Gating strategy of the LinCD7⁺ innate cell population in the human fetal intestine. t-SNE embeddings of the collective CD45⁺ cells (2.2x10⁵ cells) from 7 fetal intestines at single-cell resolution. Colors of cells represent ArcSinh5-transformed expression values of indicated markers.

(B) Monitoring t-SNE computation dynamics for each individual fetal intestine. t-SNE embeddings of the ILC mass cytometry data showing single cells at stage 4 of the optimization course of the t-SNE computation for each individual fetal intestine (N=7). Colors represent the cluster partitions.

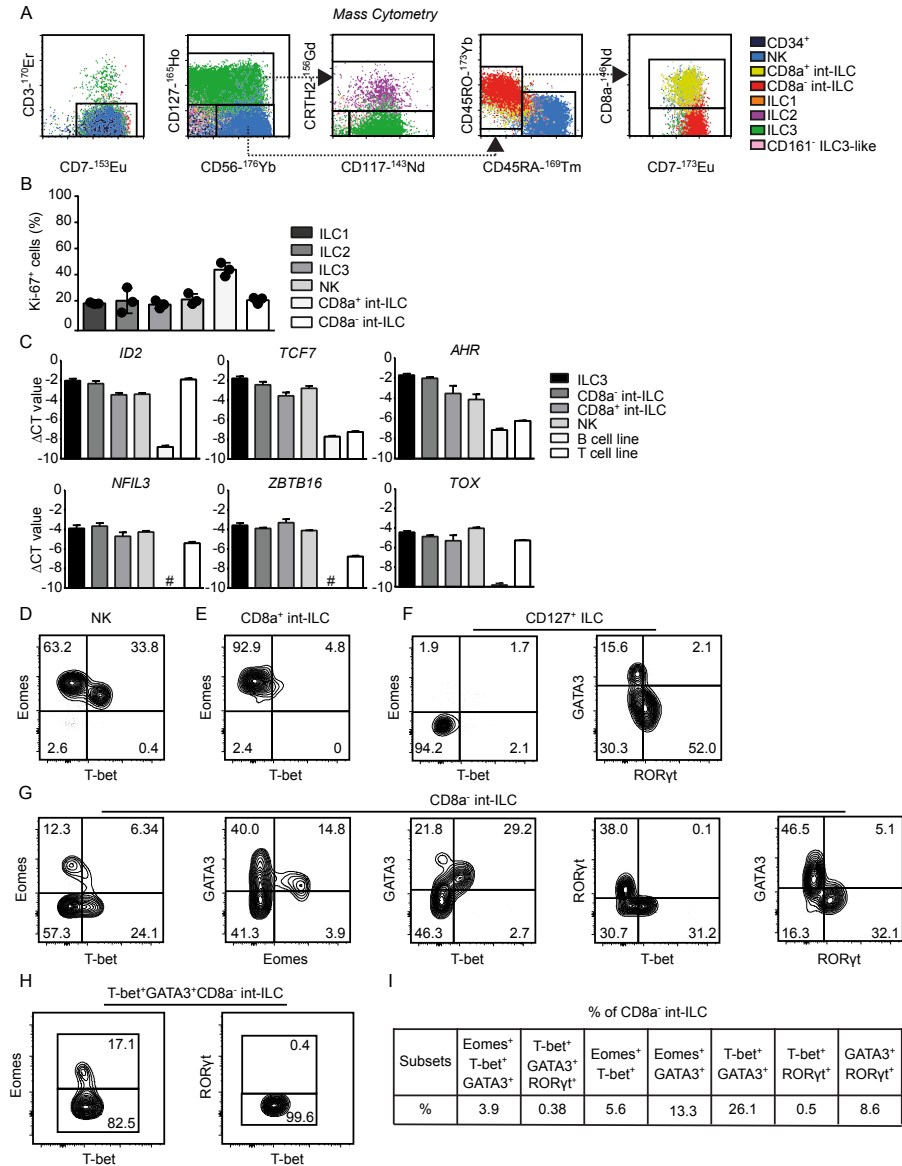


Fig. S3. Ki-67 and transcription factor expression profiles of fetal intestinal ILCs ex vivo. (A) Minimal antibody panel required for phenotyping ILC and int-ILC subsets in the human fetal intestine. Biaxial plots showing the expression of the indicated markers by ILC1, ILC2, ILC3, NK and int-ILC subsets based on mass cytometry data derived from 7 human fetal intestines. Color represents the different subsets identified by the t-SNE-based analysis shown in Fig. 1 B and numbers of x-axis and y-axis represent ArcSinh5-transformed expression values of indicated markers. (B) Quantification of Ki-67 positive cells within indicated subsets obtained from 3 different human fetal intestines (Two independent experiments). Error bar shows mean \pm SD. (C) Relative mRNA expression of ID2, TCF, AHR, NFIL3, ZBTB16 and TOX by the purified ILC subsets, B and T cell lines analyzed by RT-PCR (Three independent experiments). GAPDH as reference gene. # indicates that the Δ CT value is below -10. Error bar shows mean \pm SD. (D) Representative biaxial plots showing the expression of T-bet and Eomes, and GATA3 and ROR γ t by fetal intestinal CD127⁺ ILC. (E-F) Representative biaxial plots showing the expression of T-bet and Eomes by (E) fetal intestinal NK cells, and (F) CD8a⁺ int-ILC as defined in Fig. 3 A with flow cytometry. (G) Representative biaxial plots showing the combinatorial expression profiles of Eomes, T-bet, GATA3 and ROR γ t by fetal intestinal CD8a⁺ int-ILC. (H) Expression of Eomes and ROR γ t by fetal intestinal T-bet⁺GATA3⁺CD8a⁺ int-ILC. (I) Quantification of transcription factor positive cells of fetal intestinal CD8a⁺ int-ILC. (Two independent experiments).

Mass Cytometry Reveals Innate Lymphoid Cell Differentiation Pathways in the Human Fetal Intestine

6

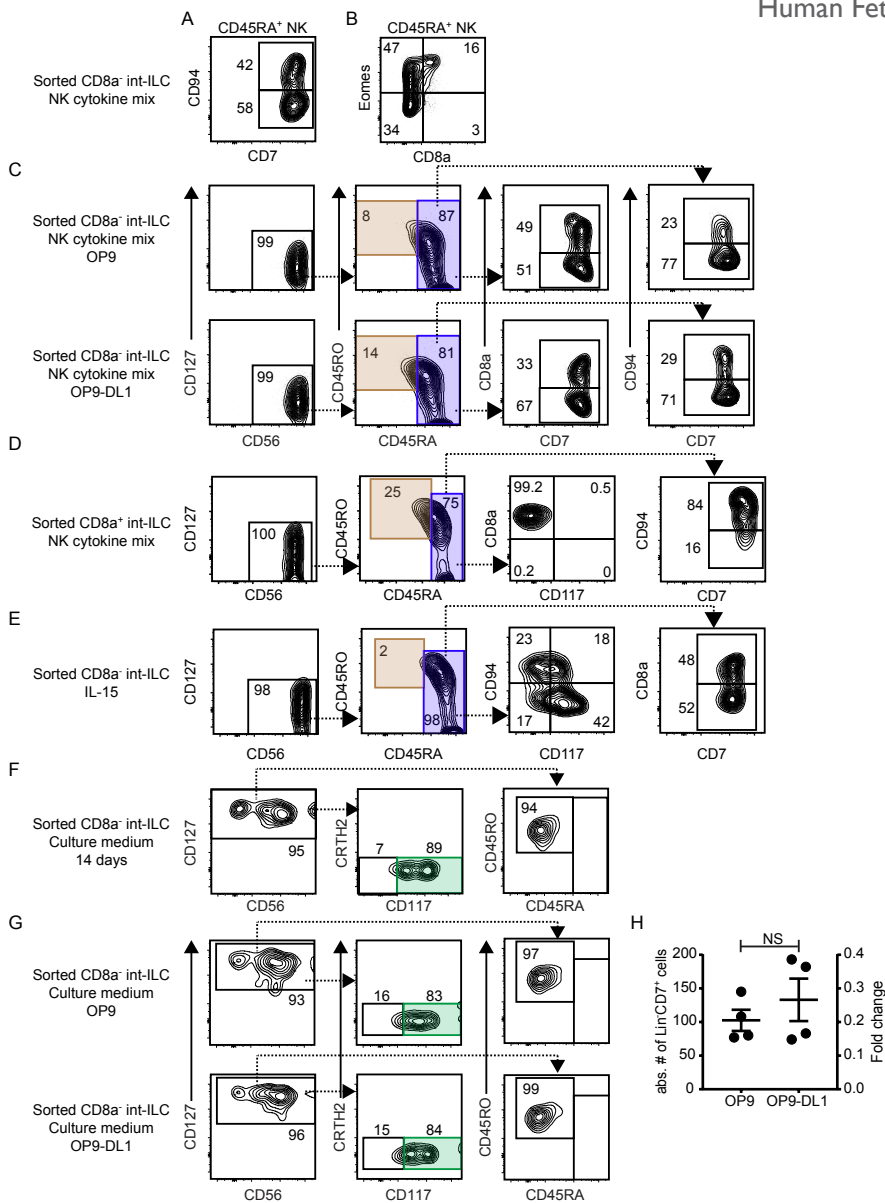


Fig. S4. CD8a⁺ int-ILC can differentiate into CD45RA⁺ NK Cells and ILC3. (A-E) Purified CD8a⁺ int-ILC (500 cells/well) and CD8a⁺ int-ILC (100 cells/well) populations were co-cultured with irradiated OP9-DL1 or OP9 stromal cells for 7 days either with culture medium supplemented with SCF, IL-7, IL-2, IL-15 (referred to as NK cytokine mix) or supplemented with IL-15. Generated cells were harvested and analyzed by flow cytometry. Duplicated wells were included for each condition in each experiment. Representative plots show a single duplicate. (A and B) Biaxial plots show the expression of CD94 (A) and the transcription factor Eomes (B) by generated CD45RA⁺ NK cells from sorted CD8a⁺ int-ILCs with NK cytokine mix. (Three to five independent experiments). (C-E) Representative biaxial plots depict the phenotypes of the generated Lin⁺CD7⁺ cells from (C) sorted CD8a⁺ int-ILCs with NK cytokine mix with irradiated OP9-DL1 or OP9 stromal cells and (D) sorted CD8a⁺ int-ILCs with NK cytokine mix and (E) sorted CD8a⁺ int-ILCs with IL-15. (Two independent experiments). (F-H) Purified CD8a⁺ int-ILC (500 cells/well) were co-cultured either with irradiated OP9-DL1 or with OP9 stromal cells with cytokine-free culture medium for 14 days (F) and 7 days (G and H). Generated cells were harvested and analyzed by flow cytometry (F and G). Representative biaxial plots depict the phenotypes of the generated Lin⁺CD7⁺ cells. (Two independent experiments). (H) Quantification in absolute cell number (left axis) and fold change (right axis) compared to the number of initially sorted cells. (Two independent experiments). Error bar shows mean ± SEM.





CHAPTER 7

Summarising Discussion



CHAPTER 7

Summarising Discussion

Definition of a distinct immune subset

It is increasingly recognized that in order to gain further insights into human disorders and develop new therapeutic strategies and diagnostic tools, it is critical to have a comprehensive overview of immune cell subsets resident in tissues under physiological and pathological conditions. Flow cytometry has been the golden standard for analyzing immune cell subsets, and with a typical experiment dozens of immune subsets can be discriminated. Due to the lack of spectrally-resolvable fluorochromes, mass cytometry utilizing metal-conjugated antibodies has shown to be a powerful tool for dissecting the immune landscape even further¹. It currently allows for the simultaneous measurement of up to 40 markers, three times as many as flow cytometry. While most mass cytometry studies have so far focused on in-depth analysis of one immune lineage¹, we choose a broad coverage approach by analyzing across all immune lineages simultaneously. We applied this to intestinal samples obtained from controls and patients with intestinal diseases, celiac disease and inflammatory bowel disease (IBD) in particular. While the role of several immune subsets in driving intestinal pathology had been studied for various intestinal diseases^{2, 3}, this broad and system-wide approach revealed previously unappreciated heterogeneity in the mucosal immune system and provided evidence for tissue- and disease-specific immune signatures.

Indeed, mass cytometry and other high-dimensional, single-cell analysis techniques have greatly increased the number of phenotypically distinct cell subsets within the immune system. In our first study on gastrointestinal disorders (**Chapter 2**) we were able to distinguish 142 distinct immune subsets using a 28-antibody panel, and in our second study focusing on IBD (**Chapter 5**) we distinguished 309 distinct immune subsets in the intestine alone using a 36-antibody panel. These findings have raised obvious questions about the true distinctiveness and function of such cell subsets, and concerns on the definition of a “subset”. Our view is that a subset is a set of similar cells displaying a distinct marker expression pattern based on the complete mass cytometry-antibody panel, where unsupervised computer-generated subset definition is manually checked for validity. Indeed, many of them could be defined as the same immune cell population displaying different levels of activation or maturation stages. To uncover potential relationships between immune subsets,

we exploited the ability of Cytosplore (**Chapter 3**) to visualize the evolution of the t-SNE map (**Chapter 6**), a pathway analysis. These results demonstrated several potential differentiation trajectories of innate lymphoid cell (ILC) subsets in the human fetal intestine, confirmed by *in vitro* experiments. This suggests that these subsets are indeed interconnected. Nonetheless, the biological significance of a large number of immune subsets we identified needs to be investigated in future studies.

Remaining challenges for data analysis

Up to recently, analysis of flow cytometry data was mainly performed with gating strategies based on primarily bimodal expression patterns. Mass cytometry data analysis, however, requires computational tools to distil this large body of data into interpretable forms. The high-dimensionality, large size, and non-linear structure of the data poses considerable challenges. Dimensionality reduction-based techniques like t-SNE offer single-cell resolution and is one of the leading techniques for data visualization and clustering. However, three major caveats to the t-SNE method were that it lacked interactivity, yields incomplete density-based clustering, and, most importantly, was limited by the number of cells that can be analyzed. Therefore, the existing dimension reduction techniques were not optimal for mass cytometry data. Through fruitful collaborations with computer scientists from Technical University Delft, we succeeded to solve these issues. We developed Cytosplore (**Chapter 3**), an interactive visual analysis system where we incorporated state-of-the-art clustering and t-SNE-based techniques, for the efficient data-driven specification of phenotypically distinct subsets in cytometry data. It provides a highly engaging user-friendly experience by providing direct feedback and linked views, and is coupled to clinical parameters allowing rapid identification and visualization of patient-specific features. In addition, the inclusion of the HSNE algorithm (**Chapter 4**) allows the exploration of millions of cells without the need for downsampling the data. What makes HSNE particularly useful is that it preserves local data structure while allowing examination of the full dataset at single-cell resolution. This application can be used not only for complex mass cytometry datasets, but also for standard 12-parameter flow cytometry datasets. Therefore, Cytosplore allows us to go beyond data sizes currently possible to handle with other tools, a useful development considering expected increases in acquisition rate and dimensionality in mass- and flow cytometry^{4, 5}.

Further analysis improvements are still needed to exploit the full potential of mass cytometry. Methods that can quantify cellular heterogeneity, identify critical cell subset features and assign biological identity to computer-identified subsets

will be particularly useful. For the latter two, a recent report has taken the first steps into this direction. Diggins *et al.* presented marker enrichment modeling⁶, an algorithm that objectively describes cell subsets by quantifying contextual marker enrichment. This provides a standardized language to annotate the key distinguishing features of immune subsets identified in cytometry data.

Moreover, despite the vast amounts of data generated by the mass cytometry community, increasing exponentially each year (**Figure 1**), there has hardly been any comparisons of datasets as of yet. This is a serious shortcoming as much more can be learned from these experiments. To accomplish this, a public mass cytometry data repository needs to be established through international efforts, with the aim of data integration. How to shape this? One of the challenges is the antibody panel composition designed specifically for each study. Different datasets can only be matched based on the presence of overlapping markers, where the accuracy of matching is proportional to the number of shared markers in the panels. Although thousands of immune-system-wide markers are available, generally the core immune markers providing phenotypic information are confined to a much smaller number. Also, recently Fluidigm started providing standardized antibody panel kits, such as the 29-antibody cocktail specifically designed for human immune monitoring. Therefore, I anticipate that many independent mass cytometry studies (will) share a sufficient number of markers for comparative dataset analysis. Machine-learning and classification methods need to be developed to impute marker expression profiles and assess cell subset similarities between mass cytometry studies. This will enable meta-analyses across multiple mass cytometry experiments, revealing differences and commonalities in cellular profiles between different types of immune-mediated diseases.

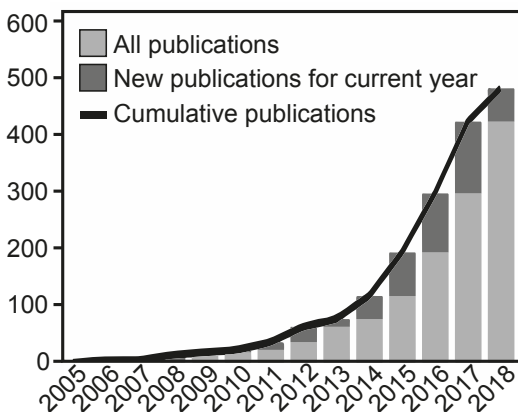


Figure 1. Number of cumulative mass cytometry publications. Quantification of number of papers as of June 2018. Adapted from <https://www.fluidigm.com/publications>

Unique individual fingerprint of the immune system

In our first study (**Chapter 2**), the peripheral blood and intestinal samples from six patients that were biopsied twice, with a 3- to 6-months time interval, clustered tightly together in the data analysis. When comparing the immune cell composition of intestinal biopsies from the same individual but at different intestinal location or inflammatory state, the large interindividual variation as compared to intraindividual variation was striking (**Chapter 5**). In several cases, samples derived from the same individual clustered together. Indeed, cell compositions and other immune markers have been described to be different across individuals by several reports investigating peripheral blood^{7, 8, 9, 10}. These studies demonstrate that the heterogeneity in the immune system increases with age, largely driven by non-inheritable factors. In addition, it was observed that collective sets of immune cell frequencies could predict diverse functional responses^{7, 8}, suggesting that the composition of an individual's immune system reflects a functional network of cell subsets and that the balance between these cell subsets determines the overall responsiveness of the immune system. In agreement, our results confirm the presence of a unique individual 'fingerprint' in immune cell composition in the periphery. In addition, we have provided evidence that the collective immune cell composition in the intestine is also individual-specific, emphasizing the need for personalized care.

Mass cytometry as an application in clinical medicine

The heterogeneous nature and suboptimal clinical response to treatment observed in gastrointestinal and other immune-mediated disorders highlight the need for improved strategies and personalized patient care. Mass cytometry has shown great promise in identifying immune profiles that associate with disease. So how far is mass cytometry as an application in clinical medicine? Recently, clinical studies implementing mass cytometry have been performed to investigate immunological aspects that underlie clinical outcomes^{11, 12}, help monitor disease progression¹³, and to predict responses to therapy^{14, 15}. As a direct diagnostic tool, mass cytometry might be rendered unsuitable due to the currently relative low sample throughput and high cost. Rather, mass cytometry is more often applied as a discovery tool. In this thesis, we have mainly investigated diagnostic specimens from untreated patients with gastrointestinal diseases, mapping immune compositions in health and disease (**Chapter 2** and **Chapter 5**). An important next step would be to design a longitudinal study where the effect of treatment (such as anti-TNF) in IBD could be examined, to identify immunological parameters that correlate with therapeutic responses.

An important consideration in the design of a longitudinal study employing mass cytometry is the need for standardizing experimental procedures thoroughly. This is especially important because of the required unbiased data analysis. Currently, mass cytometry cell acquisitions are accompanied with calibration beads for data normalization between experiments, enabling correction of signal fluctuations¹⁶. Further standardization might include multiplexing clinical samples into one processing tube using (live-cell) barcoding^{17, 18}, stained with a pre-aliquoted antibody cocktail (stable at -80 °C), combined with a consistent internal control sample for normalization of staining variability between experiments.

Results of clinical studies utilizing mass cytometry might help establish minimal sets of measurements critical in immune monitoring and personalized patient care. These could either be translated to high-throughput and cost-effective technologies, such as flow cytometry. Alternatively, if mass cytometry continues to develop further, the identification of disease-associated changes in immune composition may potentially lead to the development of unbiased diagnostic procedures based on a single mass cytometric analysis.

Rare cell subsets matter

The study of rare cell populations is of growing importance in diagnostics and therapeutics. Specifically, the detection of circulating tumor cells¹⁹, tumor stem cells²⁰, endothelial cells²¹, hematopoietic stem cells²², HIV-infected cells²³, invariant NK-T cells²⁴, fetal cells²⁵, ILCs²⁶, antigen-specific T cells²⁷, and the monitoring of minimal residual disease²⁸ provides valuable clinical information. The term “rare” typically refers to cell counts with a frequency of 0.01% or less²⁹. It is challenging to accurately identify rare cells due to the requirement of many phenotypic markers, large data sizes and limitations of pre-existing computational tools. Often, rare cells had been mistaken for noise by clustering algorithms or lost in the downstream analysis due to the necessity of downsampling the data. In fact, we have demonstrated that downsampling introduces a potential bias in observed heterogeneity in the immune system, affecting mainly rare cells (**Chapter 4**). We have shown that the HSNE method (**Chapter 4**) is superior to other single-cell analysis methods in identifying rare cell populations in mass cytometry data. Two features make HSNE particularly suitable for this: (1) The preservation of nonlinearity of the data, key for separating distinct rare cells from abundant cell populations. (2) Allowing the examination of the full dataset at single-cell resolution, providing increased detail and confidence in establishing the phenotypes of rare cells.

Our analysis on rare cells in the human fetal intestine resulted in the identification of a previously unidentified innate cell population, termed int-ILCs (**Chapter 6**). These cells have the capacity to differentiate into NK cells and ILC3-like cells *in vitro*. We speculate that this cell population provides plasticity in the intestine in response to external stimuli. Interestingly, we identified the same cells in intestinal ileum biopsies of children and adults associated with an unaffected-IBD and control profile (**Chapter 5**), while effector NK cells and ILC3s were more readily detectable in affected-IBD specimens. It is tempting to speculate that under inflammatory conditions the int-ILC may differentiate into these effector cell types in the intestine. This also illustrates that research on the physiological and early-life development of the mucosal immune system improves our understanding of factors that may contribute to derailment of disease-associated immune responses.

Moreover, our results have indicated that disease-specific immune subsets reside mainly in the affected organ and are much less readily detectable in peripheral blood (**Chapter 2**). However, upon reanalyzing the dataset using HSNE (**Chapter 4**), we were able to identify a rare population of CD28⁻ effector memory CD4⁺ T cells specifically in blood of some Crohn's disease patients, which was missed in the original analysis (**Chapter 2**) due to downsampling. This suggests that rare intestinal disease-associated CD4⁺ T cells can be detected in peripheral blood. In addition, we identified a CD4⁺ T cell effector memory population distinguished by the expression of HLA-DR and CD38 while lacking CD27 and CD127 specifically in the intestine of 17 out of 29 IBD patients (**Chapter 5**). Together with previous observations^{30, 31}, there is strong evidence that in a subgroup of IBD patients the CD4⁺ T cell population is altered during inflammation, and possibly detectable in blood. This might present an opportunity to circumvent invasive gastrointestinal endoscopy for disease monitoring, but requires further investigations. Therefore, the identification of circulating, rare immune subsets offers possibilities to determine cellular parameters that correlate with disease.

Assessing antigen-specificity

Celiac disease is an intestinal autoimmune disease driven by dietary gluten and gluten-specific CD4⁺ T cell responses. We have identified a celiac disease-associated immune composition in the small intestine, mainly characterized by the presence of distinctive TCR $\gamma\delta$ subsets and CD8⁺ T cell subsets while lacking certain innate lymphocyte subsets (**Chapter 2**). Following oral gluten challenge, concomitant with gluten-specific CD4⁺ T cells, the appearance of activated, gut-homing CD8⁺ T cells

and TCR $\gamma\delta$ cells in peripheral blood of celiac patients was detected in a recent study³². However, it is currently unclear where the gluten-specific CD4⁺ T cells reside in the high-dimensional immune landscape in the intestine we described. Possibly within the PD-1⁺CD161⁺ CD4⁺ T cell effector memory subset as this subset was increased in numbers in celiac biopsies compared with control (**Chapter 2**). As mentioned above, the CD4⁺ T cell compartment also appears to be implicated in IBD (**Chapter 5**), but unlike celiac disease the potential causative antigens in IBD are yet to be identified.

Newell *et al.* developed an elegant method that allows the simultaneous identification of many antigen-specific T cells, by combining mass cytometry with combinatorial peptide-MHC tetramers³³. Using this method, they succeeded to screen for 109 different tetramers while retaining 23 metal channels to analyze other phenotypic or functional markers in a single sample. In addition, such an approach revealed that virus-specific CD8⁺ T cells occupied distinct niches of phenotypic and functional diversity³⁴. However, these analyses focused on CD8⁺ T cells which require the more stable MHC class I tetramer reagents, while the development of MHC class II tetramers required for analyzing antigen-specific CD4⁺ T cells is more complicated. Combining mass cytometry with tetramers has a great potential in providing a comprehensive analysis of specific T cell responses, distinguishing antigen-specific T cells from bystander T cells, and might be a useful application to study inflammatory intestinal diseases.

Functionality of immune subsets

Functionality of immune cells relates to their gene and protein expression profiles. As mentioned above, studies have shown that cellular immune compositions could predict functional responses^{7, 8}. In contrast, a study on acute myeloid leukemia revealed that although surface and signaling phenotypes of immune cells displayed tight coregulation in healthy samples, this was not the case in leukemia³⁵. This raises the question to what extent the surface phenotypes of immune subsets serve as proxies of cellular state and function in intestinal disorders. We have mainly focused on characterizing the immune cell landscape in health and disease (**Chapter 2** and **Chapter 5**), not its functionality. There are several ways how mass cytometry can be utilized for assessing immune cell function. For example, once immune subsets of interest have been discovered, a minimal marker gating strategy can be devised, either supervised or automated, to specifically identify these subsets using flow cytometry. This allows for the purification of viable cells of these subsets for further *in vitro* analysis. We have applied this approach to study the functionality of various ILC subsets in the human fetal intestine (**Chapter 6**), assessing their

cytokine production profiles and differentiation potential. Alternatively, mass cytometry can also be used directly for the analysis of functional states of the immune system^{36, 37, 38, 39}. Due to the availability of many channels, mass cytometry permits the combination of multiple phenotypic surface markers with multiple functional intracellular markers, under unstimulated and stimulated conditions.

An elegant study by Bodenmiller *et al.* demonstrated the power of applying multiplexed mass cytometry for the profiling of cellular states perturbed by small molecule regulators³⁹. By dedicating 7 metals to cellular barcoding they could multiplex an entire 96-well plate, characterizing immune cell signaling dynamics and the effects of 27 inhibitors on this system. For each inhibitor, they could measure 14 phosphorylation sites in 14 cell types at 96 conditions, resulting in 18,816 quantified phosphorylation levels from each multiplexed sample. Therefore, this analysis allows the high-throughput characterization of cell type selectivity and responsiveness to a given stimulation or drug for dozens of cell types simultaneously. The cellular responsiveness can either be measured by analyzing the major signaling pathways or production of effector molecules, such as cytokines. Now that we have profiled the immune system with a 36-surface antibody panel in IBD (**Chapter 5**), it would be interesting to determine the minimal set of markers required to preserve most of the disease-associated immune heterogeneity. This would make space in the panel for building in several intracellular signaling or cytokine markers to investigate the functionality of these disease-associated subsets. A major challenge would be the determination of the minimal number of cells required per condition for a reliable read-out using this assay. With the Helios-upgraded CyTOF system, approximately 50,000 live immune cells can be detected from 2 intestinal biopsies in total, while in the original study about 200,000 cells per well was used³⁹. If feasible, this assay may provide a unique opportunity to screen for the functionality of the immune subsets implicated in IBD with a high-dimensional approach. It might also be an attractive method for drug screening of immune cells from clinical biopsies, to categorize drug effects or drug combinations, to eventually guide personalized therapeutic strategies in IBD.

The architecture of the tissue microenvironment in health and diseases

Many types of cells must cooperate in tissues in order to mount an inflammatory immune response. Therefore, we choose a broad coverage approach by analyzing across all immune lineages simultaneously. Results of the gastrointestinal studies we employed (**Chapter 2** and **Chapter 5**) elucidated that underlying the identified disease-associated profiles, the differentiating subsets were often a combination of

both the innate and the adaptive immune compartment. This raises the question whether these disease-specific cells are interacting with each other in the tissue. However, with conventional mass cytometry we analyze single-cell suspensions and, therefore, lose the spatial context. Many studies of intestinal immunology have not taken into account that the intestine comprises several anatomically defined segments that each have distinct physiological roles and immunological components⁴⁰. A promising technological development is imaging-mass cytometry, a combination of mass cytometry with laser ablation that allows the simultaneous analysis of over 30 markers on tissue sections with subcellular resolution^{41, 42}.

We performed preliminary experiments using imaging-mass cytometry with a 15-antibody panel on sections from the fetal intestine (**Figure 2**). Prior to ablation, the tissue section can be examined by a camera allowing the identification of regions of interest, such as the intestinal villi (**Figure 2A**). After data acquisition, the expression of a few individual markers can be visualized with classic coloring overlays (**Figure 2B**). The resolution of imaging-mass cytometry is comparable with standard immunofluorescence, but unhampered by autofluorescence. Coloring overlays of individual markers, however, is not capable of visualizing over 4 markers simultaneously. To comprehensively visualize all markers simultaneously at 1 μM pixel resolution, we exploit the ability of HSNE (**Chapter 4**) of allowing the high-dimensional analysis of millions of data points, followed by clustering of similar pixels. Subsequently, the pixels are projected back onto the original image, but now color-coded according to the HSNE clustering (**Figure 2C**). Using this approach we obtain an immediate, reconstructed overview of the architecture of the intestine in a complete data-driven fashion. This analysis demonstrates the presence of a tissue organization between T cells, ILCs and myeloid cells in the fetal intestine, and this will be investigated further in the future. Furthermore, we are currently working on integrating the imaging-mass cytometry analysis over several layers, from the pixel level to the cellular level to the tissue level, each interacting with another.

This provides a unique opportunity to comprehensively determine the cellular neighborhood of disease-associated immune subsets in the tissue-specific microenvironment. Ultimately, a three-dimensional architecture of the intestine could be reconstructed where the microenvironment of immune cells composed of structural proteins and stromal cells could be visualized and analyzed interactively, providing a more integrated view of disease-specific changes.

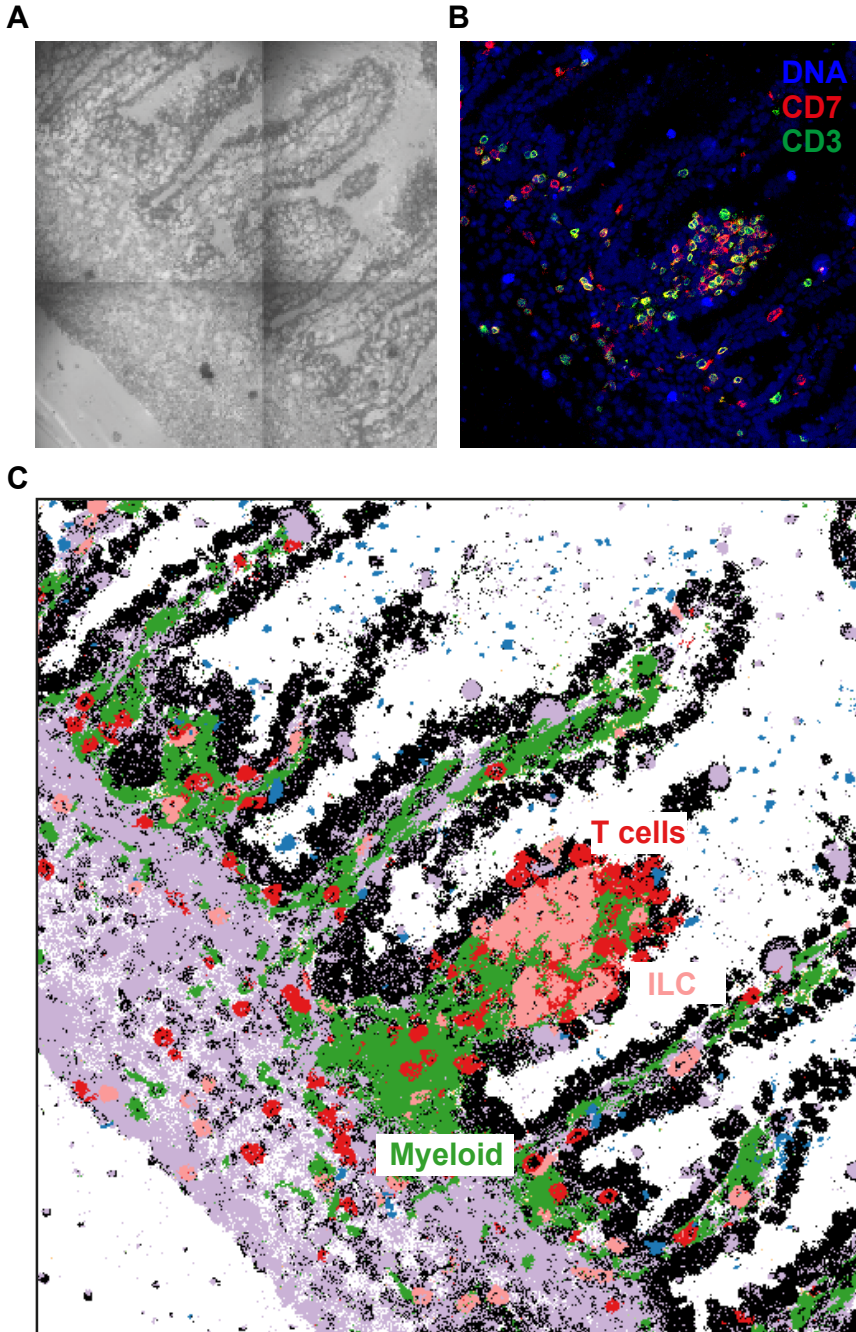


Figure 2. Imaging-mass cytometry on the human fetal intestine. (A) A camera showing regions of the tissue section prior to ablation. (B) Color overlays for the markers DNA (blue), CD7 (red), and CD3 (green). (C) HSNE analysis of the single-pixel data projected back onto the image. Color represents HSNE pixel clusters, indicating epithelium (black), nerves (purple), IgM⁺ cells (blue), T cells (red), ILCs (pink) and myeloid cells (green)

Systems Immunology

Moving forward, it will be important to investigate the immune system by integrating mass cytometry with other technologies, such as single-cell transcriptomics, proteomics, metabolomics, T cell and antibody repertoire sequencing, multi-parameter imaging and cytokine bead-based multiplex assays. Such an approach, also known as 'Systems Immunology'⁴³, will enable us to gain insight into how different components of the immune system function and interact in the tissue context in health and disease. Additionally, It would be of great value to correlate this with the composition of the microbiota, since multiple profiling studies have described characteristic shifts in the microbiota composition associated with the pathogenesis of IBD⁴⁴. Moreover, single-cell RNA sequencing of samples prior to CyTOF antibody panel design might aid in the identification of unanticipated candidate markers in an unbiased manner. A great barrier to implementing systems immunology successfully, however, is the requirement of a highly-skilled multi-disciplinary team. Collaborations between clinicians, technology experts, bioinformaticians and immunologists are key for such an undertaking. Combining these technologies will offer new opportunities to define a comprehensive landscape of the immune system and provide a framework for understanding the essential features of an immune response that may correlate with useful clinical outcomes.

Concluding remarks

Inflammatory intestinal diseases can only be understood by studying specialized cell types within the tissue niche itself. Mass cytometry and data-driven, automated analysis approaches have proven to be a powerful approach to investigate complex compositions of heterogeneous cell subsets, such as those encountered in intestinal biopsies. Future improvements on interactions between datasets and integrations with other -omics technologies, such as imaging, are required to exploit the full potential of mass cytometry. These types of data have the potential to greatly improve our understanding on human disease. In concert with clinical data, mass cytometry could enable a finer classification of patients, and might aid in the development of improved diagnostics, prognostics and personalized therapeutic regimens.

References

1. Simoni, Y., Chng, M.H.Y., Li, S., Fehlings, M. & Newell, E.W. Mass cytometry: a powerful tool for dissecting the immune landscape. *Curr Opin Immunol* 51, 187-196 (2018).
2. Jabri, B. & Sollid, L.M. Tissue-mediated control of immunopathology in coeliac disease. *Nat Rev Immunol* 9, 858-870 (2009).
3. Silva, F.A., Rodrigues, B.L., Ayrizono, M.L. & Leal, R.F. The Immunological Basis of Inflammatory Bowel Disease. *Gastroenterol Res Pract* 2016, 2097274 (2016).
4. Bendall, S.C., Nolan, G.P., Roederer, M. & Chattopadhyay, P.K. A deep profiler's guide to cytometry. *Trends Immunol* 33, 323-332 (2012).
5. Chattopadhyay, P.K., Gierahn, T.M., Roederer, M. & Love, J.C. Single-cell technologies for monitoring immune systems. *Nat Immunol* 15, 128-135 (2014).
6. Diggins, K.E., Greenplate, A.R., Leelatian, N., Wogslund, C.E. & Irish, J.M. Characterizing cell subsets using marker enrichment modeling. *Nat Methods* 14, 275-+ (2017).
7. Tsang, J.S. et al. Global analyses of human immune variation reveal baseline predictors of postvaccination responses. *Cell* 157, 499-513 (2014).
8. Kaczorowski, K.J. et al. Continuous immunotypes describe human immune variation and predict diverse responses. *Proc Natl Acad Sci U S A* 114, E6097-E6106 (2017).
9. Brodin, P. et al. Variation in the Human Immune System Is Largely Driven by Non-Heritable Influences. *Cell* 160, 37-47 (2015).
10. Carr, E.J. et al. The cellular composition of the human immune system is shaped by age and cohabitation. *Nature Immunology* 17, 461-+ (2016).
11. Fragiadakis, G.K. et al. Patient-specific Immune States before Surgery Are Strong Correlates of Surgical Recovery. *Anesthesiology* 123, 1241-1255 (2015).
12. Gaudilliere, B. et al. Clinical recovery from surgery correlates with single-cell immune signatures. *Sci Transl Med* 6 (2014).
13. Maecker, H.T., McCoy, J.P. & Nussenblatt, R. Standardizing immunophenotyping for the Human Immunology Project. *Nat Rev Immunol* 12, 191-200 (2012).
14. Heath, J.R., Ribas, A. & Mischel, P.S. Single-cell analysis tools for drug discovery and development. *Nat Rev Drug Discov* 15, 204-216 (2016).
15. Newell, E.W. & Cheng, Y. Mass cytometry: blessed with the curse of dimensionality. *Nat Immunol* 17, 890-895 (2016).
16. Finck, R. et al. Normalization of mass cytometry data with bead standards. *Cytometry A* 83, 483-494 (2013).
17. Mei, H.E., Leipold, M.D., Schulz, A.R., Chester, C. & Maecker, H.T. Barcoding of live human peripheral blood mononuclear cells for multiplexed mass cytometry. *J Immunol* 194, 2022-2031 (2015).

18. Zunder, E.R. et al. Palladium-based mass tag cell barcoding with a doublet-filtering scheme and single-cell deconvolution algorithm. *Nat Protoc* 10, 316-333 (2015).
19. Allard, W.J. et al. Tumor cells circulate in the peripheral blood of all major carcinomas but not in healthy subjects or patients with nonmalignant diseases. *Clin Cancer Res* 10, 6897-6904 (2004).
20. Al-Hajj, M. & Clarke, M.F. Self-renewal and solid tumor stem cells. *Oncogene* 23, 7274-7282 (2004).
21. Khan, S.S., Solomon, M.A. & McCoy, J.P., Jr. Detection of circulating endothelial cells and endothelial progenitor cells by flow cytometry. *Cytometry B Clin Cytom* 64, 1-8 (2005).
22. Siena, S. et al. Flow cytometry for clinical estimation of circulating hematopoietic progenitors for autologous transplantation in cancer patients. *Blood* 77, 400-409 (1991).
23. Cory, J.M. et al. Detection of Human Immunodeficiency Virus-Infected Lymphoid-Cells at Low-Frequency by Flow-Cytometry. *J Immunol Methods* 105, 71-78 (1987).
24. van der Vliet, H.J.J. et al. Circulating V alpha 24(+) V beta 11(+) NKT cell numbers are decreased in a wide variety of diseases that are characterized by autoreactive tissue damage. *Clin Immunol* 100, 144-148 (2001).
25. Beroud, C. et al. Prenatal diagnosis of spinal muscular atrophy by genetic analysis of circulating fetal cells. *Lancet* 361, 1013-1014 (2003).
26. Hazenberg, M.D. & Spits, H. Human innate lymphoid cells. *Blood* 124, 700-709 (2014).
27. Altman, J.D. et al. Phenotypic analysis of antigen-specific T lymphocytes. *Science* 274, 94-96 (1996).
28. van Dongen, J.J. et al. Prognostic value of minimal residual disease in acute lymphoblastic leukaemia in childhood. *Lancet* 352, 1731-1738 (1998).
29. Donnenberg, A.D. & Donnenberg, V.S. Rare-event analysis in flow cytometry. *Clin Lab Med* 27, 627-652, viii (2007).
30. Hegazy, A.N. et al. Circulating and Tissue-Resident CD4(+) T Cells With Reactivity to Intestinal Microbiota Are Abundant in Healthy Individuals and Function Is Altered During Inflammation. *Gastroenterology* 153, 1320-+ (2017).
31. Shale, M., Schiering, C. & Powrie, F. CD4(+) T-cell subsets in intestinal inflammation. *Immunol Rev* 252, 164-182 (2013).
32. Han, A. et al. Dietary gluten triggers concomitant activation of CD4+ and CD8+ alphabeta T cells and gammadelta T cells in celiac disease. *Proc Natl Acad Sci U S A* 110, 13073-13078 (2013).
33. Newell, E.W. et al. Combinatorial tetramer staining and mass cytometry analysis facilitate T-cell epitope mapping and characterization. *Nat Biotechnol* 31, 623-629 (2013).

34. Newell, E.W., Sigel, N., Bendall, S.C., Nolan, G.P. & Davis, M.M. Cytometry by Time-of-Flight Shows Combinatorial Cytokine Expression and Virus-Specific Cell Niches within a Continuum of CD8(+) T Cell Phenotypes (vol 36, pg 142, 2012). *Immunity* 38, 198-199 (2013).
35. Levine, J.H. et al. Data-Driven Phenotypic Dissection of AML Reveals Progenitor-like Cells that Correlate with Prognosis. *Cell* 162, 184-197 (2015).
36. Kay, A.W., Strauss-Albee, D.M. & Blish, C.A. Application of Mass Cytometry (CyTOF) for Functional and Phenotypic Analysis of Natural Killer Cells. *Methods Mol Biol* 1441, 13-26 (2016).
37. Bendall, S.C. et al. Single-cell mass cytometry of differential immune and drug responses across a human hematopoietic continuum. *Science* 332, 687-696 (2011).
38. Bjornson, Z.B., Nolan, G.P. & Fantl, W.J. Single-cell mass cytometry for analysis of immune system functional states. *Curr Opin Immunol* 25, 484-494 (2013).
39. Bodenmiller, B. et al. Multiplexed mass cytometry profiling of cellular states perturbed by small-molecule regulators. *Nat Biotechnol* 30, 858-867 (2012).
40. Mowat, A.M. & Agace, W.W. Regional specialization within the intestinal immune system. *Nat Rev Immunol* 14, 667-685 (2014).
41. Giesen, C. et al. Highly multiplexed imaging of tumor tissues with subcellular resolution by mass cytometry. *Nat Methods* 11, 417-422 (2014).
42. Chang, Q. et al. Imaging Mass Cytometry. *Cytom Part A* 91a, 160-169 (2017).
43. Davis, M.M., Tato, C.M. & Furman, D. Systems immunology: just getting started. *Nature Immunology* 18, 725-732 (2017).
44. Kostic, A.D., Xavier, R.J. & Gevers, D. The microbiome in inflammatory bowel disease: current status and the future ahead. *Gastroenterology* 146, 1489-1499 (2014).





Appendices

Nederlandse Samenvatting

Het afweersysteem

Ons afweersysteem bestaat uit een gemengde verzameling van witte bloedcellen met verschillende functies. Er zijn bijvoorbeeld afweercellen die ziekmakende indringers herkennen, 'killercellen' die tumoren vernietigen, cellen die antistoffen maken en cellen die alle rommel opruimen. Dit is een kleine greep uit het volledige assortiment afweercellen, waarvan er miljoenen overal in ons lichaam actief zijn. Op basis van hun functie worden de afweercellen onderverdeeld in hoofdgroepen, zoals T-cellen, B-cellen, NK-cellen en myeloïde cellen. Binnen die hoofdgroepen onderscheiden we weer allemaal subgroepen.

Het verschil zit onder andere in de eiwitten aan de buitenkant van de cel. Die eiwitten bepalen aan welk soort cel de afweercel kan binden, waarmee hij kan communiceren of die hij kan doden. De afweercellen kunnen we karakteriseren door deze eiwitten te bestuderen.

Chronische ontstekingsziekten in het darmstelsel

Het afweersysteem is noodzakelijk in de strijd tegen infecties die veroorzaakt worden door bacteriën, virussen of parasieten. Desalniettemin kan het afweersysteem ontsporen wat bijdraagt aan het ontstaan van (immuungerelateerde) ziekten als type I diabetes en reuma, maar ook chronische ziekten in het darmstelsel, zoals de ziekte van Crohn, ulceratieve colitis en coeliakie. Bij deze ziekten reageert het afweersysteem ten onrechte op bepaalde stoffen of valt het lichaamseigen weefsel aan.

Bij coeliakie zorgt het eten van gluten, dat onder andere in tarwe en andere granen zit, voor heftige ontstekingen in de dunne darm. Een levenslang, strikt glutenvrij dieet is de enige behandeling die we nu kennen. Sommige coeliakiepatiënten hebben milde symptomen, terwijl anderen zeer ernstige vormen ontwikkelen. Bij patiënten met de ziekte van Crohn of ulceratieve colitis reageert het afweersysteem in de darm overdreven sterk op onschadelijke bacteriën. Ook hier leidt dat tot ernstige, vaak chronische ontstekingen. De behandeling bestaat uit het toedienen van ontstekingsremmende medicijnen, maar lang niet alle patiënten reageren daar even goed op. Bij een kwart van de patiënten met de ziekte van Crohn zijn de ontstekingen dusdanig ernstig dat een operatie nodig is om de schade te herstellen. De toename in het voorkomen van deze ziekte bij jonge kinderen met vaak een agressiever

ziekteverloop is verontrustend. Waarom krijgt de één een ernstige vorm en de ander niet? Om te kunnen begrijpen hoe ziekten in/van het afweersysteem ontstaan en waarom we zulke grote verschillen zien tussen patiënten is het noodzakelijk dat de verschillende typen afweercellen in detail in kaart worden gebracht.

Massa cytometrie

Met de nu gangbare methode “flow cytometrie” kunnen cellen van elkaar worden onderscheiden door er verschillende antilichamen aan toe te voegen. Deze hechten zich aan specifieke eiwitten (markers) op het celoppervlak. Deze markers bepalen de identiteit van de cel. Aan ieder antilichaam is een specifiek lichtgevend molecuul gekoppeld dat zichtbaar gemaakt kan worden in een flowcytometer. Maar er is een limiet: er kunnen niet meer dan 12 antilichamen tegelijkertijd gemeten worden, omdat de verschillende kleuren licht elkaar dan gaan overlappen.

Met massa cytometrie, of CyTOF, is de basis hetzelfde maar hier zijn antilichamen voor detectie gekoppeld aan metalen: elk antilichaam aan een ander metaal. Door te meten welke metalen zich aan een bepaalde cel gehecht hebben, weten we met welk type cel we te maken hebben. Voor het verkrijgen van deze meetgegevens gebruiken we een Massacytometer. In dit apparaat bevindt zich een gloeiendheet plasma met een temperatuur van 2.700 °C, equivalent aan de zon, dat cellen één-voor-één tot op atoomniveau uit elkaar doet spatten. Die metaalatomen hebben allemaal een verschillende massa en die verschillen worden heel nauwkeurig gemeten met een massaspectrometer. Deze nieuwe techniek is een grote verbetering ten opzichte van de gangbare methode (flow cytometrie). Met de CyTOF kunnen we nu drie keer zoveel celoppervlakmarkers tegelijk bepalen - momenteel 40 - en in de toekomst valt dat aantal zelfs nog uit te breiden naar meer dan honderd. Dat betekent weer een enorme toename in de mate waarin cellen verder van elkaar onderscheiden kunnen worden. De acquisitie van data gaat met een razend tempo van duizend cellen per seconde. Hiermee kunnen we dus snel van honderdduizenden afweercellen uit bijvoorbeeld het darmslijmvlies of bloed in detail karakteriseren. Concluderend kunnen we zeggen dat we met de CyTOF zeer uitgebreide celanalyses kunnen uitvoeren en zodoende de complexiteit van het afweersysteem in detail kunnen bestuderen.



Analyse van complexe CyTOF-gegevens

De analyse in de eerste CyTOF studie naar diverse chronische darmziekten die wij hebben uitgevoerd hebben we gedaan met 5.2 miljoen cellen. In de tweede studie, specifiek gericht op de ziekte van Crohn en ulceratieve colitis konden we 8.9 miljoen cellen analyseren. Eén cel kan meerdere markers hebben en ook in een specifieke combinatie. Het vergt dus slimme datatechnieken om wijs te worden uit de gigantische hoeveelheid informatie die de CyTOF genereert. De methoden die er bestonden om de CyTOF data te analyseren waren nog zeer beperkt. Ze gaven een globaal beeld van alle cellen of ze gaven een gedetailleerd beeld van een willekeurig deel van de cellen. Soms maar 20%. Deze beperkingen in de analyse werden veroorzaakt door gebrek aan computerkracht. Het was daardoor onmogelijk om de verschillende cellen van elkaar te onderscheiden. Hierdoor werden onderzoekers gedwongen hun dataset te verkleinen en een willekeurig selectie van de totale hoeveelheid cellen te analyseren. Echter, de meest interessante celtypen in een weefselmonster, celtypen die te maken hebben met ziek of gezond zijn, zijn vaak zeldzaam en je mist ze als je slechts een deel van de cellen gedetailleerd bestudeert.

Een nieuwe analysetechniek genaamd *Hierarchical Stochastic Neighbour Embedding* (HSNE) die wij in samenwerking met computerwetenschappers van de Technische Universiteit Delft hebben ontwikkeld samen met de Cytosplore software, lost dat probleem op. De gebruiker krijgt eerst een tweedimensionaal plaatje op zijn computerscherm waarin de cellen uit het weefselmonster op basis van onderlinge gelijkenissen zijn gegroepeerd. De cellen staan er niet individueel in weergeven: dat zou resulteren in een onoverzichtelijke massa punten. In plaats daarvan zijn er 'landmarks', representatieve cellen die op elkaar lijkende cellen vertegenwoordigen. Dit overzicht laat de details weg, maar alle informatie is gebruikt om deze landmarks te berekenen. Vervolgens kan in stappen ingezoomd worden op een groep cellen naar keuze tot de individuele cellen met bijbehorende markers in beeld zijn. Het is te vergelijken met *Google Earth*, waar je begint met de hele aarde en kunt inzoomen tot de straat waar je woont. Deze interactieve, visuele, hiërarchische methodiek is gebruikersvriendelijk en werkt makkelijk, snel en goed. De landmarks vertegenwoordigen bekende hoofdgroepen van cellen, zoals (bepaalde) T-cellen en B-cellen van het afweersysteem. Door in te zoomen kun je zeldzamen celtypen ontdekken binnen deze hoofdgroepen die ontbreken of juist aanwezig zijn bij een bepaalde ziekte. Dat levert aanknopingspunten op voor het begrijpen van die ziekte, diagnostiek en doelgerichte behandeling.

Identificatie van ziekte-geassocieerde afweercelpopulaties

Om de verschillen tussen de afweercellen van patiënten met chronische darmziekten in kaart te brengen hebben we (een set van) bloedmonsters en stukjes darmweefsels geanalyseerd met de CyTOF. In de eerste studie waren de monsters afkomstig van patiënten met verschillende stadia van coeliakie of Crohn en van een zogeheten controlegroep – mensen met darmklachten die een endoscopie (inwendig darmonderzoek) moesten ondergaan waaruit bleek dat er geen darmontsteking te vinden was. Een van de meest opvallende resultaten was het sterke verschil tussen bloed en darmweefsel. Zonder vooraf te weten welk monster gemeten was, maakte deze techniek probleemloos onderscheid tussen afweercellen uit bloed en uit darmweefsel. Een belangrijk resultaat, want het laat zien dat een bloedmonster zeer beperkt informatie geeft over wat er in het darmweefsel aan de hand is.

Verder bleek aan de hand van onze resultaten dat het afweersysteem veel complexer is dan gedacht. Een aantal soort cellen was al bekend, maar nu blijken het er nog veel meer te zijn. We vonden in totaal 142 verschillende subgroepen van afweercellen in de weefsels die we bestudeerden. Een belangrijke bevinding was dat we met deze methode scherp onderscheid konden maken tussen de verschillende groepen patiënten. De afweercellen uit het darmweefsel van coeliakiepatiënten vormden een duidelijk aparte groep, net als die van de ziekte van Crohn patiënten, anders dan in het darmslijmvlies van gezonde mensen. Ook konden we de verschillende stadia en complicaties eenvoudig van elkaar onderscheiden.

Conclusie

De CyTOF studies hebben nieuwe inzichten gegeven in de betrokkenheid van afweercellen in chronische darmziekten. Deze verschillen in samenstelling van afweercellen tussen patiënten levert aangrijpingspunten om behandeling veel gericht op de individuele patiënt af te stemmen en zo de gezonde cellen met rust te laten. Daarnaast hebben we nu een stap gezet waarmee we de patiënten, na een behandeling bijvoorbeeld, in de loop van tijd kunnen volgen door de ziekte-specifieke abnormale cellen te volgen (immuno-monitoring). Wij verwachten dat de techniek toepassingen zal krijgen voor patiënten, voor het stellen van een diagnose en om vast te stellen of een behandeling het gewenste effect heeft.



List of Publications

van Unen V, Li N, Molendijk I, Temurhan M, Höllt T, van der Meulen-de Jong AE, Verspaget HW, Mearin ML, Mulder CJ, van Bergen J, Lelieveldt BP, Koning F. Mass Cytometry of the Human Mucosal Immune System Identifies Tissue- and Disease-Associated Immune Subsets. *Immunity* 44: 1227-39 (2016)

van Unen V, Höllt T, Pezzotti N, Li N, Reinders MJT, Eisemann E, Koning F, Vilanova A, Lelieveldt BPF. Visual Analysis of Mass Cytometry Data by Hierarchical Stochastic Neighbour Embedding Reveals Rare Cell Types. *Nat Commun* 8: 1740 (2017)

Li N, **van Unen V**, Höllt T, Thompson A, van Bergen J, Pezzotti N, Eisemann E, Vilanova A, Chuva de Sousa Lopes SM, Lelieveldt BPF, Koning F. Mass Cytometry Reveals Innate Lymphoid Cell Differentiation Pathways in the Human Fetal Intestine. *J Exp Med* 215: 1383-96 (2018)

Höllt T, Pezzotti N, **van Unen V**, Koning F, Eisemann E, Lelieveldt B, Vilanova A. Cytosplore: Interactive Immune Cell Phenotyping for Large Single-Cell Datasets. *Comput Graph Forum* 35: 171-80 (2016)

Li N, **van Unen V**, Abdelaal T, Guo N, Kasatskaya SA, Ladell K, McLaren JE, Egorov ES, Izraelson M, Chuva de Sousa Lopes SM, Höllt T, Britanova OV, Eggermont J, de Miranda NFCC, Chudakov DM, Price DA, Lelieveldt BPF, Koning F. Single-Cell Analysis Reveals the Generation of Memory CD4⁺ T-cells in the Human Fetal Intestine. *Nat Immunol* (in press)

Hollt T, Pezzotti N, **van Unen V**, Koning F, Lelieveldt BPF, Vilanova A. CyteGuide: Visual Guidance for Hierarchical Single-Cell Analysis. *IEEE Trans Vis Comput Graph* 24: 739-48 (2018)

Laban S, Suwandi JS, **van Unen V**, Pool J, Höllt T, Pezzotti N, Vilanova A, Lelieveldt BPF, Roep BO. Heterogeneity of Circulating CD8 T-cells Specific To Islet, Neo-Antigen and Virus in Patients With Type I Diabetes Mellitus. *Plos One* 8: e0200818 (2018)

Redeker A, Remmerswaal EBM, van der Gracht ETI, Welten SPM, Holt T, Koning F, Cicin-Sain L, Nikolich-Zugich J, Ten Berge IJM, van Lier RAW, **van Unen V**, Arens R. The Contribution of Cytomegalovirus Infection to Immune Senescence Is Set by the Infectious Dose. *Front Immunol* 8: 1953 (2017)

Welters MJP, Ma W, Santegoets S, Goedemans R, Ehsan I, Jordanova ES, van Ham VJ, **van Unen V**, Koning F, van Egmond SI, Charoentong P, Trajanoski Z, van der Velden LA, van der Burg SH. Intratumoral HPV16-Specific T Cells Constitute a Type I-Oriented Tumor Microenvironment to Improve Survival in HPV16-Driven Oropharyngeal Cancer. *Clin Cancer Res* 24: 634-47 (2018)

Santegoets S, van Ham JJ, Ehsan I, Charoentong P, Duurland C, **van Unen V**, Höllt T, van der Velden LA, van Egmond SL, Kortekaas K, de Vos-van Steenwijk PJ, van Poelgeest MI, Welters MJP, van der Burg SH. The Anatomical Location Shapes the Immune Infiltrate in Tumors of Same Etiology and Impacts Survival. *Clin Cancer Res* (2018)

Buckle T, van der Wal S, van Malderen SJ, Muller L, Kuil J, **van Unen V**, Peters RJ, van Bommel ME, McDonnell LA, Velders AH, Koning F, Vanhaeke F, van Leeuwen FW. Hybrid Imaging Labels: Providing the Link Between Mass Spectrometry-Based Molecular Pathology and Theranostics. *Theranostics* 7: 624-33 (2017)

Quispel WT, Steenwijk EC, **van Unen V**, Santos SJ, Koens L, Mebius R, Egeler RM, van Halteren AG. Tertiary Lymphoid Structures are Confined to Patients Presenting With Unifocal Langerhans Cell Histiocytosis. *Oncoimmunology* 5: e1164364 (2016)



Curriculum Vitae

Vincent van Unen was born on March 16th 1989 in Vlaardingen. He grew up in the city of Schiedam where he attended secondary school at SG Spieringshoek. He continued his education by studying Biomedical Sciences at the Leiden University Medical Center (LUMC) and went on an exchange to the Karolinksta Institute in Stockholm, Sweden and to the Garvan Institute of Medical Research in Sydney, Australia under the supervision of Prof. Jonathan Sprent. He followed the Biomedical Sciences Plus program as an extracurricular activity and obtained his Master's degree *cum laude*. Meanwhile, he performed additional work as a research assistant in the laboratory of Rheumatology, Pulmonology and Parasitology at the LUMC.

He completed his PhD project in the department of Immunohematology and Blood Transfusion at the LUMC under the supervision of Prof. Frits Koning. Since 2013, Vincent is the chairman of mass cytometry user meetings in the LUMC, guiding immunology researchers from several LUMC departments as well as researchers from other University Medical Centers such as the VUMC and the AMC. He visited 19 scientific meetings and symposia during his PhD period in total, of which he attended 6 as an invited speaker abroad: AH Diagnostics Seminar Day in Copenhagen, Denmark; Advanced Immune Bio-imaging Workshop in Milan, Italy; Drug Metabolism Discovery Group in Cambridge, UK; Mass Cytometry User Forum in Berlin, Germany; Fluidigm meeting in Lake Maggiore, Italy and Northern European Mass Cytometry User Group Meeting in Cambridge, UK. In addition, he supervised the internships of a Bioinformatics student and a Medicine student. He was active on the board of the LUMC Pride diversity network since 2015, focusing on equality and inclusivity for in particular lesbian, homosexual, bisexual and transgender (LGBT+) employees in academia. He was a 'Bright Sparks' candidate at the annual meeting of the Dutch Society for Immunology (NVVI) in 2017. Also, he received three awards in recognition of his work during his PhD period: the Junior Researcher Prize 2016 from the Dutch Society of Gastroenterology, the Third Takeda Research Prize 2017 from the Young Initiative on Crohn and Colitis and the Best Article Prize 2016 from the LUMC.

He recently obtained the Rubicon Fellowship from ZonMw, permitting him to conduct research as a postdoc in Prof. Mark Davis lab at Stanford University in the USA, where he will continue the investigations of the immune system in chronic intestinal diseases.



Acknowledgements

Acknowledgements

Frits Koning, de beste promotor die ik me kan indenken, mijn begeleider en 'mentor', wil ik hartelijk bedanken. Het is bewonderingswaardig hoe je mij enerzijds de ruimte hebt gegeven voor het ontplooiën van mijn wetenschappelijke creativiteit en anderzijds de weg hebt gewezen toen ik verdwaald was in details. Ook wil ik je bedanken voor de begeleiding in het traject naar academische loopbaan na deze promotie.

Li Na, my paranimf and lab *partner in crime*, thank you for your dedication in our joint research projects, and educating me in Chinese culture, language and food (我很饿)! Together, we work like a well-oiled machine as evidenced by several successful research outputs.

Mijn fantastische collega's van de groep Koning, Yvonne (*stond altijd voor mij klaar*), Allan (*enjoyed sitting behind me...*), Jeroen, Frederike, Veronica, Yannick, Zhou Lin, Natasja, Tessa, Nannan, Sanne en Laura. Bedankt voor de zeer goede sfeer en discussies op de werkvloer. De thermostaat kan weer omhoog.

The interdepartmental CyTOF team, Marjolijn, Sandra (*What happens in Berlin...*), Rene, Hesther, Anna, Vanessa, Saskia, Noel, Ruud, Guillaume (*Always humoring me*), Sanne (*See you at Stanford*), Karin, Yoanna, Jessica, Kyra, Juliette and Mikhael. Good luck taming the CyTOF. De hele afdeling IHB! In het bijzonder, Wim, Jacques, Jan Wouter, Ferry, Ramon, Frans, Bart, Jaap Jan, Frank, Jacq, Els, Sanne, Moniek, Douwe, Michael, Marry, Laura, Els, Edwin, Geert, Sebastiaan, Marieke, Brett, Antoinette, Gonca, Jan Willem, Esmé, Elena, Cynthia, Elham, Paul, Hrein, Tanja, Karin, Melissa, Anke, Dave, Helene, Paul, Koen, Arno, Cristina, Leendert, Joris, Brigitte, Rob, Anouk, Amber, Renata en Chatelene. De feestcommissie!

Hermelijn en Maria van de afdeling Parasitologie, Marco van Kindergeneeskunde, bedankt voor jullie steun.

De klinische afdelingen: MDL, Ilse, Hein, Marieke en Andrea in het bijzonder, superbedankt; Kindergeneeskunde, Joachim, Carline en Luisa; Alrijne Ziekenhuis, Sunje, Cees en Anne; Embryologie, Susana; VUMC, Chris en Gerd; en Erasmus MC, Hankje, Janneke en *bright spark* Linda. Jullie enorme inzet voor het verkrijgen van klinisch materiaal was essentieel. Ook dank aan alle betrokken patiënten voor hun participatie aan de CyTOF studies.

The bright computer scientists from the LUMC and TU Delft, Thomas, Nicola, Antonios, Tamim, Mine, Elmar, Anna, Ahmed, Marcel and Boudewijn. Our fruitful collaboration led to efficient analyses of complex data and yielded in the development of Cytosplore and HSNE. Thanks!

Yiruma pianomuziek voor de concentratie tijdens het schrijven van manuscripts.

Mijn BW-studievrienden 'Stockholm Chicks', Xiamyra Pauline, Lianne, Suzanne en Anita (*for your support*). Superfijne vriendschap!

Iedereen van dansschool Tribes Leiden, met name Rosa en Willemieke, dank jullie wel! Zonder mijn passie dans (en yoga) was ik mentaal niet zo veerkrachtig geweest gedurende mijn promotietraject. Marlieke, mijn dans en wetenschapmaatje, bedankt.

Mijn ouders en familie wil ik graag bedanken voor de wijze raad, belangstelling en luisterend oor. Jullie staan altijd voor mij klaar. Ik ben trots op mijn tweelingbroertje Jack en zus Deborah.

Als laatste mijn beste vriendin, huisgenote en paranimf. Lieve Lianne, bedankt voor jouw onvoorwaardelijke vriendschap, liefde en inspiratie.

